

Advances in Civil Engineering

Evaluation of Longwall Face Stability and Face Fall Control

Lead Guest Editor: Gao-Feng Song

Guest Editors: Ruimin Feng and Yi-Min Song





Evaluation of Longwall Face Stability and Face Fall Control

Advances in Civil Engineering

Evaluation of Longwall Face Stability and Face Fall Control

Lead Guest Editor: Gao-Feng Song

Guest Editors: Ruimin Feng and Yi-Min Song



Copyright © 2022 Hindawi Limited. All rights reserved.

This is a special issue published in "Advances in Civil Engineering." All articles are open access articles distributed under the Creative Commons Attribution License, which permits unrestricted use, distribution, and reproduction in any medium, provided the original work is properly cited.






Chief Editor

Cumaraswamy Vipulanandan, USA










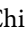



Associate Editors

Chiara Bedon , Italy
Constantin Chaliotis , Greece
Ghassan Chehab , Lebanon
Ottavia Corbi, Italy
Mohamed ElGawady , USA
Husnain Haider , Saudi Arabia
Jian Ji , China
Jiang Jin , China
Shazim A. Memon , Kazakhstan
Hossein Moayedi , Vietnam
Sanjay Nimbalkar, Australia
Giuseppe Oliveto , Italy
Alessandro Palmeri , United Kingdom
Arnaud Perrot , France
Hugo Rodrigues , Portugal
Victor Yepes , Spain
Xianbo Zhao , Australia

Academic Editors

José A.F.O. Correia, Portugal
Glenda Abate, Italy
Khalid Abdel-Rahman , Germany
Ali Mardani Aghabaglou, Turkey
José Aguiar , Portugal
Afaq Ahmad , Pakistan
Muhammad Riaz Ahmad , Hong Kong
Hashim M.N. Al-Madani , Bahrain
Luigi Aldieri , Italy
Angelo Aloisio , Italy
Maria Cruz Alonso, Spain
Filipe Amarante dos Santos , Portugal
Serji N. Amirkhanean, USA
Eleftherios K. Anastasiou , Greece
Panagiotis Ch. Anastasopoulos , USA
Mohamed Moafak Arbili , Iraq
Farhad Aslani , Australia
Siva Avudaiappan , Chile
Ozgur BASKAN , Turkey
Adewumi Babafemi, Nigeria
Morteza Bagherpour, Turkey
Qingsheng Bai , Germany
Nicola Baldo , Italy
Daniele Baraldi , Italy

Eva Barreira , Portugal
Emilio Bastidas-Arteaga , France
Rita Bento, Portugal
Rafael Bergillos , Spain
Han-bing Bian , China
Xia Bian , China
Huseyin Bilgin , Albania
Giovanni Biondi , Italy
Hugo C. Biscaia , Portugal
Rahul Biswas , India
Edén Bojórquez , Mexico
Giosuè Boscato , Italy
Melina Bosco , Italy
Jorge Branco , Portugal
Bruno Briseghella , China
Brian M. Broderick, Ireland
Emanuele Brunesi , Italy
Quoc-Bao Bui , Vietnam
Tan-Trung Bui , France
Nicola Buratti, Italy
Gaochuang Cai, France
Gladis Camarini , Brazil
Alberto Campisano , Italy
Qi Cao, China
Qixin Cao, China
Iacopo Carnacina , Italy
Alessio Cascardi, Italy
Paolo Castaldo , Italy
Nicola Cavalagli , Italy
Liborio Cavaleri , Italy
Anush Chandrappa , United Kingdom
Wen-Shao Chang , United Kingdom
Muhammad Tariq Amin Chaudhary, Kuwait
Po-Han Chen , Taiwan
Qian Chen , China
Wei Tong Chen , Taiwan
Qixiu Cheng, Hong Kong
Zhanbo Cheng, United Kingdom
Nicholas Chileshe, Australia
Prinya Chindaprasirt , Thailand
Corrado Chisari , United Kingdom
Se Jin Choi , Republic of Korea
Heap-Yih Chong , Australia
S.H. Chu , USA
Ting-Xiang Chu , China

Zhaofei Chu , China
Wonseok Chung , Republic of Korea
Donato Ciampa , Italy
Gian Paolo Cimellaro, Italy
Francesco Colangelo, Italy
Romulus Costache , Romania
Liviu-Adrian Cotfas , Romania
Antonio Maria D'Altri, Italy
Bruno Dal Lago , Italy
Amos Darko , Hong Kong
Arka Jyoti Das , India
Dario De Domenico , Italy
Gianmarco De Felice , Italy
Stefano De Miranda , Italy
Maria T. De Risi , Italy
Tayfun Dede, Turkey
Sadik O. Degertekin , Turkey
Camelia Delcea , Romania
Cristoforo Demartino, China
Giuseppe Di Filippo , Italy
Luigi Di Sarno, Italy
Fabio Di Trapani , Italy
Aboelkasim Diab , Egypt
Thi My Dung Do, Vietnam
Giulio Dondi , Italy
Jiangfeng Dong , China
Chao Dou , China
Mario D'Aniello , Italy
Jingtao Du , China
Ahmed Elghazouli, United Kingdom
Francesco Fabbrocino , Italy
Flora Faleschini , Italy
Dingqiang Fan, Hong Kong
Xueping Fan, China
Qian Fang , China
Salar Farahmand-Tabar , Iran
Ilenia Farina, Italy
Roberto Fedele, Italy
Guang-Liang Feng , China
Luigi Fenu , Italy
Tiago Ferreira , Portugal
Marco Filippo Ferrotto, Italy
Antonio Formisano , Italy
Guoyang Fu, Australia
Stefano Galassi , Italy

Junfeng Gao , China
Meng Gao , China
Giovanni Garcea , Italy
Enrique García-Macías, Spain
Emilio García-Taengua , United Kingdom
DongDong Ge , USA
Khaled Ghaedi, Malaysia
Khaled Ghaedi , Malaysia
Gian Felice Giaccu, Italy
Agathoklis Giaralis , United Kingdom
Ravindran Gobinath, India
Rodrigo Gonçalves, Portugal
Peilin Gong , China
Belén González-Fonteboa , Spain
Salvatore Grasso , Italy
Fan Gu, USA
Erhan Güneyisi , Turkey
Esra Mete Güneyisi, Turkey
Pingye Guo , China
Ankit Gupta , India
Federico Gusella , Italy
Kemal Hacıefendioğlu, Turkey
Jianyong Han , China
Song Han , China
Asad Hanif , Macau
Hadi Hasanzadehshooiili , Canada
Mostafa Fahmi Hassanein, Egypt
Amir Ahmad Hedayat , Iran
Khandaker Hossain , Canada
Zahid Hossain , USA
Chao Hou, China
Biao Hu, China
Jiang Hu , China
Xiaodong Hu, China
Lei Huang , China
Cun Hui , China
Bon-Gang Hwang, Singapore
Jijo James , India
Abbas Fadhil Jasim , Iraq
Ahad Javanmardi , China
Krishnan Prabhakan Jaya, India
Dong-Sheng Jeng , Australia
Han-Yong Jeon, Republic of Korea
Pengjiao Jia, China
Shaohua Jiang , China

MOUSTAFA KASSEM , Malaysia
Mosbeh Kaloop , Egypt
Shankar Karuppannan , Ethiopia
John Kechagias , Greece
Mohammad Khajehzadeh , Iran
Afzal Husain Khan , Saudi Arabia
Mehran Khan , Hong Kong
Manoj Khandelwal, Australia
Jin Kook Kim , Republic of Korea
Woosuk Kim , Republic of Korea
Vaclav Koci , Czech Republic
Loke Kok Foong, Vietnam
Hailing Kong , China
Leonidas Alexandros Kouris , Greece
Kyriakos Kourousis , Ireland
Moacir Kripka , Brazil
Anupam Kumar, The Netherlands
Emma La Malfa Ribolla, Czech Republic
Ali Lakirouhani , Iran
Angus C. C. Lam, China
Thanh Quang Khai Lam , Vietnam
Luciano Lamberti, Italy
Andreas Lampropoulos , United Kingdom
Raffaele Landolfo, Italy
Massimo Latour , Italy
Bang Yeon Lee , Republic of Korea
Eul-Bum Lee , Republic of Korea
Zhen Lei , Canada
Leonardo Leonetti , Italy
Chun-Qing Li , Australia
Dongsheng Li , China
Gen Li, China
Jiale Li , China
Minghui Li, China
Qingchao Li , China
Shuang Yang Li , China
Sunwei Li , Hong Kong
Yajun Li , China
Shun Liang , China
Francesco Liguori , Italy
Jae-Han Lim , Republic of Korea
Jia-Rui Lin , China
Kun Lin , China
Shibin Lin, China

Tzu-Kang Lin , Taiwan
Yu-Cheng Lin , Taiwan
Hexu Liu, USA
Jian Lin Liu , China
Xiaoli Liu , China
Xuemei Liu , Australia
Zaobao Liu , China
Zhuang-Zhuang Liu, China
Diego Lopez-Garcia , Chile
Cristiano Loss , Canada
Lyan-Ywan Lu , Taiwan
Jin Luo , USA
Yanbin Luo , China
Jianjun Ma , China
Junwei Ma , China
Tian-Shou Ma, China
Zhongguo John Ma , USA
Maria Macchiaroli, Italy
Domenico Magisano, Italy
Reza Mahinroosta, Australia
Yann Malecot , France
Prabhat Kumar Mandal , India
John Mander, USA
Iman Mansouri, Iran
André Dias Martins, Portugal
Domagoj Matesan , Croatia
Jose Matos, Portugal
Vasant Matsagar , India
Claudio Mazzotti , Italy
Ahmed Mebarki , France
Gang Mei , China
Kasim Mermerdas, Turkey
Giovanni Minafò , Italy
Masoomah Mirrashid , Iran
Abbas Mohajerani , Australia
Fadzli Mohamed Nazri , Malaysia
Fabrizio Mollaioli , Italy
Rosario Montuori , Italy
H. Naderpour , Iran
Hassan Nasir , Pakistan
Hossein Nassiraei , Iran
Satheeskumar Navaratnam , Australia
Ignacio J. Navarro , Spain
Ashish Kumar Nayak , India
Behzad Nematollahi , Australia

Chayut Ngamkhanong , Thailand
Trung Ngo, Australia
Tengfei Nian, China
Mehdi Nikoo , Canada
Youjun Ning , China
Olugbenga Timo Oladinrin , United Kingdom
Oladimeji Benedict Olalusi, South Africa
Timothy O. Olawumi , Hong Kong
Alejandro Orfila , Spain
Maurizio Orlando , Italy
Siti Aminah Osman, Malaysia
Walid Oueslati , Tunisia
SUVASH PAUL , Bangladesh
John-Paris Pantouvakis , Greece
Fabrizio Paolacci , Italy
Giuseppina Pappalardo , Italy
Fulvio Parisi , Italy
Dimitrios G. Pavlou , Norway
Daniele Pellegrini , Italy
Gatheeshgar Perampalam , United Kingdom
Daniele Perrone , Italy
Giuseppe Piccardo , Italy
Vagelis Plevris , Qatar
Andrea Pranno , Italy
Adolfo Preciado , Mexico
Chongchong Qi , China
Yu Qian, USA
Ying Qin , China
Giuseppe Quaranta , Italy
Krishanu ROY , New Zealand
Vlastimir Radonjanin, Serbia
Carlo Rainieri , Italy
Rahul V. Ralegaonkar, India
Raizal Saifulnaz Muhammad Rashid, Malaysia
Alessandro Rasulo , Italy
Chonghong Ren , China
Qing-Xin Ren, China
Dimitris Rizos , USA
Geoffrey W. Rodgers , New Zealand
Pier Paolo Rossi, Italy
Nicola Ruggieri , Italy
JUNLONG SHANG, Singapore


Nikhil Saboo, India
Anna Saetta, Italy
Juan Sagaseta , United Kingdom
Timo Saksala, Finland
Mostafa Salari, Canada
Ginevra Salerno , Italy
Evangelos J. Sapountzakis , Greece
Vassilis Sarhosis , United Kingdom
Navaratnarajah Sathiparan , Sri Lanka
Fabrizio Scozzese , Italy
Halil Sezen , USA
Payam Shafigh , Malaysia
M. Shahria Alam, Canada
Yi Shan, China
Hussein Sharaf, Iraq
Mostafa Sharifzadeh, Australia
Sanjay Kumar Shukla, Australia
Amir Si Larbi , France
Okan Sirin , Qatar
Piotr Smarzewski , Poland
Francesca Sollecito , Italy
Rui Song , China
Tian-Yi Song, Australia
Flavio Stochino , Italy
Mayank Sukhija , USA
Piti Sukontasukkul , Thailand
Jianping Sun, Singapore
Xiao Sun , China
T. Tafsirojjaman , Australia
Fujiao Tang , China
Patrick W.C. Tang , Australia
Zhi Cheng Tang , China
Weerachart Tangchirapat , Thailand
Xiixin Tao, China
Piergiorgio Tataranni , Italy
Elisabete Teixeira , Portugal
Jorge Iván Tobón , Colombia
Jing-Zhong Tong, China
Francesco Trentadue , Italy
Antonello Troncone, Italy
Majbah Uddin , USA
Tariq Umar , United Kingdom
Muahmmad Usman, United Kingdom
Muhammad Usman , Pakistan
Mucteba Uysal , Turkey

Ilaria Venanzi , Italy
Castorina S. Vieira , Portugal
Valeria Vignali , Italy
Claudia Vitone , Italy
Liwei WEN , China
Chunfeng Wan , China
Hua-Ping Wan, China
Roman Wan-Wendner , Austria
Chaohui Wang , China
Hao Wang , USA
Shiming Wang , China
Wayne Yu Wang , United Kingdom
Wen-Da Wang, China
Xing Wang , China
Xiuling Wang , China
Zhenjun Wang , China
Xin-Jiang Wei , China
Tao Wen , China
Weiping Wen , China
Lei Weng , China
Chao Wu , United Kingdom
Jiangyu Wu, China
Wangjie Wu , China
Wenbing Wu , China
Zhixing Xiao, China
Gang Xu, China
Jian Xu , China
Panpan , China
Rongchao Xu , China
HE YONGLIANG, China
Michael Yam, Hong Kong
Hailu Yang , China
Xu-Xu Yang , China
Hui Yao , China
Xinyu Ye , China
Zhoujing Ye, China
Gürol Yildirim , Turkey
Dawei Yin , China
Doo-Yeol Yoo , Republic of Korea
Zhanping You , USA
Afshar A. Yousefi , Iran
Xinbao Yu , USA
Dongdong Yuan , China
Geun Y. Yun , Republic of Korea


Hyun-Do Yun , Republic of Korea
Cemal YİĞİT , Turkey
Paolo Zampieri, Italy
Giulio Zani , Italy
Mariano Angelo Zanini , Italy
Zhixiong Zeng , Hong Kong
Mustafa Zeybek, Turkey
Henglong Zhang , China
Jiupeng Zhang, China
Tingting Zhang , China
Zengping Zhang, China
Zetian Zhang , China
Zhigang Zhang , China
Zhipeng Zhao , Japan
Jun Zhao , China
Annan Zhou , Australia
Jia-wen Zhou , China
Hai-Tao Zhu , China
Peng Zhu , China
QuanJie Zhu , China
Wenjun Zhu , China
Marco Zucca, Italy
Haoran Zuo, Australia
Junqing Zuo , China
Robert Černý , Czech Republic
Süleyman İpek , Turkey

Contents

Model Test Study on Overburden Failure and Fracture Evolution Characteristics of Deep Stope with Variable Length

Xinfeng Wang , Youyu Wei, Heyong Yuan, Yiyang Zhang, Qiao Zhang, and Wengang Liu
Research Article (16 pages), Article ID 9818481, Volume 2022 (2022)



Study of Instability Mechanism and Roof Caving Mode of Cementing Filling Stope: The Case Study of a Nonferrous Metal Mine in China

Min Zhong , Peng Yang, and Ying-Peng Hu 
Research Article (20 pages), Article ID 1658021, Volume 2022 (2022)


Research on Natural Foundation Bearing Capacity and Foundation Pit Settlement of Prefabricated Utility Tunnel

Zengshan Wang, Yanying Wang, Weike Huang, Hongwei Shan, and Li Zhu 
Research Article (11 pages), Article ID 5361199, Volume 2022 (2022)


The Study on the Characteristics of Pressure Arch above the Twin-Parallel Openings in the Jointed Rock Masses

Kunpeng Gao , Kang Liang , Leyao Wang, Changhao Li, Jinghai Yu, and Runyi Wu
Research Article (13 pages), Article ID 7943151, Volume 2022 (2022)


Coal and Gas Comining in the High-Gas Detong Mine, China: Analytical and Numerical Parameter Optimization of Gas Extraction Boreholes

Wei Wang , Zongxiang Li , Guangmin Zhao , and Yujin Chen 
Research Article (12 pages), Article ID 9552620, Volume 2022 (2022)


The Study on the Substrate Effect in the Nanoindentation Experiment of the Hybrid Material

Kang Liang, Kunpeng Gao , and Wenqing Cai
Research Article (11 pages), Article ID 5031865, Volume 2022 (2022)



Surrounding Rock Stability Classification Method of Coal Roadway Based on In Situ Stress

Yongjie Yang , Gang Huang , and Lingren Meng
Research Article (11 pages), Article ID 4493220, Volume 2021 (2021)

Temperature Control Technology for Construction of Jinsha River Bridge

Hui-Wu Jin , Guo-An Wang, and Zhan-Ming Chen
Research Article (14 pages), Article ID 3452167, Volume 2021 (2021)

Analysis of the Influence of Upper Protective Layer Mining on the Effect of Pressure Relief and Protection of Coal and Rock Masses between the Lower Overburden Layers

Jiaxin Dang , Min Tu , Xiangyang Zhang , and Qingwei Bu 
Research Article (16 pages), Article ID 8682156, Volume 2021 (2021)

A Novel Evaluation Method of Hydrogen Production from Coal Based on AHP and GRA-TOPSIS

Shuheng Zhong, Kangdi Yang , and Yongji Wang
Research Article (9 pages), Article ID 8991994, Volume 2021 (2021)

Research Article

Model Test Study on Overburden Failure and Fracture Evolution Characteristics of Deep Stope with Variable Length

Xinfeng Wang ¹, Youyu Wei,¹ Heyong Yuan,² Yiyong Zhang,¹ Qiao Zhang,¹ and Wengang Liu¹

¹College of Environment and Resources, Xiangtan University, Xiangtan, Hunan 411105, China

²Department of Civil Engineering, Anhui Communications Vocational & Technical College, Hefei, Anhui 230051, China

Correspondence should be addressed to Xinfeng Wang; wangxinfeng110@126.com

Received 10 March 2022; Revised 2 July 2022; Accepted 6 July 2022; Published 19 July 2022

Academic Editor: Qian Chen

Copyright © 2022 Xinfeng Wang et al. This is an open access article distributed under the Creative Commons Attribution License, which permits unrestricted use, distribution, and reproduction in any medium, provided the original work is properly cited.

Taking two typical stopes with variable length of working face inclined length from small to large and from large to small as the research object, the stope overburden structure model under different face length conditions is constructed through laboratory similar material simulation test, and the dynamic evolution laws of overburden instability deformation, unloading expansion, and collapse failure of forward and reverse knife handle stopes are analyzed. The three-dimensional perspective technology of parallel network electrical method is used to study the spatial distribution range and fracture development characteristics of overburden internal failure. The research shows that the overburden fracture of stope with variable length has the “time-pace-scale” evolution effect of short-time sudden change, zoning load transfer, and continuous extension. The evolution of roof fracture has experienced the development process of unloading expansion, tensile fracture instability, shrinkage deformation, and closure stability. The rise and fall of resistivity during mining in stope with variable length is closely related to the mining time step. When mining 40 cm, it is the position where the resistivity value changes suddenly. The rise of resistivity in the vertical direction makes the electric field show the transient response characteristics of dynamic expansion and rapid evolution. The development height of water conducting fracture zone of the reverse knife handle working face with the inclined length changing from large to small is slightly larger, the degree of overburden damage is high, and the fracture development is relatively sufficient.

1. Introduction

The activity of the surrounding rock in the stope is the source of the formation of mine pressure, and the appearance of the mine pressure is the specific manifestation of the activity of the surrounding rock in the stope. The root of all strata behavior in stope is the movement of upper strata caused by the mining field. Due to the differences in the surrounding rock properties, bedding structure, strength thickness, joint structure, and layer relationship of the overlying strata, the roof activity shows a variety of movement forms, and the structural characteristics of the roof determine the movement characteristics of the roof. The prevention and control concept and decision-making play a key factor [1–3], in view of the complexity and diversity of erosion rock movement, in order to

comprehensively and systematically grasp the spatial failure pattern of the roof, the instability and deformation characteristics of the surrounding rock, the migration law of overlying rock, and the characteristics of strata behavior in stope with variable length. It is necessary to conduct real-time observation and analysis on the whole process of roof fracture, roof breaking, and fracture development and evolution on the basis of profound analysis of roof spatial structure and surrounding rock characteristics [4–7]. This is important to obtain the spatial-temporal evolution law of overlying fracture field, roof displacement field, and surrounding rock fracture field, which lays a solid theoretical foundation for the study of surrounding rock control system [8–10].

Mining scholars have studied the deformation failure characteristics and dynamic response mechanism of

surrounding rock in stope with variable length. Based on the relationship between the overburden structure and the influence of large-scale breaking motion on the failure of coal and rock mass, Zhu et al. [11] studied the induced scouring mechanism of the combination mode of dynamic and static loads of the isolated island coal pillar in the irregular working face with large burial depth. Pan [12] took the occurrence principle of rock burst on the floor of all-coal roadway in the semi-isolated island working face as the research goal, established a structural model to induce underground impact pressure in the roadway, and proposed the shock initiation theory of dynamic damage of the surrounding rock of the roadway. Yang et al. [13] used the theory of overburden rock's space structure to analyze the potential area and degree of impact danger of the working face for the deeply buried irregular isolated island working face and established the use of stress online monitoring system to predict the outburst proneness of coal rock. Li et al. [7] analyzed the movement law and stress evolution characteristics of the overburden structure in the step area of the variable-length working face of Yangcheng Coal Mine. Hao et al. [14] studied the constraints and mechanical origins of dynamic disasters triggered by mining surrounding rock in the island working face with variable length and put forward the evaluation criteria for the prevention and control of shock disasters and safe and efficient mining. Around the failure characteristics of the roof surrounding rock of the coal face under different working conditions, the evolution law of the microstructure of the coal and rock mass, the distribution characteristics of the in situ stress field, and the stability control technology of the roof surrounding rock, relevant scholars have also carried out systematic research, revealing the internal mechanism of the deformation and failure of the surrounding rock of the deep stope [15–18].

To sum up, the research on the deformation, failure, and stress evolution law of surrounding rock in stope with variable length is more focused on theoretical analysis and numerical simulation, and the engineering research under experimental conditions can be used to verify the theoretical results. Laboratory similar material simulation test is a model test technology based on similarity theory. It is an important method to study natural law and solve complex engineering problems by using similarity and similar characteristics between things or phenomena. It can make up for the shortcomings of on-site monitoring and reveal the mechanical and kinematic characteristics of the simulated prototype [19–21]. Similar material simulation test is an important method to study the movement and deformation law and stress distribution characteristics of surrounding rock in the process of coal mining. With the help of physical mechanics and material science research theory, through the observation and analysis of displacement deformation, load failure, and stress-strain of the model, it can fully grasp the spatial fracture form and mechanical evolution law of stope surrounding rock [22, 23] and provide important reference value for field practice and engineering application.

2. Test Purpose and Object

2.1. Test Purpose. With the diversification of coal mining methods and the complexity of the mining environment, the working face is often affected by geological structure, folded faults, rock formation, mining conditions, and other factors, resulting in the increase or shortening of the oblique length of the working face, and mining has increased. Since most of the working faces with variable length in coal mines are mutation-type working faces, and the change mode is single, and the mining methods of multivariable working faces are relatively few. Two types of “knife-handle-style” changing face long stopes are analyzed and discussed. Through quantitative observation and qualitative research on the roof fracture shape, overlying rock migration characteristics, and crack evolution process during the mining of forward and reverse knife handle coal seams, the law of overburden deformation and failure of long stope with variable face and long stope are obtained. The evolution characteristics of fractures provide an important reference for roof management and surrounding rock prevention and control in stope with variable length.

2.2. Test Object. This similar material simulation test took the geological conditions of a stope with variable length in Huainan mining area as the research background and simulated the mining conditions of two stopes with variable length, including the forward knife handle working face and the reverse knife handle working face. The variable-length working face is 1200 m long in direction and 120–240 m long in inclination. The small plane with an inclined length of 120 m is 400 m long, and the large plane with an inclined length of 240 m is 800 m long. The advance of the working face starts from the small face to the large face, and the transition interval is the key docking area. The coal seam on this face was dominated by 13-1 coal, the total thickness of the coal seam is 3.1–5.0 m, and the average coal thickness is 3.9 m. The dip angle of the coal seam is 2–15°, the average dip angle is 7°, and the occurrence is stable. The direct roof of the working face is a composite roof composed of mudstone and 13-2 coal, with an average thickness of 3.7 m; the old roof is made of fine sandstone, with an average thickness of 10.6 m. Local fractures are developed, the connectivity and water-richness are weak, and the static storage is the main factor. The sandstone fracture aquifer on the roof of the 13-1 coal seam is the main water filling factor for this face, and it mainly enters the working face in the form of dripping water, which has little effect on the recovery. By drilling cores on the roof of the coal seam along the track 13-1 of the test working face and carrying out physic-mechanical property experiments on the rock samples taken, the mechanical parameters of the rock layers in each layer are obtained, which provides a basis for the design of model parameters.

3. Test Model Design and Monitoring Method

3.1. Design of Model Test System. This test was carried out on a three-dimensional model test platform. The three-dimensional test platform is a similar material simulation

device independently developed by the mining laboratory of Anhui University of Science and Technology, which can simulate the failure of overlying rocks in three-dimensional space. The geometric dimensions of the test platform are length \times width \times height = 2 m \times 1 m \times 2 m, and high-strength multilayer iron blocks are used to apply the load vertically. The geometric similarity ratio of the test model is 1 : 150, and the geometric size of the model is designed as length \times width \times height = 2 m \times 1 m \times 1 m, which is equivalent to the simulated stratum thickness of 150 m. Since the similar model test of the irregular stope needs to simulate the two variable-length working faces of forward knife handle, considering the size limitation of the test platform and the influence of boundary effect, the forward knife handle working face is selected. The oblique length was designed to be 80 to 160 cm, which was equivalent to the oblique length of the on-site working face of 120 to 240 m. The oblique length of the reverse knife handle working face was designed to be 80~160 cm, which was equivalent to the oblique length of the on-site working face of 120 m to 240 m. The length direction of the test platform was the oblique length direction of working face, and the width direction of the test platform was regarded as the direction of working face. The working face was pushed forward and parallel along the width direction of the platform, and 10 cm boundary coal pillars were left on both sides of the front and rear of the model to eliminate the boundary effect during mining. Protect the coal pillars to ensure normal advancement during mining at the face. The three-dimensional mining model of “knife-handle-style” variable-length working face is shown in Figure 1, and the schematic diagram of the plane model is shown in Figure 2.

According to the similarity principle and dimensional analysis requirements, combined with the lithology, bulk density, strength, and other field conditions of the roof-floor of coal seam, the similar parameters in the model are converted, and the corresponding ratio is determined. Similar materials use fine sand as aggregate, and lime and gypsum as cement. In order to accurately determine the ratio of similar materials to obtain the required parameters, a large number of standard specimens were specially selected for physical and mechanical tests, and the material ratio is adjusted through repeated tests. And finally the best ratio table of similar materials for each layer is obtained, as shown in Table 1. According to the requirements of the optimal proportion table, determine the material proportion, bulk density, layer thickness, and model size to calculate the dosage and then make a model according to the dosage requirements and sprinkle mica powder between each layer to play a layering role. In the actual model making process, because the coal seam mining of the three-dimensional model was more complicated, the coal seam can be replaced by thin wood strips of similar thickness. According to the test requirements, 8 short wood strips with a length of 80 cm, a width of 5 cm, and a thickness of 2.6 cm can be processed and made, and at the same time, 8 long wood strips with a length of 160 cm, a width of 5 cm, and a thickness of 2.6 cm can be processed and made, a total of 16 wood strips. The surrounding of the wooden strips was wrapped with

transparent tape to reduce friction. During the test process, when laying on the coal seam, all thin wooden strips were used instead. At the same time, the wooden strips are slowly pulled out to implement isometric advancement, and each time a wooden strip is pulled out is equivalent to advancing 5 cm on the working face. The coal seam of the forward knife handle working face was along the model trend (i.e., width direction), which first lay 8 short wooden strips with a length of 80 cm and then lay 8 long wooden strips with a length of 160 cm. While the laying sequence of the reverse knife handle working face was on the contrary, in the coal-bearing rock layer, 8 long wooden strips with a length of 160 cm were first laid along the model direction, and then 8 short wooden strips with a length of 80 cm were laid. The position of the eighth wooden strip was the position where the oblique length of the working face changes.

3.2. Test Monitoring Method. The self-developed parallel direct current method was used to detect the abnormal space of the overlying rock damage in the forward and reverse knife handle stope, and the three-dimensional space perspective technology of the parallel electric method was used to study the spatial distribution range and fracture development status of the internal damage of the overlying rock.

The advantage of the parallel network electrical measuring instrument is that any electrode was powered, and the potential measurement can be performed on all the other electrodes at the same time, which can clearly reflect the natural potential of the detection area and the change of the primary power field potential, and the data acquisition efficiency is greatly improved. According to the different forms of power supply, the data acquisition methods of parallel electrical method are divided into monopole powered AM method and dipole powered ABM method. The layout of AM method is the same as that of the secondary method, and the potential is collected as a single point. When one electrode supplies power, the electrode is a pole, and the remaining electrode is m pole for potential data collection. For the data collected by this method, the resistivity data of two pole and three pole devices can be extracted for inversion through postprocessing, and at the same time, high-density electrical detection can be realized. ABM electrical data acquisition is powered by dipoles; that is, two electrodes A and B are powered at the same time, without using infinite electrodes, and only a reference electrode n is set near the instrument. The data collected by this method include all the data required by all quadrupole devices. It can obtain the data measured by all kinds of quadrupole arrangement devices through one measurement, which greatly improves the collection efficiency, and the data measured by the electrodes are synchronous, which reduces the error of the collection system. For example, when 64 electrodes were arranged on the measuring line, when the AM method was used for acquisition, during the power supply of any electrode, the remaining 63 electrodes simultaneously collected the potential, so that the data acquisition efficiency was at least 63 times higher than that of

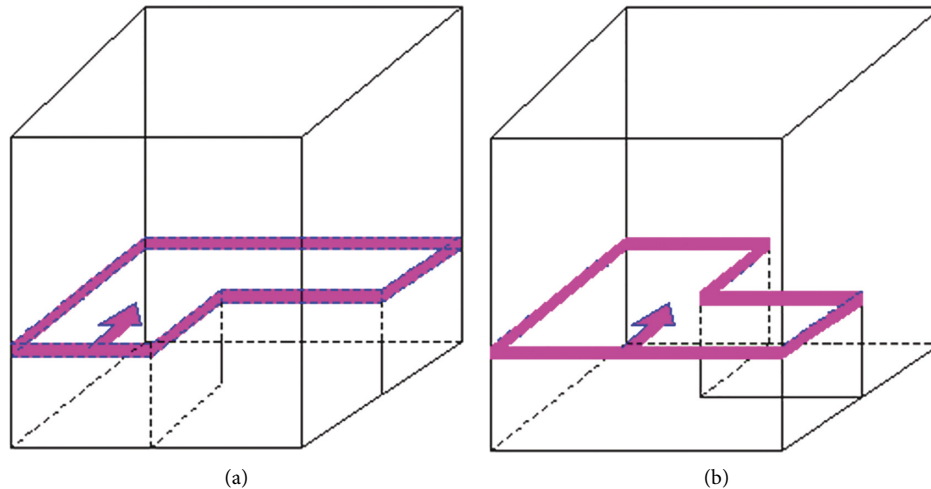


FIGURE 1: The three-dimensional mining model of working face with variable length. (a) Forward knife handle working face. (b) Reverse knife handle working face.

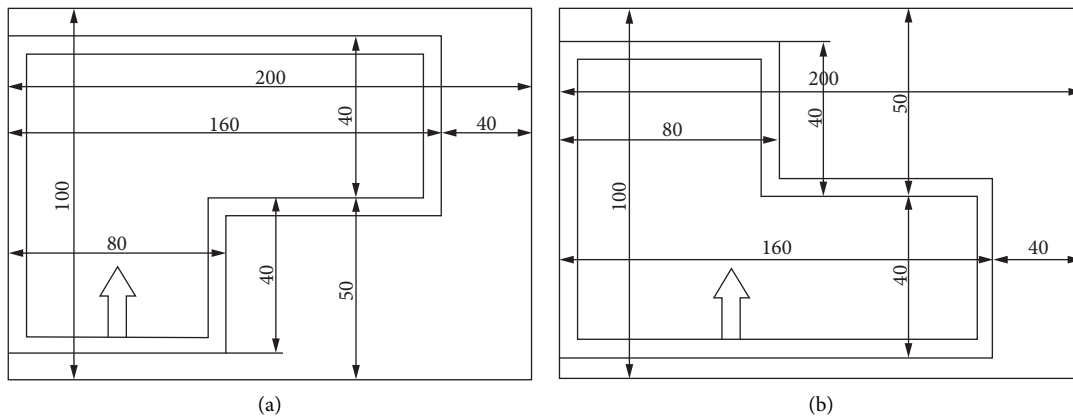


FIGURE 2: Plane model diagram of working face with variable length (unit: cm). (a) Forward knife handle working face. (b) Reverse knife handle working face.

the series acquisition. Moreover, the AM method and ABM method were used to automatically switch the electrodes in order to obtain a large number of electrical data, which can not only decompile all the data detected by the current DC high-density resistivity method but also realize the inversion of high resolution resistivity method, and good monitoring results were achieved. During observation period, the AM method data acquisition was performed using the electrode system in a single borehole, and the electrode current data were used for inversion. In order to highlight the change effect, a unified icon was used for the current ratio result image, and cold and warm tones of different colors are used to represent the degree of current change.

The experiment adopts the method of laying two layers of electrodes to collect and analyze the three-dimensional electric field spatial data. The electrode of the first layer was laid 15 cm above the coal seam of the test model, and the actual control failure height of the overlying rock was 22.5 m. Then a total of 48 electrodes were arranged, and the distance between adjacent electrodes was 3 cm. It was divided into two sides, and 24 electrodes are arranged on each side. The

specific size layout was shown in Figure 3(a). The electrode of the second layer was laid at a position 40 cm above the coal seam of the test model, and the actual control failure height of the overlying rock was 60 m. A total of 64 electrodes are arranged on the second layer, and the electrode spacing was 3 cm. It was also divided into two sides, and 32 electrodes are arranged on each side. The specific size layout was shown in Figure 3(b).

The two tests were conducted over a total of 10 days, with each test lasting for 5 days, including the installation of the test system, background value testing, data acquisition during mining, postmining stability observations, and dismantling of the observation system. The data were decompiled, dedistorted, and exported using AGI's Earth-Imager 3D software. The electrode position 1# of the 2 layers above the coal seam was taken as the coordinate origin (0, 0, 0), and the model was taken to the right as the positive x -axis direction, inwards as the positive z -axis direction and downwards as the positive z -axis direction to establish a 3D three-dimensional spatial coordinate system, as shown in Figure 4.

TABLE 1: The comparison table of the field conditions of working face and simulation parameter.

| Rock name | Prototype parameters | | | Model parameter | | | Material ratio | Water ratio |
|------------------|----------------------|----------------------------|--|-----------------|----------------------------|--|----------------|-------------|
| | Thickness (m) | Compressive strength (MPa) | Volumetric weight (kg/m ³) | Thickness (cm) | Compressive strength (MPa) | Volumetric weight (kg/m ³) | | |
| Gravel stratum | 16.3 | 140.13 | 2894 | 10.9 | 0.78 | 1608 | 9:0.5:0.5 | 1/10 |
| Sandy mudstone | 21.9 | 21.06 | 2538 | 14.6 | 0.12 | 1410 | 8:0.7:0.3 | 1/10 |
| Medium sandstone | 2.1 | 137.68 | 3390 | 1.4 | 0.76 | 1883 | 5:0.6:0.4 | 1/10 |
| Spotted mudstone | 10.2 | 34.72 | 2568 | 6.8 | 0.19 | 1427 | 9:0.7:0.3 | 1/10 |
| Medium sandstone | 3.2 | 129.60 | 3410 | 2.1 | 0.72 | 1894 | 5:0.6:0.4 | 1/10 |
| Sandy mudstone | 14.7 | 20.89 | 2507 | 9.8 | 0.12 | 1393 | 8:0.7:0.3 | 1/10 |
| Fine sandstone | 9.2 | 113.85 | 3143 | 6.1 | 0.63 | 1746 | 6:0.6:0.4 | 1/10 |
| Sandy mudstone | 9.4 | 27.53 | 2564 | 6.3 | 0.15 | 1425 | 8:0.7:0.3 | 1/10 |
| Fine sandstone | 10.3 | 108.62 | 2920 | 6.9 | 0.60 | 1622 | 6:0.6:0.4 | 1/10 |
| Sandy mudstone | 2.1 | 30.59 | 2550 | 1.4 | 0.18 | 1417 | 8:0.7:0.3 | 1/10 |
| Sandstone | 1.6 | 91.24 | 2815 | 1.1 | 0.51 | 1564 | 5:0.6:0.4 | 1/10 |
| Shale | 1.8 | 41.73 | 2595 | 1.2 | 0.23 | 1442 | 7:0.7:0.3 | 1/10 |
| 13-1 coal seam | 3.9 | 8.2 | 1326 | 2.6 | 0.05 | 737 | 10:0.5:0.5 | 1/10 |
| Mudstone | 4.1 | 28.24 | 2638 | 2.7 | 0.16 | 1465 | 7:0.7:0.3 | 1/10 |
| Sandy mudstone | 7.2 | 27.89 | 2520 | 4.8 | 0.15 | 1400 | 8:0.7:0.3 | 1/10 |
| Medium sandstone | 16.1 | 141.76 | 3426 | 10.7 | 0.79 | 1903 | 5:0.6:0.4 | 1/10 |
| Mudstone | 15.0 | 29.62 | 2530 | 10.0 | 0.17 | 1406 | 8:0.7:0.3 | 1/10 |

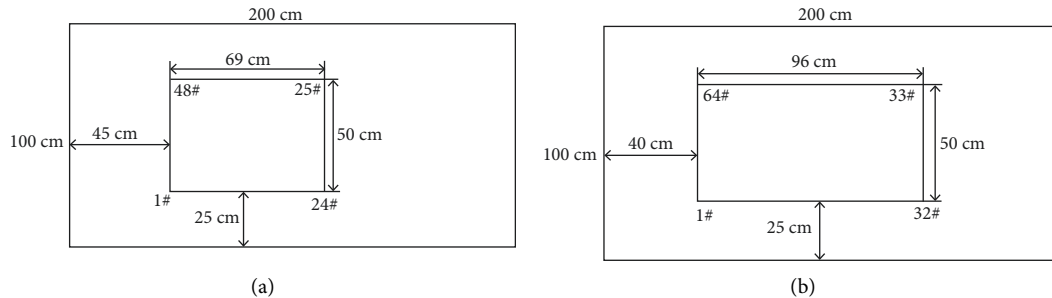


FIGURE 3: The physical model of electrical test system layout. (a) 15 cm above the coal seam and (b) 40 cm above the coal seam.

4. Characteristics of External Damage and Fracture Distribution in the Overburden of Long Variable Face Quarries

By analyzing the evolution of overburden caving failure during the mining process of the forward and reverse knife handle working face, the potential law of roof breaking and fracture development distribution characteristics of stope with variable length can be obtained. Figures 5 and 6 specifically reflected the external forms of rock failure in two types of stope with knife handle. The working face starts to move forward from the opening of incision, and when it advanced to about 30m, some of the rock formations collapsed and collapsed instantaneously after the first pressure directly on the top, and the shape of the rock formations after the collapse is relatively broken (Figure 6(a)). When the working face is continued to advance to 60 m, the immediate

roof completely collapsed, forming an irregular caving zone. The main roof began to break and collapsed in a step-down manner. During this period, cracks began to derive and develop, breaking cracks appeared above the caving zone and continued to develop to the deep level, and separated cracks formed between the strata sinking in the stage (Figures 5(b) and 6(b)). Then with the progress of coal seam mining activities, when the working face is advanced to 90 m, the main roof continued to fall in stages from bottom to top, and its fracture characteristics showed staged features. The ruptured fractures developed rapidly, and the abscission fractures expand gradually and dynamically forward, and the two fractures form fracture derivative zone in the upper space of the overlying rock (Figures 5(c) and 6(c)). Then, when the working face is advanced to 120 m, the main roof is broken periodically, part of the rock layers below the goaf is recompacted, and the fracture development

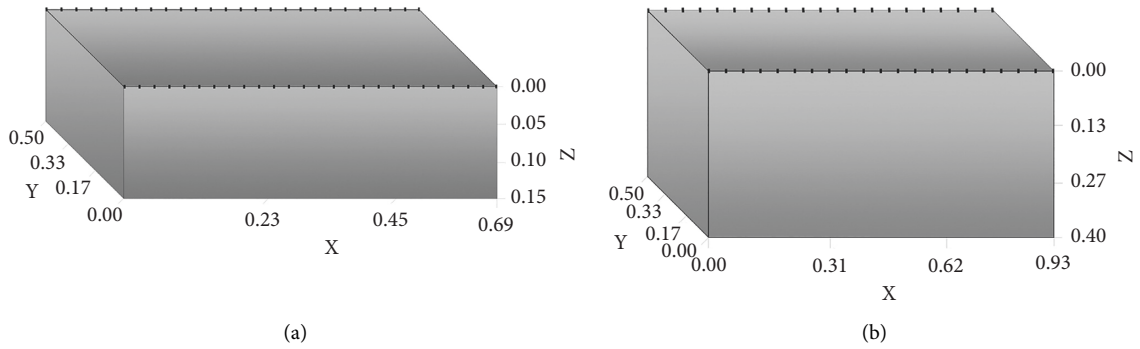


FIGURE 4: The three-dimensional space coordinate system in the different layers of the model. (a) 15 cm above the coal seam and (b) 40 cm above the coal seam.

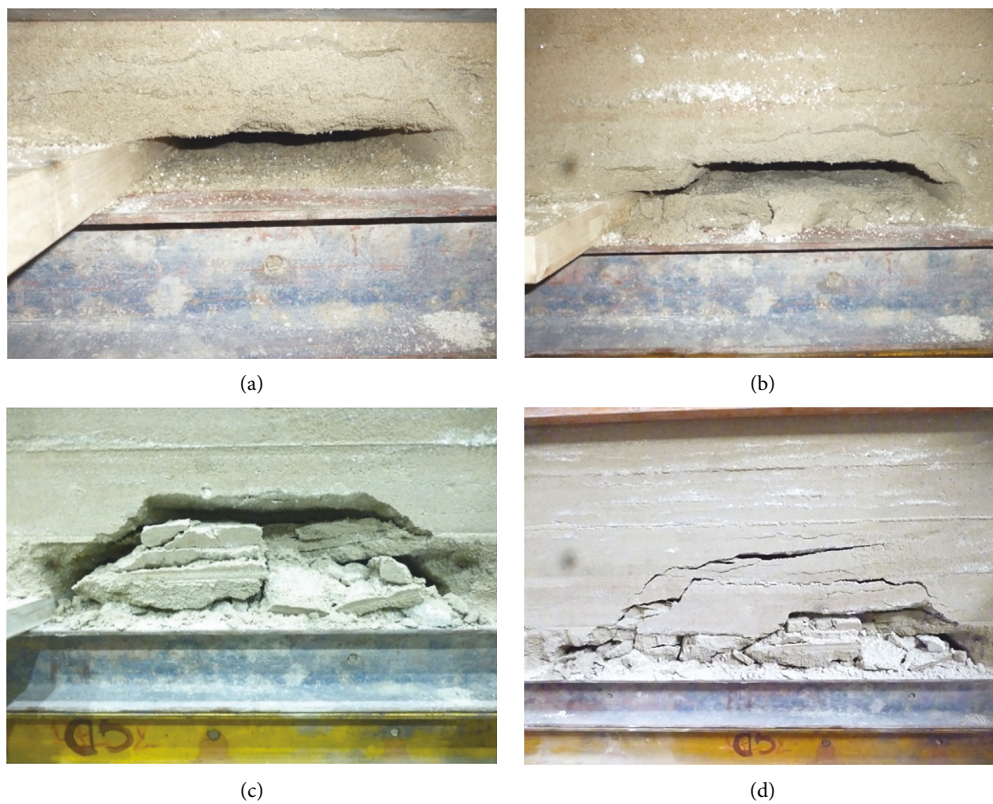


FIGURE 5: External failure form of overlying rock in forward knife handle working face. (a) Mining 30 m. (b) Mining 60 m. (c) Mining 90 m. (d) Mining 120 m.

space is extended to the high level. Nearby interlayer fissures are clearly developed (Figures 5(d) and 6(d)).

Looking at the process of the external overburden destruction of the two types of “knife-handle-type” stope with variable length, it can be found that the damage degree of the roof during the mining period of the forward knife handle working face was lower than that of the reverse knife handle working face. The failure strength of weathered rock weakened, and the roof-caving form is relatively regular. The development time of weathered rock fissures is slightly lagging behind, and the expansion space of transverse

fissures is relatively small. According to the comprehensive analysis, the deformation and failure of surrounding rock continuously develop forward and upward in the process of the two types of variable-length working faces, and there are periodic fractures and collapses. The roof fracture has the temporal and spatial characteristics of instantaneous sudden change, subsection extension, and subregional migration. The overlying rock fracture field has undergone a dynamic evolution process of pressure relief and instability, tension fracture failure, shrinking, and fitting and sealing. Its expansion space is trapezoidal to the depth developing.

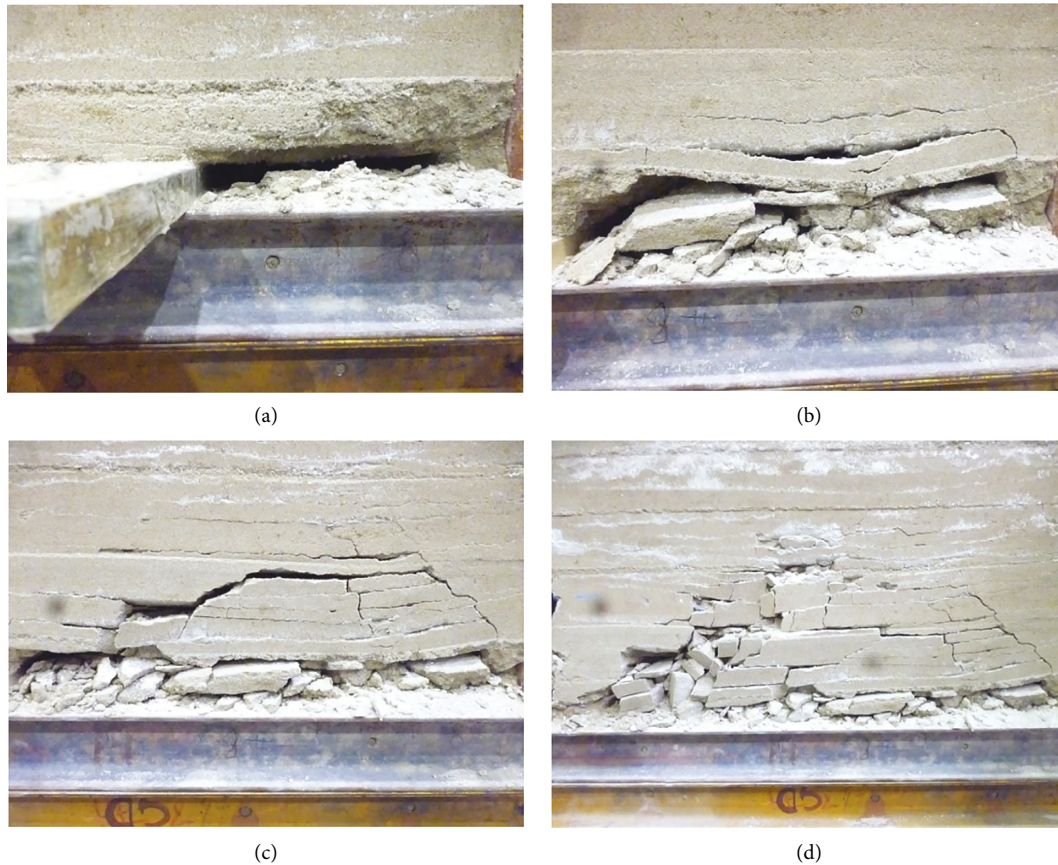


FIGURE 6: External failure form of overlying rock in reverse knife handle working face. (a) Mining 30 m. (b) Mining 60 m. (c) Mining 90 m. (d) Mining 120 m.

5. Internal Failure and Crack Evolution Characteristics of Overlying Rock in Stope with Variable Length

In order to analyze and judge the damage law of the overlying rock and temporal evolution of the fracture development in the internal three-dimensional space of the forward and reverse knife handle of two types of stope with variable length, the parallel electrical test technology is used on the site to test the various coal seam mining. Dynamic evolution characteristics of the distribution of fractures in the overlying rock are revealed through specific graphs such as resistivity three-dimensional inversion map, resistivity dynamic cross section map, resistivity slice map, and resistivity slice ratio map. The resistivity change is affected by many factors, such as hydrogeological conditions, the layered characteristics of surrounding rock, lithological characteristics, excavation disturbance and damage characteristics, stress distribution changes, displacement and deformation, and fracture evolution. It has the characteristics of sensitive response, high accuracy, timely detection response, and so on. With the help of the effective results of resistivity data monitoring, the two zone failure height in the three-dimensional space inside the overburden can be accurately determined and comprehensively evaluated.

5.1. The Internal Destruction and Fracture Development Characteristics of the Overlying Rock in the Forward Knife Handle Stope

5.1.1. Stereo Inversion Image of Resistivity. Figure 7 reflects the variation trend of the three-dimensional spatial resistivity of the overlying rock 15 cm above the coal seam of the forward knife handle working face. It can be found in the figure that the coal seam is in the mining interval of 20~60 cm, and the resistivity changes obviously. When the coal seam is advanced to 40 cm, the resistivity changed abruptly, and the increasing trend of resistivity showed a large difference in the z -axis direction. The difference in resistivity is the specific manifestation of different damage degrees inside the overlying rock, and the rise and fall of the resistivity affect the development and distribution space of the overlying fissures. Therefore, the distribution boundary of the two zones of overlying rock can be judged according to the difference of resistivity. According to the image analysis, the height of the caving zone is about -0.05 m.

Figure 8 is three-dimensional spatial resistivity inversion image of overlying rock at a position 40 cm above the coal seam of the forward knife handle working face, reflecting the electrical variability characteristics of the overlying surrounding rocks at internal rock mass space in multiple

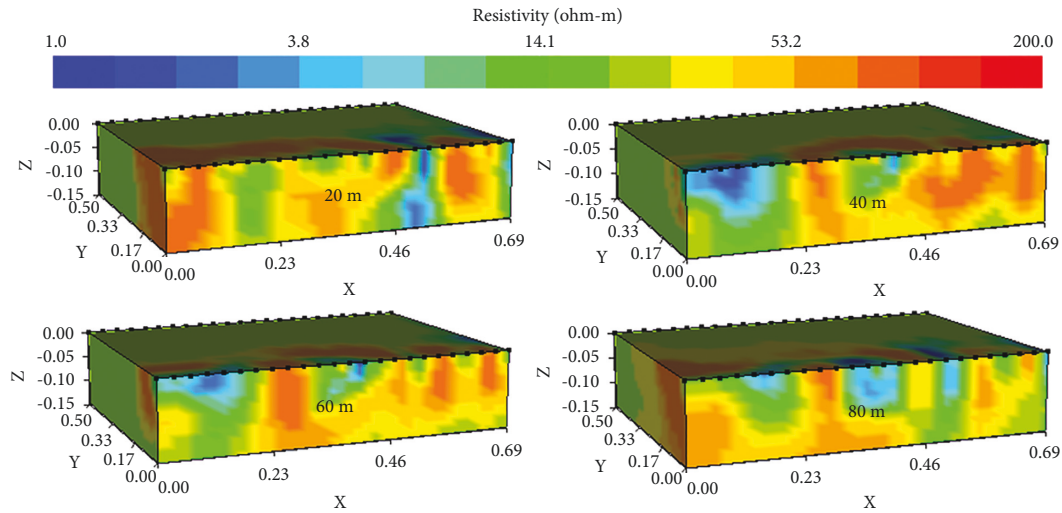


FIGURE 7: Three-dimensional resistivity inversion map of strata at 15 cm above the coal seam.

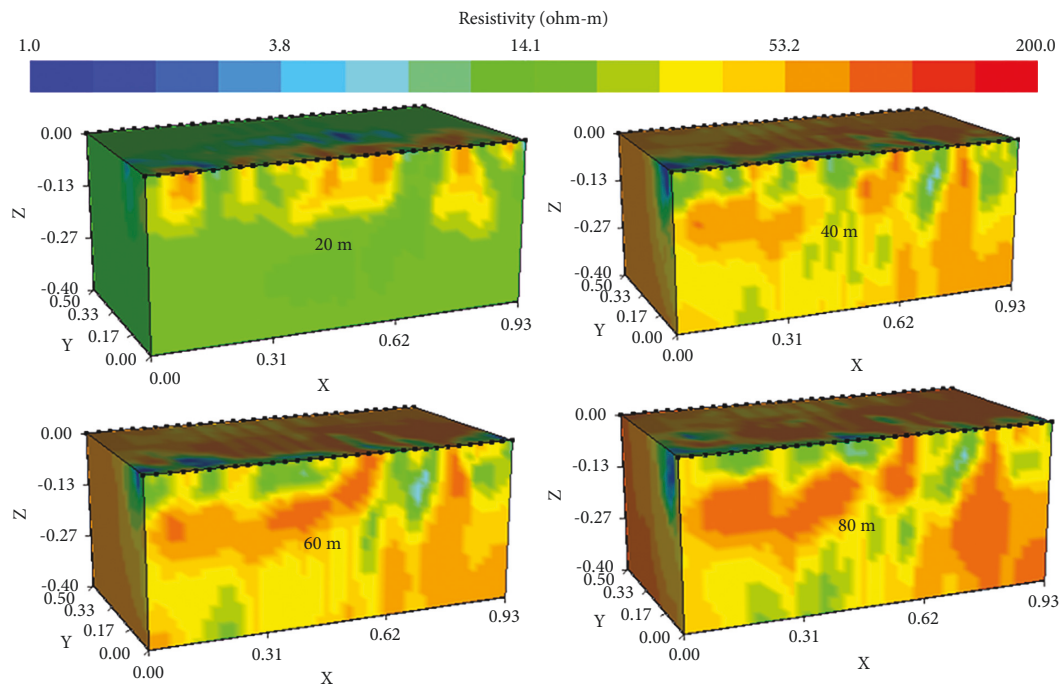


FIGURE 8: Three-dimensional resistivity inversion map of strata at 40 cm above the coal seam.

mining stages under the test of the second layer observation system. The change of resistivity can be seen directly from the figure, and the resistivity of the three-dimensional space surface background value before working face mining is relatively low. With the gradual increase of the mining degree of the working face, the resistivity increases, and the increase trend is fast. When the working face is advanced to 40 cm and enters the working face contact area, the high resistivity range expands and the cracks develop obviously, indicating that the overlying rock collapses at this stage. At the end of the working face mining, the height of the increase in resistivity in the observation space reaches -0.11 m.

Judged from the comprehensive evolution process of resistivity, the coal seam mining has an obvious change trend of resistivity in the range of 15–20 cm before and after the but joint, and this range is also the main active interval for overlying rock damage and fracture development.

5.1.2. Dynamic Evolution Process of Resistivity. Figures 9 and 10 are the internal multiangle cross-sectional views of the electric field in the three-dimensional space of the overlying rock at different layers above the coal seam of the forward knife handle working face, which can clearly reflect the

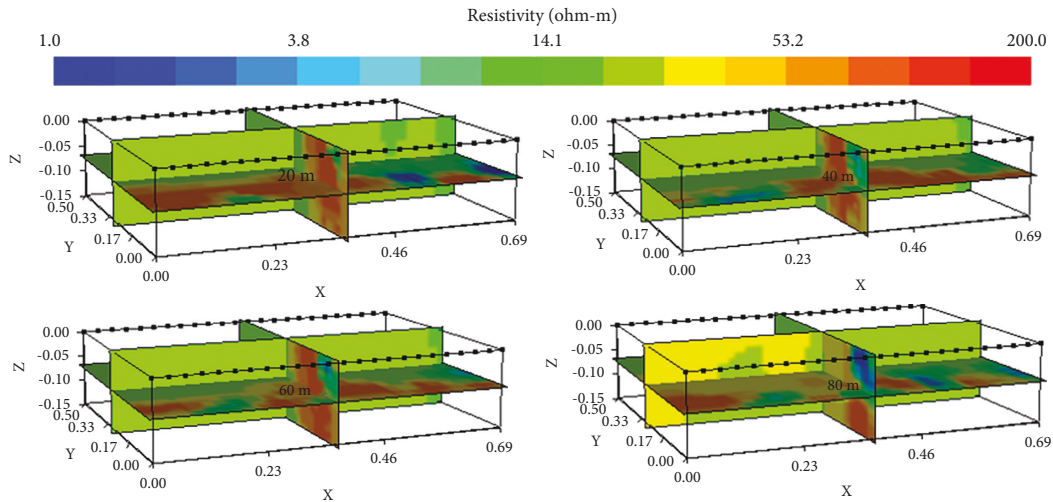


FIGURE 9: The resistivity section diagram of dynamic at 15 cm above the coal seam.

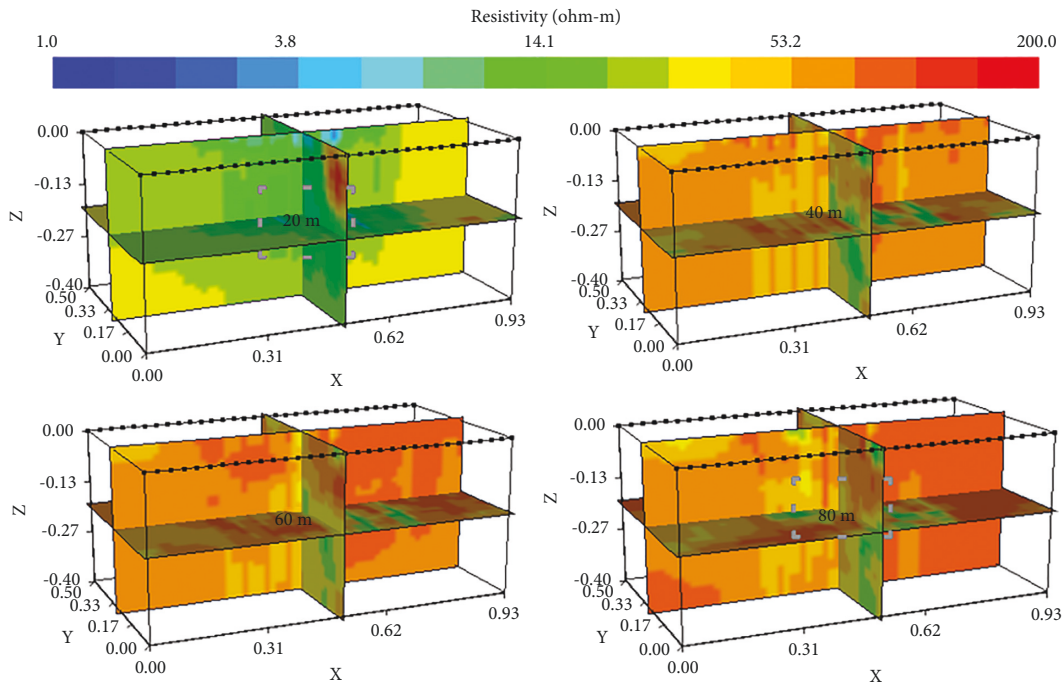


FIGURE 10: The resistivity section diagram of dynamic at 40 cm above the coal seam.

electric field response characteristics of each mining stage in the rock formation space inside the model.

According to the analysis in Figures 9 and 10, the resistivity value was small before the test starts, and the maximum resistivity reached $200 \Omega \cdot m$ at the end of the test.

The 40 cm stage of coal seam mining is the time point when the electric field fluctuates the most. At this time, the resistivity value changes greatly after the coal seam mining, and the resistivity value also changes to varying degrees in the space around the mining. When the working face is advanced to 60 cm, due to the expansion of the length, the overburden resistivity of increase area of 15 cm above the coal seam is extended to the position at 69 cm in the x-axis direction. The overburden resistivity of increase area of

40 cm above the coal seam is extended to the spatial position at 90 cm in the x-axis direction. The location where the resistivity value changes abruptly is the rapidly developing section of abscission fractures. The derivative development of vertical interlayer fractures accelerates the morphological evolution of the resistivity from irregular scattered points to strip-shaped blocks, showing a dynamic expansion spatio-temporal response features.

5.1.3. Resistivity Slice Map. Figures 11 and 12 are the slice images of the resistivity of the overlying rock at different layers above the coal seam in the forward knife handle stope at 7 different positions along the x-axis direction, and the

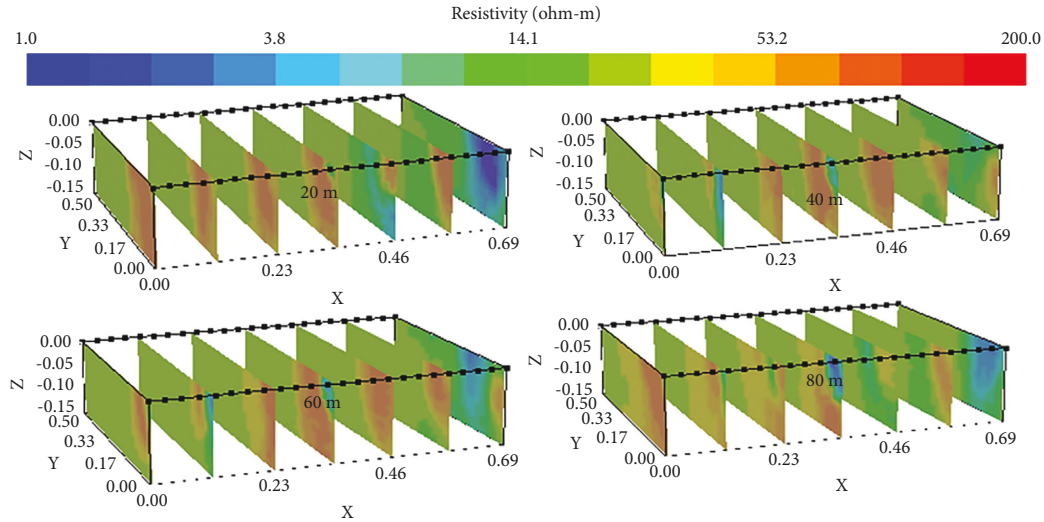


FIGURE 11: The resistivity section diagram along the x -axis direction at 15 cm above the coal seam.

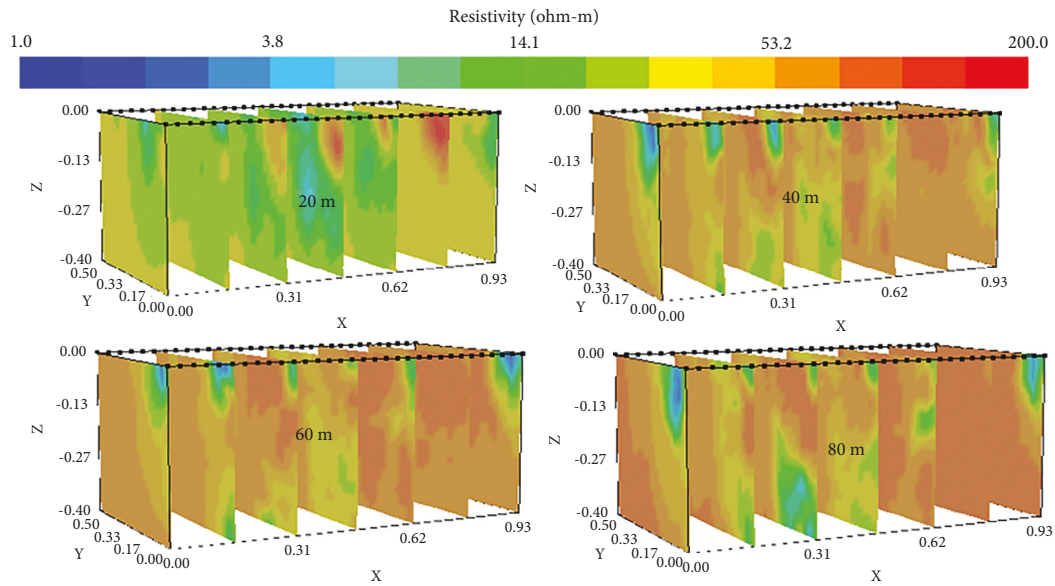


FIGURE 12: The resistivity section diagram along the x -axis direction at 40 cm above the coal seam.

damage height and dynamic changes of the overlying rock in different mining stages of the coal seam can be visually observed feature. It can be seen from the resistivity slice diagrams in Figures 11 and 12 that the area where the resistivity first changes is in the part with a smaller scale value in the y -axis direction, and the overlying rock failure height also follows this law, which fully conforms to the characteristics of rock failure resistivity increase caused by coal seam mining. The change interval of the rapid increase of resistivity is located in the mining stage of 20~60 cm, and the change of electrical characteristics is an intuitive reflection of the rupture of the internal structure of the rock stratum.

5.1.4. Resistivity Slice Ratio Diagram. Figures 13 and 14 are the ratios of the x - z plane resistivity of $y=26$ cm to the background before mining in multiple mining stages of the forward knife handle working face. It can be found that from the figure that when the working face is advanced to 20 cm, the resistivity of x - z plane remains unchanged. When the working face is advanced to 40 cm, the resistivity above 0.2~0.42 m in the x direction increases significantly.

When the working face is advanced to 60 cm, the overlying rock above the position of 0.5~0.65 m in the x -axis direction is damaged greatly. After the mining of the

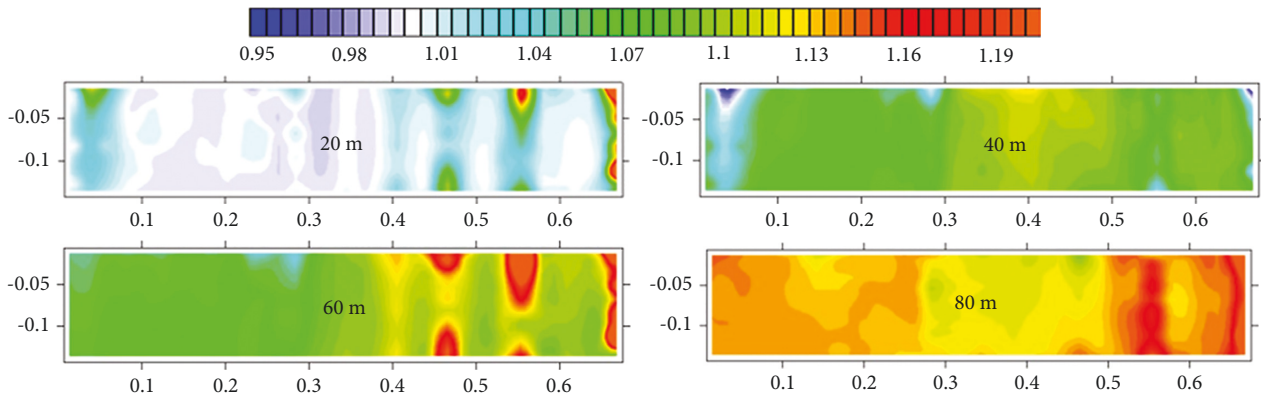


FIGURE 13: The resistivity section ratio chart in the x - z plane at 15 cm above the coal seam ($y=26$ cm).

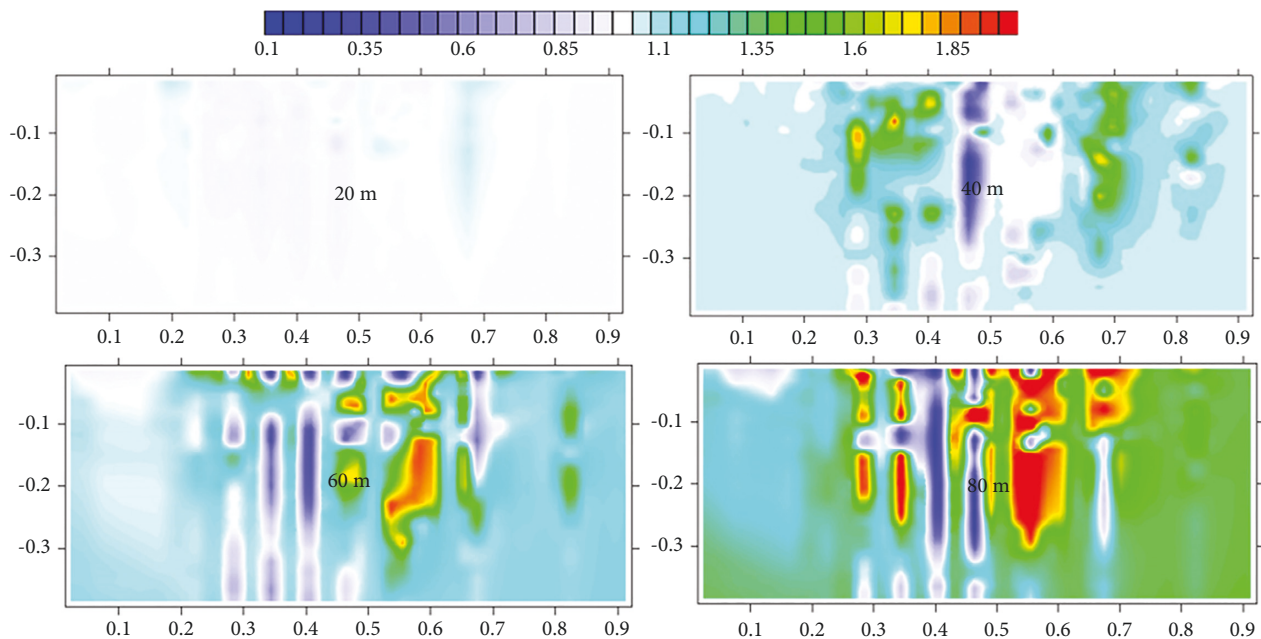


FIGURE 14: The resistivity section ratio chart in the x - z surface at 40 cm above the coal seam ($y=26$ cm).

working face is completed, the overburden failure height is roughly in the range of -0.1 m.

5.2. The Internal Damage and Fracture Development Characteristics of Overlying Rock in the Reverse Knife Handle Stope

5.2.1. Stereoscopic Inversion Image of Resistivity. Figures 15 and 16 are three-dimensional spatial resistivity stereo inversion images of the overlying rock at 15 cm and 40 cm above the coal seam of the reverse knife handle working face, which intuitively reflect the three-dimensional resistivity variation characteristics of the roof in each mining stage. The resistivity of the background value in the inner three-dimensional space of the working face before mining was relatively low, the resistivity value began to increase after the mining of 20 cm, and the surface electric field in the three-dimensional space showed cloud-like distribution characteristics. When the working face is advanced to 40 cm,

the range of resistivity elevation zone increases, the electrical properties of the rock formation show great differences in the z -axis direction, and the distribution space of the electric field in the three-dimensional space expands accordingly. After working face is advanced to 60 cm, the resistivity still maintains a rapid growth momentum, and the interlayer fractures develop and expand to a great extent. When the working face is advanced to 80 cm, the height of the increase of resistivity in the observation space reaches -0.12 m, and the failure height of the overlying caving zone is -0.07 m. In the range of 20 cm before and after the butt-joint mining, the resistivity changes obviously, and this range is also the key activity range for overlying rock damage and fracture development.

5.2.2. Dynamic Evolution Process of Resistivity. Figures 17 and 18 show the internal multiangle cross-sectional views of the three-dimensional electric field of the overlying rock at different layers above the coal seam of the

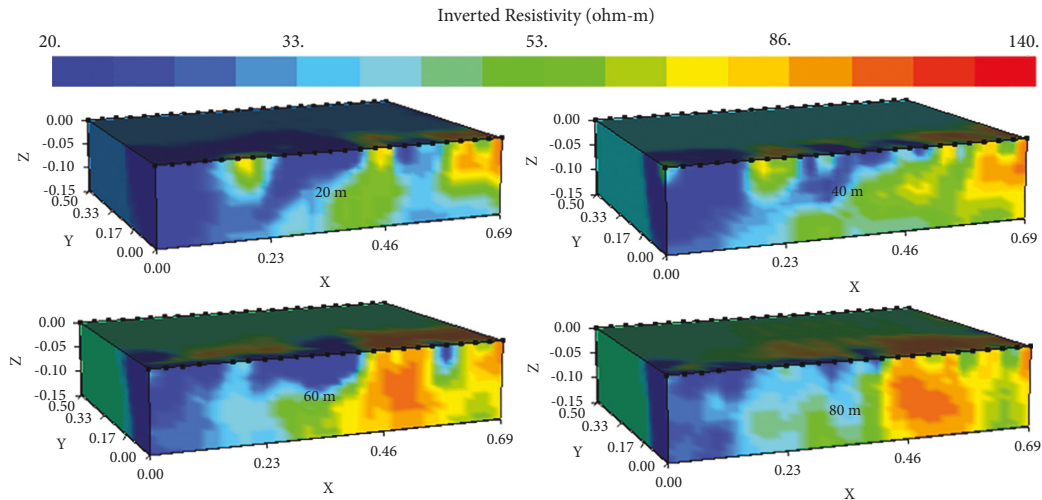


FIGURE 15: Three-dimensional resistivity inversion map of strata at 15 cm above the coal seam.

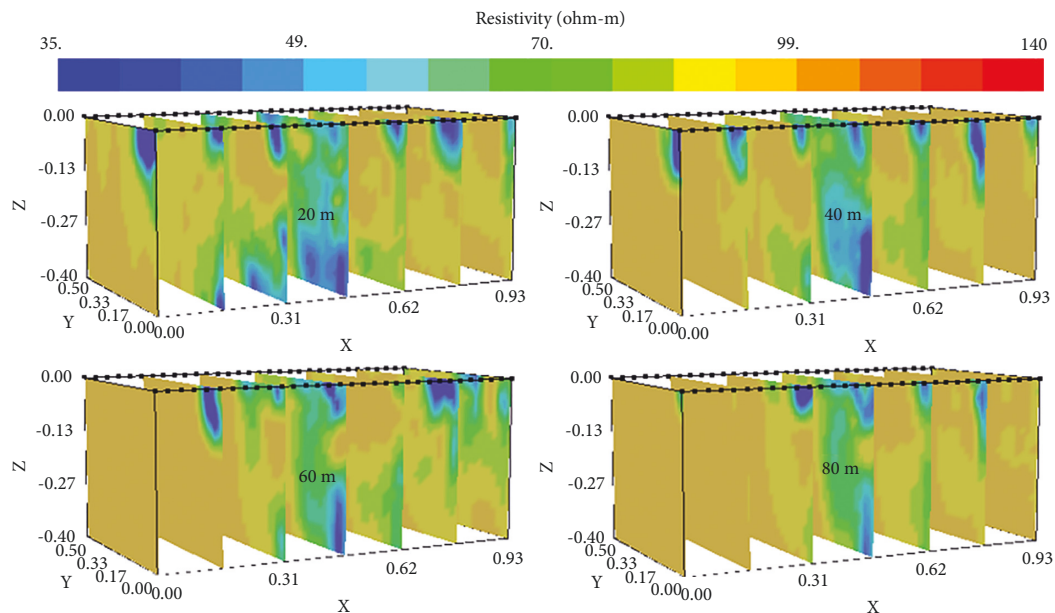


FIGURE 16: Three-dimensional resistivity inversion map of strata at 40 cm above the coal seam.

reverse knife handle working face, which better reveals the electric field response characteristics of the rock space in the model at different mining stages. Figures 17 and 18, which better reveal the electric field response characteristics of the rock formation space inside the model at different mining stages. The resistivity value of coal seam before mining is relatively small, and the maximum resistivity after mining is as high as $220 \Omega\cdot\text{m}$, an increase of nearly 5 times. The 30~50 cm range of working face mining is the time period when the electric field fluctuates the most. At this time, the space resistivity values behind and around the coal seam mining were changed to a great extent. After 60 cm of working face mining, the increased resistivity of overlying rock in the first horizon above the coal seam extends to 65 cm in the x -axis direction, and the increased resistivity of overlying rock in the second horizon extends to 93 cm in the

x -axis direction. During the mining process of working face, the location where the resistivity value changes abruptly is usually the hardest hit area of overlying rock damage. The layer damage of overlying rock leads to the rapid development of interlayer cracks, which makes the electric field show the characteristics of dynamic expansion and rapid evolution of transient response.

5.2.3. Resistivity Slice Diagram. Figures 19 and 20 are slice images of resistivity at 15 cm and 40 cm above the coal seam of reverse knife handle working face at seven different positions along the x -axis, which can intuitively reflect the development height of two zones of failure field and the dynamic evolution characteristics of roof fracture field in different mining stages. Similar to the electric field evolution

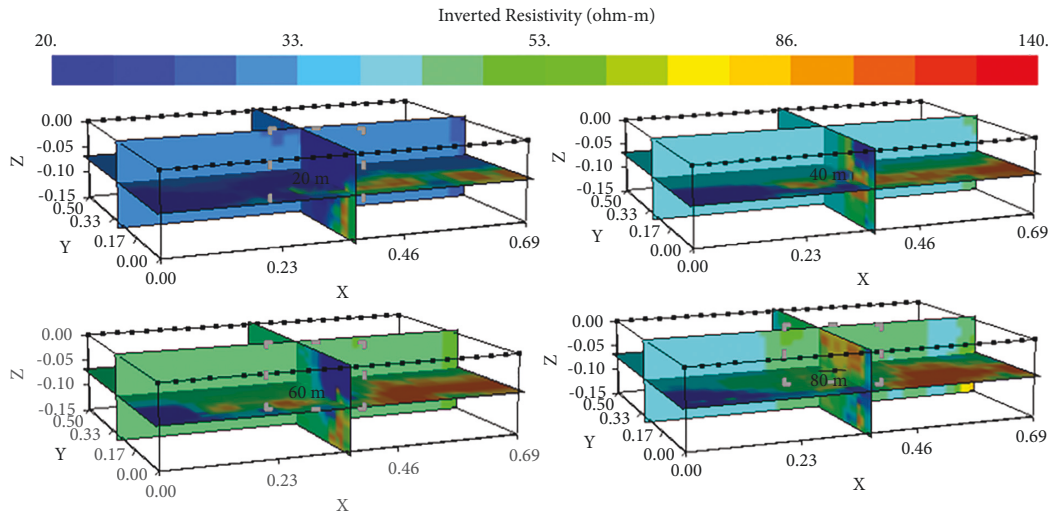


FIGURE 17: The resistivity section diagram of dynamic at 15 cm above the coal seam.

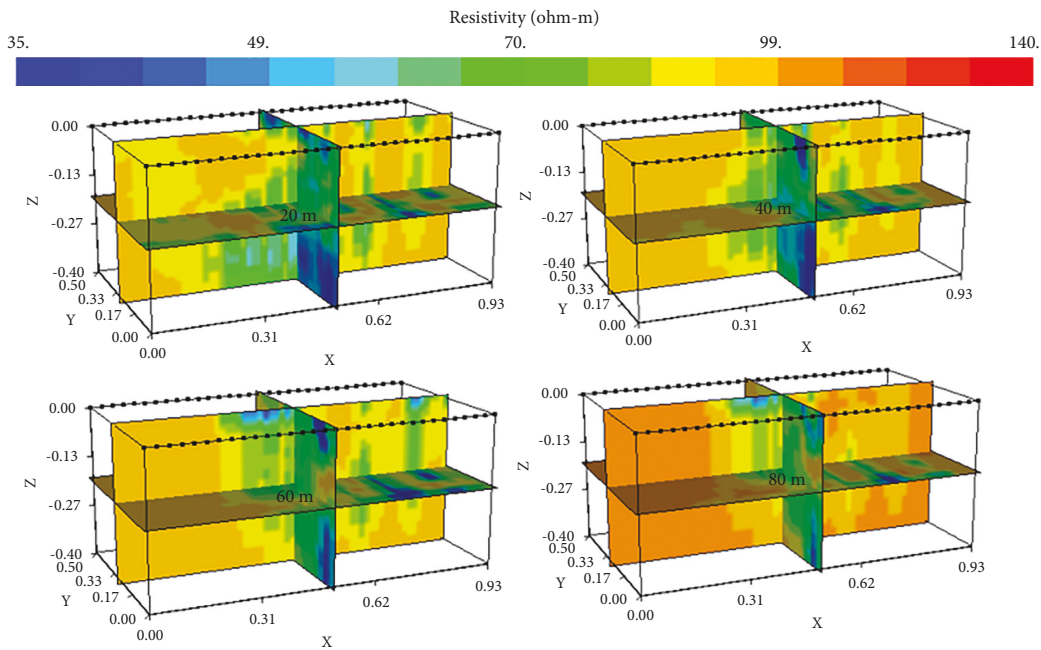


FIGURE 18: The resistivity section diagram of dynamic at 40 cm above the coal seam.

process of the forward knife handle working face, the area where the resistivity first changes is located in the area where the scale value is small in the y -axis direction, and the electrical characteristics in this change range have changed. The change of resistivity is correlated with the mining time step, which fully conforms to the law of the increase of resistivity caused by the destruction of strata caused by coal seam mining. The drastic change period of resistivity growth is located in the mining interval of about 20 cm before and after the contact area of working face. The change of electrical characteristics in this stage will induce the deformation, dislocation, and concentrated fracture of the internal structure of the rock stratum.

5.2.4. *Resistivity Slice Ratio Diagram.* Figures 21 and 22 show the ratios of the x - z plane resistivity of $y=26$ cm to the background before mining in multiple mining stages of the reverse knife handle working face. When the working face is advanced to 20 cm, the resistivity value of the x - z planes changes locally, but the overall change is not obvious. When the working face is advanced to 40 cm, the resistivity of the position above 0.26–0.52 m in the x -axis direction increases significantly; after the working face is advanced to 60 cm, the overlying rock above the position 0.45–0.63 m in the x -axis direction is damaged greatly. After the mining of the working face is completed, the overburden failure height is roughly in the range of -0.15 m. Judging from the ratio of

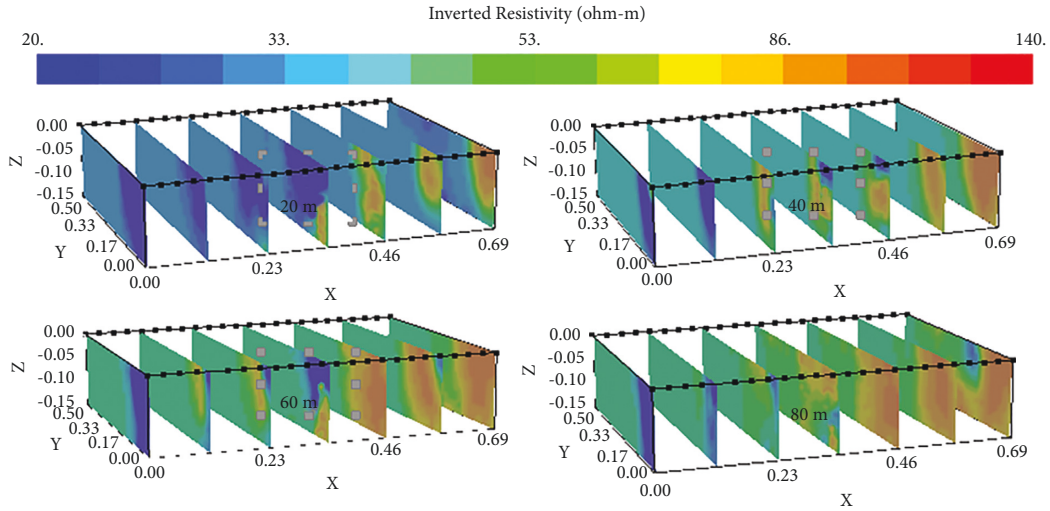


FIGURE 19: The resistivity section diagram along the x -axis direction at 15 cm above the coal seam.

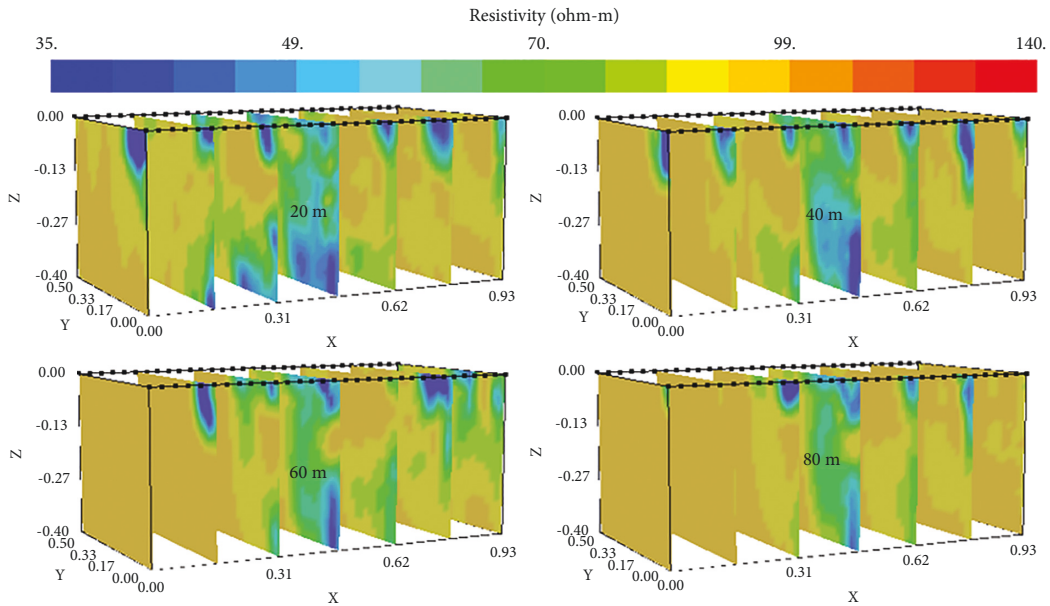


FIGURE 20: The resistivity section diagram along the x -axis direction at 40 cm above the coal seam.

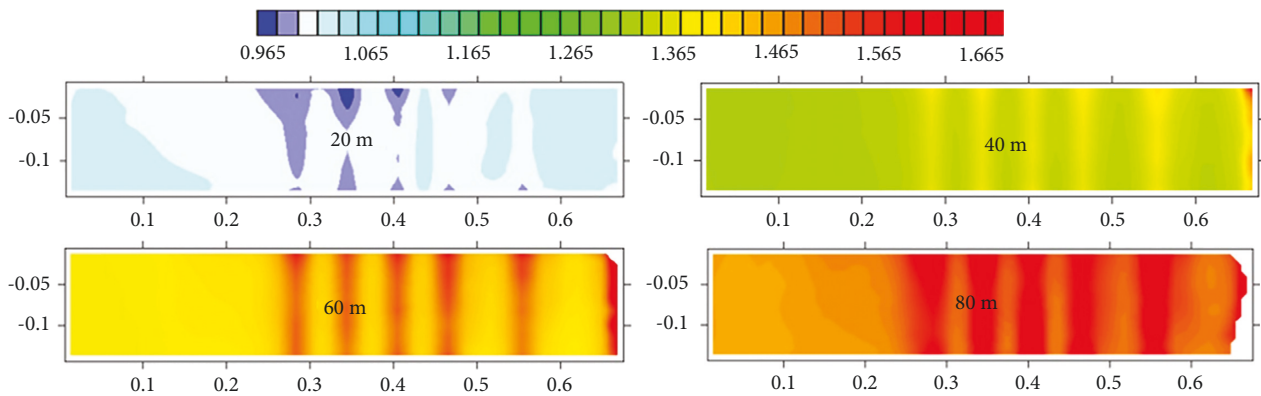


FIGURE 21: The resistivity section ratio chart in the x - z plane at 15 cm above the coal seam ($y=26$ cm).

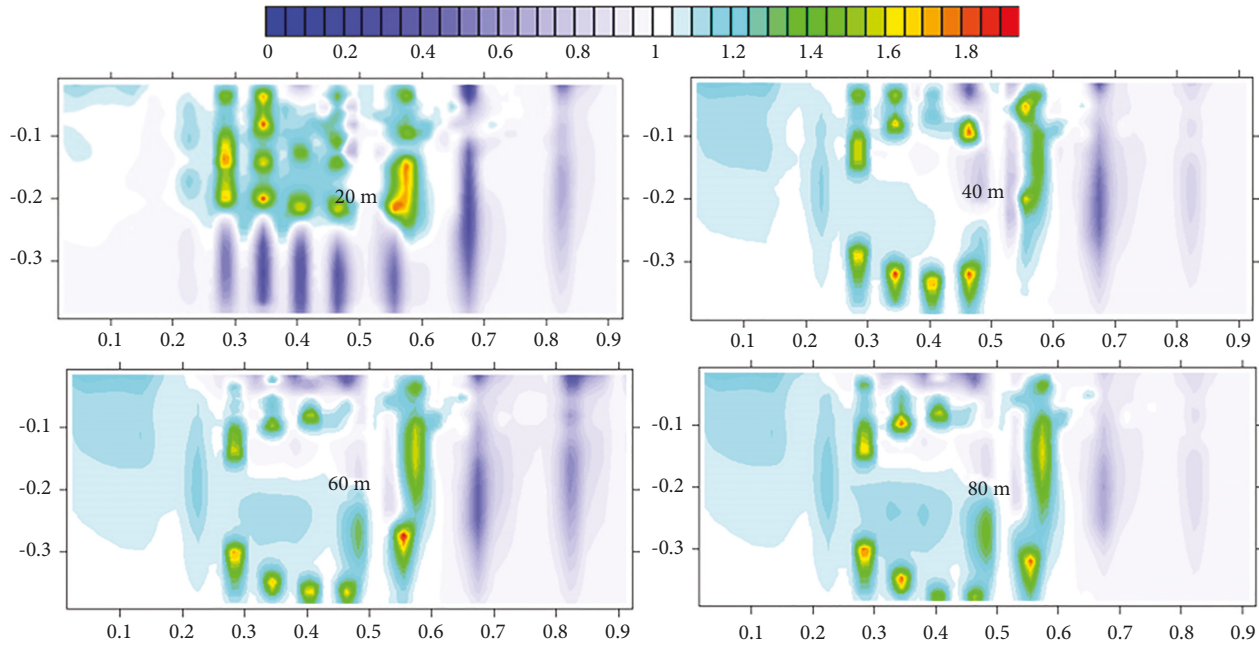


FIGURE 22: The resistivity section ratio chart in the x - z plane at 40 cm above the coal seam ($y=26$ cm).

resistivity slices at 15 cm and 40 cm above the coal seam of the working face, the resistivity variation area of the second horizon is significantly higher than that of the first horizon. The electrical characteristics are more significant, and the expansion space of the electric field dynamic response is more extensive.

6. Conclusions

- (1) Roof fracture during the mining of stope with variable length has the characteristics of mutation, regionality, and ductility. The evolution of the overlying fissure field is from pressure relief instability to tension fracture failure, then shrinking and finally fitting and sealing. The fracture expansion space is trapezoidal, from shallow to deep and from near to far. Roof damage degree of the forward knife handle stope during mining is lower than that of the reverse knife handle stope, the damage strength of the overlying rock is weakened, and roof-caving pattern is relatively regular; the development time of the overlying cracks is slightly delayed, and the expansion space of transverse cracks is relatively small.
- (2) The rise and fall of resistivity during the advancing process of “knife-handle-style” working face are closely related to the mining time step. The sharp change period of the resistivity growth of the two types of stope is located in the mining interval within 20 cm of contact area before and after working face. The change of electrical characteristics in this stage will induce the deformation, dislocation, and concentrated fracture of the internal structure of the rock stratum. At 40 cm, the resistivity value changed abruptly. The increasing trend of resistivity shows a big difference in the z -axis direction, which prompt the electric field to show the transient response characteristics of dynamic expansion and rapid evolution.
- (3) Compared with the reverse knife handle working face, the height of caving zone of the former is about 10 cm, corresponding to the actual height of 15 m. The height of the fissure zone is about 30 cm, corresponding to the actual height of 45 m. The height of the later is about 12 cm, corresponding to the actual height of 18 m. Height of the fissure zone is 35 cm, corresponding to the actual height of 52.5 m. The development height of the two zones of the forward knife handle working face is slightly larger, the degree of damage to the overlying rock is higher, and the development of fissures is relatively sufficient.
- (4) In this paper, the mechanical evolution characteristics of roof deformation and instability, load transfer, stress evolution, and collapse failure of two typical variable face length stopes with variable face length from small to large and from large to small are studied by using laboratory similar material simulation test and parallel network electrical method three-dimensional perspective technology. In the later stage, the engineering verification will be carried out in combination with the existing theoretical analysis and model test results to further deepen the research on relevant topics.

Data Availability

The data used to support the findings of this study are included within the article.

Conflicts of Interest

The authors declare that they have no conflicts of interest regarding the publication of this paper.

Acknowledgments

This work was supported by the National Natural Science Foundation of China (Grant no. 51904266), Excellent Youth Project of Hunan Provincial Department of Education (Grant no. 21B0144), and 2022 Funding Project for Young Backbone Teachers in Colleges and Universities in Hunan Province and Research Project on Teaching Reform of Colleges and Universities in Hunan Province in 2020 (Grant no. HNJG-2020-0231).

References

- [1] X. F. Wang, M. Y. Lu, and Y. H. Gao, "Structural mechanical characteristics and instability law of roof key block breaking in gob side roadway," *Advances in Civil Engineering*, vol. 2020, Article ID 6682303, 2020.
- [2] G. R. Feng and P. F. Wang, "Stress environment of entry driven along gob-side through numerical simulation incorporating the angle of break," *International Journal of Mining Science and Technology*, vol. 30, pp. 189–196, 2018.
- [3] C. J. Hou, X. Y. Wang, and J. B. Bai, "Basic theory and technology study of stability control for surrounding rock in deep roadway," *Journal of China University of Mining & Technology*, vol. 50, no. 01, pp. 1–12, 2021.
- [4] H. Wu, B. Dai, L. Lu, R. Zhao, G. Liang, and W. Liang, "Experimental study of dynamic mechanical response and energy dissipation of rock having a circular opening under impact loading," *Mining, Metallurgy & Exploration*, vol. 38, no. 2, pp. 1111–1124, 2021.
- [5] X. F. Wang, *Slope Length Effect of Roof Fracture Mechanism and Stress Distribution Characteristics of Irregular Stope*, Anhui University of Science and Technology, Huainan, 2015.
- [6] B. W. Lu, C. W. Liu, and H. Xie, "Law of overburden strata movement and mining roadway deformation under mining influence in the unequal length of working face," *Metal Mine*, vol. 01, pp. 34–38, 2016.
- [7] Y. Y. Li, S. C. Zhang, and L. Q. Gao, "Mechanism and prevention of pressure burst in step region based on overburden strata movement of unequal length working face," *Rock and Soil Mechanics*, vol. 37, no. 11, pp. 3283–3290, 2016.
- [8] Y. G. Wang, W. B. Guo, and E. H. Bai, "Characteristics and mechanism of overlying strata movement due to high-intensity mining," *Journal of China Coal Society*, vol. 43, pp. 28–35, 2018.
- [9] D. D. Chen, F. L. He, and S. R. Xie, "Time-space relationship between periodic fracture of plate structure of main roof and rebound in whole region with elastic foundation boundary," *Chinese Journal of Rock Mechanics and Engineering*, vol. 38, no. 06, pp. 1172–1187, 2019.
- [10] X. F. Wang, M. Z. Gao, and Y. X. Chen, "Analysis of Fracturing Characteristics of stope roof based on elastic thin plate theory," *Metal Mine*, vol. 06, pp. 24–28, 2015.
- [11] G. A. Zhu, L. M. Dou, and Y. Liu, "Rock burst mechanism analysis on deep irregular island face," *Journal of Mining & Safety Engineering*, vol. 33, no. 04, pp. 630–635, 2016.
- [12] J. F. Pan, "Start-up principium of rock burst in whole coal roadway floor in half-island face," *Journal of China Coal Society*, vol. 36, pp. 332–338, 2011.
- [13] G. Y. Yang, F. X. Jiang, and C. W. Wang, "Prevention and control technology of mine pressure bumping of coal mining face in seam island based on deep mining and thick topsoil of complex spatial structure of overlying strata," *Chinese Journal of Geotechnical Engineering*, vol. 36, no. 01, pp. 189–194, 2014.
- [14] J. Hao, M. W. Xu, and W. B. Wu, "Study on the prevention and control of dynamic disasters at an isolated island working face," *China Earthquake Engineering Journal*, vol. 39, no. 05, pp. 976–980, 2017.
- [15] X. Li, Z. Xu, and Y. Xu, "Characteristics and trends of coal mine safety development," *Energy Sources, Part A: Recovery, Utilization, and Environmental Effects*, vol. 2020, no. 12, 19 pages, Article ID 1852339, 2020.
- [16] S. Liu, X. Li, D. Wang, and D. Zhang, "Investigations on the mechanism of the microstructural evolution of different coal ranks under liquid nitrogen cold soaking," *Energy Sources, Part A: Recovery, Utilization, and Environmental Effects*, vol. 2020, no. 07, 17 pages, Article ID 1841856, 2020.
- [17] X. L. Li, S. J. Chen, S. M. Liu, and Z. H. Li, "AE waveform characteristics of rock mass under uniaxial loading based on Hilbert-Huang transform," *Journal of Central South University*, vol. 28, no. 6, pp. 1843–1856, 2021.
- [18] P. Guo, X. Zhang, Y. Peng, M. He, C. Ma, and D. Sun, "Research on deformation characteristic and stability control of surrounding rock during gob-side entry retaining," *Geotechnical & Geological Engineering*, vol. 38, no. 3, pp. 2887–2902, 2020.
- [19] X. J. Zhu, G. L. Guo, and J. F. Cha, "Optical image method to deformation monitoring of similar material model," *Journal of China University of Mining & Technology*, vol. 44, no. 01, pp. 176–182, 2015.
- [20] H. C. Li, *Similar Simulation Test of Mine Pressure*, Journal of China University of Mining & Technology, China, 1988.
- [21] D. Z. Kong, Y. Xiong, and Z. Cheng, "Stability analysis of coal face based on coal face-support-roof system in steeply inclined coal seam," *Geomech. Eng.*, vol. 25, no. 03, pp. 233–243, 2021.
- [22] Y. Xue, T. Teng, and X. H. Wang, "Analysis of fracturing model and caving law of stope roof," *Science Technology and Engineering*, vol. 16, no. 07, pp. 156–161, 2016.
- [23] F. L. He, W. R. He, and D. D. Chen, "First fracture structure characteristics of main roof plate considering elastic-plastic deformation of coal," *Journal of China Coal Society*, vol. 45, no. 08, pp. 2704–2717, 2020.

Research Article

Study of Instability Mechanism and Roof Caving Mode of Cementing Filling Stope: The Case Study of a Nonferrous Metal Mine in China

Min Zhong ^{1,2}, Peng Yang,^{1,3} and Ying-Peng Hu ²

¹School of Civil and Resource Engineering, University of Science and Technology Beijing, Beijing 100083, China

²School of Environment and Resources, Southwest University of Science and Technology, Mianyang, Sichuan 621010, China

³Beijing Key Laboratory of Information Service Engineering, Beijing Union University, Beijing 100101, China

Correspondence should be addressed to Ying-Peng Hu; huyan_nice@163.com

Received 28 December 2021; Revised 25 March 2022; Accepted 13 April 2022; Published 9 May 2022

Academic Editor: Gaofeng Song

Copyright © 2022 Min Zhong et al. This is an open access article distributed under the Creative Commons Attribution License, which permits unrestricted use, distribution, and reproduction in any medium, provided the original work is properly cited.

The downward layered cemented filling method, which is generally used in the mining of high-value metal mines with poor surrounding rock quality, is widely believed to not cause large-scale instability of the roof strata in the mining area. However, a nonferrous metal mine in northern China, which has been using the downward cemented filling method, suddenly suffered a violent collapse accident of the stope roof, and the surface is accompanied by significant subsidence on a large scale. The accident revealed that the roof collapse mechanism still needed further research. In this paper, field investigation and numerical simulation were combined to study the mechanism of roof collapse. Based on the input data including in-situ stress state, geological occurrence pattern, and mining steps, the particle flow code (PFC) was used to simulate the stress and displacement changes of the rock mass under mining disturbance. These results indicate that the failure process of the overlying rock mass can be divided into four stages due to the special geological conditions of the mine: pillar stability stage, pillar chain failure stage, roof filling caving stage, and gneiss plug settlement stage. In the early stage of mining, the pillars between the mined-out drifts could effectively support the overlying rock mass due to the small exposed roof. As more drifts were mined, the vertical pressure on the pillars was added. When the number of mining drifts reached five, one of the pillars was firstly destroyed due to overloading, and then the pressure of the overlying strata was transferred to the surrounding pillars, leading to the subsequent failure of other pillars. When pillars were damaged, arch caving appeared inside the roof filling material. Finally, the vertical shear resistance capacity of the gneiss mass above is insufficient, owing to the steeply dipping joints. Finally, the gneiss above was subject to sudden plug settlement along the vertical joints. It should be noted that the stope mining management of the mine has a significant impact on production safety. In order to ensure the stability of the stope formed by cemented filling method, the dense distribution of simultaneous mining drifts should be avoided and the mine-out areas should be backfilled in time.

1. Introduction

Underground mining would destroy the equilibrium state of the rock mass and eventually lead to surface deformation, which threatens the safety of people and surface structures. The study of this complex process is not only of great practical significance but also of great interest. It is widely believed that the caving method causes the most severe surface subsidence [1–3]. In the process of overlying rock mass caving caused by the goaf, the caving failure will

develop upward according to the arch shape, due to the stress arch. Surface damage caused by caving failure is also a progressive process. When the caving failure is transmitted to the surface, a small collapse pit will be formed at first, then the cracks will loosen under the action of tensile stress, and finally, the collapse pit will gradually expand due to the lateral collapse of the surrounding rock mass [4–7].

Engineering geological conditions (joints, faults, and surface morphology, etc.) also affect the development form, process, and scope of surface collapse. Joints will affect the

development direction of caving failure and the range of surface failure will change accordingly. Faults near mining areas also inhibit the spread of surface damage. The various and complex topography can also lead to multiple failure modes, such as landslides caused by underground mining under mountains [8–10].

In contrast, the filling method can effectively suppress surface deformation. Backfilling goaf with cement dry material can effectively restrain further deformation of the surrounding rock. Meanwhile, cementing materials applied to backfill goaf such as cement slurry can significantly reduce the displacement of rock strata [11, 12]. By constantly backfilling the goaf, the existing goaf is small and scattered. This improves the stress state of the surrounding rock, and the narrow mined-out area also inhibits the failure expansion of the surrounding rock mass, so the filling method generally does not cause severe surface failure. Even when the surface deforms, it is slight and slow subsidence.

Many studies have been carried out by researchers to study the deformation mechanism of surface subsidence through theoretical analysis, physical modelling, field observation, and numerical simulation. In terms of theoretical research, Ding et al. analyzed the mechanism of surface deformation caused by underground mining in the Hemushan Iron Mine through the elastic mechanics method, predicted the damage range of the surrounding rock of the cylindrical caved space, and revealed the impact of the gravel on the stability of the caved space [13]. However, there have been only a few theoretical studies due to the complexity of the problem. Moreover, most theoretical models are based on many simplifications. Therefore, it is difficult to explain the rock mass failure mechanism caused by mining under complex conditions through theoretical formulas.

As for physical modelling, Ghabraie used physical modelling to investigate the surface subsidence mechanism and substrata movement characteristics [14]. Ren constructed a physical model to simulate the deformation and failure of ground surface and rock mass around the mined-out area [15]. Due to the use of similar materials that can reproduce the similar characteristics of the in-situ rock mass characteristics, the simulation results are intuitive and related to the actual situation. However, for the operability of the experiment, some artificial uncertainties are often introduced, so the physical model cannot fully reproduce the surface subsidence and rock failure process in the field.

Field monitoring is the most direct method of surface deformation research, and the monitoring data can truly reflect the surface displacement law. Surface monitoring methods including theodolite, total station, and global positioning system (GPS). For example, GPS is applied to monitor the surface deformation of many metal mines, such as Kiirunavaara mine, Jinchuan Nickel mine, and Chengchao Iron Mine, and the detailed monitoring data obtained are used to analyze the surface deformation characteristics and formation movement mechanism caused by underground mining [16–18]. The deformation of deep strata can be monitored by microseismic and extensometer [19, 20]. However, these field monitoring methods are limited to

recording ground deformation, and mechanical mechanism analysis is lacking. Therefore, stress redistribution and fracture initiation and propagation caused by underground mining cannot be revealed only by the monitoring data.

In recent years, the development of computer technology has made numerical simulation a low-cost and efficient research method. Much simulation software based on different principles has been used to study surface subsidence and rock movement caused by mining. According to the calculation principle, these pieces of simulation software can be divided into three categories: (1) continuous medium method, namely, FLAC3D, RFPA2D, ABAQUS, etc. [7, 21, 22]; (2) discontinuous medium method, namely, UDEC, 3DEC, DDA, PFC2D, etc. [23–30]; and (3) Mixed methods, namely, ELFEN [8, 31, 32].

The continuum method considers the model as a continuous and inseparable object. The continuum method can reveal the stress distribution characteristics of the surrounding rock caused by underground mining and obtain the final surface damage range [33]. Because the elements in the continuum method cannot be separated, it is naturally difficult to simulate the collapse separation process of the surrounding rock. For the discontinuous medium method, the numerical model consists of many discontinuous elements, which are connected by bond elements. Once some limit conditions are met, the bond element is broken so that the discrete element is separated. In this way, the large deformation of the rock mass can be simulated and the collapse process of the rock mass can be reproduced [24, 26–30].

One of the key factors for reliable numerical simulation is the correct selection of parameters. The mechanical parameters of small intact rock can be measured through laboratory experiments. However, for the engineering scale, the mechanical response characteristics of large rock mass with random geological features such as joints are different from those of small intact rock. The Hoek–Brown criterion is widely regarded as an effective method to obtain the calculated parameters of rock mass in engineering scale. Due to the subjective judgment involved in this evaluation method, the back analysis of the parameters should be carried out based on the existing failure phenomenon [33].

The filling method is effective in inhibiting the deformation of the surrounding rock and maintaining the stability of the slope and surface. However, the surface collapse accident at a nonferrous metal mine in north China deserves more attention.

Due to the poor quality of the rock mass, the mine adopts the downward layered cemented filling method. In the long-term mining process, the surface can maintain a stable state. However, in March 2016, the roof strata of the goaf located 120 m underground suddenly collapsed, and then the surface collapsed violently. The surface area of the collapse pit exceeds 10000 square meters. Severe surface deformation poses a great threat to the safety of surface personnel and structures, and seriously interferes with normal mining. Due to the filling mining method, the mine did not form a large-scale goaf, but several narrow mined-out areas located at the depth of 120 m underground caused sudden caving of the

overlying strata and rapid surface collapse. This failure mechanism and rock movement law are worthy of further study in order to provide the reference for the safety of mining in the next step.

In this paper, we investigate the field damage of the mine, then establish a two-dimensional numerical model using PFC2D. The calculated parameters are obtained by trial-and-error tests referring to field damage. Finally, the whole process from pillar destruction to surface collapse is reproduced. Through field investigation and numerical simulation, the mechanism of instantaneous large-scale surface collapse in a nonferrous mine is studied.

2. Engineering Background

2.1. Ore Body Layout and Mining Situation. The nonferrous metal mine is a nickel mine located in north China and has multiple ore bodies. The 1# ore body is the main industrial ore body, and the plane shape of the ore body is gourd-shaped (Figure 1). The ore body strikes NW30° and dips 50°–80° toward SW, which is mainly located between exploration lines 4 and 12 and is 400 m long.

As shown in Figure 2, the overlying rock layer of the ore body consists of two lithological groups, the surface layer is Quaternary sediments with a thickness of 50 m, and the lower part is gneiss with a thickness of 50 m. Tectonic joint groups exist in gneiss, which is smooth and has weak fillings. There is a fault in this area, which strikes NW and dips 80°–85° toward SW.

The mining area was completed and put into operation in 2010, with a designed annual output of 165 t. Due to the poor rock mass quality and high-value ore, downward cemented filling method was adopted to maintain stope stability and reduce loss and dilution, which is shown in Figure 3. There are two sublevels at 1642 m and 1546 m level. As of March 2016, the working face in the upper mining area has reached 1614 m level, forming a 30 m thick cemented filling body. And the working face in the lower mining area has reached 1504 m level, forming a 42.5 m thick cemented filling body. At this time, the stop at the 1613 m level was damaged, resulting in surface collapse. Figure 4 shows the mining status at this time.

2.2. Rock Mass Properties and In Situ Stress. In order to obtain the mechanical properties of the surrounding rock mass and ore body, some relatively complete rock blocks are extracted from the mine and made into standard samples with the diameter of 50 mm and the height of 100 mm. Then, the mechanical properties of the intact rock are obtained by an unconfined uniaxial compression test in the laboratory. The geological strength index (GSI) of rock mass is calculated according to rock quality designation (RQD) values [34]. Finally, the mechanical parameters of rock mass are obtained through the generalized Hoek–Brown criterion [35], as shown in Table 1.

Many in-situ stress measurements have been carried out in the long-term mining process of the mine. The measured value of in-situ stress in the drift near the 5# exploration line

at 1610 m level is selected to construct the in-situ stress state of the study area.

The magnitudes and directions of in-situ stress are obtained from the measurement results. The maximum principal stress is 4.2 MPa, of which the dip is 10° and the dip direction is 325°. The middle principal stress is 3.2 MPa, of which the dip is 80° and the dip direction is 145°. And, the minimum principal stress is 0.8 MPa, of which the dip is 3° and the dip direction is 48°.

3. Investigation of Surface and Underground Stope

After long-term mining with the filling method, the non-ferrous metal mine has formed the stratum status as shown in Figure 4. The surface remained stable after years of mining. In March 2016, when the 1613 m sublevel was mined, the stope pillars were suddenly destroyed, causing the roof to collapse. At this time, most of the mined-out areas in the mine had been filled, only a few of the mined-out drifts at the level of 1613 m had not been filled yet. However, the destruction of the overlying strata was still developing rapidly and then the surface collapsed violently. In order to reveal the mechanism of rock failure, detailed field investigations were carried out from the underground stope at 1613 m level to the surface.

The investigation starts from the 1613 m level where the damage first occurred. According to the mining plan, there would be several unfilled drifts at this level before filling together. The height of a single drift is generally only 3–5 m and the width is only 4–6 m. The failure first occurred in these narrow drifts. According to the survey, the damaged area is mainly concentrated between 5# and 7# exploration lines.

As shown in Figure 5, the roof of the drifts between the 5# and 7# exploration lines collapsed, and the collapsed broken rock filled the drifts. Due to the expansion characteristics, the gravel falling from the roof quickly filled the narrow space, so as to restrain the deformation of the surrounding rock.

Therefore, the damage range of the overlying rock mass caused by the deep underground narrow and scattered goaf is limited, and the damage of roof rock mass is difficult to be transmitted to the surface. However, in this case, the overburden of the stope was greatly deformed and the surface collapsed.

In order to study the failure characteristics of the overlying rock mass, field investigations were also carried out at the 1630 m and 1650 m levels. As shown in Figure 6, the drifts at the 1630 m level near the 7# exploration line had an overall staggered settlement of 3 m.

As shown in Figure 7, the drifts between the 5# and 7# exploration line at the 1650 m level had overall subsidence.

The roof of the drift near the 5# exploration line had 0.4 m subsidence, the damage extended about 70 m along the drift, and the bottom of the drift had a subsidence of 2 m (Figure 7(a)). The damage near the 7# exploration line was 60 m along the drift. The roof had obvious fracture damage and staggered subsidence of 0.3 m. The bottom plate had

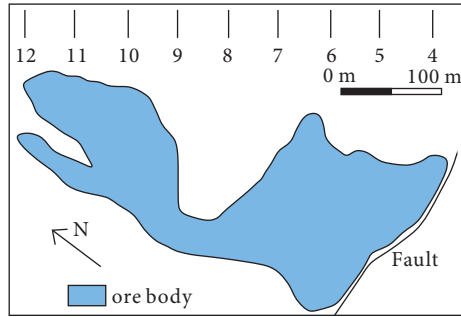


FIGURE 1: The plane projection map of the 1 # ore body at the 1650 m level.

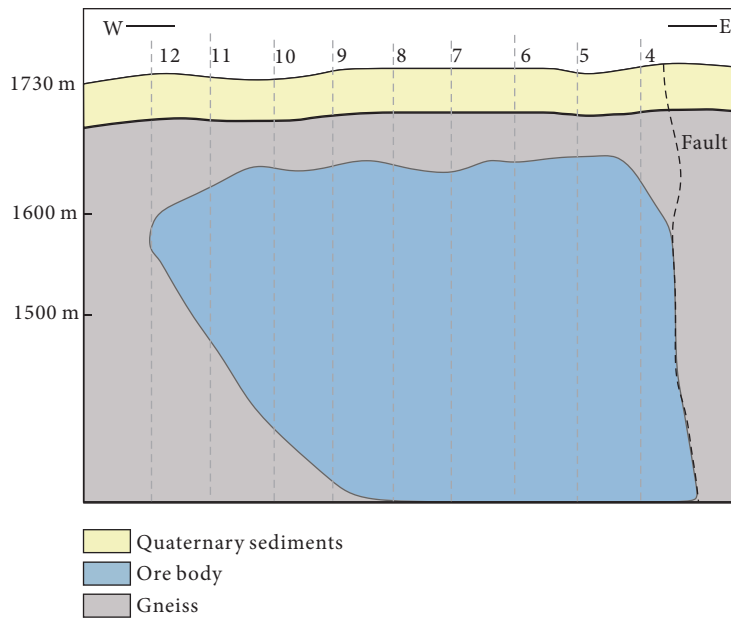


FIGURE 2: The longitudinal projection map of the 1 # ore body.

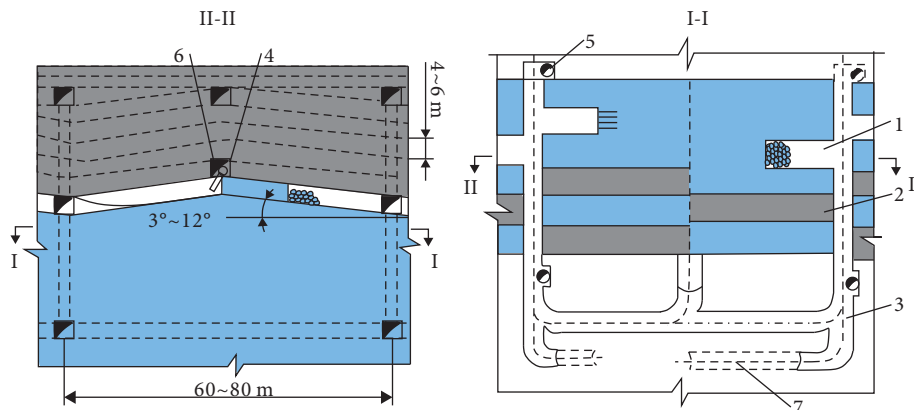


FIGURE 3: Schematic diagram of the stope of downward cemented filling method. (1-mining drift; 2-filling drift; 3-sublevel haulage road; 4-sublevel filling road; 5-orepass; 6-filling material transportation pipeline; 7-ramp; ore (blue); cemented backfill body (grey)).

greater subsidence, with a settlement of about 1 m (Figure 7(b)). The north side wall of the drift near the 6# exploration line was broken along the drift, with dislocation at the fracture and floor uplift of about 1 m (Figure 7(c)).

Compared with the failure between 5# ~ 7# exploration lines, the rock mass near the 9 # exploration line had no obvious damage, and the roadway could still maintain stability (Figure 7(d)). It can be seen that the rock mass

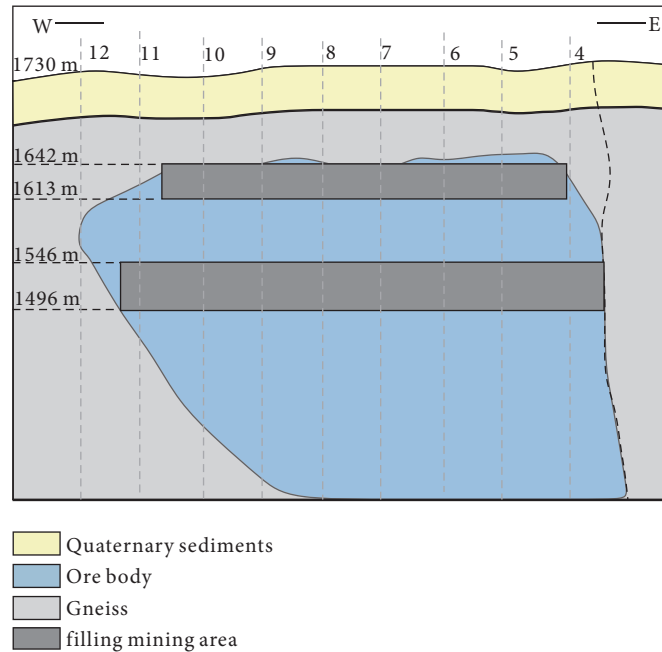


FIGURE 4: The vertical projection map of mining status.

TABLE 1: Mechanical parameters of the rock mass.

| Rock type | Bulk density (kg/m^3) | Compressive strength (MPa) | Tensile strength (MPa) | Elastic modulus (GPa) | Internal friction angle ($^\circ$) |
|--------------|-------------------------------------|-------------------------------|---------------------------|--------------------------|---|
| Gneiss | 2700 | 17.2 | 1.7 | 37.2 | 27 |
| Quaternary | 2000 | 1.7 | 0.31 | 8.2 | 21 |
| Ore body | 2800 | 14.3 | 1.8 | 28.1 | 28 |
| Filling body | 2200 | 6.5 | 0.8 | 9.2 | 23 |

failure caused by slope instability has an obvious influence range, and the expansion of failure in rock mass was mainly in the vertical direction.

Although the overburden is 80 m thick and the rock mass at this level moves only 1-2 m downward, the movement of the rock stratum is still rapidly transmitted to the surface and causes surface collapse. The collapse pit is still distributed between 5# and 7# exploration line, with an area of more than 10 thousand square meters (Figure 8).

4. Analysis on the Collapse Mode of the Stope Roof

According to a large number of cases, the instability of underground stope may lead to two failure modes of overburden, progressive arch caving failure and sudden plug subsidence [7, 36].

As shown in Figure 9, the arch failure of the rock mass is more common. The roof rock stratum is affected by tension, and the failure surface expands upward in an arch shape. This failure development is gradual, and the collapsed gravel mostly presents a loose state.

Due to the expansion characteristics of loose gravel, if the goaf is small, it will be quickly filled with expanded gravel. Without compensation space, further deformation and failure of surrounding rock are restrained.

Therefore, for the deeply buried goaf, only a large enough goaf can provide enough space to transfer the damage of the roof to the surface. Even if the damage develops to the surface, the surface damage process is gradual. First, cracks appear on the surface, then small collapse pits appear, and finally, the rock mass on the pit wall falls to expand the collapse pit.

Another common failure is plug settlement. After the goaf is formed, the overburden loses its lower support, and the steep weak surface reduces the shear resistance of the roof rock mass. After the through shear surface is formed, the overburden settles rapidly. This kind of damage is rapid, and the roof of the goaf tends to sink as a whole rather than break and collapse (Figure 10).

According to the damage investigation in the previous section, the roof failure mechanism of the nonferrous metal mine is relatively complex. A large number of loose gravels are observed at the 1613 m level, which shows that the roof of the goaf has collapsed. While at the 1630 m

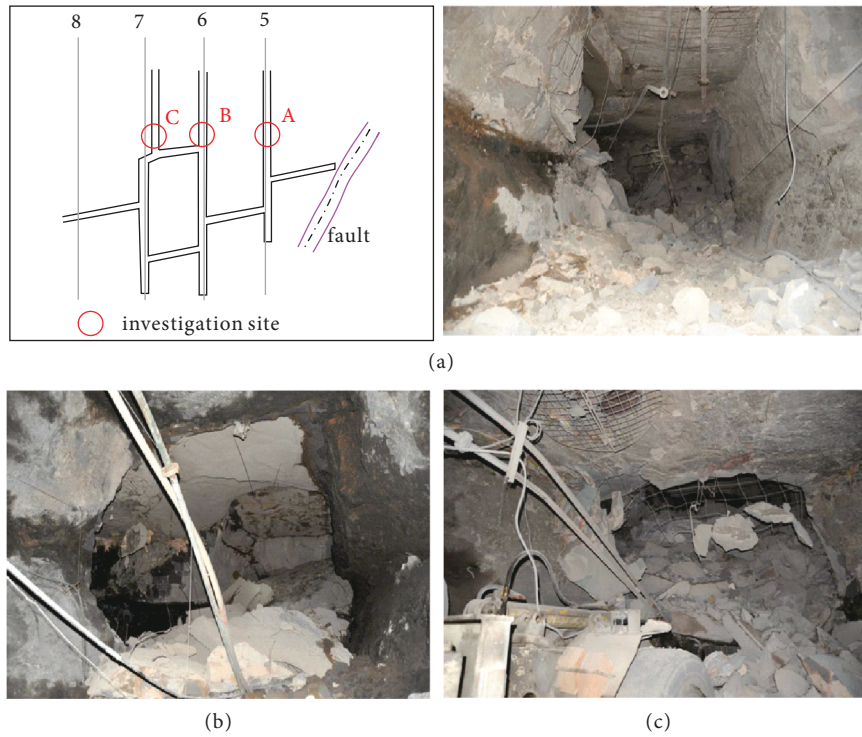


FIGURE 5: The location of the investigation and the filed destructions at the 1613 m level.

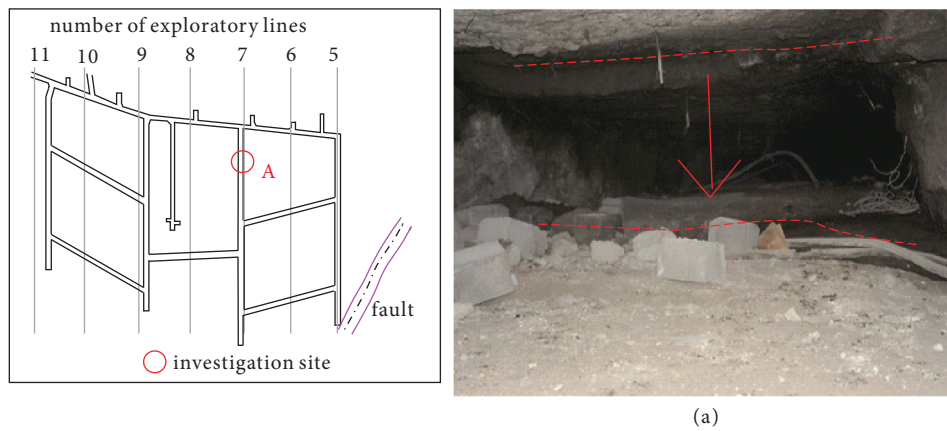


FIGURE 6: The location of the investigation and the filed destructions at the 1630 m level.

level, about 20 m above the roof, the drift has only sunk as a whole, which shows that the lower caving failure has not developed to this level.

Although, due to inaccessibility, it is impossible to directly observe the height of the caving failure of the roof, the development height of the failure can be estimated by theoretical calculation. Assuming that the height of the initial goaf is H_1 , the height of the roof failure is H_2 .

The crushing expansion coefficient is η ; then, the height of the crushed rock pile is $\eta \cdot H_2$; the height of the gap between the

top of the crushed rock pile and the goaf is Δ ; and the spatial relationship is shown in Figure 11.

Then, the gap can be calculated according to the following formula:

$$\Delta = H_2 + H_1 - \eta H_2. \tag{1}$$

When $H_1 = H_2(\eta - 1)$, $\Delta = 0$.

At this time, the falling loose bodies will fill the mined-out area, and there is not enough space to

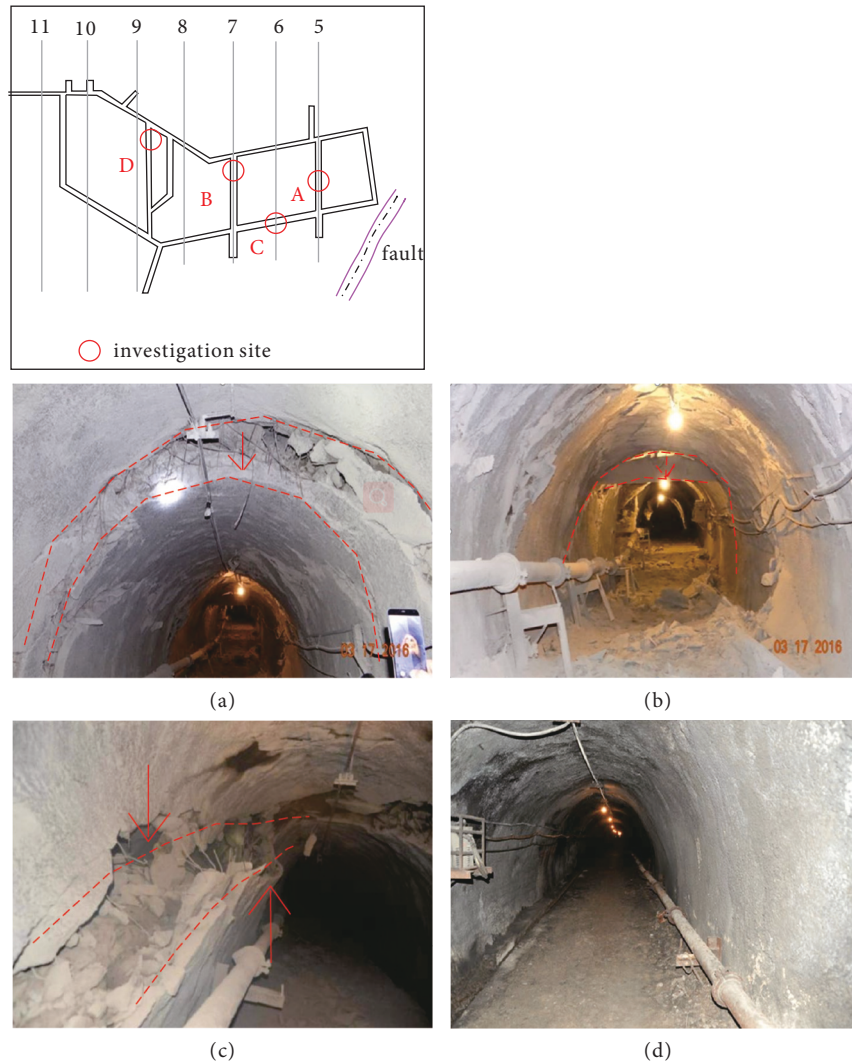


FIGURE 7: The location of the investigation and the filed destructions at the 1650 m level.

accommodate the broken roof rock mass. When the falling debris is full of the mined-out area, the falling height of the roof can be calculated as follows:

$$H_2 = \frac{H_1}{(\eta - 1)} \quad (2)$$

The looseness coefficient is the ratio of the volume of gravel to the volume of intact rock mass. So, it has no units. The height of the mine-out area is the layered height of 5 m. Substituting the above data into equation (2), it can be got that,

$$H_2 = \frac{H_1}{\eta - 1} = \frac{5}{1.5 - 1} = 10 \text{ m.} \quad (3)$$

It can be seen that the caving failure of the roof stops when it develops to the level of 1628 m. At this time, the goaf is filled with gravels. Gneiss is located above the 1642 m level. Due to the steep dominant joint surface of the gneiss, the shear resistance of overlying strata can only be provided by the shear strength and friction between joints. However, according to the geological data and field investigation, there

are weak interlayers between the joints in gneiss, and the shear resistance is poor. Although the arch caving failure did not develop into gneiss, the failure of the lower filling material led to the decline of support capacity. When the supporting force of the lower part and the shear resistance of the lateral joint cannot bear the gravity of the overlying strata, the gneiss will sink along the joint in a piston manner. The overall staggered subsidence of the roadway shown in Figures 6 and 7 is favorable to prove that the gneiss has overall plug subsidence.

Therefore, the stope instability of the nonferrous metal mine leads to a composite failure mode of the overlying strata. In this mode, the lower filling body has arched caving, and the upper gneiss has instantaneous plug settlement as shown in Figure 12.

5. Study on the Mechanism of Stope Instability

Because this accident involves rock mass collapse and large surface deformation, it is more necessary to reveal the whole process from the initial fracture to the large-scale instability of the overlying strata.

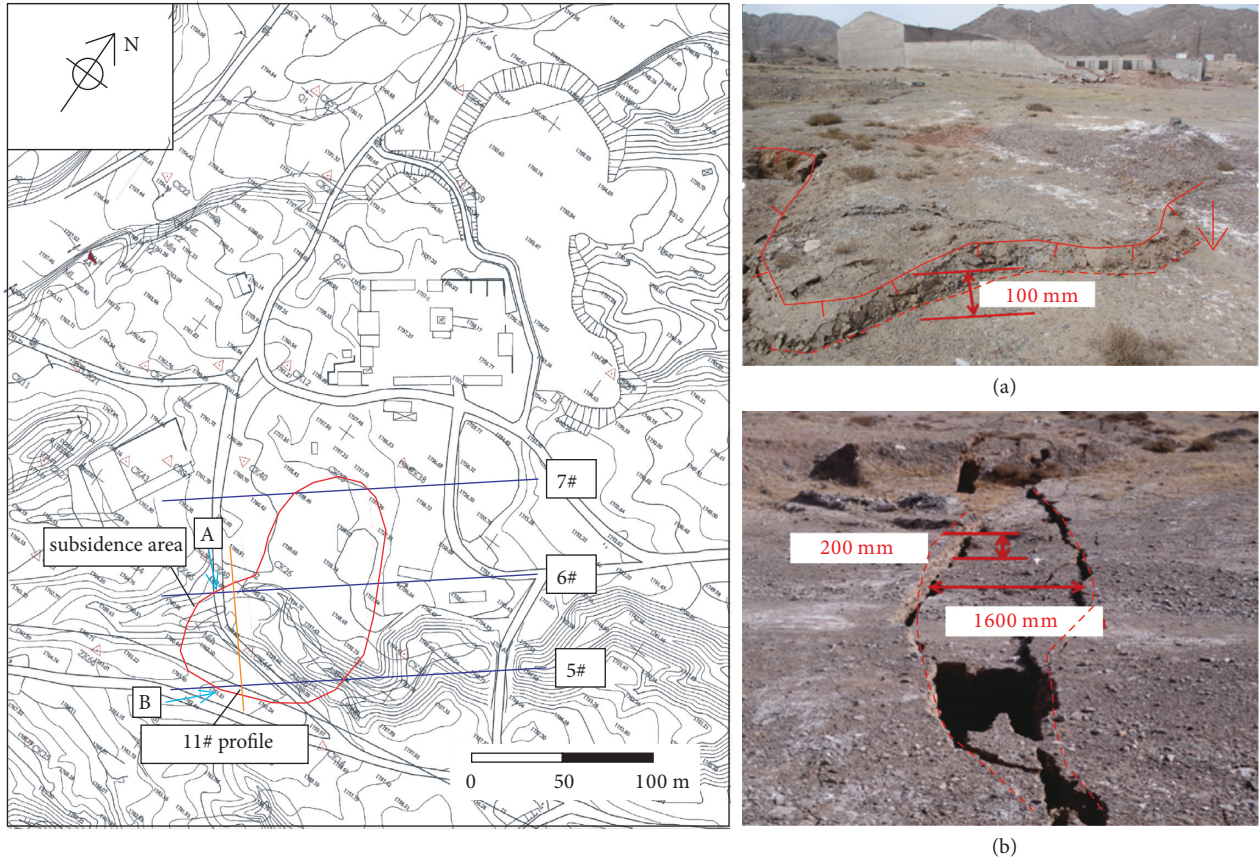


FIGURE 8: The location of the investigation and the damage at the site on the surface.

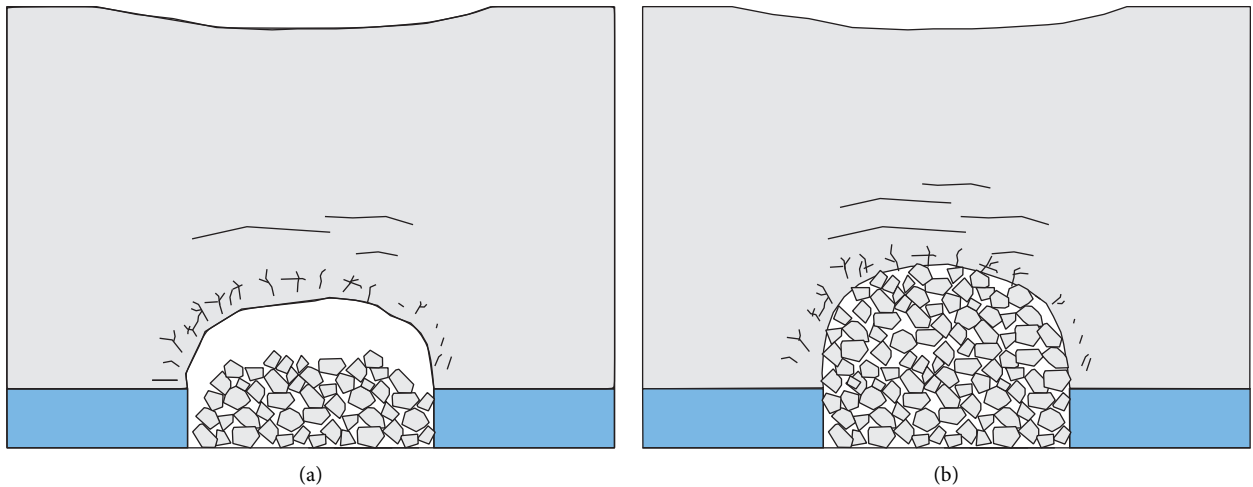


FIGURE 9: The process of arched caving in the roof strata. (a) Initial caving of the roof strata. (b) Natural termination of rock strata fall.

Compared with the continuous medium method, the discrete element method is more suitable for the case study. Based on the discrete element method (DEM), the particle flow code (PFC) uses an assembly of cemented particles to simulate the intact material. The PFC can simulate the whole process of the rock mass from crack initiation to disintegration depending on its particle flow characteristics. The contact between particles makes the development process of

material failure more realistic. Therefore, the PFC has been successfully applied to the research in the field of mining engineering [37–39].

Diego used the PFC to study synthetic rock mass (SRM) modelling techniques, successfully simulating the mechanical behavior of jointed rock masses, and obtained predictions of rock mass scale effects, anisotropy, and brittleness [40]. Svartsjaern studied the gradual collapse process of the

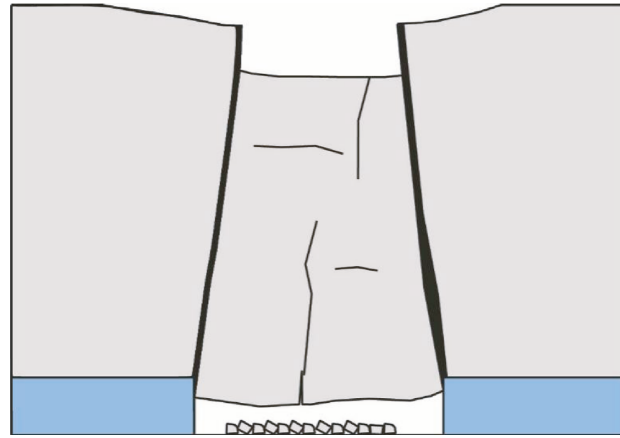


FIGURE 10: The plug subsidence of the overlying strata.

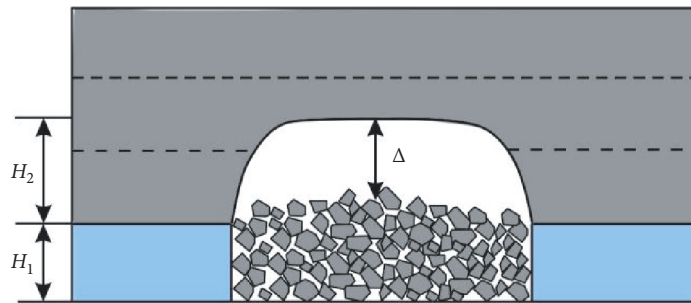


FIGURE 11: Schematic diagram of roof caving.

ground surface induced by sublevel caving at the Kiirunavaara Mine with the PFC, and the simulation results were consistent with the actual situation [28]. Li studied the mechanical mechanism of surface subsidence and filling material movement caused by underground mining in Hongling lead-zinc mine through the PFC [41]. It is revealed that the collapsed waste rock in the mined-out area can provide support force for the surrounding rock and restrict the further collapse of the hanging wall.

5.1. Microscopic Parameter Calibration and Numerical Model Setup. In this study, the two-dimensional particle flow code (PFC2D) was used to investigate the mechanism of strata movement and surface subsidence induced by underground mining. The basic contact model between particles is generally the contact bond model (CBM) or the parallel bond model (PBM). The contact bond can only transmit the force, while the parallel bond can transmit both force and moment between particles. The PBM is a more realistic bond model for modelling the rock-like material and has been successfully used in previous studies, which was therefore adopted in this study [37–39, 41].

Parallel bonds break when the maximum tensile stress of parallel bonds between particles exceeds their tensile strength or the maximum shear stress of parallel bonds exceeds their shear strength under external forces. This results in the formation of micro-tension or shear cracks. When many adjacent micro-cracks occur, they connect with

each other and form large cracks, which lead to the failure of the complete material. Finally, the bond behavior is replaced by the loose behavior.

In addition to the above two contact models, the PFC also contains a smooth joint model (SJM) which can effectively simulate the mechanical response of joints in the rock mass. The smooth-joint model simulates the behavior of a planar interface with dilation regardless of the local particle contact orientations along the interface. In this model, particles are allowed to slide past one another without over-riding one another. It is a major breakthrough to represent discontinuities as planar surfaces associated to a realistic behavior for structural defects [42–44].

Therefore, the PFC model using the parallel bond and smooth joint model is suitable for simulating the whole process of cracking and breaking of rock mass.

The PFC uses an assembly of bonded particles to simulate the mechanical response of rock mass, of which the model parameters are to describe the mechanical properties between particles, such as the normal stiffness and shear stiffness of the contacts. These microscopic parameters are not directly and necessarily related to the macroscopic mechanical parameters of the rock mass simulated by the particle assembly. Therefore, a series of numerical simulation experiments (uniaxial compression, tensile strength test, biaxial compression test, etc.) are required to conduct trial-and-error tests to obtain the mechanical parameters of the microscopic particles that match the actual rock mass

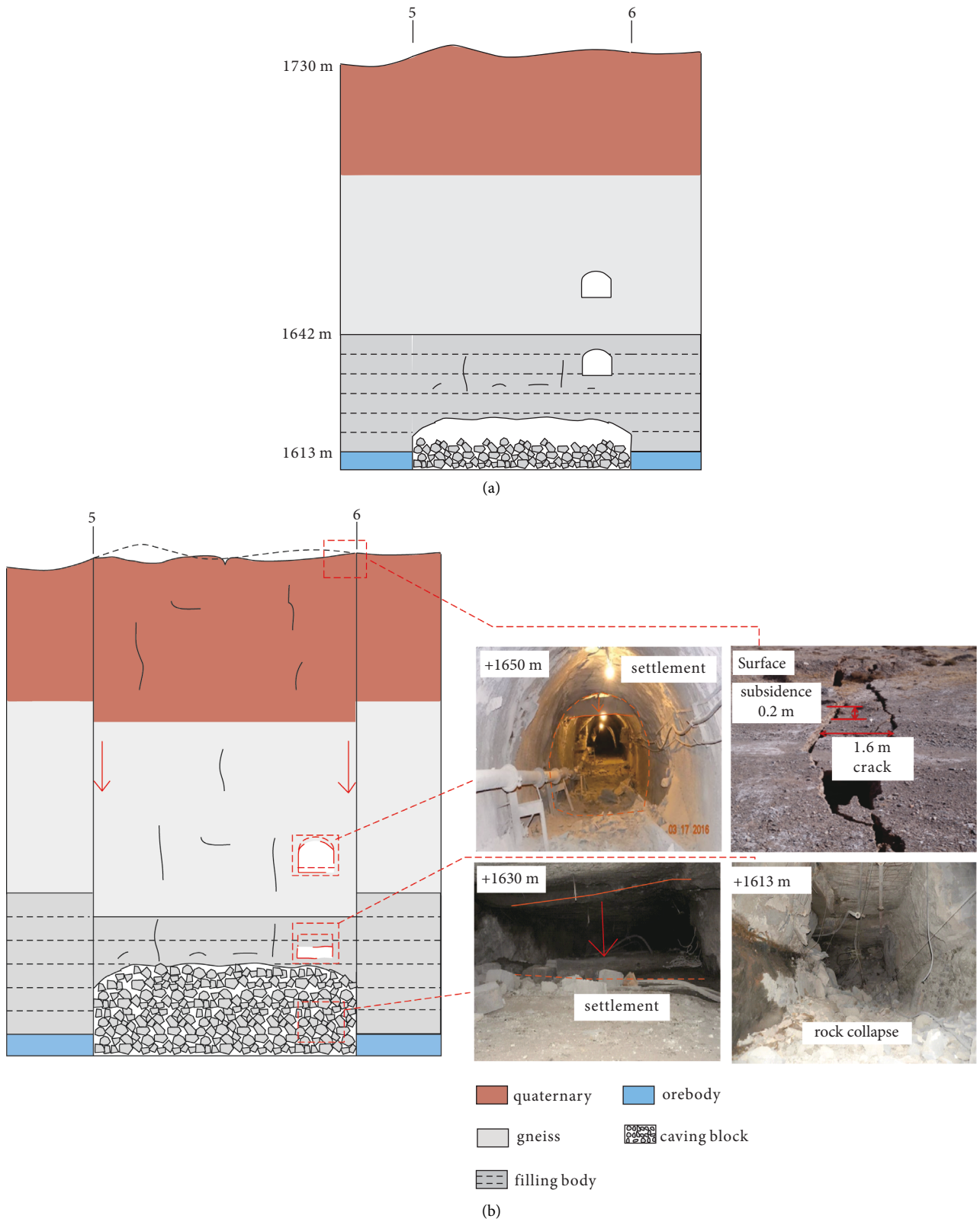


FIGURE 12: The failure process of overburden rock formation caused by underground mining. (a) Step 1: Arched caving of the roof filling body. (b) Step 2: Plug-subsidence of the upper gneiss.

TABLE 2: Microscopic parameters of the rock.

| Parameters | Value | | | |
|--------------------------------------|--------|----------|--------------|-----------------|
| | Gneiss | Ore body | Filling body | Quaternary soil |
| Density (kg/m ³) | 2700 | 2800 | 2200 | 2000 |
| Contact bond modulus (GPa) | 17.94 | 14.35 | 4.36 | 4.36 |
| Contact bond stiffness ratio | 1.57 | 1.57 | 1.57 | 1.57 |
| Friction coefficient | 0.25 | 0.25 | 0.25 | 0.25 |
| Parallel bond tensile strength (MPa) | 5.79 | 4.63 | 2.07 | 0.56 |
| Parallel bond cohesion (MPa) | 4.83 | 3.86 | 1.73 | 0.47 |
| Parallel bond friction angle (°) | 40 | 42 | 39 | 38 |
| Parallel bond modulus (GPa) | 17.94 | 14.35 | 4.36 | 4.36 |
| Parallel bond stiffness ratio | 1.57 | 1.57 | 1.57 | 1.57 |

parameters [41]. According to the rock mass parameters shown in Table 1, the corresponding microscopic parameters are shown in Table 2.

The mechanical parameters of joints are often difficult to obtain, which usually need to be judged by experience according to the field conditions. Because additional parameter matching process is needed in the PFC model, it is too complex to obtain the micro parameters corresponding to the actual joints in PFC simulation. It is widely recognized that the strength of joints is much lower than that of rocks. Therefore, the reduction of the strength parameters of the smooth joint model can also effectively reflect the mechanical response characteristics of joints in the model, and the final effect of this simulation also proves this feasibility. The joint parameters shown in Table 3 are used in this paper.

The 11 # profile in Figure 8 is selected as the research object. Due to the complex geological conditions, the profile is moderately simplified on the premise of retaining the main engineering geological elements, as shown in Figure 13. According to this profile, a two-dimensional numerical model including 122087 particles is established in the PFC to simulate the rock strata movement caused by underground mining (Figure 14).

In this mine, filling mining has been carried out simultaneously at both levels, forming the engineering geological status as shown in Figure 4. The failure occurred in the upper mining area, so the model only included the strata above the 1613 m level. Four rock strata are successively distributed in the model from top to bottom, which are 50 m thick Quaternary strata, 50 m thick gneiss, 30 m thick cemented filling body, and 15 m thick ore body, respectively, as shown in Figure 14. There are two groups of dominant joints in the gneiss, the projection of which in this section is horizontal (dip 3°) and vertical (dip 88°), respectively. Geological data show that the joints in gneiss have good continuity, so the joints in the model are assumed to be consecutive joints. To simplify the model, the joint spacing is enlarged by integer multiples. Although this change will reduce the authenticity of simulation results in some aspects, it can still explain the failure mechanism of the roof in essence. At the same time, due to the filling process, there is a hexagonal contact surface of the filling body in the filling body, which is also considered as a kind of joint. Finally, considering the simulation accuracy and simulation efficiency, the particle radius is 0.25 m–0.38 m.

5.2. Model Boundary Conditions. In-situ stress should be applied to the model prior to numerical simulation of underground mining. The vertical stress is set as gravity, while the direction of horizontal stress is not in the same plane as the strike direction of the 11 # profile. Therefore, before being applied to the model, the horizontal stress should be first converted to the inclination direction of the profile, and the horizontal stress of the profile is 4.2 MPa.

The initial stress is applied to the PFC model through the following procedure. In the first stage, the top of the PFC model was unconstrained to maintain the natural state, and the wall boundary constraints were adopted at the bottom and both sides. The displacements of both sides and the bottom boundary were fixed; then gravity was applied to each particle of the model. Finally, the model was run to balance. In the second stage, the horizontal displacement of the left and right walls was released to adjust the horizontal pressure on the model. The FISH language built in the PFC was used to compile the servo program, which could adjust the position of the walls to make the actual horizontal in-situ stress of 4.2 MPa on the model according to the monitored pressure on the wall. In the third stage, sufficient time steps were run to make the model reach the equilibrium state.

5.3. Simulation Schemes and Measurement Schemes. In this study, the PFC2D is used to simulate the surface collapse accident caused by underground mining in a nonferrous metal mine, and the process and mechanism of the movement of overburden strata ultimately caused by the instability of several narrow mined-out areas are studied.

The downward layered cemented filling method has always been adopted in this mine. First, it was mined along the drifts and cemented filling was carried out after the mining was completed. After the filling body was cured, the adjacent drifts were exploited again. In order to improve the mining efficiency, cemented filling was usually only carried out once after 5 drifts had been exploited. The damage happened just after the five drifts were mined and before the filling was completed. Therefore, in this simulation, 6 drifts were planned to be exploited sequentially from the middle to both sides. As shown in Figure 15, the drifts were numbered from 1 # to 6# according to the mining sequence.

In order to record the stress evolution of roof and pillar during excavation, a set of stress measuring circles was set up

TABLE 3: Microscopic parameters of the joints.

| Joint type | Normal stiffness (GPa) | Shear stiffness (GPa) | Friction coefficient | Cohesion (Pa) | Tensile strength (Pa) |
|---|------------------------|-----------------------|----------------------|---------------|-----------------------|
| Dominant joint of the gneiss | 15.0 | 10.0 | 0.1 | $2.50E + 04$ | $1.00E + 04$ |
| Boundary surface of the filling body approach | 15.0 | 10.0 | 0.1 | $6.00E + 03$ | $4.00E + 03$ |

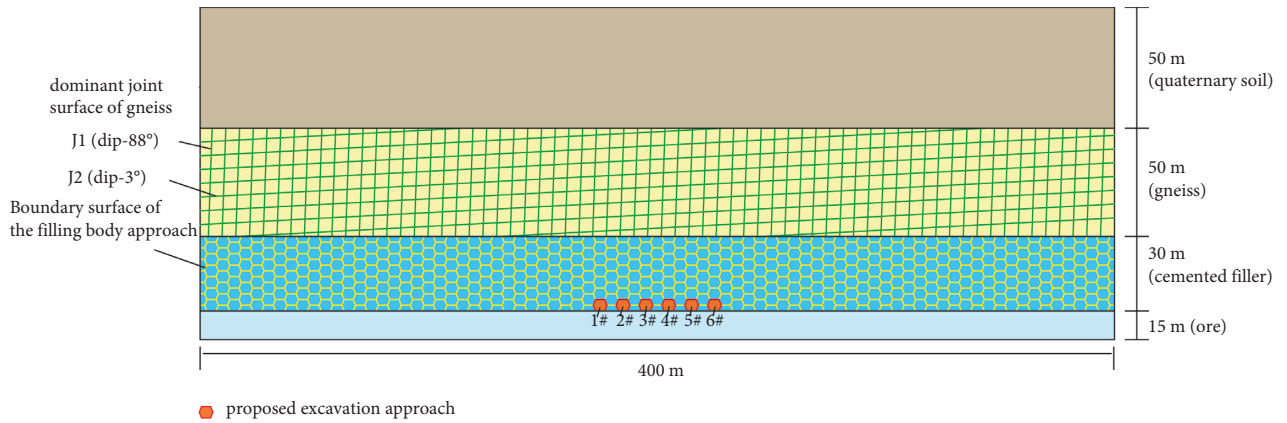


FIGURE 13: Schematic diagram of the simplified 11# profile.

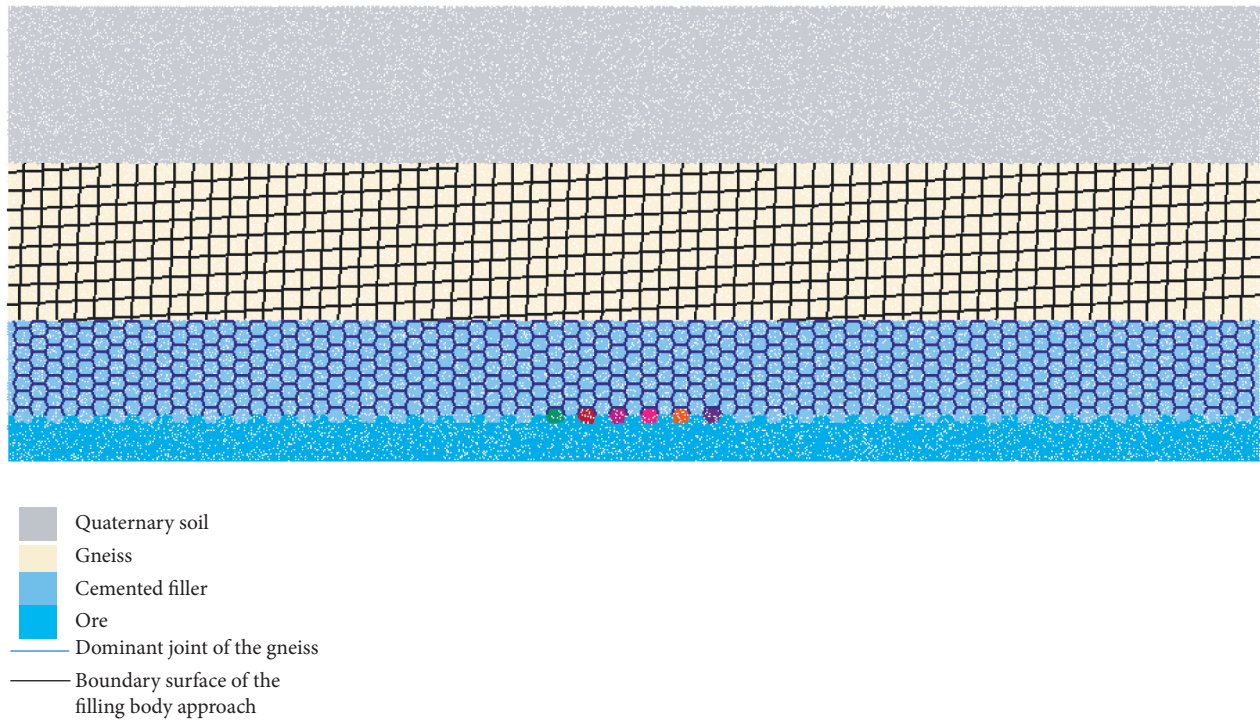


FIGURE 14: The PFC numerical model of the simplified 11# profile.

in the model as shown in Figure 15. The radius of the stress measuring circle in pillars is 3 m (from 1 to 5), and that in the roof is 4 m (from 6 to 8).

5.4. Numerical Results and Analysis. In this section, the mechanical mechanism of the strata movement and surface collapse caused by underground mining is studied. Figure 16

shows the failure process and corresponding stress evolution of rock mass during excavation simulation. The left figure shows the failure process of rock mass during simulation, in which the red mark is the location of particle bond fracture to characterize the failure cracks of the rock mass. The right figure shows the distribution of contact force, which reflects the transfer path of force inside the model. Blue lines

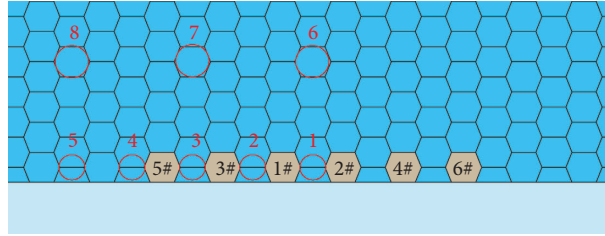


FIGURE 15: Layout of stress measurement circles and drifts mining sequence (Circles 1–8 are stress measurement circles; the mining sequence of the drifts is from 1 # to 6 #).

indicate compressive force, red indicates tensile force, and line thickness indicates the magnitude of force.

As shown in Figures 16(a) and 16(b), after excavation of the 1 # drift, the surrounding rock can be maintained stable with only a few cracks in the roof. Excavation results in a stress state change of the surrounding rock. Tensile stress occurs in the roof, where compressive stress decreases. And, the concentration of compressive stress occurs on both sides of the drift.

As shown in Figures 16(c) and 16(d), the roofs remain stable and the pressure of the intermediate pillar is significantly concentrated after excavation of the two approaches.

After excavation of three drifts, the stope remains stable despite the increase of cracks in the roof of the 1# drift. Figure 16(f) shows that a smaller stress arch occurs in the roof at this time, which is a sign of further roof failure, with pressure apparently concentrated towards both pillars. When four drifts are excavated, the pressure of the pillars increases further, but the stability can be maintained.

When five adjacent drifts are mined, the vertical stress on the pillars exceeds their strength limit and cracks are found throughout the pillars. The force chain inside the four pillars disappears, indicating that the pillars have lost their bearing capacity at this time. A lot of tension cracks and stress arching appear in the roof filling body. The vertical pressure can only be transmitted to both sides along the stress arch, and the compressive stress concentration occurs in the surrounding rock outside of the 5# and 4 # drifts. Horizontal joints make gneiss present horizontal layered structure. Under the compression of horizontal in-situ stress exceeding vertical in-situ stress, the layered structure just maintains stability, but this stability is very fragile.

When the number of drifts mined reaches 6, the ore pillar between drift of 4 # and 6# is rapidly destroyed, which further expands the span of the collapsed goaf. Meanwhile, the stress arch in the backfill body is destroyed, the backfill body is broken as a whole and cannot bear the vertical pressure. Cracks develop upward in the overlying gneiss and are widely distributed in the model, developing upward only along vertical joints. As shown in Figure 16(l), the original arch stress in the filling body disappears, and the newly formed random stress chain is the contact force formed by the collapse of the scattered body.

The original horizontal layered force chain in gneiss is destroyed. There are obvious vertical force chains on the left and right sides of the overlying gneiss, while the middle part

still maintains the original stress state. It can be seen that vertical shear failure occurs at both sides of the rock mass, while the middle of the gneiss remains intact, that is, plug subsidence occurs. This indicates that the gneiss has undergone plug settlement.

When the number of drifts mined reaches six, as shown in Figures 16(k) and 16(l), the pillar between 4 # route and 6# route is destroyed rapidly, which further expands the span of the goaf. Then, the roof filling body is broken, and the stress arch is completely destroyed, which loses its support capacity.

The cracks only develop upward along the vertical joints in the gneiss above, where they are not widely distributed as in the filling body. As shown in Figure 16(l), after the stress arch in the filling body disappears, the newly formed random force chain shows the contact force generated by the collapse gravels accumulation.

The original horizontal layered force chain in gneiss is destroyed. There are obvious vertical force chains on the left and right sides of the overlying gneiss, while the middle part still maintains the original stress. It can be seen that vertical shear failure occurs at both sides of the gneiss, while that of the middle remains intact. This indicates that the gneiss has undergone plug settlement.

As shown in Figure 17, the evolution of the vertical displacement cloud diagram of the model during mining also clearly reflects the failure process of the rock mass. When four drifts are exploited, the roof strata can still maintain stability. When five drifts are mined, the roof filling body has arched caving; after six drifts are mined, the arched caving damage of the backfill body continues to develop upward, and when it develops to the overlying gneiss, it causes plug subsidence of the gneiss along the vertical joints.

In order to monitor the stress evolution process of the surrounding rock and pillar of the stope roof, as shown in Figure 15, several stress measurement circles are arranged in the model. Figure 18 shows the evolution of vertical stress in the pillar and roof strata, respectively, during the mining process. When the first drift is excavated, the vertical stress will be transferred to both sides, and the compressive stress concentration will occur in the surrounding rock on the side wall of the drift. When multiple drifts are excavated, the compressive stress will be redistributed in the formed pillars, and the farther away from the middle drift, the smaller the increased stress. When more than 5 drifts are excavated, the redistributed vertical stress in the ore pillar exceeds the acceptable limit, the chain failure occurs in a short period of time, and the bearing capacity is lost.

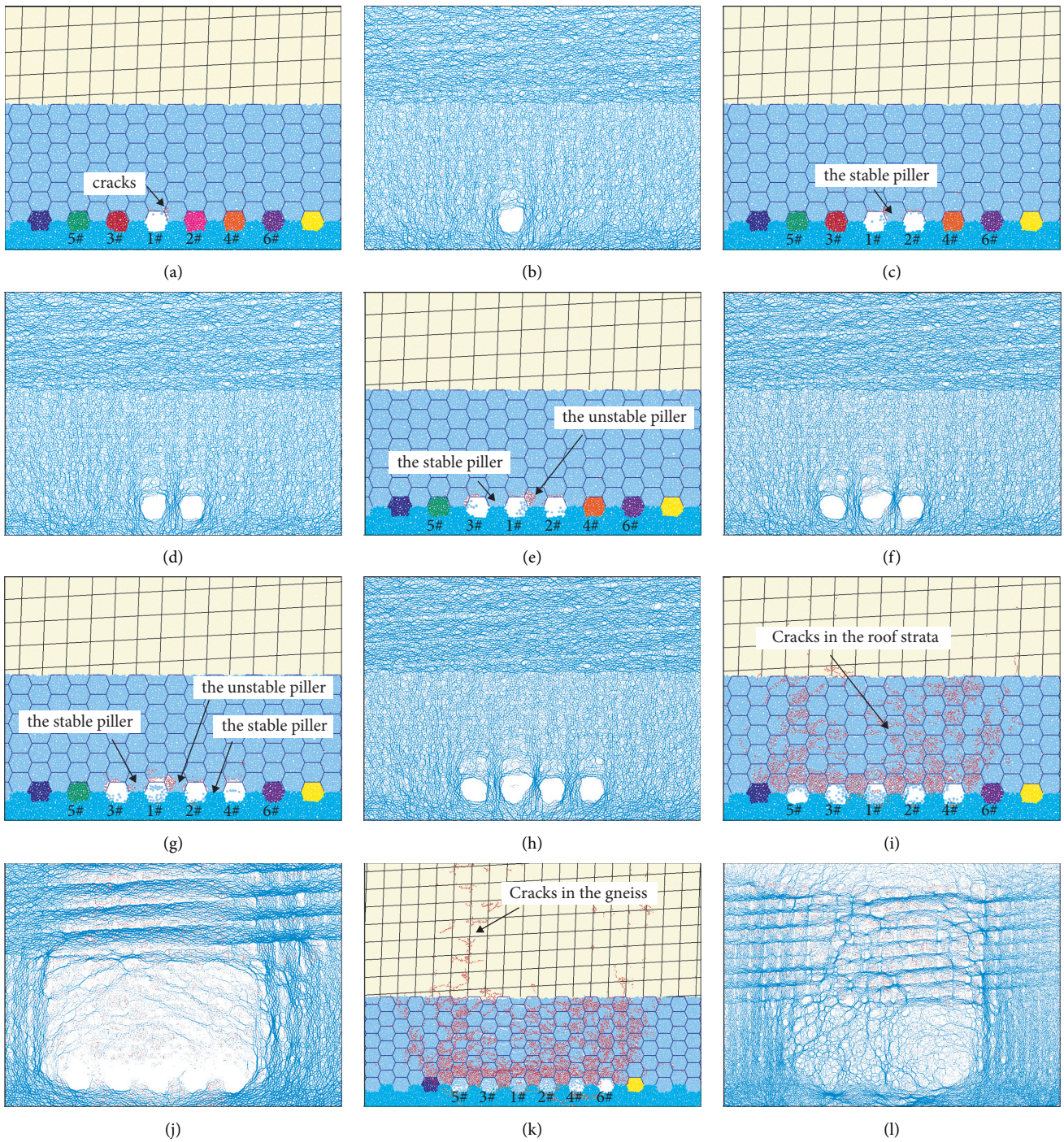
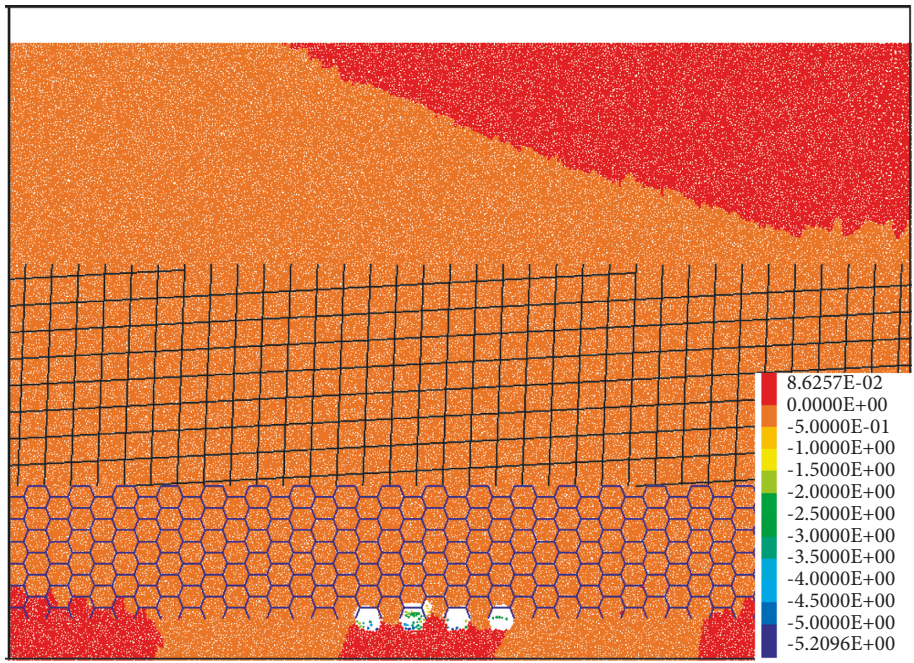
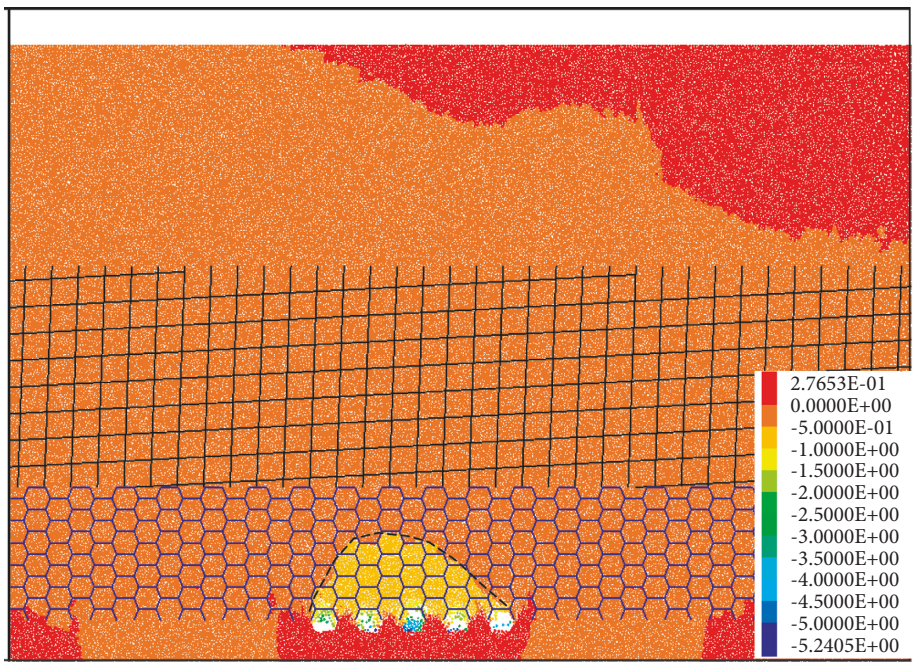


FIGURE 16: Illustrations of instability process of the pillars and roof. Left: The failure and fracture development of the model. Right: The contact force chain of the model (blue represents pressure and red represents tension). (a)–(b) The 1 # drift is excavated; (c)–(d) The 2 # drift is excavated; (e)–(f) The 3 # drift is excavated; (g)–(h) The 4 # drift is excavated; (i)–(j) The 5 # drift is excavated; (k)–(l) The 6# drift is excavated.

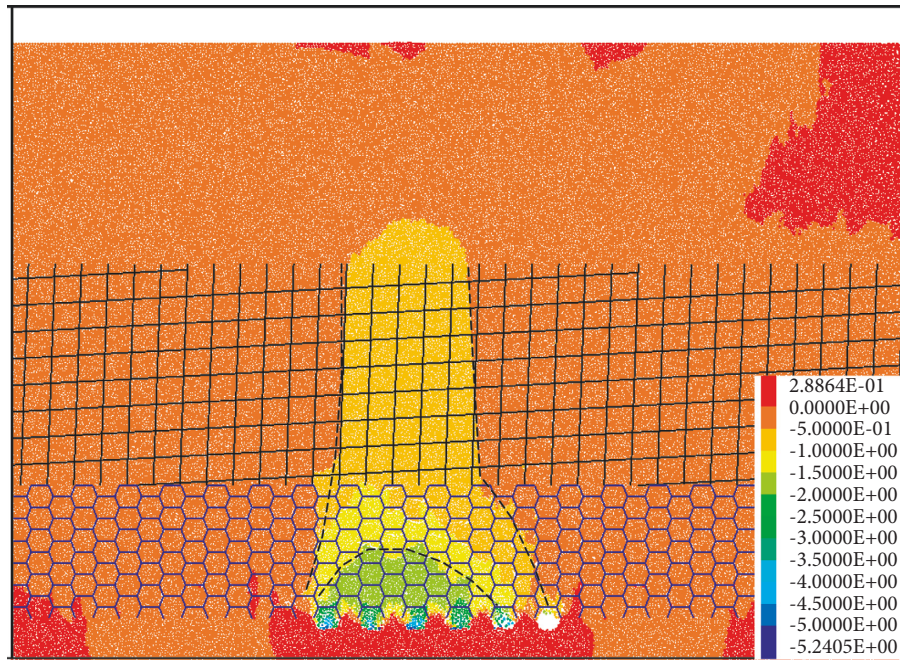


(a)

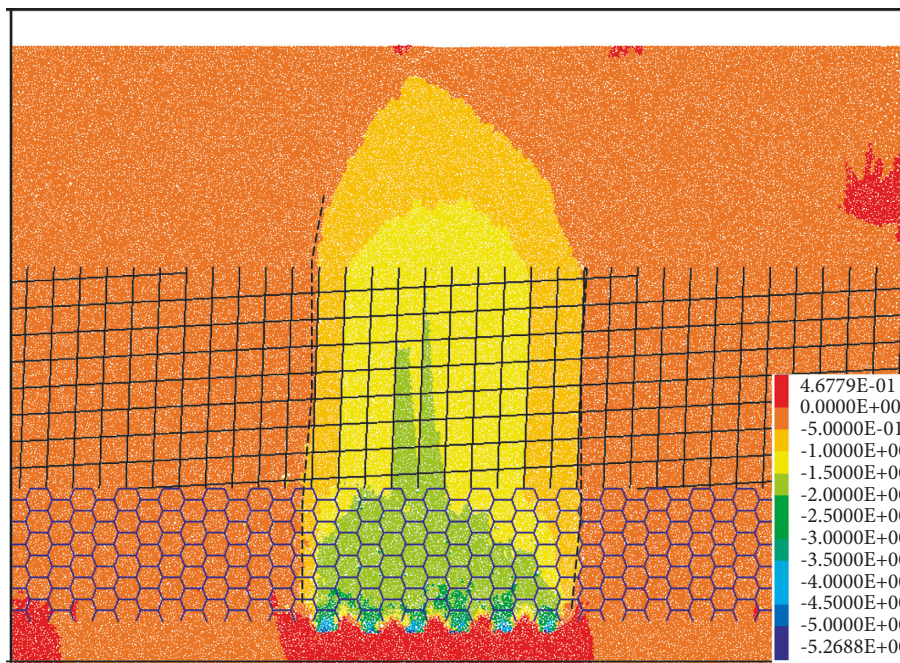


(b)

FIGURE 17: Continued.

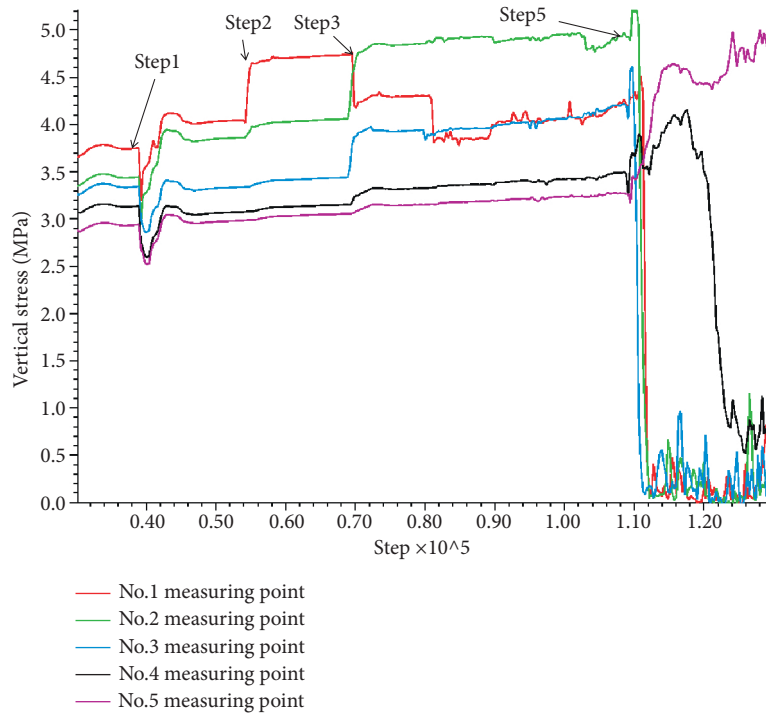


(c)

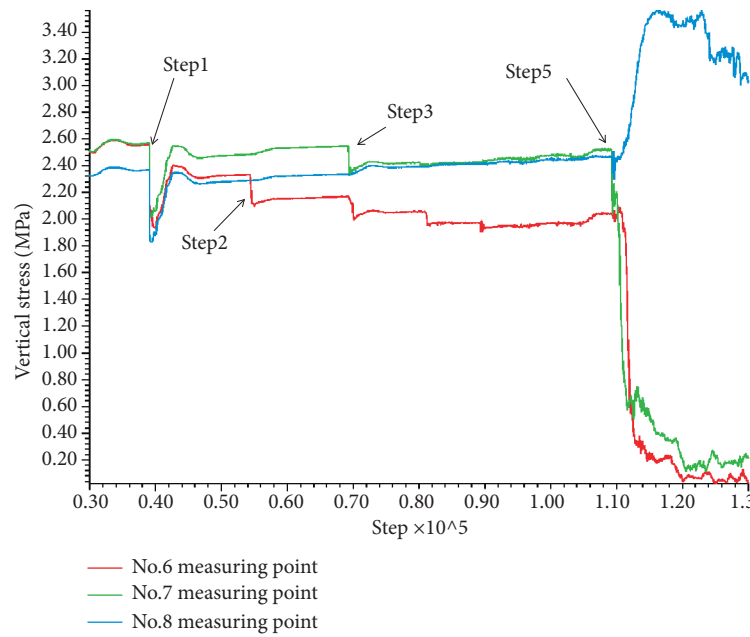


(d)

FIGURE 17: Displacement cloud diagram of the model during mining process. (a) Steady state of the roof. (b) Arch caving of roof filling body. (c) Initial stage of plug subsidence of overlying gneiss. (d) Late stage of plug subsidence of overlying gneiss.



(a)



(b)

FIGURE 18: Vertical stress of rock mass during mining. (a) Vertical stress of the pillar during mining. (b) Vertical stress of roof filling body during mining.

It can be seen that the numerical simulation results are very consistent with the field, indicating that the established numerical model can be used to study the mechanism of overburden stratum damage and surface subsidence caused by underground mining in this mine.

6. Conclusions

Field investigation, engineering geological analysis, and the PFC numerical simulation were carried out on the surface collapse accident of a nonferrous mine in northern China using the cemented filling mining method. The mechanism of violent failure of overlying composite strata caused by multiple adjacent narrow goaf was researched. The following conclusions are drawn:

- (1) From the field investigation results, it can be seen that the starting position of the underground failure is at the 1613 m level, where the pillar is unstable and damaged, and the roof backfill body is broken and caved. The caving damage caused by the backfill body does not develop to the surface but is terminated below the 1630 m level. Above the 1630 m level, the overall plug subsidence occurred in the rock mass.
- (2) The failure process of the overlying rock mass can be divided into four stages due to the special geological conditions of the mine: pillar stability stage, pillar chain failure stage, roof filling caving stage, and gneiss plug settlement stage. According to the method of interval mining, when no more than 4 drifts are mined, the stope can be in a stable state. When more than 4 drifts are mined and cannot be filled in time, the pillars are damaged successively in a short interval. After the chain failure of pillars, the filling material of the roof collapses, and the caving arch develops upward. As the collapsed gravels fill the narrow mine-out areas, the caving failure of the filling body develops to the level of 1625 m and stops. Horizontal joints (dip 3°) make gneiss present a horizontal layered structure, while horizontal in-situ stress is greater than vertical in-situ stress. After the lower filling body loses its bearing capacity, the compression of horizontal in-situ stress keeps the layered gneiss stable for a short time. Under the mining disturbance, this stability is quickly destroyed, and the gneiss above the stope produces overall shear slip along the vertical joints (dip 88°), which eventually leads to the plug subsidence of gneiss.
- (3) According to the field investigation, engineering geological analysis and numerical simulation, the roof instability of the narrow goaf deeply buried underground in the mine finally leads to the failure accident of large-scale instantaneous settlement of the surface, which is determined by many factors. Among them, the unique geological condition is the internal cause, and the underground mining activities are the inducement. In the process of surface collapse, the combination of internal and external factors leads to the mechanism of rock stratum movement and the phenomenon of surface damage.

Therefore, in order to prevent such damage accident, during mining, the number of continuous mining drifts in any mining area is suggested not to exceed 4, and the next group of drifts should not be exploited before filling the last group.

Data Availability

The data used to support the findings of this study are available and can be demanded from the corresponding author.

Conflicts of Interest

The authors declare that they have no conflicts of interest.

Acknowledgments

The authors would like to thank the financial support provided by the National Natural Science Foundation of China (Grant no. 51534003).

References

- [1] X. Cui, Y. Gao, and D. Yuan, "Sudden surface collapse disasters caused by shallow partial mining in Datong coalfield, China," *Natural Hazards*, vol. 74, no. 2, pp. 911–929, 2014.
- [2] M. Eremin, E. Gabriel, and I. Smolin, "Numerical simulation of roof cavings in several Kuzbass mines using finite-difference continuum damage mechanics approach," *International Journal of Mining Science and Technology*, vol. 30, no. 2, pp. 157–166, 2020.
- [3] S. Wang, X. Li, and S. Wang, "Separation and fracturing in overlying strata disturbed by longwall mining in a mineral deposit seam," *Engineering Geology*, vol. 226, no. 30, pp. 257–266, 2017.
- [4] F. G. Bell, T. R. Stacey, and D. D. Genske, "Mining subsidence and its effect on the environment: some differing examples," *Environmental Geology*, vol. 40, no. 1–2, pp. 135–152, 2000.
- [5] M. Svartsjaern, "A prognosis methodology for underground infrastructure damage in sublevel cave mining," *Rock Mechanics and Rock Engineering*, vol. 52, no. 1, pp. 247–263, 2019.
- [6] E. Can, Ş. Kuşcu, and M. E. Kartal, "Effects of mining subsidence on masonry buildings in Zonguldak hard coal region in Turkey," *Environmental Earth Sciences*, vol. 66, no. 8, pp. 2503–2518, 2012.
- [7] L. C. Li, C. A. Tang, X. D. Zhao, and M. Cai, "Block caving-induced strata movement and associated surface subsidence: a numerical study based on a demonstration model," *Bulletin of Engineering Geology and the Environment*, vol. 73, no. 4, pp. 1165–1182, 2014.
- [8] A. Vyazmensky, D. Elmo, and D. Stead, "Role of rock mass fabric and faulting in the development of block caving induced surface subsidence," *Rock Mechanics and Rock Engineering*, vol. 43, no. 5, pp. 533–556, 2010.
- [9] E. T. Brown, *Block Caving Geomechanics (International Caving Study I, 1997–2000)*, University of Queensland, JKMRRC monograph series in mining and mineral processing, Brisbane, 2003.
- [10] B. H. G. Brady and E. T. Brown, *Rock Mechanics: For Underground Mining*, Springer, Berlin, 2013.

- [11] K. Skrzypkowski, "3D numerical modelling of the application of cemented paste backfill on displacements around strip excavations," *Energies*, vol. 14, no. 22, p. 7750, 2021.
- [12] K. Skrzypkowski, "Compressibility of materials and backfilling mixtures with addition of solid wastes from flue-gas treatment and fly ashes," *E3S Web Conf*, vol. 71, p. 7, 2018.
- [13] H. Ding, S. Chen, S. Chang, G. Li, and L. Zhou, "Prediction of surface subsidence extension due to underground caving: a case study of hemushan Iron mine in China," *Mathematical Problems in Engineering*, vol. 2020, Article ID 5086049, 10 pages, 2020.
- [14] B. Ghabraie, G. Ren, X. Zhang, and J. Smith, "Physical modelling of subsidence from sequential extraction of partially overlapping longwall panels and study of substrata movement characteristics," *International Journal of Coal Geology*, vol. 140, pp. 71–83, 2015.
- [15] W. Ren, C. Guo, Z. Peng, and Y. Wang, "Model experimental research on deformation and subsidence characteristics of ground and wall rock due to mining under thick overlying terrane," *International Journal of Rock Mechanics and Mining Sciences*, vol. 47, no. 4, pp. 614–624, 2010.
- [16] T. Villegas, E. Nordlund, and C. Dahnér-Lindqvist, "Hangingwall surface subsidence at the Kiirunavaara mine, Sweden," *Engineering Geology*, vol. 121, no. 1–2, pp. 18–27, 2011.
- [17] H. Zhao, F. Ma, Y. Zhang, and J. Guo, "Monitoring and mechanisms of ground deformation and ground fissures induced by cut-and-fill mining in the Jinchuan mine 2, China," *Environmental Earth Sciences*, vol. 68, no. 7, pp. 1903–1911, 2013.
- [18] X. Song, C. Chen, K. Xia, K. Yang, S. Chen, and X. Liu, "Analysis of the surface deformation characteristics and strata movement mechanism in the main shaft area of Chengchao Iron Mine," *Environmental Earth Sciences*, vol. 77, no. 9, p. 335, 2018.
- [19] G. Cheng, T. Ma, C. Tang, H. Liu, and S. Wang, "A zoning model for coal mining - induced strata movement based on microseismic monitoring," *International Journal of Rock Mechanics and Mining Sciences*, vol. 94, pp. 123–138, 2017.
- [20] K. Xia, C. Chen, and Y. Deng, "In situ monitoring and analysis of the mining-induced deep ground movement in a metal mine," *International Journal of Rock Mechanics and Mining Sciences*, vol. 109, pp. 32–51, 2018.
- [21] N. Xu, P. H. S. W. Kulatilake, H. Tian, X. Wu, Y. Nan, and T. Wei, "Surface subsidence prediction for the WUTONG mine using a 3-D finite difference method," *Computers and Geotechnics*, vol. 48, no. 3, pp. 134–145, 2013.
- [22] F. Zhang, T. Yang, L. Li, Z. Wang, and P. Xiao, "Cooperative monitoring and numerical investigation on the stability of the south slope of the Fushun west open-pit mine," *Bulletin of Engineering Geology and the Environment*, vol. 78, no. 4, pp. 2409–2429, 2019.
- [23] Q. Wu and P. H. S. W. Kulatilake, "Application of equivalent continuum and discontinuum stress analyses in three-dimensions to investigate stability of a rock tunnel in a dam site in China," *Computers and Geotechnics*, vol. 46, pp. 48–68, 2012.
- [24] M. Svartsjaern, D. Saiang, E. Nordlund, and A. Eitzenberger, "Conceptual numerical modeling of large-scale footwall behavior at the Kiirunavaara mine, and implications for deformation monitoring," *Rock Mechanics and Rock Engineering*, vol. 49, no. 3, pp. 943–960, 2016.
- [25] S. F. Wang and X. B. Li, "Dynamic distribution of longwall mining-induced voids in overlying strata of a coalbed," *International Journal of Geomechanics*, vol. 17, no. 6, Article ID 04016124, 2017.
- [26] T. Villegas and E. Nordlund, "Numerical simulation of the hangingwall subsidence using PFC2D," in *Proceedings of the 5th International Conference and Exhibition on Mass Mining*, Sweden, June 2008.
- [27] T. F. V. Barba and E. Nordlund, "Numerical analyses of the hangingwall failure due to sublevel caving: study case," *International Journal of Mining and Mineral Engineering*, vol. 4, no. 3, pp. 201–223, 2013.
- [28] M. Svartsjaern and D. Saiang, "Discrete element modelling of footwall rock mass damage induced by sub-level caving at the Kiirunavaara Mine," *Minerals*, vol. 7, no. 7, p. 109, 2017.
- [29] L. Zhao and W. Jin-an, "Accident investigation of mine subsidence with application of particle flow code," *Procedia Engineering*, vol. 26, pp. 1698–1704, 2011.
- [30] B. Tan, F. Ren, Y. Ning, R. He, and Q. Zhu, "A new mining scheme for hanging-wall ore-body during the transition from open pit to underground mining: a numerical study," *Advances in Civil Engineering*, vol. 2018, Article ID 1465672, 17 pages, 2018.
- [31] A. Vyazmensky, D. Stead, D. Elmo, and A. Moss, "Numerical analysis of block caving-induced fa in large open pit slopes: a finite element/discrete element approach," *Rock Mechanics and Rock Engineering*, vol. 43, no. 1, pp. 21–39, 2010.
- [32] D. Stead, E. Eberhardt, and J. S. Coggan, "Developments in the characterization of complex rock slope deformation and failure using numerical modelling techniques," *Engineering Geology*, vol. 83, no. 1–3, pp. 217–235, 2006.
- [33] E. Trigueros, M. Cánovas, J. Arzúa, and M. Alcaraz, "Stability of an abandoned siderite mine: a case study in northern Spain," *Open Geosciences*, vol. 13, no. 1, pp. 359–376, 2021.
- [34] V. I. I. Marinos, P. Marinos, and E. Hoek, "The geological strength index: applications and limitations," *Bulletin of Engineering Geology and the Environment*, vol. 64, no. 1, pp. 55–65, 2005.
- [35] E. Hoek, C. Carranza-Torres, and B. Corkum, "Hoek–Brown failure criterion-2002 edition," *Proc NARMS-Tac*, vol. 1, no. 1, pp. 267–273, 2002.
- [36] K.-S. Woo, E. Eberhardt, D. Elmo, and D. Stead, "Empirical investigation and characterization of surface subsidence related to block cave mining," *International Journal of Rock Mechanics and Mining Sciences*, vol. 61, pp. 31–42, 2013.
- [37] D. O. Potyondy and P. A. Cundall, "A bonded-particle model for rock," *International Journal of Rock Mechanics and Mining Sciences*, vol. 41, no. 8, pp. 1329–1364, 2004.
- [38] C. J. Li and X. B. Li, "Influence of wavelength-to-tunnel-diameter ratio on dynamic response of underground tunnels subjected to blasting loads," *International Journal of Rock Mechanics and Mining Sciences*, vol. 112, pp. 323–338, 2018.
- [39] X. B. Li, C. J. Li, W. Z. Cao, and M. Tao, "Dynamic stress concentration and energy evolution of deep-buried tunnels under blasting loads," *International Journal of Rock Mechanics and Mining Sciences*, vol. 104, pp. 131–146, 2018.
- [40] M. I. Diego, *Bonded Particle Model for Jointed Rock Mass*, KTH Royal Institute of Technology, Stockholm, Sweden, 2010.
- [41] X. Li, D. Wang, C. Li, and Z. Liu, "Numerical simulation of surface subsidence and backfill material movement induced by underground mining," *Advances in Civil Engineering*, vol. 2019, Article ID 2724370, 17 pages, 2019.
- [42] W. Zhao, R. Huang, and M. Yan, "Study on the deformation and failure modes of rock mass containing concentrated parallel joints with different spacing and number based on

- smooth joint model in PFC,” *Arabian Journal of Geosciences*, vol. 8, pp. 7887–7897, 2015.
- [43] M. H. Mehranpour and P. H. S. W. Kulatilake, “Improvements for the smooth joint contact model of the particle flow code and its applications,” *Computers and Geotechnics*, vol. 87, pp. 163–177, 2017.
- [44] J. A. Vallejos, K. Suzuki, A. Brzovic, and D. M. Ivars, “Application of Synthetic Rock Mass modeling to veined core-size samples,” *International Journal of Rock Mechanics and Mining Sciences*, vol. 81, pp. 47–61, 2016.

Research Article

Research on Natural Foundation Bearing Capacity and Foundation Pit Settlement of Prefabricated Utility Tunnel

Zengshan Wang,¹ Yanying Wang,¹ Weike Huang,² Hongwei Shan,² and Li Zhu ³

¹CCCC Xiong'an Investment Co., Ltd., Baoding, Hebei 071700, China

²CCCC-SHEC Sixth Engineering Co., Ltd., Xi'an, Shaanxi 710075, China

³CCCC-SHEC Engineering Design and Research Institute, Xi'an 710199, China

Correspondence should be addressed to Li Zhu; zhuli10@ccccltd.cn

Received 23 February 2022; Accepted 23 March 2022; Published 4 April 2022

Academic Editor: Gaofeng Song

Copyright © 2022 Zengshan Wang et al. This is an open access article distributed under the Creative Commons Attribution License, which permits unrestricted use, distribution, and reproduction in any medium, provided the original work is properly cited.

Prefabricated assembled integrated pipe corridor has the significant advantages of fast assembly, controlled quality of factory prefabricated forming, short construction period, energy saving and environmental protection compared with on-site casting. In this paper, a shallow plate load field test was carried out to test the bearing capacity of the natural foundation of the assembled pipe corridor and a numerical simulation analysis of the settlement of the substrate was carried out in combination with the typical local soft soil geological conditions, using the JXSG-6 beam making site in Gu'an South of the Beijing-Xiong Intercity Railway in Xiong'an New Area as the test site. The results of the study show that: during the vertical loading to 320 kPa, the overall displacement settlement of the foundation soil of each experimental group is small, mainly elastic deformation, and the final settlement of each test group is 6.68 mm, 10.89 mm and 5.38 mm respectively, with no cracks and no damage to the foundation soil. According to the calculation of the straight line section of the load settlement data, the average value of the foundation soil bearing capacity deformation modulus is 43.1 MPa, and the average value of the foundation stiffness of the 0.8 m diameter circular bearing plate is 78.2 MPa/m, which can provide a parameter basis for the structural design of the pipe corridor and the subsequent superstructure test calculation. However, due to the large stiffness difference between the structure of the pipe gallery and the soil, the soil settlement deformation process and the pipe gallery relative displacement, the shear effect on both sides of the pipe gallery; differential settlement under the influence of the local surface of the pipe gallery may occur tensile damage, the maximum displacement concentrated on both sides of the pit reached 0.6 mm, in the acceptable range. Therefore, the lower base of the pipe corridor has good bearing capacity and can meet the construction requirements of the installation stage of the integrated pipe corridor sections.

1. Introduction

The Xiongan New Area is another new area of national significance, following the Shenzhen Special Economic Zone and Shanghai Pudong New Area. As an important part of the urban infrastructure construction in the Xiongan New Area, the construction of an underground integrated pipe corridor is of great significance in ensuring the safety of municipal pipelines, improving the utilisation of underground space, beautifying the urban environment and avoiding repeated excavations on the road surface [1–3]. The typical assembled pipe corridor structure designed by China Communications

Construction Group is 15.9 m in width, 4.9 m in height and 6 m in length for a single longitudinal section, which is the largest cross-section and the largest lifting tonnage in China [4, 5]. At present, the research on the support structure deformation, pit bottom uplift and surface settlement in the process of foundation excavation is more mature, but for the integrated pipe corridor project not only needs to focus on the safety of foundation excavation, but also needs to study in depth the settlement of the integrated pipe corridor in the foundation pit itself [6–10].

With the construction of integrated pipe corridors in full swing in recent years, especially prefabricated pipe corridors

after installation, settlement at the joints due to differences in foundation bearing capacity, resulting in incidents such as leakage of integrated pipe corridors are common [11, 12]. Huang and Fan [13] studied the influence of the depth of foundation reinforcement on the force performance of the integrated pipe corridor structure on soft ground, and the vertical displacement of the integrated pipe corridor structure and the vertical displacement of the surface soil within the width were influenced by the depth of foundation reinforcement; Hu et al. [14] studied the influence of the elastic modulus of the weak soil layer on the force performance of the prefabricated assembled integrated pipe corridor, and the results showed that the reduction of the elastic modulus of the weak soil layer would The results show that the reduction of the elastic modulus of the weak soil layer will aggravate the uneven settlement of the corridor, and the weak soil layer has a greater influence on the longitudinal and transverse internal forces of the corridor structure; Wang studied the load deformation law of the prefabricated integrated corridor structure under uneven settlement conditions with the [15] help of Midas Gen finite element simulation software.

In this paper, a shallow plate load field test was carried out on the bedding layer in the construction area of the pipe corridor, using the JXSG-6 beam making site in Gu'an South of the Xiongan New Area Beijing-Xiongan Intercity Railway as the test site, and the test results were obtained. The COMSOL software was used to establish a numerical model to monitor the stress and displacement of the foundation pit to obtain the overall map and slice map of the stress and displacement distribution characteristics respectively, which were analysed to obtain the settlement characteristics of the foundation pit. This study can effectively guarantee the safe and rapid construction of the integrated pipe corridor section installation stage and provide practical guidance for the integrated pipe corridor project.

2. Project Overview

The project site is located in NA8 Road, the start-up area of Xiongan New Area, Hebei Province. This test is mainly in the NA8 line NA8K1 + 564 to NA8K2 + 380 section of the pipe corridor section installation of the whole process of key technology test research. The excavation base of the assembled integrated pipe corridor pit is in-situ soil with bedding treatment on it. Therefore, the bearing performance of the original soil of the pit is directly related to the treatment measures of the upper bedding layer, and whether the assembled integrated pipe corridor meets the settlement control standard [16, 17]. According to the preliminary survey site, the base elevation -2.085 m, the original ground elevation 7.911 m (as shown in Figure 1), three groups of test site are to powder clay, powder soil for the bearing layer, according to the survey design specification, powder clay, powder ground foundation bearing capacity characteristic value for 130 kPa, the test choose the bearing capacity characteristic value of 2.5 times, that is, 320 kPa as the loading limit value.

3. Shallow Plate Load Test

The shallow plate load test is an in-situ test method [18] to measure the pressure and deformation characteristics of the foundation soil by applying a load to the foundation soil step by step on a certain area of bearing plate, which can reflect the comprehensive characteristics of the strength and deformation of the foundation soil in the range of 1.5 to 2.0 times the diameter or width of the bearing plate under the bearing plate. The test was carried [19] out on the site of the integrated corridor. The test was carried out on the in-situ soil of the excavated pit in the construction area of the integrated pipe corridor, and the shallow plate load test was carried out.

3.1. Basic Principle of Test. The pressure-settlement curve (P-S curve) obtained from the typical plate load test can be divided into three stages:

- (1) Linear deformation stage: when the pressure is less than the proportional limit pressure p_0 , P-S shows a linear relationship. At this time, the shear stress generated at any point in the loaded soil is less than the shear strength of the soil. The deformation of the soil is mainly caused by the decrease of the void in the soil, and the deformation of the soil is mainly vertical compression.
- (2) Shear deformation stage: when the pressure is greater than p_0 and less than the limit pressure p_u , the P-S relationship changes from a straight line to a curve relationship. The slope of the P-S relationship curve increases with the increase of pressure p , and the soil is in addition to vertical compression. In the edge of the plate has a small range of soil shear stress reached or exceeded the shear strength of soil, and began to develop to the surrounding soil. The deformation is caused by both vertical compression and shear deformation of soil particles.
- (3) Failure stage: when the pressure is greater than the ultimate pressure p_u , the settlement increases sharply. Even if the pressure is no longer increased, the bearing plate is still sinking. The continuous sliding surface is formed inside the soil, and the uplift and annular or radial cracks occur around the bearing plate. The shear stress at each point in the sliding soil reaches or exceeds the shear strength of the soil.

3.2. Test Technical Requirements

- (1) Load test should adopt circular rigid bearing plate, according to the soft and hard soil or rock fracture density to choose the appropriate size; the area of bearing plate in shallow plate loading test of soil should be greater than 0.25 m^2 .
- (2) The test pit can be square and circular, and its width is greater than three times the width of the bearing plate, so is its diameter. The measured object should

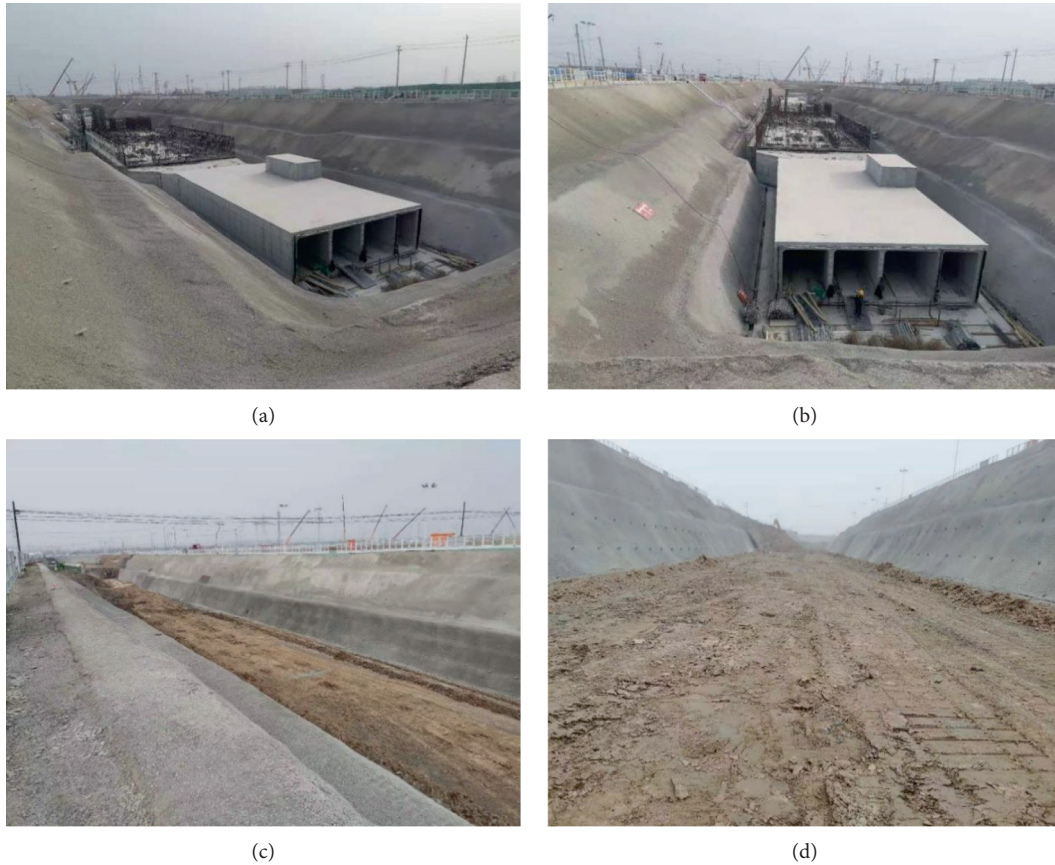


FIGURE 1: Site survey map.

avoid disturbance and keep the original state as far as possible. The sand cushion with thickness less than 20 mm should be laid at the bottom of the test pit to leveling and quickly install the equipment. The settlement measuring instrument is uniformly installed.

- (3) The maximum loading should not be less than twice of the design requirements, and the loading classification should be greater than 7. Generally, the equal incremental load applied is about 1/10 of the predicted ultimate load, and the measurement accuracy of the load should be at the maximum load of $\pm 1\%$.
- (4) The loading methods include conventional slow method, fast method and equal settlement rate method. This paper only introduces the slow method. When the test object is soil, the settlement is measured at intervals of 10, 10, 10, 15 and 15 after each load is applied, and then the settlement is measured at intervals of 30 min. When the settlement is less than or equal to 0.1 mm per hour after continuous reading for two hours, it can be considered that the settlement has reached the relatively stable standard and the next load is applied. When the test object is rock mass, the settlement is measured once at intervals of 1, 2, 5 min, and then every 30 min. When the reading difference of three

consecutive times is less than or equal to 0.01 mm, it can be considered that the settlement has reached the relatively stable standard and the next load is applied.

- (5) When one of the following cases occurs, the test can be terminated, and the load at the termination is the pilot limit load. When the soil around the bearing plate is obviously lateral extrusion, the surrounding rock and soil appear obvious uplift or radial cracks continue to develop; the settlement of the load at this level increases sharply, which is five times larger than that of the load at the upper level, that is, there is a sharp drop in the P-S curve; when a certain load does not meet the stability standard for 24 hours; when the ratio of the total settlement to the diameter of the bearing plate $s/b > 0.06$.

3.3. Test Scheme and Equipment. The rock and soil at the bottom of the test pit or test well should be avoided from disturbance and kept in its original structure and natural moisture, and a medium or coarse sand bedding layer of not more than 20 mm should be laid under the pressure plate to level it and make uniform contact with the soil, and test equipment should be installed as soon as possible, as shown in Figure 2.

The equipment arrangement mainly includes: loading and pressure stabilisation system, counterforce platform

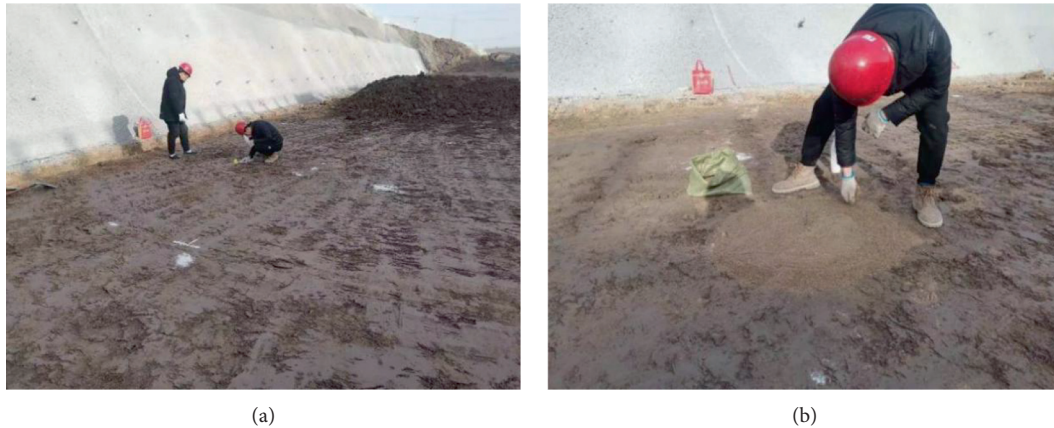


FIGURE 2: Positioning (a) with medium coarse sand leveling (b).

system and observation system. The loading method adopts the slow maintenance load method, using the four vertical bearing plates installed in the bearing plate edge length direction percentage table or displacement meter to observe and record the settlement, to determine the load added at each level by the oil pressure gauge on the jack. The load is applied by means of jack ballast test equipment, through high pressure oil pump, ballast platform as a counterforce device, the pressure is steadily transferred to the bearing plate, the equipment consists of the following three parts: (a) loading and pressure stabilisation system: by the bearing plate, loading jack, column, pressure stabiliser and tripod to support the pressure stabiliser. The loading jack, pressure stabiliser, oil storage tank and high pressure oil pump are connected by high pressure hoses to form an oil circuit system. (b) Counter force platform system: including two parts: truss and ballast test block, the truss consists of central column sleeve, depth adjusting screw, inclined support tube, etc. (c) Observation system: four displacement meters are arranged at each corner of the straight side of the loading plate for settlement observation with an accuracy of not less than ± 0.01 mm.

3.4. Loading and Observation Scheme. The test was carried out using the existing assembled pavement concrete piles on-site, with a prepressure load of 5% of the maximum load and a prepressure time of 5 min. After completion of the prepressure, the piles were unloaded to zero and the initial readings of the displacement measuring instruments were readjusted to zero.

According to the Technical Specification for Building Foundation Inspection JGJ 340-2015, the total loading of the load test is generally not less than 2 times the design bearing capacity, and this test is loaded [19] according to 3 times the design bearing capacity. The ultimate load in the test was 400 kPa as the front leg pad of the corridor machine was designed and controlled in accordance with the dimension of the base pressure not exceeding 130 kPa. The load was loaded in 10 equal steps using stacking blocks, each in 40 kPa increments, and the accuracy of the load measurement was not less than $\pm 1\%$ of the maximum load.

After each level of loading is completed, three settlement measurements are taken at 10 min intervals, then two readings are taken at 15 min intervals and thereafter every 30 min until the settlement is less than 0.1 mm per hour continuously, then the settlement is considered to have reached a relatively stable standard and the next level of loading is applied. The conditions for termination of the test include: significant lateral extrusion of the soil around the bearing plate, significant uplift of the surrounding rock and soil or continued development of radial cracks; a sharp increase in settlement, the appearance of landfall sections on the load-settlement curve and settlement at this level of loading greater than five times the settlement at the previous level of loading; the settlement rate does not reach the relative stability standard for 24 hours under a particular level of loading; the ratio of the total settlement to the diameter (or width) of the bearing plate exceeds 0.06. If one of the above conditions is met, the corresponding previous level of load is the ultimate load. After the test has been completed, the unloading is carried out in three equal stages. After each stage of unloading, the rebound value is read at 15 min intervals, and after two readings, the next stage of loading is read at 30 min intervals. After all unloading, the rebound value is read again at 3 h intervals.

3.5. Analysis of Experimental Data. For the determination of the characteristic value of foundation bearing capacity, when there is a proportional limit on the curve, take the load value corresponding to the proportional limit; when the ultimate load is less than twice the load value corresponding to the proportional limit, take half of the ultimate load value; when it cannot be determined according to the requirements of the above two paragraphs, take the load corresponding to $s/b = 0.01$, but its value should not be greater than half of the maximum loading; when the measured values of the three test points When the extreme difference between the measured values of the three test points does not exceed 30% of their average value, the average value is taken as the characteristic value of the foundation bearing capacity of the soil layer. The modulus of deformation E_0 for the shallow

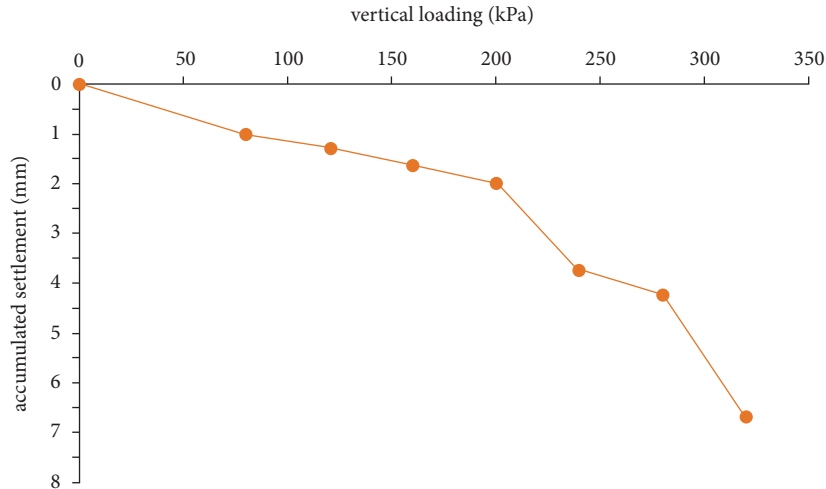


FIGURE 3: Pictures of test loading process.

TABLE 1: Load settlement data curve.

| Loading (kPa) | 0 | 80 | 120 | 160 | 200 | 240 | 280 | 320 |
|-----------------------------|------|------|------|------|------|------|------|------|
| Level settlement (mm) | 0.00 | 1.01 | 0.27 | 0.34 | 0.37 | 1.75 | 0.49 | 2.45 |
| Accumulated settlement (mm) | 0.00 | 1.01 | 1.28 | 1.62 | 1.99 | 3.74 | 4.23 | 6.68 |

plate load test is calculated according to the following formula [20–22].

$$E_0 = I_0(1 - \nu^2) \frac{pd}{s}, \quad (1)$$

where, I_0 —shape factor of the rigid bearing plate; ν —Poisson's ratio of the soil; d —edge length of the bearing plate, m; p —load for linear section of P-S curve, kPa; s —settlement corresponding to p , mm.

3.6. Main Test Results. The load test of the foundation bearing capacity of the assembled integrated pipe corridor, the cumulative loading time on-site were 35 h, 49 h, 26.5 h. According to the calculation of the difference of the test data, the settlement of the three groups of tests was 1.37, 2.34 mm, 2.34 mm and 2.34 mm respectively for the load value of 130 kPa. 1.37 mm, 2.34 mm When loaded to 320 kPa, the cumulative settlement of the foundation was 6.68 mm, 10.89 mm and 5.38 mm respectively, with a small total settlement. The modulus of mat deformation was calculated according to equation (1) above, where $I_0 = 0.785$, $\nu = 0.35$, $d = 0.8$ m, $p = 120$ kPa, $s = 4.23$ mm, 8.43 mm, 4.32 mm, and the calculated modulus of mat deformation $E_0 = 51.7$ MPa, 33.2 MPa, 44.4 MPa, with the mean value of 43.1 MPa. The foundation stiffness p/s of the 0.8 m diameter circular bearing plate are 94 MPa/m, 60 MPa/m and 81 MPa/m respectively, and the average value is 78.2 MPa/m.

The first set of test data and P-S diagram are shown in Figure 3. According to the test data (As shown in Table 1), it can be seen that when the load reaches 320 kPa, the

settlement of this stage is five times that of the upper stage. The termination of loading can be regarded as the occurrence of ultimate failure. The upper stage 280 kPa is taken as the ultimate load, and 1/2 is the eigenvalue of ultimate bearing capacity, namely 140 kPa.

The second group of test data and P-S diagram, as shown in Figure 4, according to the test data (As shown in Table 2), it can be seen that when the loading to 320 kPa, there is no termination of loading conditions, to achieve a relatively stable standard termination of loading, the bearing capacity of the test point reached the survey design value of 160 kPa.

The third group of test data and P-S diagram, as shown in Figure 5, according to the test data (As shown in Table 3), it can be seen that when the loading to 320 kPa, there is no termination of loading conditions, to achieve a relatively stable standard termination of loading, the bearing capacity of the test point reached the survey design value of 160 kPa. Take three groups of data average value as foundation bearing capacity characteristic value of 153 kPa.

4. Numerical Simulation Study of Foundation Settlement

4.1. Numerical Model and Boundary Conditions. The integrated pipe corridor stage size single section is 4 compartment pipe corridor, the width of this simulation is selected as 4 m small prefabricated pipe corridor, the section length is 13.0 m, the height is 4.2 m, the dead weight is 201 t. In the field construction, the main structure of the pipe corridor using C45 high performance concrete, the pipe corridor model in this numerical simulation using nonvariable type material for reduction. Also in the modelling process the mattress bedding and

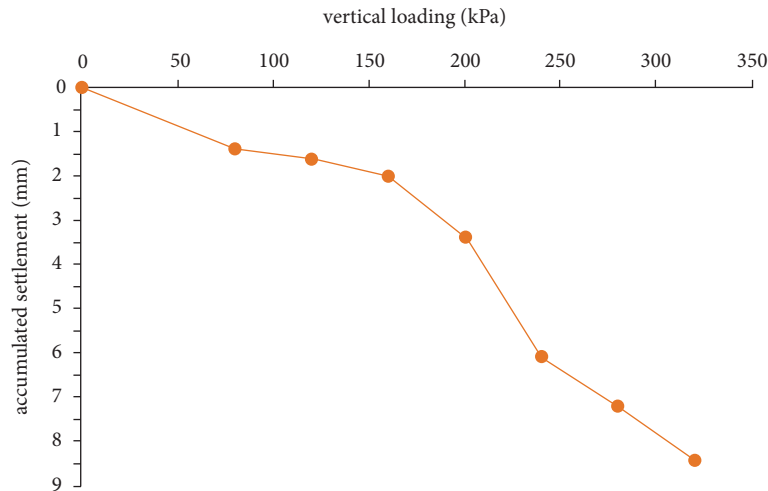


FIGURE 4: Pictures of test loading process.

TABLE 2: Load settlement data curve.

| Loading (kPa) | 0 | 40 | 80 | 120 | 160 | 200 | 240 | 280 | 320 |
|-----------------------------|------|------|------|------|------|------|------|------|-------|
| Level settlement (mm) | 0.00 | 1.38 | 0.23 | 0.38 | 1.39 | 2.70 | 1.12 | 1.23 | 2.46 |
| Accumulated settlement (mm) | 0.00 | 1.38 | 1.61 | 1.99 | 3.38 | 6.08 | 7.20 | 8.43 | 10.89 |

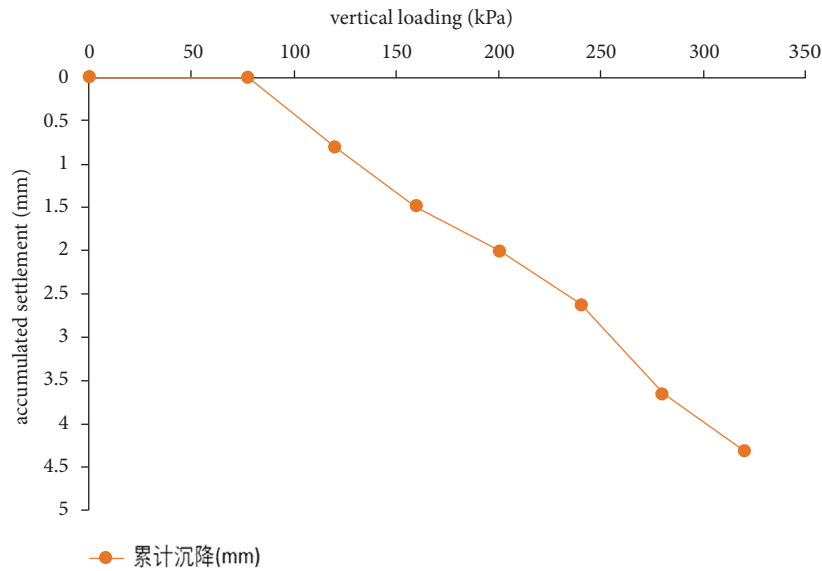


FIGURE 5: Pictures of test loading process.

subgrade were reasonably simplified due to the small size of only 10 cm–20 cm. According to the analysis of the borehole sampling, the powdered clay and powdered soil are the bearing layer, therefore this simulation will be set up according to the parameters of powdered clay for the stratum underneath the pipe corridor, with the dimensions of length x width x height, $20 \times 6 \times 3$. The numerical model was established using COMSOL software as shown in Figure 6. According to the ground investigation data, test data, combined with the experience of similar projects and reference literature, the material parameters were determined comprehensively.

4.2. Numerical Simulation Results and Analysis

4.2.1. *Pit Stress Analysis.* By monitoring the stresses, a characteristic map of the stress distribution is obtained, as shown in Figure 7.

It can be seen from Figure 7 that the downward tangential stress is mainly generated at the interface between the two sides of the pipe gallery. The positive and negative signs of the stress are mainly caused by the different local coordinate systems of the interface element. When the direction of the tangential stress is

TABLE 3: Load settlement data curve.

| Loading (kPa) | 0 | 40 | 80 | 120 | 160 | 200 | 240 | 280 | 320 |
|-----------------------------|------|------|------|------|------|------|------|------|------|
| Level settlement (mm) | 0.00 | 0.00 | 0.80 | 0.69 | 0.51 | 0.62 | 1.04 | 0.66 | 1.06 |
| Accumulated settlement (mm) | 0.00 | 0.00 | 0.80 | 1.49 | 2.00 | 2.62 | 3.66 | 4.32 | 5.38 |

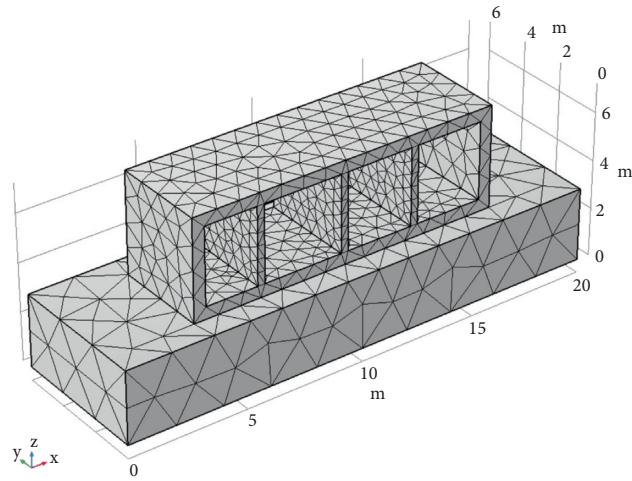
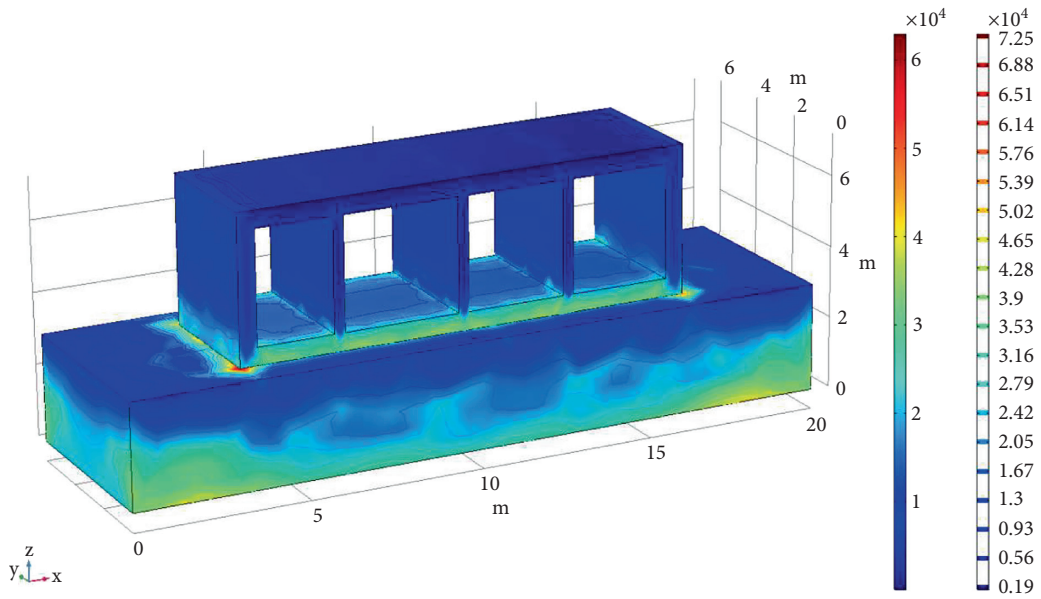
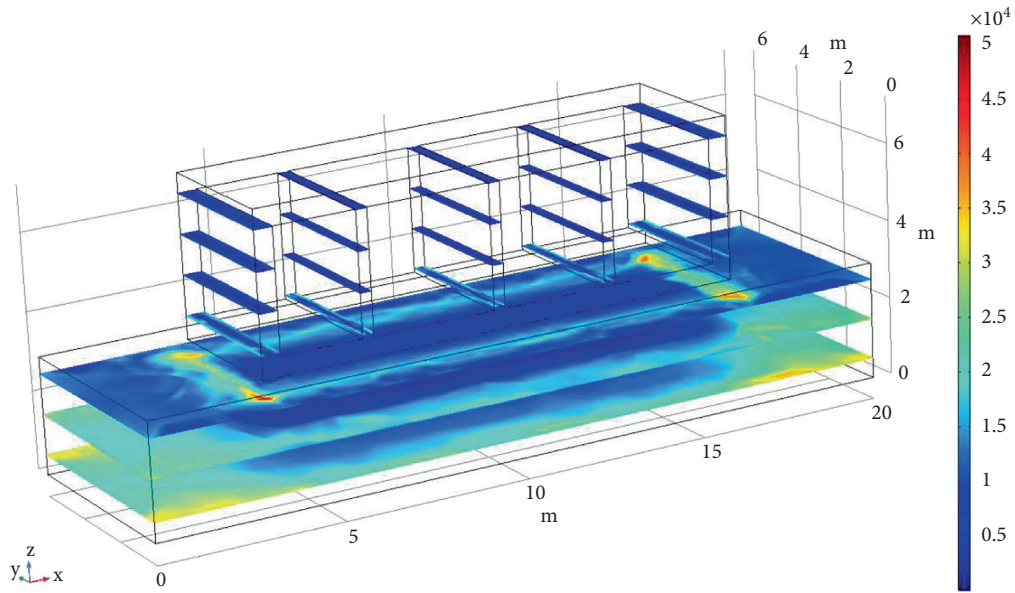


FIGURE 6: Numerical modelling.



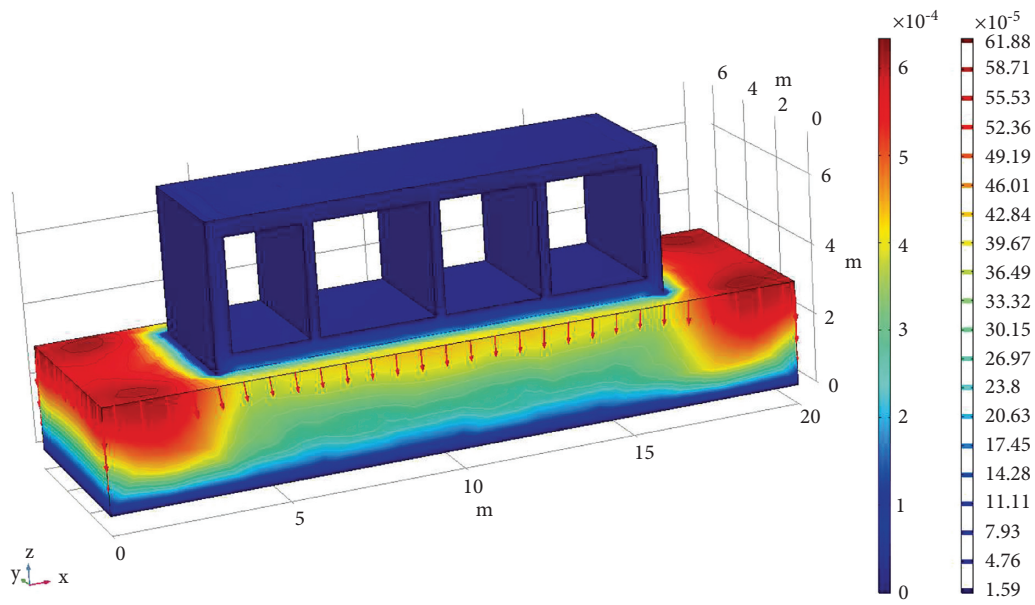
(a)

FIGURE 7: Continued.



(b)

FIGURE 7: Stress distribution characteristics. (a) Overall view. (b) Slice map.



(a)

FIGURE 8: Continued.

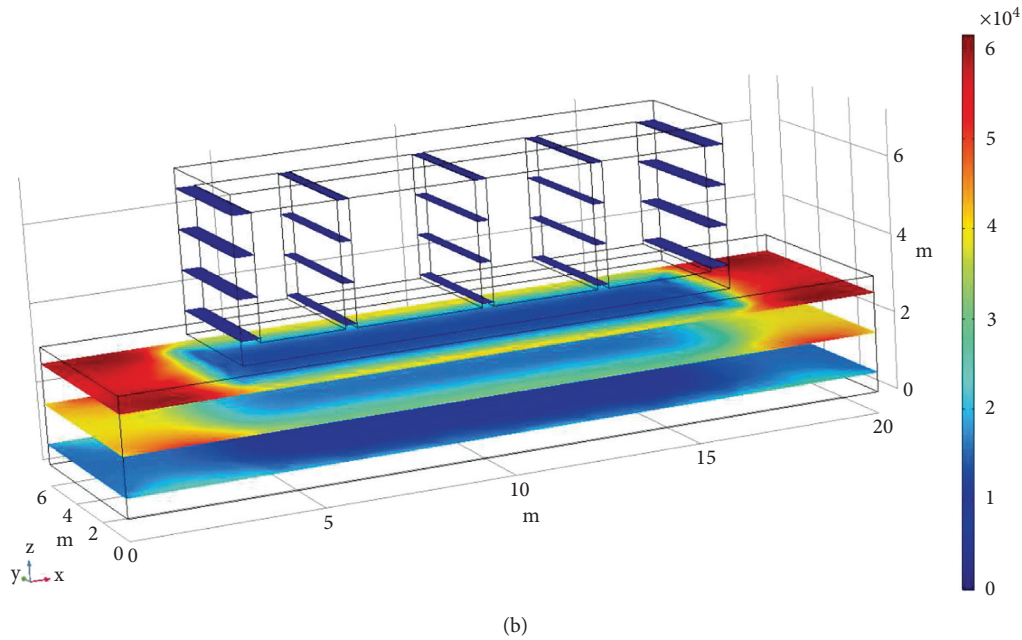


FIGURE 8: Map of displacement distribution characteristics. (a) Overall view. (b) Slice map.

consistent with the direction of the local coordinate axis, it is positive, and vice versa. Therefore, although the tangential stress is positive on the left and negative on the right, it is actually downward. The stress of the side wall near the intersection of the two sides of the pipe gallery and the rock layer is large. From the stress slice diagram in Figure 7(b), it can be seen that taking the interface at the right wall of the first section of the pipe gallery as an example, the bottom stress of the side wall is 25 kPa–45 kPa, which is positive and the direction is upward. The tangential stress at the top of the sidewall is -30 kPa \sim -60 kPa, negative and downward. It can be speculated from the stress diagram that the stress of the two sides and the four corners of the contact between the pipe gallery and the base is relatively concentrated, which may cause large displacement. The bearing capacity of the undisturbed soil of the foundation pit is directly related to the treatment measures of the upper cushion. Therefore, it is necessary to strengthen the cushion treatment of this part.

4.2.2. Foundation Pit Displacement Analysis. By monitoring the displacements, a map of the displacement distribution characteristics was obtained, as shown in Figure 8.

Due to the stiffness difference between the pipe gallery structure and the surrounding soil, the pipe gallery structure also plays a certain role in limiting the settlement of the surrounding soil. The maximum surface settlement below the segmental pipe gallery is about 0.2 mm, which is smaller than that of the surrounding soil. Figure 8(b) Slice diagram shows that the vertical displacement of the soil below the elevation of the pipe gallery bottom plate, from the cross-sectional direction of

the pipe gallery (z axis direction), the settlement of the soil on both sides of the bottom plate at the end of the segmental pipe gallery is the largest, up to 0.6 mm, by contrast, the settlement of the soil at the bottom plate of the center of the pipe gallery is smaller, about 0.2 mm; that is, because of the laying of the segmental pipe gallery, the land on both sides of the base has been squeezed, resulting in displacement, and larger than the land under the pipe gallery. In conclusion, the overall displacement is in a stable state, and the main displacement occurs in the corners and on both sides. It is necessary to pay attention to the treatment of the foundation in this part. The settlement of the bottom and foundation of different pipe gallery will directly affect the overall mechanical performance of the pipe gallery. If there is a certain range of cushion separation will lead to uneven stress of the pipe gallery, affecting the performance of the use, serious concrete cracking, affecting the normal use and safety of the structure [23].

5. Conclusion

- (1) Combined with the existing ground survey report and on-site observation, the current test pit of CCCC (construction pit of integrated pipe corridor) and CCCC is located in the same area of Rongdong, and the two are close to each other, and the elevation is roughly in the same range (test site elevation -2.085 m; original ground elevation 7.911 m), and most of the soils are powder and powder clay. The results are a guide to the design of the bedding layer for the assembled integrated pipe corridor.
- (2) According to the ground survey, it is known that the characteristic value of foundation bearing capacity of

powder soil and powder clay is 130 kPa, according to the specification, the total loading amount is generally not less than 2 times of the design bearing capacity, this test is considered according to 2.5 times of the design bearing capacity, i.e. 320 kPa (diameter of bearing plate 0.8 m). Test results show that the vertical loading to 320 kPa process, each experimental group foundation soil overall displacement settlement is small, mainly for the elastic deformation, foundation soil no cracks, no damage phenomenon, take three groups of data average value as foundation bearing capacity characteristic value of 153 kPa.

- (3) According to the calculation of the straight line section of the load settlement data, the foundation soil bearing capacity deformation modulus is $E = 51.7$ MPa, 33.2 MPa, 44.4 MPa, and the average value of deformation modulus is 43.1 MPa, and the foundation stiffness of 0.8 m diameter circular bearing plate is 94 MPa/m, 60 MPa/m, 81 MPa/m, and the average value is 78.2 MPa/m. The mean values of 78.2 MPa/m can be used as a basis for the structural design of the corridor and the subsequent superstructure test calculations.

Through numerical simulation research found that the soil settlement deformation process and the pipe corridor relative displacement, the shear effect on both sides of the pipe corridor; differential settlement under the influence of the local surface of the pipe corridor may occur tensile damage, the maximum displacement concentrated in both sides of the pit reached 0.6 mm, in the acceptable range. Therefore, the lower base of the pipe corridor has good bearing capacity and can meet the construction requirements of the installation stage of the integrated pipe corridor sections. It is possible to avoid structural misalignment points and prevent The study will help similar projects in the future. This study will be useful for similar projects in the future. The study will be useful for similar projects in the future.

Data Availability

All data, models, and code generated or used during the study appear in the submitted article.

Conflicts of Interest

The authors declare that there are no conflicts of interest.

References

- [1] Z. Tan, X. Chen, X. Wang, and M. Huang, "Construction management mode and key technology of urban underground integrated pipe corridor," *Tunnel construction*, vol. 36, no. 10, pp. 1177–1189, 2016.
- [2] H. Wang, "Some problems in the construction of urban underground integrated pipe corridor projects in China," *Tunnel construction*, vol. 37, no. 05, pp. 523–528, 2017.
- [3] Z. Jia, Z. Chen, and W. Li, "The present situation and development of urban underground comprehensive pipe gallery," *Jiangxi building materials*, vol. 2016, no. 22, pp. 6–7, 2016.
- [4] B. Wang and S. Dai, "A brief discussion on the necessity of construction of underground integrated pipeline corridor in China's cities and its development prospects," *Anhui Architecture*, vol. 22, no. 6, p. 43+159, 2015.
- [5] H. Zhou and Q. Jiang, "Preliminary interpretation of the guidance on promoting the construction of integrated urban underground pipe corridors," *Environment and Sustainable Development*, vol. 40, no. 05, pp. 58–59, 2015.
- [6] F. Yang, "Preliminary discussion and analysis of construction methods for urban underground municipal integrated pipeline corridors," *Anhui architecture*, vol. 23, no. 3, pp. 88–91, 2016.
- [7] X. You, "Status and development trend of urban integrated pipe corridor," *Urban housing*, vol. 24, no. 3, pp. 6–9, 2017.
- [8] Y. Wang, "The development and outlook of urban underground multi-utility tunnel in China," *Engineering Technology Research*, vol. 2017, no. 8, pp. 244–245, 2017.
- [9] Z. Tian, *Experimental Study on the Force Performance of Assembled Laminated concrete Underground Integrated Pipe Corridor*, Harbin Institute of Technology, Harbin, China, 2016.
- [10] D. Kong, Y. Xiong, Z. Cheng, N. Wang, G. Wu, and Y. Liu, "Stability analysis of coal face based on coal face-support-roof system in steeply inclined coal seam," *Geomech. Eng.* vol. 25, pp. 233–243, 2021.
- [11] L. Zhou, "Research on key technologies for the construction of safety monitoring system of urban underground integrated pipe corridor [J]," *Modern surveying and mapping*, vol. 39, no. 6, pp. 39–41, 2016.
- [12] J. Yang and W. Wei, "Design and construction research of the urban underground pipe gallery structure," *Engineering Construction and Design*, vol. 2017, no. 6, pp. 19–20, 2017.
- [13] X. Huang and X. Fan, "Analysis of the applicability of HS model in numerical simulation of foundation pit engineering," *Journal of Water Resources and Construction Engineering*, vol. 16, no. 2, pp. 115–120, 2018.
- [14] X. Hu, S.-nan Fu, Lv Liang, C. Xiao-wen, and W. Xue, "Analysis of force performance of prefabricated assembled integrated pipe corridor under soft soil layer," *Construction Technology*, vol. 47, no. 12, pp. 118–121, 2018.
- [15] Y. Wang, "A brief discussion on the design of urban underground integrated pipe corridor and the application of open excavation method construction technology," *Engineering quality*, vol. 34, no. S1, pp. 154–158, 2016.
- [16] J. Ren, "A brief discussion on the necessity of urban underground integrated pipeline corridor," *Science and technology information*, vol. 12, no. 17, p. 63, 2014.
- [17] H. Wu, G. Zhao, and S. Ma, "Failure behavior of horseshoe-shaped tunnel in hard rock under high stress: phenomenon and mechanisms," *Transactions of Nonferrous Metals Society of China*, vol. 32, no. 2, pp. 639–656, 2022.
- [18] L. Sun, "An exploration of the structural design and construction of urban underground integrated pipeline corridors," *Science and technology wind*, no. 24, p. 152, 2012.
- [19] S. Yao and Z. Wang, "Research on the construction technology of urban underground integrated pipe corridor," *Green environmental protection building, materials*, no. 01, p. 111, 2017.

- [20] L. Dong and Z. Gao, "Exploration and practice of the sponge city construction in obsolete region," *Environmental Engineering*, vol. 37, no. 7, pp. 13–17, 2019.
- [21] Y. Gong, Y. Chen, L. Yu et al., "Effectiveness analysis of systematic combined sewer overflow control schemes in the sponge city pilot area of Beijing," *International Journal of Environmental Research and Public Health*, vol. 16, no. 9, p. 1503, 2019.
- [22] L. Zhou, "Discussion on waterproofing design and construction method of urban underground comprehensive pipe gallery," *Jiangxi building materials*, vol. 2017, no. 22, p. 106–111, 2017.
- [23] J. Cao, N. Zhang, S. Wang, D. Qian, and Z. Xie, "Physical model test study on support of super pre-stressed anchor in the mining engineering," *Engineering Failure Analysis*, vol. 118, Article ID 104833, 2020.

Research Article

The Study on the Characteristics of Pressure Arch above the Twin-Parallel Openings in the Jointed Rock Masses

Kunpeng Gao ¹, Kang Liang ¹, Leyao Wang,¹ Changhao Li,² Jinghai Yu,¹ and Runyi Wu¹

¹Nanjing Vocational University of Industry Technology, Nanjing 210023, China

²Yuwu Mining Co.Ltd., Lu'an Group, Changzhi 046103, China

Correspondence should be addressed to Kang Liang; liangk@niit.edu.cn

Received 29 November 2021; Accepted 12 February 2022; Published 8 March 2022

Academic Editor: Gaofeng Song

Copyright © 2022 Kunpeng Gao et al. This is an open access article distributed under the Creative Commons Attribution License, which permits unrestricted use, distribution, and reproduction in any medium, provided the original work is properly cited.

The self-bearing capacity of the rock masses has been a hot pot in the research of supporting technology in underground engineering. The pressure arch has been considered the main hypothesis to explain the self-bearing capacity of the rock masses. In this paper, the engineering of the twin-parallel openings in the jointed rock masses was selected as the background of the research. The characteristics of the deformation or the movement of the rock masses above the openings were studied based on the pressure arch theory. The difference between the single opening and the twin-parallel openings has been revealed, and the mechanism has also been illustrated. Besides, the joints' strength, the in situ stress ratio, the distance between the two openings, and the excavation sequence were selected as the variable parameters, and their influences have also been illustrated by the DEM method.

1. Introduction

With the development of underground engineering, the engineering of the twin-parallel openings has been gradually more and more frequently encountered in mining or tunnel engineering. The more complicated regularity of the deformation and movement of the rock masses shall be induced by the neighbor opening, especially in the joint rock masses. It has brought new challenges to design the economic support to control the deformation and movement of rock masses under this engineering condition.

In underground engineering, the initial equilibrium within the rock masses will be disturbed when the opening is excavated, and the stress of the rock masses in the vicinity of the opening will be redistributed correspondingly and immediately. The rock masses around the opening will start to deform or move towards the excavation space until the supporting structure can bear the additional stress induced by the deformation or movement of the rock masses [1–6]. Formerly, the supporting structure only referred to the man-made construction, including the steel support, the concrete wall. With the going deep of the research work, the self-bearing capacity of rock masses has been revealed and been

gradually considered as the primary factor to maintain the stability of the rock masses. The formation process of this understanding could be divided into three phases. Firstly, the self-bearing structure of rock masses was revealed, especially the concept of the pressure arch was formed. Secondly, the corresponding support design method, which was based on the concept that the main purpose of the supporting was to enhance the self-bearing capacity of the rock masses, was used for real engineering. This phase could be represented by the proposing and applying of the “New Austrian tunnelling method” [7–11]. And finally, this philosophy of the support design has been accepted by most scholars and engineers in the world, and how to improve the bearing capacity of the self-bearing structure of the rock masses and assist the rock masses in stabilizing itself have become a hot spot in the study of the underground engineering [12].

The arch effect is a common phenomenon in nature. This effect could help long-span structure remain stable and has usually been used to construct the bridge, the gymnasium, and other large space buildings. As a rule-of-thumb, the pressure arch of rock masses, which has a similar stress characteristic with the ordinary arch, has been considered as

the main type of the self-bearing structure of rock masses. When the opening is excavated, the weight of the overburden has mainly been converted into compressive stress and transferred to the abutments through the pressure arch. The direction of the principal stress of the rock masses within the arch area has been deflected, and the stress value has elevated, while the stress of the rock masses below the arch area has decreased significantly. The overlying weight has been resisted by the pressure arch finally. The formation of a pressure arch could prevent the further deformation or movement of the rock masses [13–16].

Various relevant factors for the arch formation have been selected as the study objects. The cover depth and the in situ stress ratio have been considered as the most important factor which could influence the formation and the characteristics of the pressure arch [15, 17, 18]. As a rule-of-thumb, the greater depth and the greater in situ stress ratio have a significant positive impact on the formation of the pressure arch and the stability of the opening, especially when the in situ stress ratio and the arching degree are lower. Besides that, the strength of the rock masses, the excavation roof rise-to-span ratio, and so on have also been considered and could be beneficial or adverse to the formation of the pressure arch in different engineering conditions. However, the influence has been slightly weak.

The method used to study the pressure arch of the rock masses has been mainly focused on the numerical simulation method or the simplified mechanical model. The in situ observation method has been seldom used due to economic and technical restrictions. The mechanical model has been built based on the Voussoir beam or the arch theory [13, 19–21]. The thrust line could be used to evaluate the arch behavior of the rock masses [22]. Due to the complexity of underground engineering, the mechanical model has only assisted researchers in finding the relevant factors of the formation or the failure modes of the rock pressure arch. To further reveal the mechanism of the pressure arch, laboratory experiments, which mainly refer to the physical simulation experiment, have been employed [14, 20, 23]. To a certain extent, the physical simulation experiment could reflect the real regularity. However, the deeper mechanism of the pressure arch could not be revealed due to the monitoring methods and economic considerations. Hence the numerical simulation method has gradually become the priority method to research the pressure arch. The finite difference method (FDM, e.g., FLAC, FLAC3D) and the finite element method (FEM, e.g., ABAQUS, ANSYS), which are based on the continuous medium, have been widely used to reflect the redistribution of the stress and the development of the pressure arch under the various parameters or the different engineering conditions [15–18], [24–27]. However, the continuous medium method could not well reflect the regularity of the movement of the rock masses. The discontinuous faces, e.g., joints, faults, have a nonnegligible impact on the deformation of the rock masses. Hence, the numerical method which is based on the discontinuous theory has been gradually adopted to research the problem in underground engineering. The representative method includes the discrete element method (DEM, e.g., UDEC

[19], PFC3D [28]) and the discrete element discontinuous deformation analysis (DDA) [13, 21].

Previous studies have obtained the profound comprehension of the pressure arch in the surrounding rock masses of the opening. However, accurate evaluation of the characteristics of the arch distribution above the twin-parallel openings in the jointed rock masses is still a challenging task. The joint leads to the anisotropic deformation of the rock masses and weakens the strength of the rock masses and has a nonnegligible influence on the deformation of the rock masses. In addition, the neighbor opening shall inevitably influence the movement or the deformation of the surrounding rock masses of the other opening.

This paper aimed to gain an in-depth understanding of the characteristics of the pressure arch above the twin-parallel openings in the jointed rock masses. The difference of the pressure arch between the twin-parallel openings and the single opening was discussed. The friction angle of the joints (φ), the in situ stress ratio (K_0), and the distance between the twin-parallel openings (L) were selected as the study parameters. Their effect was obtained by the numerical simulation method, respectively. With 20 groups of the numerical simulation, the characteristics of the pressure arch above the twin-parallel openings and the influence of the study parameters were analyzed in detail and clearly revealed.

2. The DEM Model

The chief stumbling block to research the pressure arch in the rock masses is that the pressure arch has been hard to investigate, and this difficulty has also limited the previous progress of understanding the pressure arch. With the numerical simulation method development, it becomes possible to observe the formation and the distribution of pressure arch directly and thoroughly. The discrete element method (DEM) is a discontinuous-based method, which treats the analysis domain as an assemblage of discrete blocks and is very suitable to the studies of jointed rock masses or blocky systems. It could well evaluate the influence of the discontinuous faces on the deformation or the movement of the rock masses by directly constructing the discontinuous faces (such as joints, faults) in the model. To achieve a clear understanding of the characteristics of pressure arch above the twin-parallel openings in the jointed rock mass, five series of numerical experiment were employed with the DEM method.

The laminated rock mass, which usually belongs to the sedimentary rock mass, was considered in this study. The laminated rock mass usually exhibits a geological structure known as “mechanical layering” where the joints are bounded by the bedding plane boundaries and usually nearly perpendicular to the bedding planes [13]. The laminated rock mass is frequently encountered in underground excavations in metro construction, the tunneling engineering, and coal or metal mining. Based on the structural features in the laminated rock mass, two sets of orthogonal discontinuous faces were constructed in the model, which simulated the vertical joints and the horizontal stratum faces, respectively.

The numerical model was illustrated in Figure 1. The height of the research domain was 100 m, and the width was 200 m. The thickness of each rock layer was 1 m, and the spacing between joints was also 1 m. Both openings' span were set as 10 m, and the distance between them was set as L .

The rock material was regarded as linearly elastic with $\rho = 2700 \text{ kg/m}^3$, Young's modulus $E = 10 \text{ GPa}$, and Poisson's ratio $\nu = 0.25$. The joints' deformation and movement were assumed to follow the Coulomb-Slip model, with the tensile and cohesion strength set as zero to simplify the computation, and the friction angle of the joints (φ) was selected as a variable in this study. The gravitational acceleration g was set as 10 m/s^2 , and the in situ (horizontal/vertical) stress ratio (K_0) changed in the range from 0.3 to 1.2 in this paper. Besides, the sequence of the excavation of the two openings was also considered in the simulation.

The two lateral sides of the model were fixed in the horizontal direction, and the bottom boundary of the model was fixed in the vertical direction.

The computation was divided into two stages. At the first stage, the vertical in situ stress ρgh and horizontal in situ stress $K_0 \rho gh$ were added to the analysis domain, where h was the overburden depth and K_0 was the in situ (horizontal/vertical) stress ratio that was also called the lateral pressure ratio. An in situ stress equilibrium in the analysis domain could be achieved after tens of thousands of iterations. At the second stage, the displacement constraint where the two openings were located were removed simultaneously or successively to simulate the different excavation sequences.

The detailed studied parameter design of the numerical experiments was shown in Table 1.

Series *a* was aimed to compare the difference of the characteristics of the pressure arch between the twin-parallel openings and the single opening. The numerical model of case *a1* was only designed with one opening, and the other settings were the same as case *a2*.

Series *b* was designed to reveal the effect of joint's strength. To simplify the analyzing process, only the friction angle of the joints (φ) was selected as the representative parameter to reflect the strength of the joints. The friction angle in this series varied as 5° , 10° , 15° , 20° , 25° , 30° , and the other parameters were kept constant.

Series *c* was employed to reflect the influence of the in situ stress ratio (K_0). The values of the in situ stress ratio were chosen as 0.3, 0.5, 0.7, 1, 1.2, and the other parameters were fixed. The cases were numbered as *c1-c5* in Table 1.

Series *d* focused on the effect of the distance between the two openings (L). The distance value varied as 5 m, 10 m, 15 m, 20 m, 30 m, 40 m, 50 m. The other parameters remained unchanged. The cases were designated as *d1-d7*, which are shown in Table 1.

Series *e* were conducted to examine the influence of the excavation sequence. There were two excavation situations considered in this study. In the first situation, two openings were excavated at the same time. In the second situation, one opening was excavated firstly, and after achieving the stress equilibrium, the other opening started to be excavated. The other parameters remained fixed. The cases were labeled by *e1-e4*.

3. Results and Discussions

To reveal the regularity related to the pressure arch above the twin-parallel openings of the jointed rock masses, the results of the numerical experiments mentioned above were analyzed in this section. The analysis domain was selected as 100 m width and 50 m height, which could speed up the data processing with ensuring the accuracy of the analysis. The middle rock wall was one of the characteristic structures of the engineering of the twin-parallel openings. The magnitude of the vertical stress in the middle rock wall was analyzed to reveal the difference among the cases in one series due to the main direction of the maximum principal stress in the middle rock wall being vertical. The directions of the maximum principal stresses in the rock masses above the opening were deflected greatly; hence the direction of the maximum principal stress of the rock masses upper the middle of the opening was analyzed to reflect the influence of the different conditions.

3.1. The Characteristics of the Stress Distribution. A representative model case (case: *a2*) of the twin-parallel openings was compared with the model of the single opening (case: *a1*). All the conditions were the same except the openings number in the two comparative cases.

The distribution of the maximum principal stress ($\sigma_{\text{max-principal}}$) vectors after excavation is shown in Figure 2. Before the excavation, the maximum principal stress was mainly in the vertical direction, while the minimum principal stress was in the horizontal direction when the in situ ratio (K_0) was less than 1. The magnitude of the maximum principal stress and the minimum principal stress increased linearly with depth increasing. Following the excavation, the maximum principal stress in the vicinity of the opening was redistributed immediately. The closer to the opening, the greater the direction of the maximum principal stress deviated from the vertical direction. The characteristics of the distribution of the maximum principal stress could be discussed from the following two aspects.

3.1.1. The Partition of Rock Masses. Whether the single opening or the twin-parallel openings, according to the characteristics of the maximum principal stress vectors, the surrounding rock masses above the opening could be divided into three areas. The three areas are the local pressure arch area, the global pressure arch area, and the uninfluenced area, respectively, from the roof of the opening to the ground.

The local pressure arch area has been characterized by the obvious deflection of the maximum principal stress, especially the nearly horizontal maximum principal stress appearing. The local pressure arch could be further divided into two zones according to nearly horizontal maximum principal stress. One zone refers to the margin of this area, where the stress has significantly deflected an arch-shaped structure formed according to the arch-similar shape of the maximum principal stresses trace in this zone. The weight of the overburden has been sustained by this arch-shaped

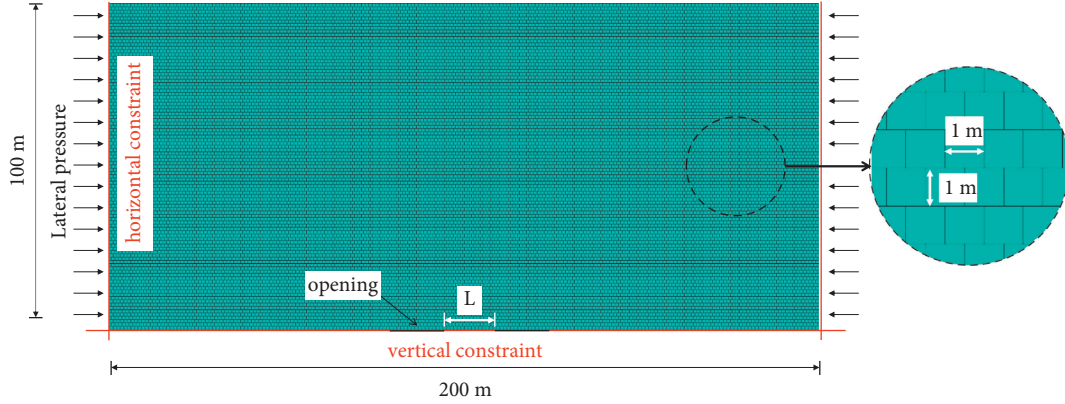


FIGURE 1: Numerical models used in the simulation.

TABLE 1: Design of the numerical experiment.

| Series | Case | φ (°) | K_0 | L | Excavation sequence |
|--------|---------|---------------|-------|-------------|---------------------|
| a | a1 | 20 | 0.7 | One opening | — |
| | a2 | 20 | 0.7 | 5 | One time |
| b | b1 | 5 | 0.7 | 10 | One time |
| | b2 | 10 | 0.7 | 10 | One time |
| | b3 | 15 | 0.7 | 10 | One time |
| | b4 | 20 | 0.7 | 10 | One time |
| | b5 | 25 | 0.7 | 10 | One time |
| | b6 | 30 | 0.7 | 10 | One time |
| c | c1 | 20 | 0.3 | 10 | One time |
| | c2 | 20 | 0.5 | 10 | One time |
| | c3 (b4) | 20 | 0.7 | 10 | One time |
| | c4 | 20 | 1 | 10 | One time |
| | c5 | 20 | 1.2 | 10 | One time |
| d | d1 (a2) | 20 | 0.7 | 5 | One time |
| | d2 (b4) | 20 | 0.7 | 10 | One time |
| | d3 | 20 | 0.7 | 15 | One time |
| | d4 | 20 | 0.7 | 20 | One time |
| | d5 | 20 | 0.7 | 30 | One time |
| | d6 | 20 | 0.7 | 40 | One time |
| | d7 | 20 | 0.7 | 50 | One time |
| e | e1 (b4) | 20 | 0.7 | 10 | One time |
| | e2 | 20 | 0.7 | 10 | Two times |
| | e3 | 5 | 0.5 | 10 | One time |
| | e4 | 5 | 0.5 | 10 | Two times |

structure and has been transferred to the abutments. Beneath this structure is the other zone; the maximum principal stress of the rock mass has changed from the vertical to the almost horizontal direction. The stress state of this zone is like a beam and presents the rock masses that only support its own weight, and this zone could also be named the loosened zone. In this zone, the rock masses have no longer resisted the overlying pressure, and two common failure modes of the rock masses could be generated under their own weight, including sliding failure along the joints and the snap-through failure, as shown in Figure 3.

The mechanism of the sliding failure of the rock masses under the arch structure in the local pressure arch area is illustrated in Figure 4. The beam concept in mechanics is used in the following analysis. The stability of the beam

highly depends on the shear resistance provided by the joints. The maximum shear stress τ_{\max} in the beam is as follows:

$$\tau_{\max} = \frac{bq}{2h}, \quad (1)$$

where b was the wide of the opening, q was the pressure of the overburden weight, h was the thickness of the beam.

Supposing that the shear strength of the joints was τ_f , and according to the Mohr-Coulomb model,

$$\tau_f = \sigma f_k, \quad (2)$$

where σ referred to the normal stress in the joints' face and could be computed by $\sigma = K_0 q$, K_0 was the in situ stress ratio. f_k was expressed by $f_k = c/\sigma + \tan\varphi$, and c was the cohesion, φ was the friction angle. The stability condition could be obtained as follows:

$$h = \frac{0.5b}{K_0 f_k}. \quad (3)$$

It could be seen that the magnitude of the K_0 was a key factor to ensure the beam sustainable.

The other possible failure mode is a snap-through failure. The theory of the thrust line based on the arch structure could be used to assess the possibility of this type of failure [21, 22]. The thrust line is a curve representing the equilibrium of the beam under the vertical loading. The snap-through failure shall happen when the thrust line exceeds the beam upper boundary, as shown in Figure 3. The mechanical calculation model is shown in Figure 4. The position of the thrust line could be computed as follow.

Assume one point $i(x, y)$ located on the thrust line, the bending moment (M) of this point could be given by the following:

$$M = \frac{qx}{2}(b-x) - Hy. \quad (4)$$

Let $M = 0$, the position of the thrust line could be obtained as follows:

$$y = \frac{qx}{2H}(b-x). \quad (5)$$

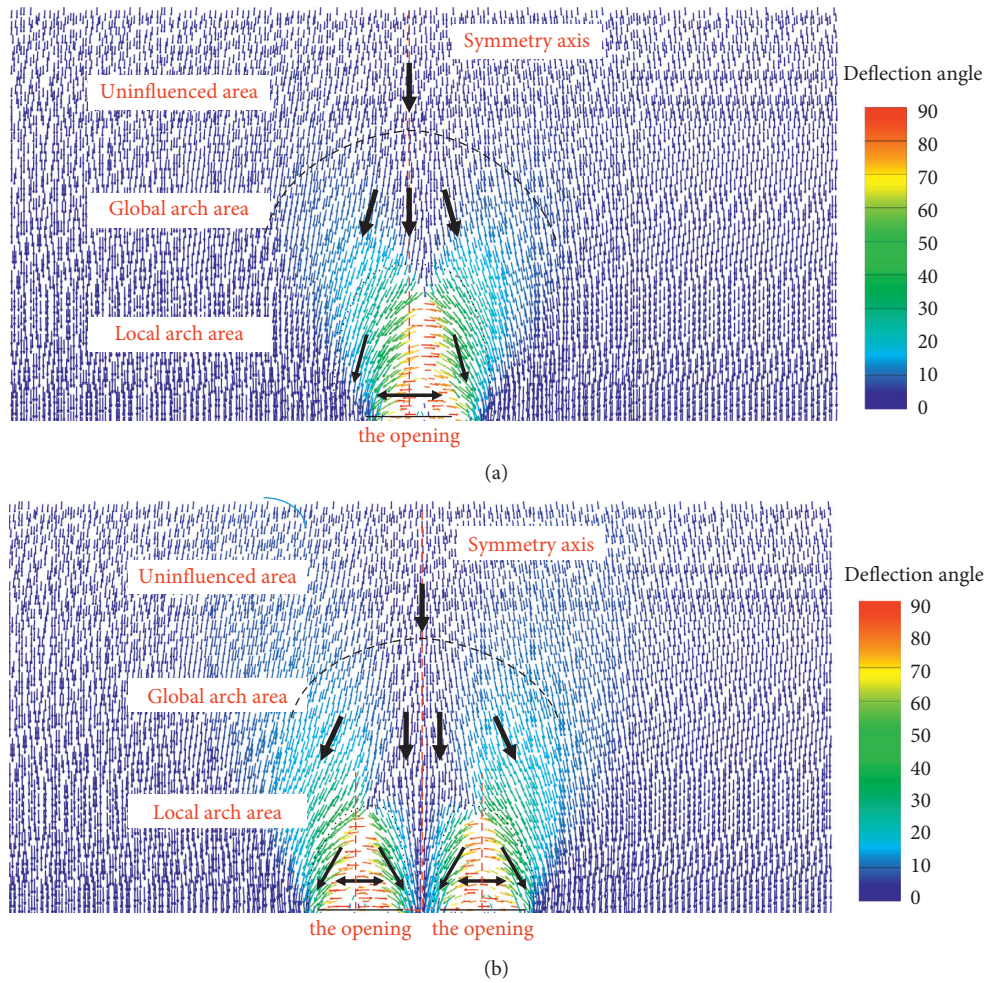


FIGURE 2: The maximum principal stress vector after excavation. (a) Case a1, single opening; (b) Case a2, twin-parallel opening.

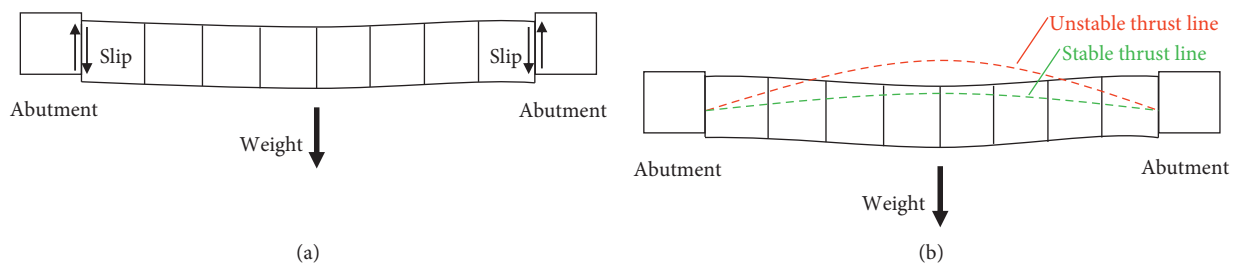


FIGURE 3: The failure modes of the loosened zone. (a) The slip failure; (b) The snap failure.

It could be seen that the horizontal force H has a significant influence on the position of the thrust line. Furthermore, the in situ ratio has determined the possibility of the occurrence of the snap-failure.

The global pressure arch area is above the local pressure arch area, and the extent of the maximum principal stress deflection is much less than the local pressure arch area. There is no horizontal stress. The maximum principal stresses in the middle of this area are almost vertical. The rock masses in this area have mainly acted as a stress-transfer

role, and it could be considered as a transition area of the stress redistribution.

Over the global arch area, the stress state of rock masses has no obvious variation. The maximum principal stress has remained in the vertical direction and linearly increased with the depth.

It must be noted that the separation of the middle rock wall around the opening is relative complexity. The middle rock wall should not be totally contained in the local pressure arch. Only the part in which the direction of the

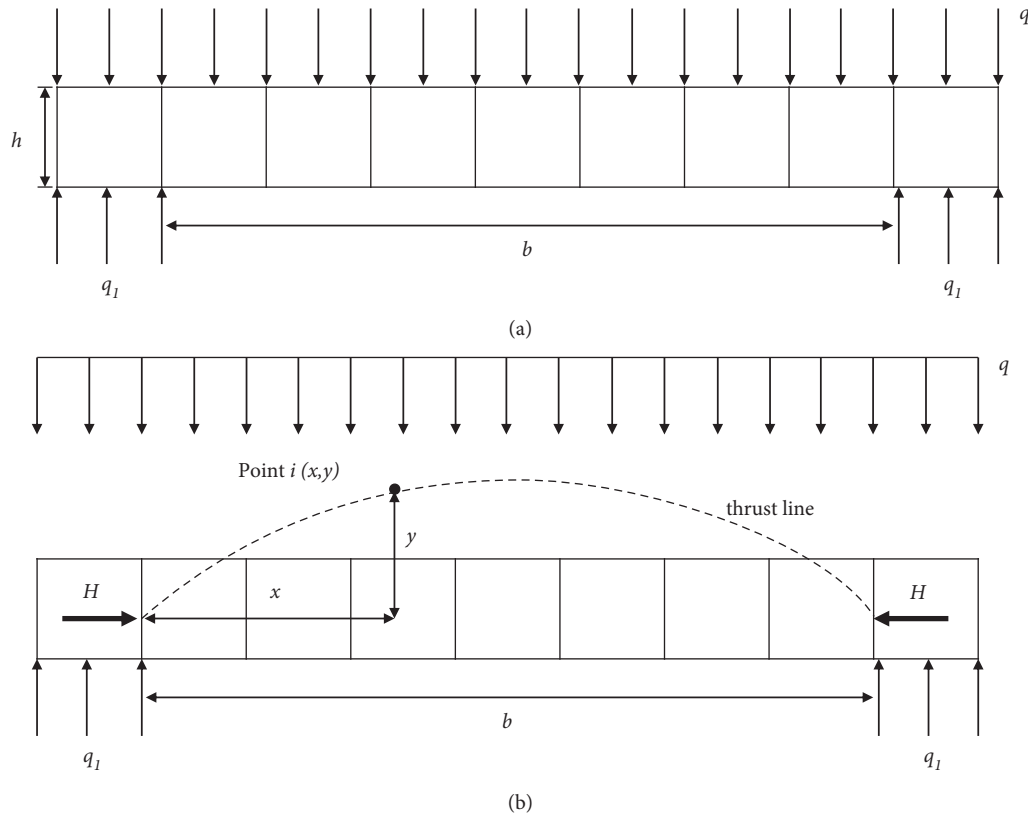


FIGURE 4: The mechanical model of the loosened zone. (a) The slip failure; (b) The snap-through failure.

principal stress has been significantly shifted could be considered in the area of the local pressure arch. And the middle part of the middle rock wall could not be classified as any separation due to the principal stress being still vertical. The area of the middle rock wall which is above the local pressure arch, could be considered as part of the global arch area, following the partition principle described in this paper.

3.1.2. The Differences between the Single Opening and the Twin-Parallel Openings. In the single opening condition, the stress distribution is symmetric around the middle line of the opening, whereas the axis of symmetry changes to the middle line of the middle rock wall, and the stress in the vicinity of one opening has not been symmetry around the middle line of the opening in the condition of the twin-parallel opening.

On the single opening condition, the directions of the maximum principal stress of the rock masses on the left of the symmetry axis shift to the left, and the right points to the right. However, under the condition of the twin-parallel openings, although the directions of the maximum principal stress have been symmetry about the middle line of the middle rock wall, the directions of rock masses on the one side of the symmetry axis are not unanimous. Three areas could be divided based on the direction of the maximum principal stress, as shown in Figure 5. The formation

mechanism of this phenomenon could be illustrated as follow.

Assuming one single opening, the direction of the maximum principal stress is symmetrical around the middle line of the opening; the stress on the left of the symmetry axis shifts to the left, and the right stress points to the right. Consider the twin-parallel openings, when the distance of the two openings is small. The resultant stress could be computed as Figure 5. The magnitudes of the stresses induced by the two openings at the same position in area 1 are nearly equal, and the directions of the stresses are almost symmetrical; hence the directions of the resultant stress in area 1 are almost vertical. In area 2, the directions of the resultant stress are different between the upper and lower section. To illustrate the reason for the difference, the left half of the model is taken as an example. In the upper of area 2, the stresses induced by the left opening (the stress vector coloured by green in Figure 5) slightly deflects and points to the right side. The stresses induced by the right opening (the stress vector colored by red in Figure 5) mainly point to the left side. The horizontal components of the red stress vectors are bigger than the green stress vectors. It results in the resultant stress (the resultant stress vector colored by black in Figure 5) pointing to the left. Following the depth increases, the direction of the red stress vectors gradually changes to the vertical direction, and the horizontal component of the red stress is inadequate to offset the horizontal component of the green stress; hence the resultant stress

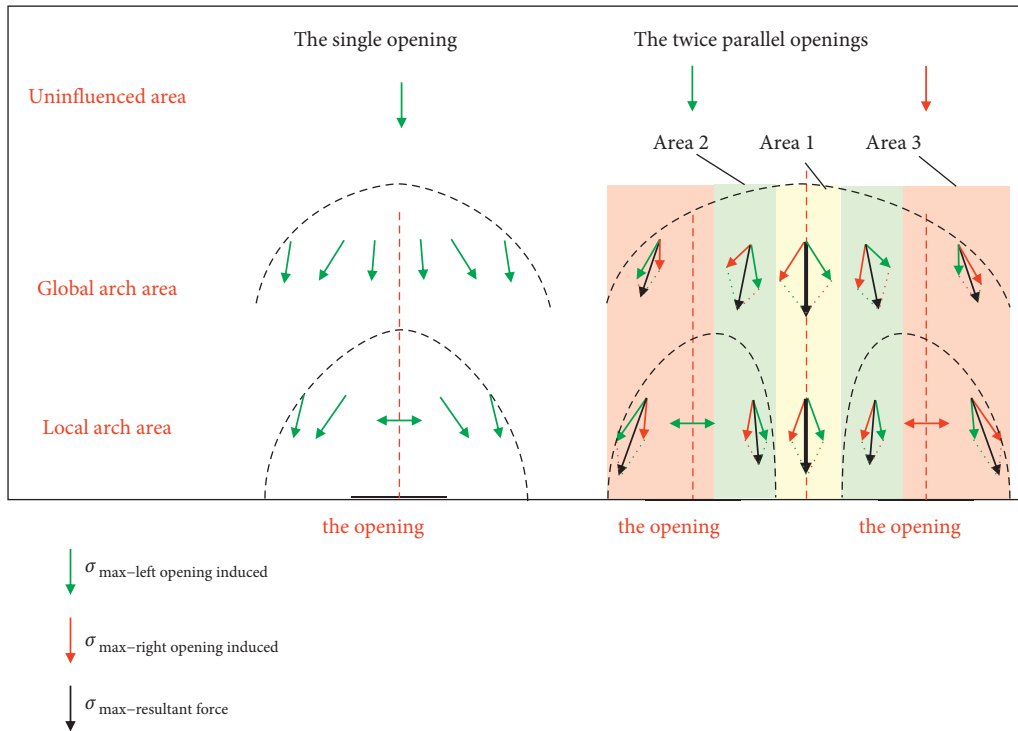


FIGURE 5: The mechanical analysis of the direction of the maximum principal stress of the rock masses.

gradually points to the right again. The direction of the maximum principal stresses in area 3 is consistent with the stress distribution of the single opening condition due to the directions of stress induced by two openings being similar.

3.2. Effect of the Joints' Strength. To examine the effect of the joint's strength on the formation of the pressure arch, six cases with the friction angle (φ) of the joints from 5° to 30° were designed and simulated (case: b1-b6). Cohesion was not considered in this paper because it could simplify the process of computing and result in analysis using one parameter to evaluate the joint's strength.

3.2.1. The Stress in the Middle Rock Wall. As mentioned above, the maximum principal stresses of the middle rock wall have mainly pointed to the vertical direction. Therefore, the differences between the cases in series *b* have mainly concentrated on the magnitude of the vertical stress. A survey line is set along the middle of the middle rock wall; the stress of the points located on or near this line could be obtained. The curves of the vertical stress versus the distance to the opening are shown in Figure 6.

There are two distinctly different parts of the change of the stress along the middle line of the middle rock wall. In the first part, the stresses have exceeded the origin in situ stress and increased with the decreasing of the distance to the opening (the red area in Figure 6). It indicates that the pressure arch delivers the overlaying stress to the middle rock wall. The increment of the stress has induced the additional strain, and the additional strain of the rock masses of this area has offered the deformation space for

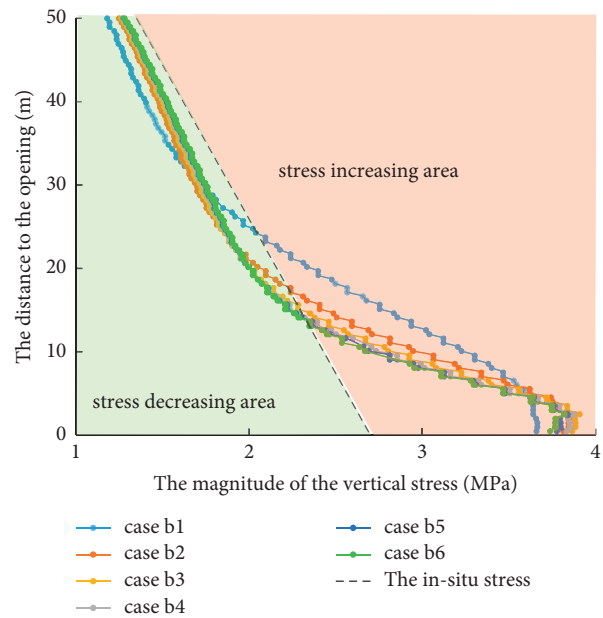


FIGURE 6: The relationship between the vertical stress and the distance to the opening.

the upper rock masses. The stress relief shall occur in the upper of the middle rock wall immediately, and then the stresses of the upper rock masses have fallen below the in situ origin stress, as shown in the green area in Figure 6. The curves in the green area are the second part mentioned above. The in situ stress could be computed by the formula " ρgh ". This process has been illustrated in Figure 7.

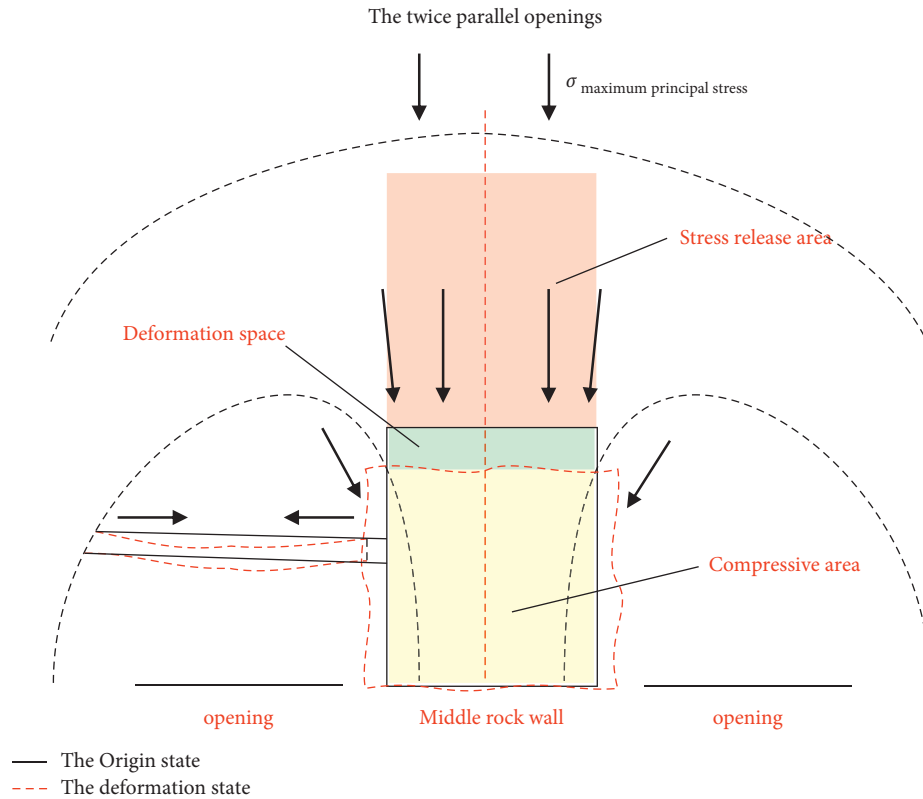


FIGURE 7: The illustration of the stress change in the middle rock wall.

With the increasing of the friction angle (φ) of the joints, the magnitude of the stresses is different at the same distance to the opening. When closing to the opening, the smaller friction angle (φ) of the joints leads to the greater stress. It means that the greater overlying pressure, which is applied on the local pressure arch, could be formed in the rock masses with the lower joint's strength. In other words, the local pressure arch shall transfer the greater overlying stress to the middle rock wall when the strength of joints is lower. The greater stress results in the greater strain of the lower part of the middle rock wall and the greater release space for the upper rock masses, and then the stress decrease of the upper rock masses is increased. Hence, the stress is lower when the friction angle (φ) is lower at a far distance to the opening, as shown in the green area in Figure 6.

3.2.2. *The Stress above the Opening.* The direction of the maximum principal stress of the rock masses above the opening was selected as an indicator to reveal the influence of different friction angle (φ) of joints. The curves of the direction of the maximum principal stress, which is defined by the angle between the stress and the horizontal direction versus the distance to the opening, are shown in Figure 8.

When the distance to the opening is large, the stress vector mainly points to the vertical, and the amplitude of direction change is small (Section 1 in Figure 8). And then, the vector changes to horizontal quickly until nearly approaching the horizontal direction (Section 2 in Figure 8). Finally, the stress was mainly along the horizontal

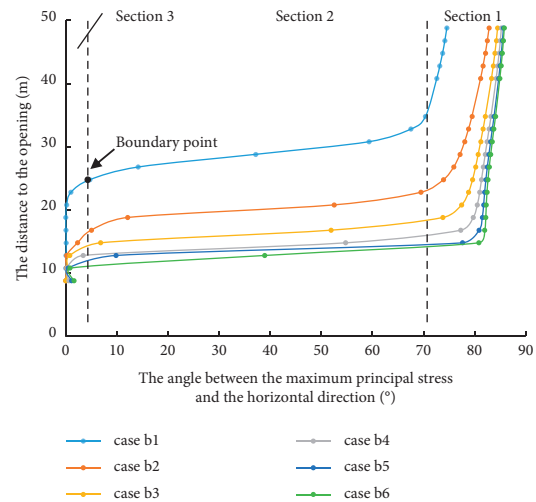


FIGURE 8: The relationship between the direction of the maximum principal stress and the distance to the opening.

direction and almost no longer changed with the distance decreasing (Section 3 in Figure 8). A typical point, as shown as the boundary point in Figure 8, could be noticed. Below this point, the maximum principal stress has begun to shift to the horizontal, which means that the area below this point is the local pressure arch, according to the definition of the local pressure arch in this paper. In other words, this point could be regarded as the upper boundary of the local arch.

The greater the friction angle (φ) of the joints, the smaller the distance between the boundary point and the opening. It shows that the local pressure arch position has a close relationship with the strength of joints, and the higher strength rock masses could lead to the lower local arch. The approximate distance between the boundary point and the opening is 23 m in case a1, whereas only 15 m in case a2 with the friction angle (φ) of the joints has been only improved 5° . From case a2 to case a6, the increment of the friction angle of the joints is 20° . However, the distance between the boundary point and the opening has been changed to 5 m. The upper boundary of the local arch has an obvious change with the variation of the joint's strength when the joint's strength is relatively small, to put it differently, the position of the local pressure arch has been more sensitive to the changes of the joints' strength when joints' strength is small.

3.3. Effect of the In Situ Stress Ratio

3.3.1. The Stress in the Middle Rock Wall. The curves of the magnitude of the vertical stress versus the distance to the opening are shown in Figure 9. The vertical stress in the middle rock wall could not be significantly affected by the change of the in situ ratio (K_0). The vertical stress of the upper rock masses of the middle rock wall has been released due to the compression deformation of the lower rock masses, and the value of vertical stress of the upper rock masses in the middle rock wall has decreased to below the in situ vertical stress, whereas the lower has increased to exceed the in situ stress, as mentioned above.

3.3.2. The Stress above the Openings. The curves of the angle between the maximum stress and the horizontal direction versus the distance to the opening have been plotted in Figure 10. The curves of the cases with different in situ stress ratios have presented two typical shapes, which means there are two different characteristics of the stress distribution while the in situ ratio is bigger than 1 or less than 1. When the in situ ratio is less than 1 and the distance to the opening is large, the maximum principal stress has mainly pointed to the vertical direction and is slightly deflected. Following the distance decreases, the direction of the stress has rapidly changed to the horizontal in the several meters. And then, the stress has mainly pointed to the horizontal direction. However, when the in situ ratio is greater than 1, the origin maximum principal stress has pointed to the horizontal direction before the opening. After the excavation, the stress has been redistributed, and the direction of the stress of the rock masses, which are relatively far from the opening, have slightly shifted to the vertical. And with the distance to the opening decreasing, the direction of the stress has gradually recovered the horizontal direction.

When the in situ ration is larger than 1, the arch structure would no longer mainly transfer the overlying pressure to the abutments. The overlying pressure is generally considered to be induced by the weight of the overlying rock masses. The lateral pressure would be the main force that the arch should bear. The mechanism of the arch

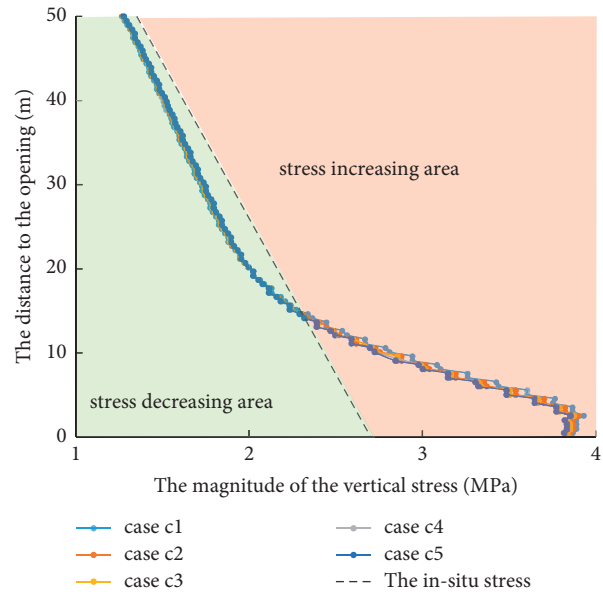


FIGURE 9: The relationship between the vertical stress and the distance to the opening.

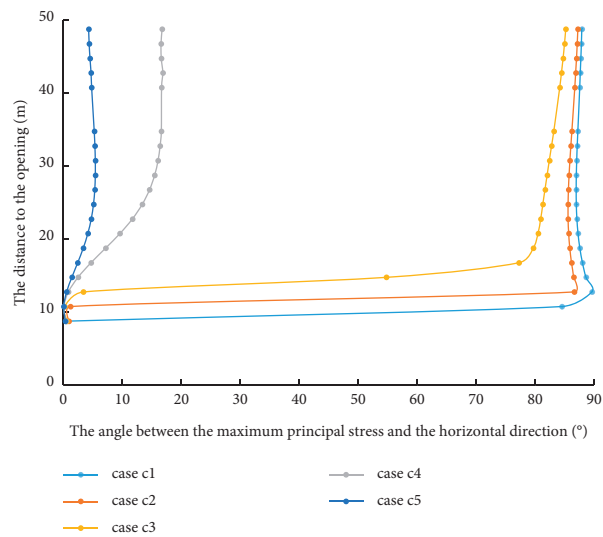


FIGURE 10: The relationship between the direction of the maximum principal stress and the distance to the opening.

formation and deformation should be thoroughly reanalyzed.

3.4. Effect of the Distance of the Twin-Parallel Openings. Seven cases with varies L (the distance between the two openings, or the width of the middle rock wall) of 5 m, 10 m, 15 m, 20 m, 25 m, 30 m, 40 m, 50 m were considered to reveal the effect of the distance between the two openings. The vertical stress of the middle rock wall and the direction of the maximum principal stress has been analyzed in this section.

3.4.1. The Stress in the Middle Rock Wall. Similar to the previous series, a survey line is set along the middle of the

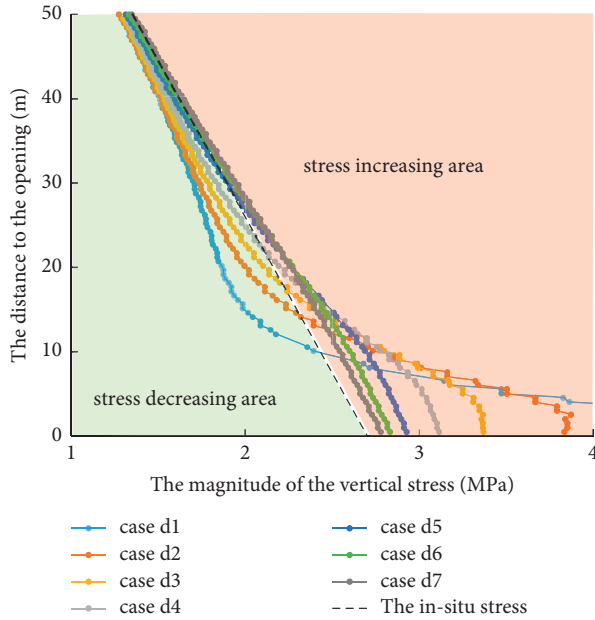


FIGURE 11: The relationship between the vertical stress and the distance to the opening.

middle rock wall, and the stress of the points located on or near this line has been extracted. The curves of the vertical stress versus the distance to the opening are shown in Figure 11.

As shown in Figure 11, the larger the distance between the two openings (L), the closer the vertical stress curves and the in situ stress line are to each other. Especially, in case d6 ($L = 40$ m) and case d7 ($L = 50$ m), the stress curves have almost coincided with the in situ stress line. It shows that the neighbor opening has nearly no effect on the other opening when their distance is greater than 40~50 m in the model of this paper.

Besides, the shape characteristic of the curves of the different cases has been mainly consistent. As analyzed above, the vertical stress has exceeded the in situ origin stress in the rock masses closing to the opening, and the compression deformation of the lower rock masses induces the stress relief of the upper rock masses in the middle rock wall. This shape characteristic could not change with various distances between the two openings (L).

3.4.2. The Stress above the Openings. The curves of the angle between the maximum principal stress and the horizontal direction versus the distance to the opening with various L have been shown in Figure 12.

The results have presented a certain fluctuation among the different cases in the series d ; however, it could still reflect some regularity with the change of the distance between the two openings (L). The main characteristic of the curves of the different cases has remained unanimous with the previously analyzed. In the upper of the rock masses above the opening (approximately $h > 15$ m in this paper), the deflection angle of the direction of the stress has gradually decreased with the L (the distance between the two

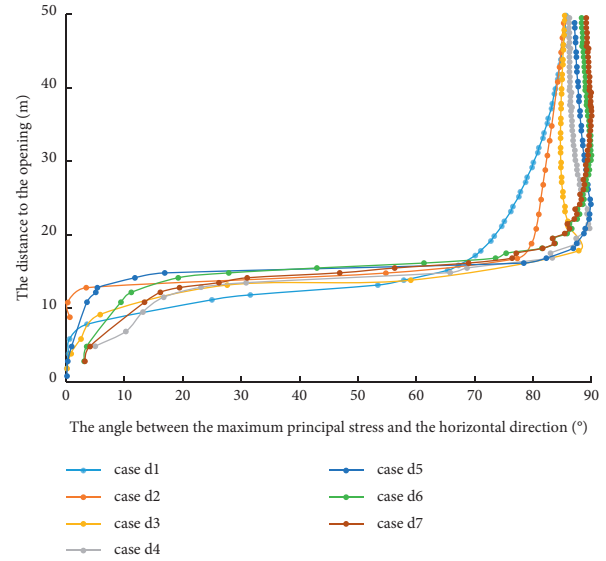


FIGURE 12: The relationship between the direction of the maximum principal stress and the distance to the opening.

openings) increasing at the same distance to the opening. The influence of the neighbor opening on the other opening has been obviously weakened with the L increasing. The position of the boundary point, which is considered as the upper boundary of the local arch in this paper, has decreased from case c1 ($L = 5$ m) to case c7 ($L = 50$ m). It shows that the pressure acting on the local pressure arch has decreased with the L (distance between the two openings) increasing. In other words, the neighbor opening has induced the weakening of the rock masses strength and the increment of the overlying pressure. The influence would be weakened with the L (the distance between the two openings) increasing.

3.5. Effect of the Excavation Sequence. To investigate the influence of the excavation sequence, the series e was designed. Firstly, cases e1 and e2, which had the same parameter values, were compared. However, there were no obvious differences between cases e1 and e2, according to the magnitude of the vertical stress in the middle rock wall and the direction of the maximum principal stress above the opening.

Considering that the reason for no obvious difference between case e1 and e2 was that there was no collapse in these two cases, and the stress in case e2 could be recovered after the neighbor opening excavating. Case e3 and case e4, in which the collapse could occur, were employed to further research. However, it is still not significantly changed between cases e3 and e4. Hence, it could be concluded that the sequence of the excavation has only a slight impact on the deformation of the rock masses above the opening.

The curves of the magnitude of the vertical stress in the middle rock wall and the direction deflection of the maximum principal stress versus the distance to the opening have been shown in Figures 13 and 14, respectively. And the curve of case e1 has been almost covered by case e2 in Figure 13.

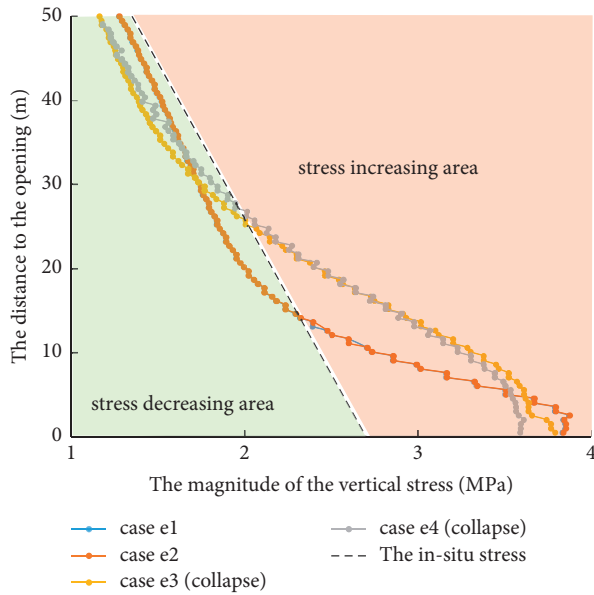


FIGURE 13: The relationship between the vertical stress and the distance to the opening. The rock masses in cases e1 and e2 are not collapsed, whereas the collapse has occurred in cases e3 and e4.

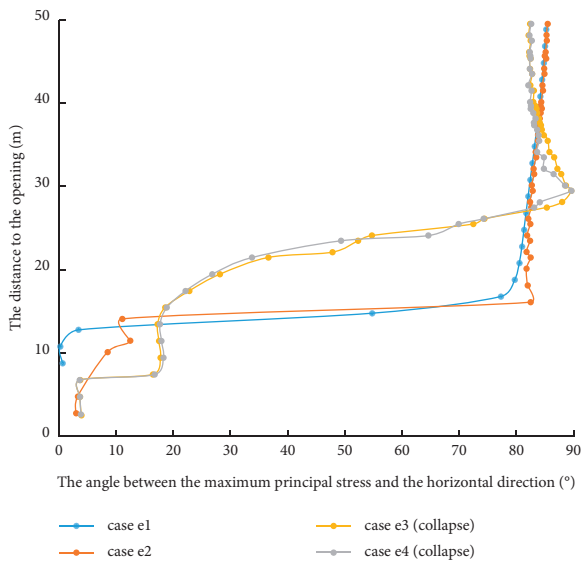


FIGURE 14: The relationship between the direction of the maximum principal stress and the distance to the opening.

4. Conclusion

In this paper, the characteristics of pressure arch above the twin-parallel openings in the jointed rock masses were studied using the DEM method. Five series of numerical experiments were conducted with different research parameters. The joint's strength (φ), the in situ ratio (K_0), the distance between the two openings (L), and the excavation sequence were considered as the examined variables, respectively. The followings are mainly conclusions obtained in this paper.

- (1) Whether single opening or the twin-parallel openings, the rock masses above the opening could be divided into three areas based on the direction of the maximum principal stress after excavation. The local arch area, which is closed to the opening, is characterized by the heavy deflection of the maximum principal stress and the appearance of the horizontal maximum principal stress. The local arch area could be further divided into two zones, including the zone of the margin of this area where the heavy deflection of the maximum principal stress has been distributed, and the zone of the loosened rock masses where the horizontal maximum principal stress has been mainly appearance. The global arch area, which is above the local area, is generally symmetric of the middle line of the opening (the single opening condition) or the middle line of the middle rock wall (the twin-parallel opening condition). The uninfluenced area, which is located above the global area, is the area that the maximum principal stress remains vertical as before excavating.
- (2) There are two modes of failure which could occur in the loosened zone of the local arch area, including the sliding failure and the snap-through failure. The mechanical analysis of the two modes has been given in this paper, respectively.
- (3) The differences in the distribution of the maximum principal stress above the opening between the single opening and the twin-parallel openings are mainly focused on the stress distribution around the area of the middle rock wall. In the twin-parallel openings situation, although the maximum principal stresses are still symmetrical about the middle line of the middle rock wall, the stresses around the opening are no longer symmetrical about the middle line of the opening. Besides that, the directions of the maximum principal stresses around the middle rock wall are not unique. The mechanism of this phenomenon has been illustrated using the superposition of stresses.
- (4) The lower friction angle (φ) leads to the lower strength of the joints, and the lower strength of joints could result in the greater overlying pressure and the higher position of the local arch. The stress change is more sensitive to the friction angle (φ) when the friction angle (φ) is lower, including the magnitude of the vertical stress in the middle rock wall and the direction of the maximum principal stress above the opening.
- (5) The in situ stress ratio (K_0) has a key impact on the failure modes of the loosened zone, according to the mechanical analysis. Besides, the directions of the maximum principal stresses above the opening have also been strongly influenced by the in situ stress ratio (K_0). At the same distance to the opening, the greater the in situ stress ratio (K_0), the greater the maximum principal stresses are deflected. However,

the magnitude of the vertical stress in the middle rock wall has been slightly impacted with the in situ stress ratio changing. It is worth noting that the distribution of the in situ maximum principal stress has been distinctly different when the in situ stress ratio is bigger than 1 or less than 1, and this could result in the different deformation mechanisms of the rock arch. When the in situ stress ratio is bigger than 1, all the conclusions should be reanalyzed thoroughly.

- (6) The influence of the neighbor opening has been decreased with the increasing of the distance between the two openings (L), according to the magnitude of the vertical stress in the middle rock wall and the direction of the maximum principal stress above the opening. In this paper, when $L \geq 40 \sim 50 m$, the influence has been weak. Besides, the pressure of the local arch bearing has also been decreased with the increase of the L , which could be reflected by the change of the upper boundary of the local arch.
- (7) There is no obvious difference between the once excavation and the twice excavation in the models of this paper, whether the collapses occur or not. The excavation sequence has a slight influence on the deformation or the movement of the rock masses above the opening.

Data Availability

The data used in this study have already been posted in this paper.

Conflicts of Interest

The authors declare that there are no conflicts of interest regarding the publication of this paper.

References

- [1] D. Kong, Y. Xiong, Z. Cheng, N. Wang, G. Wu, and Y. Liu, "Stability analysis of coal face based on coal face-support-roof system in steeply inclined coal seam," *Geomech Eng*, vol. 25, no. 3, pp. 233–243, 2021.
- [2] Z.-Q. Yang, C. Liu, F.-S. Li, L.-M. Dou, G.-W. Li, and D.-W. Wang, "The mechanism and application of high-pressure water jet technology to prevent compound dynamic disaster," *Arabian Journal of Geosciences*, vol. 14, 2021.
- [3] H. Wu, D. Ma, A. J. S. Spearing, and G. Zhao, "Fracture phenomena and mechanisms of brittle rock with different numbers of openings under uniaxial loading," *Geomechanics and Engineering*, vol. 25, no. 6, pp. 481–493, 2021.
- [4] D. Kong, S. Pu, Z. Cheng, G. Wu, and Y. Liu, "Coordinated deformation mechanism of the top coal and filling body of gob-side entry retaining in a fully mechanized caving face," *International Journal of Geomechanics*, vol. 21, Article ID 4021030, 2021.
- [5] J. Chen, P. Liu, H. Zhao, C. Zhang, and J. Zhang, "Analytical studying the axial performance of fully encapsulated rock bolts," *Engineering Failure Analysis*, vol. 128, Article ID 105580, 2021.
- [6] J. Chen and D. Li, "Numerical simulation of fully encapsulated rock bolts with a tri-linear constitutive relation," *Tunnelling and Underground Space Technology*, vol. 120, Article ID 104265, 2022.
- [7] L. V. Rabcewicz, "The new austrian tunnelling method," *Water Power*, vol. 65, 1964.
- [8] H. Yoshimura, T. Yuki, Y. Yamada, and N. Kokubun, "Analysis and monitoring of the Miyana railway tunnel constructed using the New Austrian tunnelling method," *International Journal of Rock Mechanics and Mining Sciences & Geomechanics Abstracts*, vol. 23, no. 1, pp. 67–75, 1986.
- [9] C. W. Ng, K. M. Lee, and D. K. Tang, "Three-dimensional numerical investigations of new Austrian tunnelling method (NATM) twin tunnel interactions," *Canadian Geotechnical Journal*, vol. 41, no. 3, pp. 523–539, 2004.
- [10] N. E. Yasitli, "Numerical modeling of surface settlements at the transition zone excavated by New Austrian Tunneling Method and Umbrella Arch Method in weak rock," *Arabian Journal of Geosciences*, vol. 6, no. 7, pp. 2699–2708, 2013.
- [11] A. R. Sogut and E. Eser, "Engineering geological investigations of T-11 tunnel along Burdur-Antalya high-speed railway," *Arabian Journal of Geosciences*, vol. 13, no. 16, 2020.
- [12] C. C. Li, "Rock support design based on the concept of pressure arch," *International Journal of Rock Mechanics and Mining Sciences*, vol. 43, no. 7, pp. 1083–1090, 2006.
- [13] D. Bakun-Mazor, Y. H. Hatzor, and W. S. Dershowitz, "Modeling mechanical layering effects on stability of underground openings in jointed sedimentary rocks," *International Journal of Rock Mechanics and Mining Sciences*, vol. 46, no. 2, pp. 262–271, 2009.
- [14] H. Asaei, M. Moosavi, and M. A. Aghighi, "A laboratory study of stress arching around an inclusion due to pore pressure changes," *Journal of Rock Mechanics and Geotechnical Engineering*, vol. 10, no. 4, pp. 678–693, 2018.
- [15] C. N. Chen, W.-Y. Huang, and C.-T. Tseng, "Stress redistribution and ground arch development during tunneling," *Tunnelling and Underground Space Technology*, vol. 26, no. 1, pp. 228–235, 2011.
- [16] C. Jin, A. Shao, D. Liu, T. Han, F. Fan, and S. Li, "Failure mechanism of highly stressed rock mass during unloading based on the stress arch theory," *International Journal of Geomechanics*, vol. 18, Article ID 4018146, 2018.
- [17] S. He, D. Wang, X. Liu, and J. Zhang, "Assessment of the arching effect and the role of rock bolting for underground excavations in rock masses—a new numerical approach," *Arabian Journal of Geosciences*, vol. 13, no. 13, 2020.
- [18] X. X. Kong, Q. S. Liu, Q. B. Zhang, Y. X. Wu, and J. Zhao, "A method to estimate the pressure arch formation above underground excavation in rock mass," *Tunnelling and Underground Space Technology*, vol. 71, pp. 382–390, 2018.
- [19] Y. Zhao, S. Wang, Y. Zou, X. Wang, B. Huang, and X. Zhang, "Pressure-arching characteristics of fractured strata structure during shallow horizontal coal mining," *Tehnicki vjesnik - Technical Gazette*, vol. 25, no. 5, 2018.
- [20] X. Shao, L. Wang, X. Li et al., "Conversion mechanism of a continuous pressure arch structure in strip filling mining," *Arabian Journal of Geosciences*, vol. 14, no. 18, 2021.
- [21] L. He and Q. B. Zhang, "Numerical investigation of arching mechanism to underground excavation in jointed rock mass," *Tunnelling and Underground Space Technology*, vol. 50, pp. 54–67, 2015.
- [22] Z. Huang, E. Broch, and M. Lu, "Cavern roof stability-mechanism of arching and stabilization by rockbolting,"

- Tunnelling and Underground Space Technology*, vol. 17, no. 3, pp. 249–261, 2002.
- [23] S. R. Wang, X. G. Wu, Y. H. Zhao, P. Hagan, and C. Cao, “Evolution characteristics of composite pressure-arch in thin bedrock of overlying strata during shallow coal mining,” *International Journal of Applied Mechanics*, vol. 11, no. 3, Article ID 1950030, 2019.
- [24] J. K. Lee, H. Yoo, H. Ban, and W.-J. Park, “Estimation of rock load of multi-arch tunnel with cracks using stress variable method,” *Applied Sciences*, vol. 10, no. 9, p. 3285, 2020.
- [25] Y. Zhao, S. Wang, P. Hagan, and W. Guo, “Evolution characteristics of pressure-arch and elastic energy during shallow horizontal coal mining,” *Tehnicki vjesnik - Technical Gazette*, vol. 25, no. 3, 2018.
- [26] S. Wang, X. Wu, Y. Zhao, and P. Hagan, “Mechanical performances of pressure arch in thick bedrock during shallow coal mining,” *Geofluids*, vol. 2018, Article ID 2419659, 13 pages, 2018.
- [27] X. Kong, Q. Liu, Y. Pan, and J. Liu, “Stress redistribution and formation of the pressure arch above underground excavation in rock mass,” *European Journal of Environmental and Civil Engineering*, vol. 25, no. 4, pp. 722–736, 2021.
- [28] X. Wang, H. Kang, and F. Gao, “Numerical study on the formation of pressure arch in bolted gravel plate,” *Computers and Geotechnics*, vol. 130, Article ID 103933, 2021.

Research Article

Coal and Gas Comining in the High-Gas Detong Mine, China: Analytical and Numerical Parameter Optimization of Gas Extraction Boreholes

Wei Wang ^{1,2}, Zongxiang Li ¹, Guangmin Zhao ², and Yujin Chen ³

¹College of Safety Science and Engineering, Liaoning Technical University, Liaoning, 123000, China

²Division of Energy, Shuifan Group Co., Ltd, Jinan 25000, China

³Shuifan Zhongxing Group Co., Ltd, Jinan 25000, China

Correspondence should be addressed to Zongxiang Li; lzx6211@126.com

Received 2 December 2021; Accepted 4 February 2022; Published 4 March 2022

Academic Editor: Gaofeng Song

Copyright © 2022 Wei Wang et al. This is an open access article distributed under the Creative Commons Attribution License, which permits unrestricted use, distribution, and reproduction in any medium, provided the original work is properly cited.

The upper corner gas overrun caused by goaf gas gushing in the high-gas mine can be mitigated by roof positioning of long boreholes in the goaf fracture zone, creating an artificial gas migration channel and achieving safe comining of coal and gas. This study numerically simulated the fracture evolution in the coal rock overlying goaf in workface #2-104 of the Detong Mine, China. Using the O-shaped circle theory and the FLAC^{3D} commercial software package, the range parameters of goaf fracture zone gas-concentrated areas were obtained by defining the pressure relief coefficient, which provided a basis for the arrangement of holes in the goaf located at 15 m from the workface goaf collapse zone to the workface floor and 15–60 m from the structure zone to the workface. According to the obtained goaf parameters, the distribution and migration law in the goaf under the conditions of initial state and extraction with different roof borehole parameters were simulated by the FLUENT software. The optimal borehole location was 30 m from the floor and 25 m from the return airway. The field experiment with three boreholes arranged in the optimal extraction position provided the extraction concentration in the borehole above 30%, the gas extraction volume of 12 m³·min⁻¹, and the concentration at the upper corner below 1%, which ensured safe coal and gas comining.

1. Introduction

While coal mining intensity and depth keep growing annually with increased coal demand, mine productivity is restricted by gas outburst risks. Since mining gas is also a clean energy resource, the realization of coal and gas comining is conducive to improving the utilization rate of resources and reducing greenhouse gas emissions [1]. Influenced by the mining and overburden, the fracture zone generated by the bending and separation of the goaf roof becomes a high-concentration gas area, which is the key area to control goaf gas and prevent the overrun of the upper corner gas of the mining face [2]. A recent theoretical study comprehensively integrated the O-shaped circle theory, pressure relief mining and pumping, and coal and gas comining [3]. Based on the subsidence of a coal mine in

Britain, Fang et al. [4] reported that the compaction and stress recovery of rock mass in goaf were mainly related to mining height, buried depth, and other parameters. They performed the numerical regression analysis of the goaf compaction mechanical properties via the FLAC^{3D} software. Cheng et al. [5] concluded that the mining fracture of the overburden had the characteristics of \cap -shaped high cap. Qian and Xu [6] revealed a circular fault zone developed above the goaf, constituting a gas accumulation zone and migration channel. Yavuz [7] analyzed the elliptical paraboloid zone's pressure relief gas extraction mechanism and proposed the corresponding coal and methane comining technology. Karacan et al. [8] investigated the effect of the coal mining fracture field on mining stress distribution and coal seam gas pressure. Guo et al [9] coupled the permeability field with the results of the mechanical model and

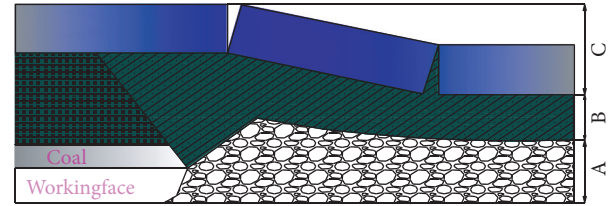
proposed a comprehensive “dynamic” gas reservoir model to simulate the effect of gas gushing and extraction on goaf gas production. Li et al. [10] analyzed the evolution and development law of the goaf gas macroflow channel based on the scale and time effect of the rock mass. Although the above studies provide a theoretical basis for gas accumulation in the goaf and the realization of coal and gas cominging, no practical control measures have been proposed. The method proposed in Li et al. [10] can solve the problem of gas accumulation and lacks operability in practical applications. According to the evolution of goaf overburden fracture under mining, the extraction height of roof HLB and its optimal extraction parameters were determined through numerical simulation.

2. Fracture Development of Overburden and Gas Accumulation in the Upper Corner in Goaf

After mining the coal seam, the coal rock mass accumulates in goaf. According to the evolution of coal rock mass, accumulation state, and gas flow characteristics, the mining space can be subdivided into collapse zone, fracture zone, and bending subsidence zone [11]. The coal seam mining reduces the goaf support, triggering numerous secondary fractures in the collapse and fracture zones, which turn into the main migration channel for the gas. With the workface advance, macrocracks developed in the overburden in the middle of goaf are gradually compacted and closed by the ground pressure. The porosity in goaf exhibits nonuniform and continuous distribution patterns, resulting in an O-shaped structure zone [12]. The gas in goaf floats up and accumulates in the O-shaped structure zone due to the buoyancy, forming gas concentration areas. The schematic diagram of the three-band distribution has been shown in Figure 1. Due to goaf air leakage, gas flows into the upper corner, resulting in gas overrun [13].

Under U-shaped ventilation conditions, the air flow in the goaf flows from the transportation lane of the working face to the cut-off hole of the working face, a small part of which flows to the goaf, and most of the working face flows. The air leakage in the goaf presents a parabolic shape, which brings out the gas in the deep part of the goaf, where the upper corners of the working surface meet, so that the upper corner of the working surface has a higher gas concentration. At the same time, because the upper corner of the coal mining face is close to the coal wall and the goaf, when the wind flow passes the end of the working face, the wind speed near the coal wall is reduced due to the sudden vertical turn of the roadway, and vortex phenomenon appears in the upper corner of the working face. There is a phenomenon of air circulation in the vicinity, so that the gas in the goaf and working face is not easily taken away by the wind, and the gas in the upper corner is prone to accumulate.

Therefore, besides controlling the air leakage in goaf, one has to provide the goaf gas control and upper corner gas overrun prevention. To this end, a continuous artificial negative pressure channel should be set in the gas



(A) Collapse zone
(B) Fracture zone
(C) Bending subsidence zone

FIGURE 1: Distributions of three fracture development zones of overburden in the goaf. (A) Collapse zone. (B) Fracture zone. (C) Bending subsidence zone.

concentration area in the fracture zone, overlying the goaf to drain the gas in goaf by the pressure gradient to prevent gushing out of high-concentration gas.

3. Determination of the High-Efficiency Pumping Area of Goaf Gas

3.1. Evolution of Goaf Overburden Simulated by FLAC^{3D}.
To investigate the evolution of overburden in goaf after coal seam mining and determine the optimal position of roof HLB, this study used the FLAC^{3D} software package for simulating the plastic stress variation and distribution of overburden after coal seam mining, which provided a basis for studying goaf gas movement law and determining the optimal extraction parameters.

Detong Coal Mine is located in Linfen City, Shanxi Province, and the mine field is located in the north of Hedong Coal Field, the coal mining method of the working face has adopted the strike longwall mining method, the average thickness of the coal seam is 5 m, the mining height is 4 m, and the coal seam is buried at a depth of about 390 m. The “U” type ventilation method is used and the roof lithology is sandy mudstone and mudstone, and the floor lithology is mudstone and sandy mudstone. Based on workface 20104 of the Detong Mine, distance a model with a length of 430 m, a width of 295 m, and a height of 382.3 m was established in this paper. According to the field measurement results, the model’s vertical and horizontal stresses (σ_z and σ_x) were 20 and 18 MPa, respectively. The main mechanical parameters of numerical simulation were obtained based on the geological data and geological histogram. The Mohr–Coulomb criterion was adopted for stresses in the simulation [14]. The particular strata of the coal rock mass are described in Table 1, and the established model is shown in Figure 2(a).

The length of a unit square in Figure 2 in the direction of the coal seam advance was 5 m. When the excavation length reached 120 m, the plastic failure area continued to expand along the advancement direction but remained stable and unchanged in the vertical direction. The range of the plastic failure area was 60 m from the floor, and its upper limit could be considered the upper bound of the fracture zone [15], which was consistent with the calculation results. Thus,

TABLE 1: Physical and mechanical properties of rock strata.

| Stratum | Buried depth, m | Thickness, m | Density, $\text{kg}\cdot\text{m}^{-3}$ | Bulk modulus, GPa | Shear modulus, GPa | Internal friction angle | Cohesion, MPa | Tensile strength, MPa |
|--------------------------|-----------------|--------------|--|-------------------|--------------------|-------------------------|---------------|-----------------------|
| Argillaceous sandstone | 0 | 100 | 2790 | 8.6 | 4.65 | 34 | 4.31 | 1.8 |
| Coarse sandstone | -100 | 178 | 2860 | 2.9 | 2.5 | 32 | 2.1 | 2.1 |
| Siltstone | -278 | 54 | 2540 | 5.38 | 2.74 | 35 | 2.23 | 0.6 |
| Medium grained sandstone | -332 | 35 | 2650 | 7.2 | 3.53 | 35 | 3.26 | 2 |
| Conglomerate rock | -367 | 10 | 2610 | 4.55 | 2.58 | 32 | 2 | 2.4 |
| Coal | -377 | 5.3 | 1400 | 1.19 | 0.37 | 23 | 0.8 | 0.5 |
| Siltstone | -382.3 | 3.4 | 2580 | 5.61 | 2.35 | 36 | 2.15 | 0.7 |

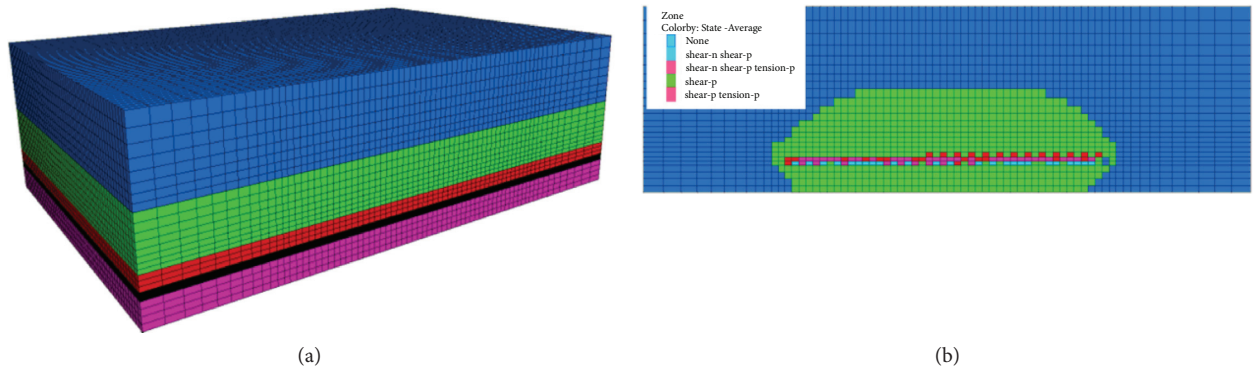


FIGURE 2: Numerical calculation model (a) and stress state distribution map (b) of the goaf.

it could be concluded that the upper limit of the fracture zone was 60 m.

The goaf collapse zone could be determined according to the value and direction of the maximum and minimum horizontal principal stresses σ_H and σ_h after mining. At $\sigma_H > 0$ and $\sigma_h > 0$, it was a bidirectional tensile stress zone mainly distributed in the goaf collapse zone rock mass [15].

In this way, the distributions of the maximum and minimum horizontal principal stresses were obtained through FLAC^{3D} numerical simulation, as shown in Figure 3.

According to the simulation results, coal seam mining led to stress redistribution in the surrounding rock mass. In the process of stress balancing, a series of mechanical effects such as overburden caving, collapse, separation, and displacement of the overlying coal seam strongly manifested themselves. With the workface advance, the goaf behind the workface was gradually compacted under the overburden weight. As observed, the goaf caving zone was mainly distributed within 15 m from the floor, so the distance from the collapse zone to the floor in further calculations was taken as 15 m.

3.2. Distribution of Gas Infiltration Zone in Goaf Undermining. In the process of gas adsorption-desorption dynamic equilibrium, if the gas is in a saturated adsorption state, the adsorbed gas will be desorbed as the coal body is unloaded; if the gas is in an unsaturated adsorption state, the

coal body needs to reach a certain value when the pressure is relieved. The pore gas pressure is reduced to the critical gas desorption pressure and the gas is desorbed. This pressure relief value can be called the effective pressure relief coefficient for gas desorption and drainage. In other words, the lower the saturation of gas adsorption, the higher the degree of pressure relief required for large-scale gas desorption. To observe the coal rock mass evolution after coal seam excavation, the pressure relief coefficient r was defined as

$$\gamma = 1 - \frac{\sigma_Z}{\sigma_0}, \quad (1)$$

where σ_Z is the vertical pressure after coal seam excavation and σ_0 is the initial pressure.

A previous study [16] revealed that the effective extraction range of gas required a great pressure relief degree of coal rock. Based on the research results, the effective pressure relief coefficient can be preset at 0.8 (i.e., $\sigma_z = 0.2\sigma_0$), which corresponds to the efficient extraction range. The numerical simulation performed via FLAC^{3D} software predicted the distribution of workface vertical pressure. The simulation results were sliced according to the distribution range of the collapse and fracture zones, yielding the stress distributions in goaf at different heights, as shown in Figure 4.

According to the pressure relief distribution of the vertical slice, the O-shaped compaction stress rising area was observed in the overlying strata of the workface, and a “vertical stress relief ring” was observed near the O-shaped

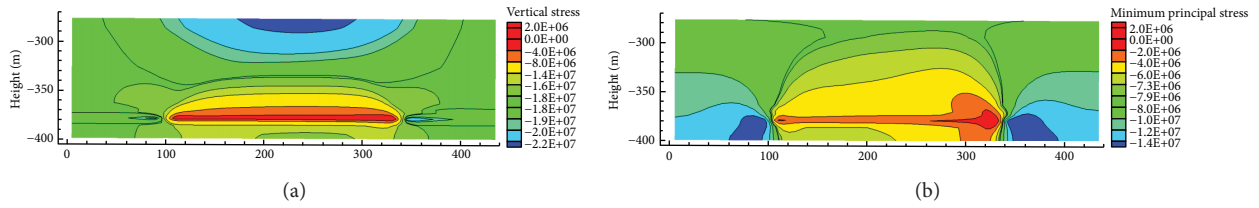


FIGURE 3: Distributions of the maximum (a) and minimum (b) principal stresses in goaf along the strike direction.

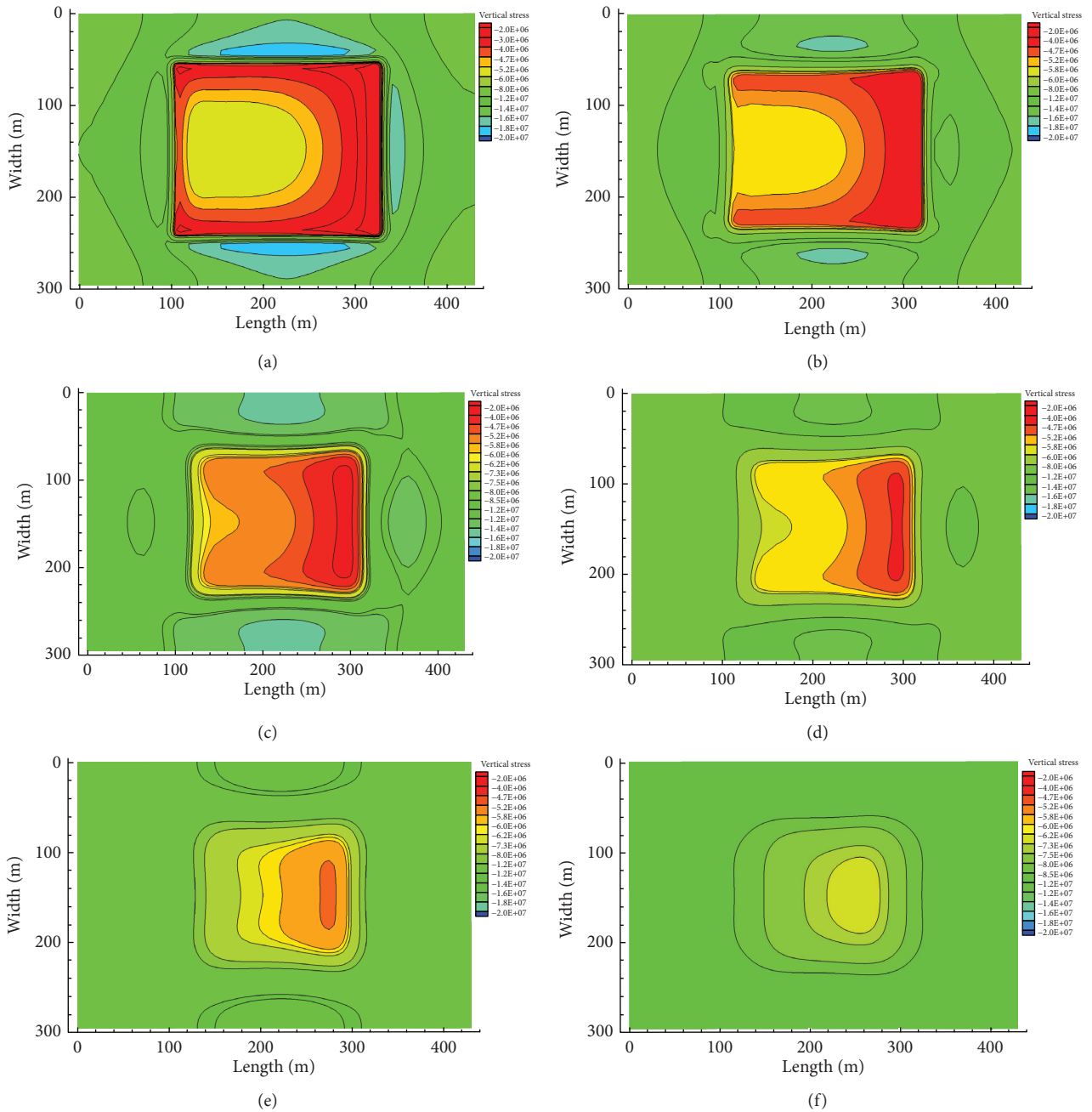


FIGURE 4: Vertical stress distribution at various horizontal distances from the floor: (a) 0 m; (b) 10 m; (c) 30 m; (d) 45 m; (e) 60 m; (f) 75 m.

compaction stress rising area. With an increase in the slice height, the stress in the pressure relief area of the overburden increased gradually and returned to the initial rock stress value; the stress variation rate in the surrounding rock gradually decreased, which was in line with the O-shaped circle theory [3]. As observed, a large pressure relief area was observed near the back of the workface. With an increase in goaf height, the range of the pressure relief area gradually reduced, and this area should be avoided in the extraction drilling arrangement to prevent the borehole cut-off, which would deteriorate the gas extraction efficiency.

The simulation results revealed that the area with an initial vertical pressure of 20 MPa and pressure relief coefficient of 0.8 was within the range of 0–45 m from the floor height. To avoid the drilling being cut off, the drilling should avoid the area with the pressure relief coefficient >0.8 . The optimal height range of the pressure relief channel was 15–45 m. According to the distribution range of pressure relief coefficient and trigonometric function, the effective pressure relief angle of gas efficient extraction range was 76° in the strike and 85° in the dip directions. The area with a pressure relief coefficient of 0.2 was a low-permeability gas area, which could be used as a compaction area. According to the simulation results, the distance between the boundary of the compaction area and the workface was 20 m.

4. Gas Migration Law in Goaf Pressure Relief Area

The migration of gas mixture in goaf was comprehensively affected by air leakage, emission amount of workface gas, and the pressure of coal rock mass in goaf. A further numerical simulation was performed for the case study of workface #2-104 of the Detong Mine, China.

$$\frac{\partial(\rho k)}{\partial t} + \frac{\partial(\rho \mu_i k)}{\partial x_i} = \frac{\partial[(\mu + (\mu_i/\sigma_k))(\partial k/\partial x_j)]}{\partial x_j} + G_k + G_b - \rho \varepsilon - Y_M + S_k, \quad (3)$$

$$\frac{\partial(\rho \varepsilon)}{\partial t} + \frac{\partial(\rho \mu_i \varepsilon)}{\partial x_i} = \frac{\partial[(\mu + (\mu_i/\sigma_\varepsilon))(\partial \varepsilon/\partial x_j)]}{\partial x_j} + C_{1\varepsilon} \times \frac{\varepsilon}{k} (G_k + C_{3\varepsilon} G_b) - G_b - C_{2\varepsilon} \rho \frac{\varepsilon^2}{k} + S_\varepsilon,$$

where μ_i is the turbulent viscosity, μ_i is the average velocity, ρ is the density, G_k is the turbulent kinetic energy generation term caused by velocity gradient, S_ε/S_k are the custom source terms, and $C_{1\varepsilon}/C_{2\varepsilon}/C_{3\varepsilon}$ are the empirical coefficients.

4.2. Gas Sources in Goaf Analysis and Calculation. The gas sources of goaf mainly included the gas gushing out of workface (q_1), of adjacent layer (q_2), and out of goaf (q_3). Under the action of buoyancy and air leakage, part of the gas gushed out with airflow, and the other part floated up and was stored into the cracks induced by mining.

These processes are expressed as follows [20]:

4.1. Goaf Gas Migration Control Equation and Assumptions. For the convenience of calculation, the go extraction area (goaf) was simplified as follows:

- (1) The influence of shearer, hydraulic prop, and electromechanical equipment on the fluid in coal mining workface was ignored
- (2) The mining workface, intake airway, return airway, and goaf areas were assumed to be cuboids, and the gas was treated as an incompressible ideal gas
- (3) The goaf was assumed to be porous and isotropic [17]
- (4) The gas flow was regarded as isothermal motion, and the influence of water vapor and other gases in goaf was ignored

According to the above assumptions, the goaf can be geometrically modeled and meshed, as shown in Figure 5.

According to the above assumptions, the gas mixture flow in goaf satisfied the mass and momentum equations [18].

The fluid flow in the goaf followed Darcy's law, which could be expressed as

$$s_i = -\frac{\mu}{\alpha} \nu_j, \quad (2)$$

where s_i is the source term of the i^{th} momentum equation; μ is the viscous resistance coefficient, $Pa \cdot s$; α is the permeability coefficient of porous media, m^2 ; ν_j is the velocity component.

The flow model that could deal with the turbulent state of gas flow was $k-\varepsilon$ turbulent model, derived by a rigorous statistical technique, and the equations of turbulent kinetic energy k and dissipation rate ε were as follows [19]:

$$q_1 = \lambda \cdot \frac{m}{H} (W_0 - W_c),$$

$$q_2 = \sum_{i=1}^n (W_{0i} - W_{ci}) \cdot \frac{m_i}{H}, \quad (4)$$

$$q_3 = l \cdot q_0 \cdot v_0 \left[\exp\left(-\sqrt{\frac{l_1}{v_0 t}}\right) + \exp\left(-\sqrt{\frac{l_2}{v_0 t}}\right) \right],$$

where q_1 is the amount of gas gushing from the mining layer, q_2 is the amount of gas gushing from the adjacent layer, q_3 is the amount of gas gushing from the residual coal in the goaf, λ is the gas gushing coefficient, W_0 and W_c are the initial and

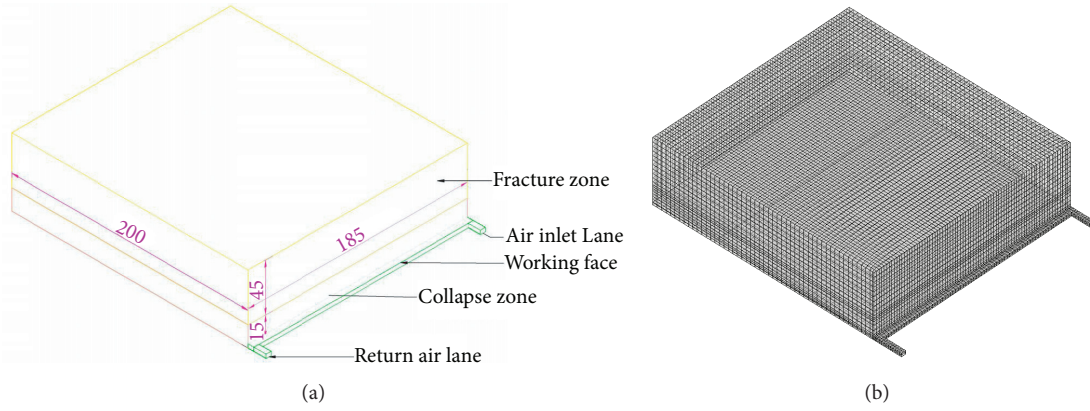


FIGURE 5: Numerical simulation model. (a) Geometric model of working face. (b) Mesh generation of working face.

residual gas contents, respectively, m is the mining layer thickness, i is the parameter of the i^{th} adjacent coal seam, V_0 is the mining velocity of workface, t is the coal seam exposure time, l is the perimeter of roadway section, l_1 is the workface length, l_2 is the strike length of goaf, and q_0 is the gas gushing intensity of the coal wall.

4.3. CFD Numerical Simulation of Mixture Gas Flow in Goaf. The parameter values of each calculation formula shown in Table 2 were obtained based on the field measured data and the empirical formula.

Therefore, parameters q_1 , q_2 , and q_3 were taken as 2.97×10^{-5} , 1.85×10^{-9} , and $2.6 \times 10^{-8} \text{ kg} \cdot (\text{m}^3 \cdot \text{s})^{-1}$, respectively.

4.3.1. Geometric Model. According to the actual dimensions of the site and used scale, the geometric model was set as follows:

- (1) The coal mining face's length, width, and height dimensions were $185 \times 5 \times 4 \text{ m}$, and the space type was fluid
- (2) The scale of the intake and return airway was $10 \times 4 \times 4 \text{ m}$, and the space type was fluid
- (3) The scale of goaf was $185 \times 200 \times 60 \text{ m}$, the fracture and collapse zones were 45 and 15 m from the floor, respectively, and the space type was porous media

4.3.2. Boundary Conditions. The return airway was set as "Out-flow" in the simulations, while the intake airway was assigned a "Velocity-in" value of $2.5 \text{ m} \cdot \text{s}^{-1}$.

Since the goaf was regarded as porous media, its permeability was required for calculations. Therefore, the following permeability model based on sigmoid function was used to simulate the permeability parameter evolution [21].

$$\kappa = \kappa_{\min} + \frac{\kappa_z}{1 + e^{\alpha_1 x - 5}} + \frac{\kappa_z}{(1 + e^{\alpha_2 x - 5})(1 + e^{\alpha_1 x - 5})} \left(y \leq \frac{l_y}{2} \right), \quad (5)$$

$$\kappa_z = \begin{cases} \kappa_{\max} - \kappa_{\min}, & z, \text{ at collapse,} \\ \frac{\kappa_{\max} - \kappa_{\min}}{1 + e^{(z - Z_c) - 10}}, & z, \text{ at fracture,} \end{cases} \quad (6)$$

where $\alpha_1 = (10/x_0)$, x_0 is the strike compaction boundary (preset at 70 m); $\alpha_2 = (10/y_0)$, y_0 is the inclination compaction boundary (preset at 20 m); l_y is the workface incline length; κ_{\min} is the porosity of crushed rock mass after compaction, ranging from 0.1~0.17 [19]; κ_{\max} is the maximum porosity at the workface, which could be obtained by measurement and is commonly ranged from 0.31~0.4 [22].

Substituting equations (5) and (6) into the Kozeny-Carman function [23], one can obtain the goaf permeability distribution [24]:

$$\partial = \frac{D_p^2}{180} \cdot \frac{k^3}{(1 - k)^2}, \quad (7)$$

where ∂ is permeability at maximum porosity, k is porosity, and D_p is the average particle size, ranging from 0.014 to 0.016 m.

The permeability was compiled with User Defined Functions (UDF) and Renormalization Group (RNG) $k - \epsilon$ model [25] was adopted to simulate the mixture gas flow in stope considering the turbulence. The distribution of gas in goaf was obtained.

Figure 6 shows the gas concentration distribution in the return airway side section and the goaf plan at different heights. As observed, the gas concentration distributions of the intake and return airways were quite different. The gas concentration of the intake airway was lower, and the low-concentration area was larger than that of the return airway. In the vertical direction, significant stratification of gas was observed near the workface due to air leakage. The closer it

TABLE 2: Calculation formula parameter value.

| Symbol | Parameter | Value | Unit |
|-----------|--|----------------------|---|
| H | Mining height | 5 | m |
| λ | Gas gushing coefficient | 1.2 | |
| W_0 | Initial gas content of coal seam | 11.7 | $\text{m}^3 \cdot \text{t}^{-1}$ |
| W_c | Residual gas content | 3.95 | $\text{m}^3 \cdot \text{t}^{-1}$ |
| m | Mining layer thickness | 5 | m |
| v_0 | Mining velocity of workface | 4.1×10^{-3} | $\text{m} \cdot \text{min}^{-1}$ |
| q_0 | Gas gushing intensity of the coal wall | 0.0401 | $\text{m}^3 \cdot (\text{m}^2 \cdot \text{min})^{-1}$ |
| l_1 | Workface length | 185 | m |
| l_1 | Strike length of goaf | 200 | m |

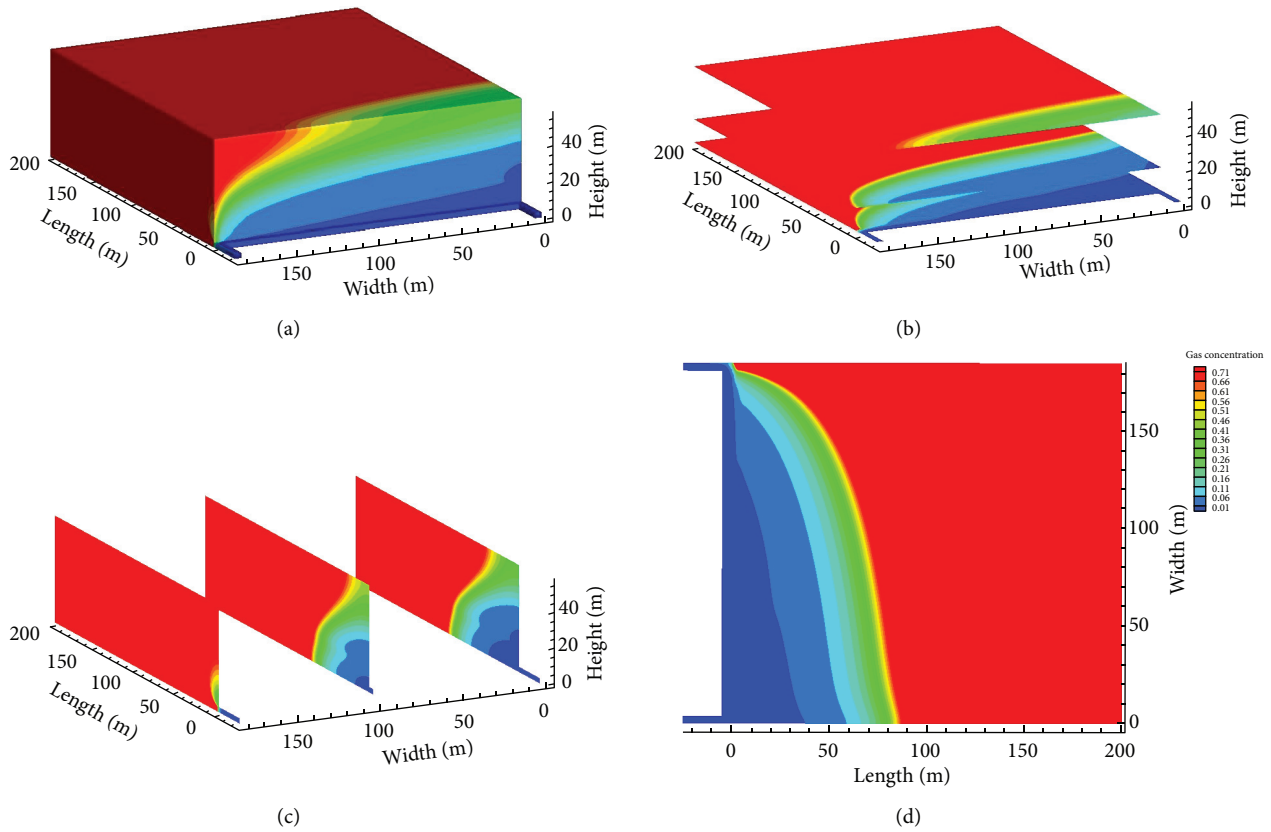


FIGURE 6: Cloud maps of gas distribution in goaf: (a) 2D scheme; (b) plane map; (c) profile; (d) at a 2 m height.

was to the mining area, the lower the gas concentration was. The upper and deep parts of the goaf were high-concentration gas accumulation areas. Meanwhile, the vortex was developed near the return airway in the workface under the action of negative pressure and coal wall, and the airflow velocity decreased, resulting in gas accumulation and overrun, jeopardizing production safety. The specific distribution was as follows.

Along the strike direction of goaf, the gas concentration in the intake airway was nearly zero due to the influence of fresh airflow. However, the amount of fresh air entering the goaf decreased with the deepening of goaf, and the gas concentration grew from 1 to 60%. The gas concentration near the workface on the return air side was no less than 6%, with a large gradient and high concentration. In the vertical

direction, the gas concentration in the return airway was high, with up to 30% being concentrated in the range of 0–30 m in the vertical height and 0–20 m behind the workface.

With no countermeasures, the gas in goaf would get into the return airway under air leakage in the workface. At the same time, due to the action of negative pressure and coal wall, the vortex develops near the upper corner, resulting in the gas overrun in the upper corner, jeopardizing production safety in goaf under HLBs.

For the optimal extraction position obtained above, i.e., 15–45 m in the vertical direction, with the respective support of coal wall and overburden pressure, the optimal position in the horizontal direction can be determined as follows [26]:

$$S = h \cos(\alpha - \beta) + \frac{\gamma(L - L_b)}{2}, \quad (8)$$

where α is the collapse angle of fault zone on the return airway side, set at 85° ; β is the dip angle of the coal seam, set at 0° ; L is the advancing distance of the workface, set at 200 m; γ is the modification coefficient, set at 1. The compaction area width was preset at 20 m, while a 21.3 m horizontal distance from the return airway was adopted.

The borehole type of the roof's HLB diameter extraction was defined as "Velocity-in," the velocity was $-5 \text{ m}\cdot\text{s}^{-1}$, and the diameter was 203 mm.

Figure 7 shows the gas concentration distribution of goaf for the HLB (borehole) located 15 m from the floor and 21.3 m from the return airway. As observed, the HLB played a key role in gas drainage in the goaf; the gas in the goaf was discharged by the negative pressure of the HLB and the ventilation airflow. The HLB presence changed the gas flow field at the return air side and the fracture zone. The gas converged to the HLB. The gas concentration at the return air side was lower than that without extraction.

Cloud diagrams of the plane distribution of gas concentration in the goaf, as shown in Figure 8, indicate that the gas concentration in the upper corner decreased to 4% (which was significantly lower than that without extraction), while the low-concentration area at the return air side increased. A negative pressure zone was developed between the gas near the extraction port and the fracture zone, which forced the high-concentration (up to 30%) gas extraction from the fracture zone.

To further study the HLB location effect on the gas distribution in goaf, the gas concentration distribution and extraction volume with the HLBs in different positions were simulated. The preset HLB distances from the floor were 20, 30, and 40 m, respectively, and those from the return airway were 25, 30, and 35, respectively. The results are listed in Table 3.

As observed in Table 3, the optimal extraction parameter corresponded to the borehole located 30 m from the roof and 25 m from the return airway. At this HLB location, the high-concentration gas in the fracture zone could be extracted without affecting the original ventilation airflow. The gas concentration at the upper corner was significantly reduced, and the extraction concentration reached the maximum value. However, simulation results implied that a single borehole could not control the gas concentration at the upper corner within the safe range ($>1\%$).

According to the data in Table 4, the relationship between the HLB parameters and the gas concentration in the drainage pipeline and the gas concentration in the upper corner is obtained through data fitting.

The relationship between the HLB and the gas concentration of the drainage pipeline [27]:

$$W_c = 20.6 + 1.12x + 0.00086x^2 - 0.0163h^2 - 0.00101h^2. \quad (9)$$

The relationship between the HLB and upper corner gas concentration:

$$W_u = 6.95 + 0.03h + 0.0045x^2 - 0.275x, \quad (10)$$

where W_c is the gas concentration in the drainage borehole, W_u is the gas concentration in the upper corner, x is the distance from the return air tunnel, and h is the height from the floor.

Hence, the number of boreholes should be increased to the number determined by the following equation:

$$N = \frac{4K(Q_j - Q_f)}{VC\pi D^2}, \quad (11)$$

where Q_j and Q_f are the absolute gas emissions of the workface and air row, respectively, K is the disbalance coefficient ranging between 1.2 and 1.7⁶, V is the gas flow rate in the sealed pipe, and C is the gas volume fraction in the extraction pipe (%). The actual values of the respective parameters were substituted into equation (11), yielding the required number of boreholes $N = 3$.

According to observation Figures 9 and 10, gas in the fracture zone was accumulated in the borehole under the negative pressure of the borehole; a large amount of high-concentration gas was extracted, and as the high-concentration gas in the goaf moved to the deep part of the goaf as a whole, the gas emission amount was reduced. The gas concentration slice of $Z = 2 \text{ m}$ in the goaf showed that the gas brought out by the airflow entering the goaf was reduced; the upper corner gas concentration was less than 1%, the production safety was ensured, and the safe coming of coal and gas could be realized.

5. Analysis of Drilling and Extraction Effect in Roof Strike

5.1. HLB Application Site Design. According to the simulation results, three directional HLBs were drilled in the roof of workface # 2-104 of the Detong Mine; the drilling yard was located at the paralleled return airway (see Table 4 and Figure 11).

After the completion of drilling construction, continuous observation was performed on the variation of parameters in the process of the workface advance to 200 m, the variation laws of gas concentration in the upper corner and HLB, and the extraction volume with the advance of workface during mining.

5.2. Field Application Analysis. As observed in Figure 12, the variation of gas concentration in the HLB borehole could be subdivided into three stages. In the first stage, the workface advanced by 20 m in the initial mining; fissures above the goaf were rarely developed, and there was no gas concentration area in the goaf. In this case, the gas concentration and net gas extraction amount were almost zero. In the second stage, the workface advanced by 30-75 m; the goaf roof began to collapse under the overburden pressure, the "three-zone" of goaf began to emerge, and the fractures in the fracture zone formed a gas migration channel. At this stage, the gas concentration and volume in the boreholes increased. In particular, gas concentrations in the three

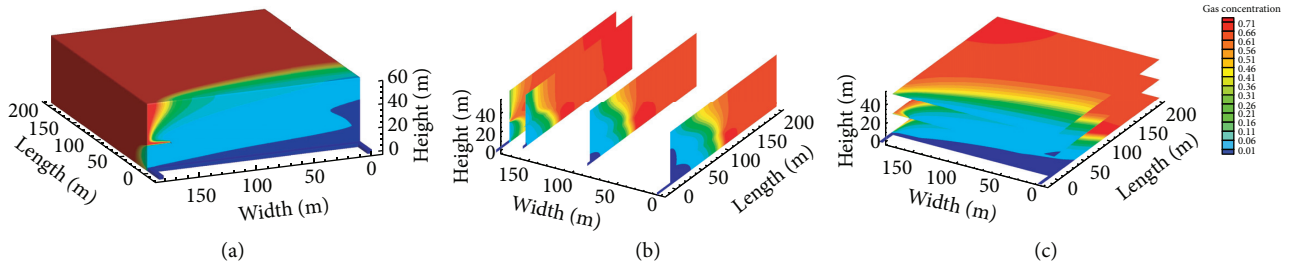


FIGURE 7: Cloud maps of gas concentration distribution during goaf drainage: (a) in 2D model; (b) in the vertical direction (dip); (c) in the longitudinal (strike) direction.

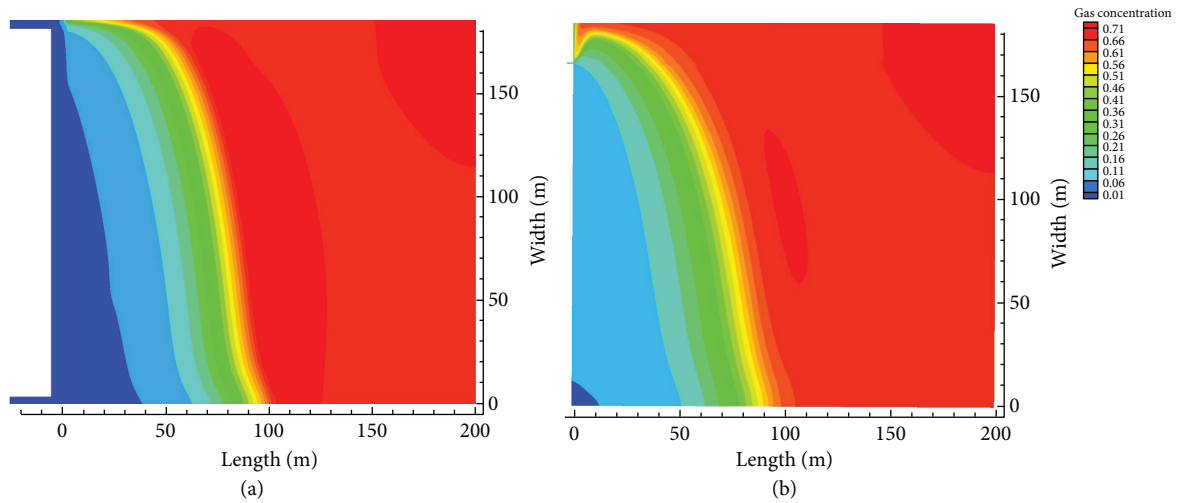


FIGURE 8: Cloud diagrams of the plane distribution of gas concentration in the goaf: (a) 2 m from the floor; (b) 15 m from the floor.

TABLE 3: Gas concentrations at nine different HLB locations.

| HLB location | | Gas concentration, % at the extraction port in the upper corner | |
|---------------------------|------------------------------------|---|-----|
| Distance from the roof, m | Distance from the return airway, m | | |
| 20 | 25 | 33.5 | 4 |
| 20 | 35 | 30.3 | 4.3 |
| 20 | 45 | 26.8 | 4.6 |
| 30 | 25 | 37.5 | 3.4 |
| 30 | 35 | 34.5 | 3.8 |
| 30 | 45 | 32.8 | 4.1 |
| 40 | 25 | 36.4 | 3.9 |
| 40 | 35 | 31.5 | 4.2 |
| 40 | 45 | 29.5 | 4.5 |

TABLE 4: Construction parameters of roof HLBs.

| Hole | Drilling depth/m | Drilling diameter/mm | The horizontal distance between the final hole and roadway/m | The vertical distance between the final hole to the roof/m |
|------|------------------|----------------------|--|--|
| 1 | 763 | 203 | 30 | 30 |
| 2 | 782 | 203 | 25 | 30 |
| 3 | 800 | 203 | 20 | 30 |

boreholes exceeded 35%, and the gas extraction volume was $10\text{ m}^3 \cdot \text{min}^{-3}$. At the third stage, when the workface was advanced to 75 m, the fracture zone above the goaf remained

stable and shifted with the advancement of the workface. The residual coal and gas desorbed by the coal wall in the goaf continued to accumulate in the goaf, resulting in gas

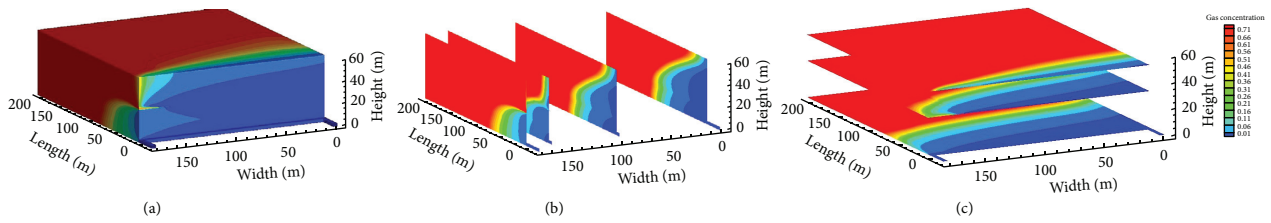


FIGURE 9: Gas concentration distribution in goaf during drainage of three boreholes: (a) vertical; (b) longitudinal.

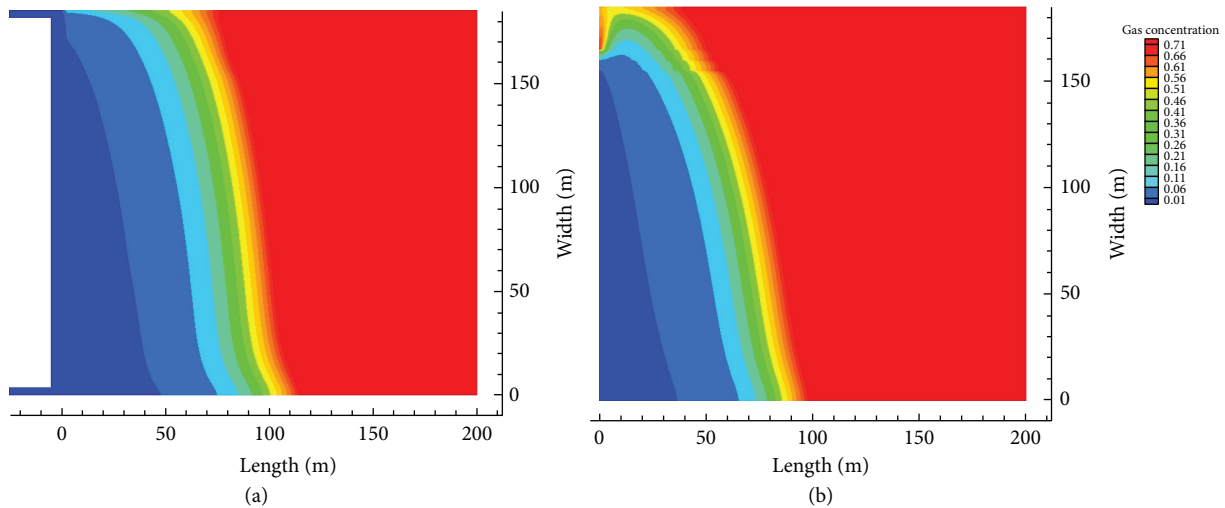


FIGURE 10: Plane distribution cloud diagram of gas concentration in goaf during drainage of three boreholes: (a) 2 m from the floor; (b) 15 m from the floor.

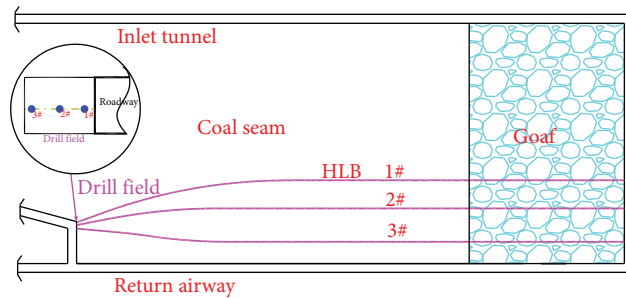


FIGURE 11: HLB construction diagram.

concentration areas in the deep part of the goaf. Then, the gas floated up to the fracture zone, and the gas concentration in the borehole had a stable and high level. Additionally, a periodic pressure variation of goaf was observed; the gas concentration of the three boreholes was 30–38%, and the gas extraction volume was maintained at $12 \text{ m}^3 \cdot \text{min}^{-3}$.

In the first and second stages, gas concentration in the upper corner was consistent with the gas extraction volume of the borehole. In a rising trend, the maximum gas concentration in the upper corner reached 0.8%. In the third

stage, when the gas concentration and gas extraction volume in the borehole reached a high level, the gas concentration at the upper corner was relatively low, and vice versa. The gas concentration in the upper corner was maintained within the safe range of 0.5–0.6%, and roof HLB parameters obtained by the numerical simulation were quite reliable.

Comparing the actual results on site with the numerical simulation results, the changes in borehole concentration and the upper corner gas concentration were basically consistent with the simulation results. The actual field data is

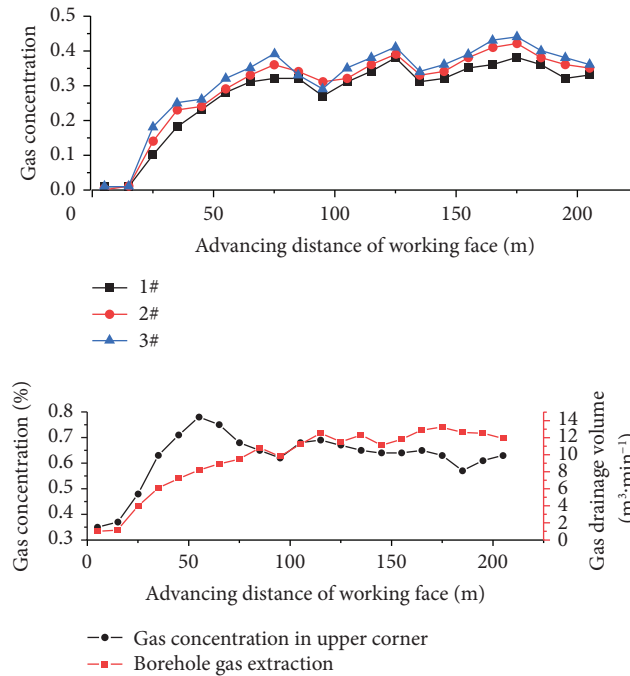


FIGURE 12: Dynamic change of gas in drainage borehole and upper corner with the movement of working face.

higher than the simulation result. In the following research, the numerical model should be further optimized to avoid errors.

6. Conclusions

Coal mining induces deformation and damage of goaf overburden, resulting in many secondary fractures and gas concentration areas. The gushing of high-concentration gas seriously restricts mining production safety. Therefore, the roof-drilled highly located boreholes (HLBs) are constructed to create an artificial channel to drain the high-concentration gas stored in the fracture zone and improve the production safety with coal and gas coming. Theoretical analysis and FLAC^{3D} numerical simulation were applied to the case study of workface #2-104 of the Detong Mine (China), yielding the goaf overburden stress evolution pattern. Through analysis, it was found that the range of goaf collapse zone was located 15 m from the floor, and the range of fracture zone was 15–60 m from the floor. By defining the pressure relief coefficient, the optimal extraction range of the fracture zone was assessed as 15–45 m; the effective pressure relief angles were 76° in the strike and 85° in the dip. FLUENT software was used to provide the numerical simulation of gas migration law in goaf under initial and different extraction parameters. The results showed that the optimal position of roof-drilled HLB was 30 m from the floor and 25 m from the return airway. It was verified that the problem of the upper corner gas overrun could be mitigated by drilling three directional HLBs. Engineering practice revealed that when three roof-drilled HLBs were located 30 m from the workface floor and 25 m from the return airway, the gas concentration in the boreholes exceeded 30%, while the gas concentration in the upper corner did not

exceed 0.8%. The accuracy of the simulation results was verified, which provided a reference for solving gas overrun problems in similar coal mines and realizing effective coal and gas coming.

Data Availability

The data that support the findings of this study are available from the corresponding author upon reasonable request.

Conflicts of Interest

The authors declare that they have no conflicts of interest.

References

- [1] Y. Peng, Q. Qi, Y. Wang, Z. Deng, H. Li, and C. Li, "Study of field measurement of mining-induced coal fracture field and its application," *Chinese Journal of Rock Mechanics and Engineering*, vol. 29, no. S2, pp. 4188–4193, 2010.
- [2] C. Karacan, G. Esterhuizen, S. Schatzel, and W. P. Diamond, "Reservoir simulation-based modeling for characterizing longwall methane emissions and gob gas vent hole production," *International Journal of Coal Geology*, vol. 71, no. 2-3, pp. 225–245, 2007.
- [3] C. Li, Y. Zhang, J. Li, and G. Zhang, "Highly located boreholes drainage technology of gas macroscopic flow channel in goaf," *Journal of Mining & Safety Engineering*, vol. 34, no. 2, p. 7, 2017.
- [4] X.-Q. Fang, Y.-Q. Geng, and M. Wang, "Kilometer directional drilling: simultaneous extraction of coal and gas from a high-gas coal seam," *Journal of China University of Mining and Technology*, vol. 41, no. 6, pp. 885–892, 2012.
- [5] Y. P. Cheng, Q.-X. Yu, L. Yuan, and P. Li, "Experimental research of safe and high-efficient exploitation of coal and pressure relief gas in long-distance," *Journal of China*

- University of Mining and Technology*, vol. 33, no. 2, pp. 132–136, 2004.
- [6] M. G. Qian and J. L. Xu, "Study on the "O shape" circle distribution characteristics of mining induced fracture in the overburden strata," *Journal of China Coal Industry*, vol. 5, pp. 20–23, 1998.
- [7] H. Yavuz, "An estimation method for cover pressure re-establishment distance and pressure distribution in the goaf of longwall coal mines," *International Journal of Rock Mechanics and Mining Sciences*, vol. 41, no. 2, pp. 193–205, 2004.
- [8] C. Ö. Karacan and R. M. Goodman, "Hydraulic conductivity changes and influencing factors in overburden determined by slug tests in gob gas ventholes," *International Journal of Rock Mechanics and Mining Sciences*, vol. 46, no. 7, pp. 1162–1174, 2009.
- [9] H. Guo, L. Yuan, B. Shen, Q. Qu, and J. Xue, "Mining-induced strata stress changes, fractures and gas flow dynamics in multi-seam longwall mining," *International Journal of Rock Mechanics and Mining Sciences*, vol. 54, pp. 129–139, 2012.
- [10] S. Li, H. Lin, P. Zhao, P. Xiao, and H. Pan, "Dynamic evolution of mining fissure elliptic paraboloid zone and extraction coal and gas," *Journal of China Coal Society*, vol. 39, no. 8, pp. 1455–1462, 2014.
- [11] V. Palchik, "Formation of fractured zones in overburden due to longwall mining," *Environmental Geology*, vol. 44, no. 1, pp. 28–38, 2003.
- [12] M. Qin, "Study on the treatment of upper corner gas based on the roof-drilling holes," *Innovation and Application of Engineering Technology*, CRC Press, Florida, USA, 2017.
- [13] G. Si, S. Jamnikar, J. Lazar et al., "Monitoring and modelling of gas dynamics in multi-level longwall top coal caving of ultra-thick coal seams, part I: borehole measurements and a conceptual model for gas emission zones," *International Journal of Coal Geology*, vol. 144–145, pp. 98–110, 2015.
- [14] Q. Bai, S. Tu, Y. Yuan, and F. Wang, "Back analysis of mining induced responses on the basis of goaf compaction theory," *Zhongguo Kuangye Daxue Xuebao/Journal of China University of Mining and Technology*, vol. 42, no. 3, pp. 355–361, 2013.
- [15] Z. Meng, J. Zhang, X. Shi, Y. Tian, and Y. Chao, "Calculation model of rock mass permeability in coal mine goaf and its numerical simulation analysis," *Journal of China Coal Society*, vol. 41, no. 8, pp. 1997–2005, 2016.
- [16] L. Yuan, H. Guo, B.-T. Shen, Q.-D. Qu, and X. Junhua, "Circular overlying zone at longwall panel for efficient methane capture of multiple coal seams with low permeability," *Journal of China Coal Society*, vol. 36, no. 3, p. 365, 2011.
- [17] J. Ma, Y. Sun, and B. Li, "Simulation of combined conductive, convective and radiative heat transfer in moving irregular porous fins by spectral element method," *International Journal of Thermal Sciences*, vol. 118, pp. 475–487, 2017.
- [18] Z. Qin, L. Yuan, H. Guo, and Q. Qu, "Investigation of longwall goaf gas flows and borehole drainage performance by CFD simulation," *International Journal of Coal Geology*, vol. 150–151, pp. 51–63, 2015.
- [19] H. Zhao, W. Pan, and X. Wang, "Numerical simulation on distribution of gas concentration in goaf under condition of mining thin coal seam," *Journal of China Coal Society*, vol. 36, pp. 440–443, 2011.
- [20] W. Wang, Z. Li, and H. Yu, "Goaf Gas control improvement by optimizing the adjacent roadway large-diameter boreholes," *Advances in Civil Engineering*, vol. 2021, Article ID 1933010, 13 pages, 2021.
- [21] W. Wei, Y. Cheng, H. Liu, Z. Fang, X. Li, and R. Zhao, "Permeability model of gob based on sigmoid function and application in the airflow field simulation," *Journal of Mining & Safety Engineering*, vol. 34, no. 6, p. 1232, 2017.
- [22] Z.-X. Li, S.-L. Ji, and Z.-Y. Ti, "Two-phase miscible diffusion model and its solution between gas in goaf and atmosphere," *Chinese Journal of Rock Mechanics and Engineering*, vol. 24, no. 16, pp. 2971–2976, 2005.
- [23] B. Tan, J. Shen, D. Zuo, and X. Guo, "Numerical analysis of oxidation zone variation in goaf," *Procedia Engineering*, vol. 26, pp. 659–664, 2011.
- [24] G. Wang, H. Xu, M. Wu, Y. Wang, R. Wang, and X. Zhang, "Porosity model and air leakage flow field simulation of goaf based on DEM-CFD," *Arabian Journal of Geosciences*, vol. 11, no. 7, pp. 1–17, 2018.
- [25] V. Yakhot, S. A. Orszag, S. Thangam, T. B. Gatski, and C. G. Speziale, "Development of turbulence models for shear flows by a double expansion technique," *Physics of Fluids A: Fluid Dynamics*, vol. 4, no. 7, pp. 1510–1520, 1992.
- [26] S.-G. Li, P.-Y. Xu, P. Zhao, and H. Lin, "Aging induced effect of elliptic paraboloid zone in mining cracks and pressure released gas drainage technique," *Coal Science and Technology*, vol. 46, no. 9, pp. 146–152, 2018.
- [27] B. Zhao, G. Wen, J. Nian et al., "Numerical simulation study on the multi-physical field response to underground coal and gas outburst under high geo-stress conditions," *Minerals*, vol. 12, no. 2, Article ID 151, 2022.

Research Article

The Study on the Substrate Effect in the Nanoindentation Experiment of the Hybrid Material

Kang Liang,^{1,2} Kunpeng Gao ,¹ and Wenqing Cai²

¹Nanjing Vocational University of Industry Technology, Nanjing 210023, China

²Tongji University, Shanghai 200092, China

Correspondence should be addressed to Kunpeng Gao; gao.kunpeng@foxmail.com

Received 2 November 2021; Accepted 14 December 2021; Published 4 January 2022

Academic Editor: Gaofeng Song

Copyright © 2022 Kang Liang et al. This is an open access article distributed under the Creative Commons Attribution License, which permits unrestricted use, distribution, and reproduction in any medium, provided the original work is properly cited.

The nanoindentation (NI) experiment is an effective method to evaluate the micromechanical property of materials. The substrate effect is a nonnegligible factor which could influence the accuracy of the NI experiment result. Large numbers of previous studies have focused on the substrate effect based on the coating/substrate model, whereas the substrate effect in the testing of the hybrid material was rarely involved. The real NI experiment and the numerical simulation method were adopted to reveal the characteristics of the substrate effect in the NI experiment of the hybrid material in this paper, such as the rock or cement material. The peak displacement h_{peak} and the residual displacement h_{residual} of the indenter, which could obtain directly from the NI experiment and were usually considered as key basic variables to calculate other parameters, were selected as evaluation indexes of the substrate effect. The results indicated that there was a significant difference of the NI experiment result between the coating/substrate and the hybrid material under the same condition. The lateral boundary stiffness and discontinuous face were considered as main factors that induced this difference, and their effect were analysed, respectively. Young's modulus E_s and Poisson's ratio μ_s of the substrate were selected as the variables in the parametric study, and the relationship between them and the NI experiment result were discussed.

1. Introduction

The nanoindentation experiment (NI experiment) is one of the most powerful techniques for evaluating the micro-mechanical behaviour of materials related to the mining engineering, such as the rock or the cement material [1–8]. This method records the applied load and the indentation depth during the indenter contacting the target object, such as the thin films and the small volumes of materials, and then the hardness, the elastic modulus, and other mechanical parameters of the material could be computed based on the Oliver–Pharr's method or other methods.

However, the substrate effect is a nonnegligible factor which could seriously affect the NI experiment accuracy [2, 5, 9–17]. For instance, this effect was dramatically shown in one of our experiments. During this experiment, the indentation depths of unhydrated cement granular were extremely different in various substrate materials in the same

experiment conditions (the indenter, loading, etc.). The indentation depths in different substrate materials ranged from 71 to 500 nm under 1 mN load. The detail of this experiment was introduced in Section 2.

This huge difference reveals the dramatically substrate effect in the NI experiment, and some studies have already focused on this inevitable influence of the substrate. Various potentially relevant factors have been selected as study objects. The indentation depth is considered as a directly factor which is closely related to substrate effect, because the indentation depth could be obtained in NI experiment directly [3, 13, 18]. As a rule of thumb, deep indentation depth could induce strong substrate effect, and the substrate effect could be ignored when the relative indentation depth (RID, the penetration divided by the coating thickness) is less than 0.1 [3, 13]. This RID value is not stringent enough under different coating/substrate combinations, indenter shape, indenter size, surface roughness, and so on [3, 13, 19, 20].

The yield stress and the elastic modulus ratio between the coating and substrate, that is, E_c/E_s , are considered as prime parameters, which could influence the RID values [13, 15]. When $\sigma_{yc}/\sigma_{ys} < 10$, the RID <10% could be applicable, and RID value should be less than 5% when $\sigma_{yc}/\sigma_{ys} \geq 10$ and $E_c/E_s > 0.1$ [15].

Previous studies have obtained profound comprehension of substrate effect; however, accurate evaluation of substrate effect in the hybrid material, that is, the rock or the cement material, is still a challenging task. The previous studies mainly focused on coating/substrate model, in which the testing object (coating) covers the substrate material. This model could be credible in laminated composites or coating materials, but it should not be suited in the hybrid material. In the hybrid material, the testing object is usually embedded in the mixed material, and the mechanic response is inevitably influenced by surrounding materials.

This paper aimed to gain an in-depth understanding of the substrate effect in the NI experiment of the hybrid material. The basic mechanical properties (Young's modulus and Poisson's ratio) of substrate, which were usually considered as prime effect factors [13, 15], were selected as study parameters, and the numerical simulation method was selected. With 27 groups of numerical experiments, the substrate properties' influence in hybrid material on the NI experiment was illustrated by analysing the peak displacement (h_{peak}) and residual displacement (h_{residual}) of the indenter under the same loading, which were usually considered as key direct data of NI experiment results [3, 10, 19, 21, 22].

2. Experiment

To reveal the substrate effect in the hybrid material, a series of experiments were conducted with the NI technology. The hybrid material was selected as the hardening cement, and the tested object was selected as the unhydrated cement granular, which was unavoidable and existed in the hardening cement. Besides, an epoxy resin sample, which contained unhydrated cement granular, was also conducted as the limiting case.

The hardening cement was made up of the Portland cement P.II 42.5 in this experiment, and its chemical constitutions are listed in Table 1. The water-cement ratio of cement was set as 0.4 in all cement samples. The adhesive strength of epoxy resin is 6Mpa. The detailed test process is as follows.

2.1. The Sample preparation. The epoxy sample is prepared as follows. The cement particles greater than $80\mu\text{m}$ were selected using cement sifter and then dealt with the drying oven for 2 hours at 105°C . The dried selected cement particles were mixed with epoxy resin on a mass ratio of 3 : 1 and then curing this mixture for 10 days before test.

The cement samples are prepared as follows. The cement with a water-to-cement ratio of 0.4 was cast into cylinder specimens (10 mm diameter) and then was cured in a sealed and saturated moisture environment at $20 \pm 2^\circ\text{C}$ for 1 day, 28 days, and 60 days, respectively.

2.2. Polishing Procedures. Firstly, samples used in this experiment were cut to 10 mm height. Secondly, samples were polished on silicon carbide papers down till 4000 grades and then polished using charoet or flannel polishing pad to obtain a smooth surface at both ends. The tilt angle of two ends of planes is less than on degree, measured by vernier. The ethanol is used to clean the samples during polishing process.

2.3. Experimental Methods. The type of indenter adopted the common Berkovich indenter in all experiments. The NI depth and load were recorded during the test. The maximum load is set as 1Mn ($P_{\text{max}} = 1\text{mN}$), and the loading shape is set as trapezoidal defined by 10 s loading time, 5 s holding time, and 10 s unloading time.

Following the experiment procedure mentioned above, the typical load-depth curves for respective test conditions are shown in Figure 1. Two key points of curves were selected as study indicators: the peak depth h_{peak} (peak indenter displacement) and the residual displacement h_{residual} of indenter after unloading. This is because h_{peak} and h_{residual} were generally considered as the key parameters, which could be obtained directly in the NI experiment, to calculate mechanical parameters of material according to Oliver-Pharr's model or other methods. In other words, h_{peak} and h_{residual} would differ under different substrates if the substrate effect existed under the same loading.

The strength of various substrates and the corresponding NI results is presented in Table 2. The strength of cement cases referred to the compressive strength, and the bonding strength was used in the epoxy resin case.

The results show the peak indenter displacement in tests ranges from 71 to 94 nm in substrate of cement and more than 500 nm in substrate of epoxy resin. The substrate's property has a significant effect on the test result. The higher the strength of the substrate, the smaller the peak indenter displacement at the same peaking load. In other words, the softer substrate results in higher peak indenter displacement. The residual displacement has more complex relationship with the substrate strength. When the substrate strength is lower (i.e., epoxy resin), the residual displacement is much greater than the higher strength substrate cases. When the substrate strength increases, the residual displacement becomes smaller and seems to present a fluctuating tendency (58.60 nm \rightarrow 65.18 nm \rightarrow 30.88 nm). It could be referred that the overall relationship between the residual displacement and the strength is negative correlation, but when the strength is relatively higher, fluctuation will appear.

3. Numerical Simulation

The conclusion, which has been obtained in Section 2, is relatively rough and unconvincing limiting to the NI experiment number. To obtain a clear understanding of the substrate effect in the hybrid material, numerical investigations were conducted with FEM by considering various substrates with different Young's modules and Poisson's ratios in numerical models of the hybrid material or

TABLE 1: Chemical compositions of cement (in mass percent).

| Na ₂ O | MgO | Al ₂ O ₃ | SiO ₂ | SO ₃ | K ₂ O | CaO | TiO ₂ | MnO | Fe ₂ O ₃ | SrO |
|-------------------|------|--------------------------------|------------------|-----------------|------------------|------|------------------|------|--------------------------------|------|
| 0.29 | 1.09 | 3.91 | 21.4 | 1.85 | 0.64 | 66.5 | 0.18 | 0.08 | 2.75 | 0.06 |

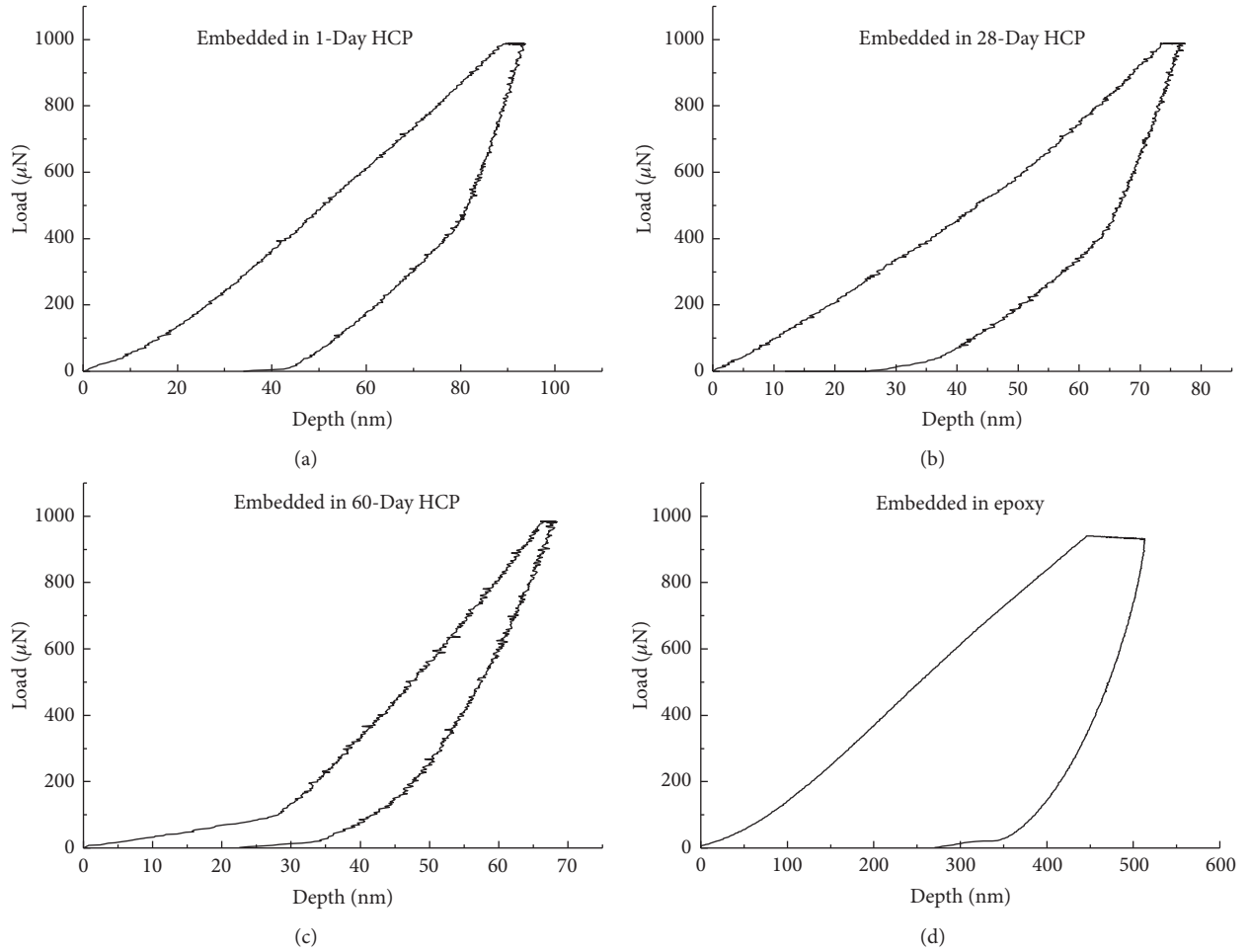


FIGURE 1: Typical load-depth curves of cement particles.

TABLE 2: NI results of cement particles under different embedded conditions.

| Embedded condition | 1-day HCP | 28-day HCP | 60-day HCP | Epoxy resin |
|----------------------------|-----------|------------|------------|-------------|
| Strength (MPa) | 11.44 | 67.73 | 68.54 | 6 |
| h_{peak} (nm) | 94.38 | 93.14 | 71.83 | 589.14 |
| h_{residual} (nm) | 58.60 | 65.18 | 30.88 | 424.21 |

coating/substrate combination, respectively. As a widely used method, the FEM method could well reflect the deformation and mechanical law of various type of materials and structure, with lower economic and time costing. In this paper, a general-purpose FEM package ABAQUS was used.

The substrate effect was reflected by the difference of indentation depth (h_{peak} and h_{residual}) under the same load [12, 15]. Three series of numerical experiments were designed to investigate substrate effect on the NI experiment, as shown in Table 3. Series 1 and series 2 focused on the influence of Young's modules and Poisson's ratios of the substrate in the hybrid material. Series 3 considered to reveal

the difference between the hybrid material and the coating/substrate combination using a coating/substrate model.

A simplified plane model, using the necessary axial symmetry conditions, was adopted, in both the model of the hybrid material and coating/substrate combination, to avoid long time costing and decrease convergence difficulties [3, 11, 15, 19, 21, 23, 24]. Previous studies show that the result difference between the 2D model and 3D model is within a few percent in the nanoindentation simulation, and this simplification usually has an accurately indication of the reality [13].

The analysis domain consisted of three parts, the indenter, the testing material, and the substrate (see Figure 2).

TABLE 3: Design of the numerical experiment and computation results.

| Series | Case | Substrate | | h_{peak} (nm) | h_{residual} (nm) |
|---------------------------------|-------------|-------------|---------|------------------------|----------------------------|
| | | E_s (GPa) | μ_s | | |
| 1 (the hybrid material model) | a1 | 1 | 0.2 | 1257.99 | 218.67 |
| | a2 | 2 | 0.2 | 735.36 | 174.80 |
| | a3 | 3 | 0.2 | 556.39 | 167.40 |
| | a4 | 4 | 0.2 | 465.67 | 159.62 |
| | a5 | 5 | 0.2 | 410.71 | 155.22 |
| | a6 | 6 | 0.2 | 373.81 | 152.45 |
| | a7 | 7 | 0.2 | 347.28 | 150.94 |
| | a8 | 8 | 0.2 | 327.26 | 146.66 |
| | a9 | 9 | 0.2 | 311.91 | 149.94↑ |
| | a10 | 10 | 0.2 | 299.05 | 146.08↓ |
| | a11 | 20 | 0.2 | 241.55 | 149.59↑ |
| | a12 | 30 | 0.2 | 221.86 | 154.30 |
| | a13 | 40 | 0.2 | 211.85 | 153.24↓ |
| | a14 | 50 | 0.2 | 205.77 | 157.12 |
| | a15 | 60 | 0.2 | 201.72 | 150.29 |
| | a16 | 70 | 0.2 | 198.81 | 153.45↑ |
| | a17 | 80 | 0.2 | 196.61 | 154.91 |
| | a18 | 90 | 0.2 | 194.89 | 153.92↓ |
| | a19 | 100 | 0.2 | 193.51 | 156.09↑ |
| 2 (the hybrid material model) | b1 | 50 | 0.05 | 204.594 | 150.480 |
| | b2 | 50 | 0.10 | 204.999 | 150.649 |
| | b3 | 50 | 0.15 | 205.389 | 155.587 |
| | b4 | 50 | 0.20 | 205.765 | 157.122 |
| | b5 | 50 | 0.25 | 206.129 | 156.584↓ |
| | b6 | 50 | 0.30 | 206.479 | 151.733 |
| | b7 | 50 | 0.35 | 206.815 | 152.096↑ |
| | b8 | 50 | 0.40 | 207.138 | 152.114 |
| 3 (the coating/substrate model) | c1 (vs a1) | 1 | 0.2 | 1171.84 | 164.906 |
| | c2 (vs a14) | 50 | 0.2 | 210.702 | 158.043 |
| | c3 (vs a19) | 100 | 0.2 | 197.13 | 158.862 |
| | c4 (vs b1) | 50 | 0.05 | 210.693 | 158.286 |
| | c5 (vs b8) | 50 | 0.4 | 210.721 | 153.688 |

In the hybrid material model, the substrate was $30\ \mu\text{m} \times 30\ \mu\text{m}$, and the testing target was $5\ \mu\text{m} \times 5\ \mu\text{m}$. In the model of coat/combination, the substrate was $25\ \mu\text{m} \times 30\ \mu\text{m}$, and the testing target was $5\ \mu\text{m} \times 30\ \mu\text{m}$. The testing material (or the coating) was assumed to be elastic plastic, with Young's modulus $E_t = 50\text{GPa}$, Poisson's ratio $\mu_t = 0.2$, and plastic yield strength $\sigma_s = 300\text{MPa}$. The substrate was assumed to be linearly elastic with different Young's modulus and Poisson's ratio (see Table 3).

Although a Berkovich indenter was used in real tests, previous studies have rarely constructed the indenter model as the Berkovich shape due to the complicated element mesh division and stress concentration. Referring to the relevant literatures [5, 9, 11, 13, 15, 21, 24], the indenter was modeled as a cone with a rounded tip in this paper. The half-included angle of the cone (α) was 70.3° , whereas the tip radius (R) was $100\ \text{nm}$. The indenter was assumed as a rigid body, since otherwise it would be difficult to distinguish the influence of the indenter and the substrate material on the simulation result [5, 11, 19, 21]. An investigating point was set on the rigid reference point of indenter, which could monitor the

indentation depth and corresponding force. This point could output the force and displacement of indenter of every computing increment in the simulation.

The contact between the indenter and the testing material, and the contact between testing material and substrate were both modeled using the "frictionless" contact option. This option allowed frictionless sliding between two surfaces, and this simplification could satisfy the simulation's accuracy [3]. The bottom boundary of the model was fixed in the vertical direction, and the left side boundary of the model was fixed in the horizontal direction.

The mesh elements near the contact area were refined so that the deformation and stress gradients could be accurately described. The mesh became progressively coarser at distances further away from the main deformation area. The 2D numerical mesh and boundary conditions are illustrated in Figure 2.

The computation process was divided into two stages. At the first stage, a vertical load of $500\ \mu\text{N}$ was gradually applied on the rigid reference point of indenter. During this process, the testing material (or the coating) deformation transferred from elastic to plastic, and the substrate significantly

deformed correspondingly. With dozens of iterations, a strict equilibrium was achieved. In the second stage, the load which was applied on the rigid reference point was designed to decrease to zero. In this process, the elastic deformation of the system gradually recovered, whereas the plastic deformation was retained.

4. Results and Discussion

4.1. Characteristics of the Hybrid Material Substrate Effect. Series 3 and relevant cases of series 1 and 2 (cases a1, a14, a19, b1, and b8) are selected to be analysed in this section. The substrate's property of cases in series 3 is the same as relevant cases in series 1 and 2, but the numerical model was different. The characteristics of the hybrid material are revealed by contrastive analysing of the difference between them. Through the cases comparison, two conclusions could be observed.

4.1.1. The Difference of the NI Experiment Results. There is a significant difference of experiment results between the hybrid material and the coating/substrate combination when the substrate has a similar property. In the comparative group of c1 versus a1, h_{peak} and h_{residual} obtained by the hybrid material model are both bigger than the results obtained by the coating/substrate combination model, whereas the conclusion is reverse in other comparative groups.

The numerical model's difference between series 3 and relevant cases of series 1 and 2 is mainly the lateral boundary condition of the testing area. In series 3 (coating/substrate combination model), the testing area is actually surrounded by the same material and under the lateral stress derived from the deformation of the same material. In case c1, the lateral stress is derived from the coating material with Young's modulus $E_t = 50\text{GPa}$, whereas the lateral stress is provided by the substrate with Young's modulus $E_s = 1\text{GPa}$ in the comparative case a1. The low lateral stiffness leads to the bigger strain in the lateral direction and the bigger displacement in the loading direction. As the strength of the substrate increases, the lateral substrate of relevant cases in series 2 and 3 could provide a "harder" boundary than the coating/substrate combination cases in series 3 ($E_s \geq 50\text{GPa}$ in cases a14, a19, b1, and b8), and the indenter displacement is smaller correspondingly in hybrid material models. Only Young's modulus of the substrate E_s is considered in the above analysis; that is because Poisson's ratio μ_s has a little effect on the experiment result from series 2, and the NI experiment result difference mainly comes from Young's modulus in this paper study.

4.1.2. The Characteristic of Stress Distribution. The discontinuous face existed in the model results in the discontinuous of stress distribution and induces stress concentration around the junction of discontinuous faces in the hybrid material model.

In order to reveal the Mises stress distribution pattern around the discontinuous face, 22 measurement points were designed near the interface. The positions of points are

shown in Figure 3, and the Mises stress of each point could be seen in Table 4. Generally speaking, the stress of the testing area is higher than the near position of substrate (the stress difference value is positive), excluding the area of bottom corner of the testing area where the stress concentration occurs. The discontinuous face decreases the stress transfer significantly. Besides that, an interesting finding was revealed. The stress difference between both sides of the discontinuous is generally gradually decreased in the horizontal direction along with the distance to the indenter increasing, whereas it fluctuated in the vertical direction, excluding the area of stress concentration.

4.2. Effect of Substrate Young's Modulus in the Hybrid Material. To examine the effect of Young's modulus on the NI experiment, 19 cases with Young's modulus ranging from 1 GPa to 100 GPa were designed and simulated (cases a1–a19). The calculated curves of force versus indentation depth are shown in Figure 4, and the curve shape is similar to the testing result in Section 2. The peak displacement (h_{peak}) and the residual displacement (h_{residual}) of the indenter were selected as study indicators. h_{peak} and h_{residual} of each group are list in Table 3, and the curve of indenter displacement versus substrate Young's modulus is presented in Figure 5.

As shown in Table 3 and Figure 5, the h_{peak} value varies from 1257.99 nm to 193.51 nm, with E_s increasing from 1 GPa to 100 GPa. The decreasing trend of h_{peak} is markedly different before and after a critical point where E_s is approximately equal to 15 GPa. Before the critical point, h_{peak} drops substantially from 1257.99 nm (case a1) to 299.05 nm (case a10), with E_s just increasing from 1 GPa to 10 GPa, only increment of 9 GPa, whereas the decreasing value is only 105.54 nm, with E_s rising from 10 GPa to 100 GPa. The decreasing trend of the curve is significantly slowed down. The bigger E_s , the smaller decreasing rate. It could be concluded that h_{peak} will be nearly constant when E_s is large enough. In other words, the indentation experiment result has a more sensitive to the lower E_s .

Furthermore, the residual displacement curve shown in Figure 5 is relatively flatter. The h_{residual} value varies from 218.67 nm (maximum value, case a1) to 146.08 nm (minimum value, case a10), while E_s is less than 8 GPa (case a8), and h_{residual} is decreasing from 218.67 nm to 146.66 nm, correspondingly. Then, the curve starts to fluctuate with general increasing trend, following E_s further increase, but the increment is only 9.43 nm (compare case a8 to a19). Based on the observation, the relatively lower E_s has a nonnegligible impact on h_{residual} , when the plastic property of testing material is considered. The influence of the higher E_s is slightly poor regularity but generally enlarges the residual displacement.

The conclusion obtained by numerical experiment is much similar to the phenomenon reflected by experiments in Section 2.

4.3. Effect of Substrate Poisson's Ratio. Eight cases with various μ_s (Poisson's ratio of the substrate) of 0.05, 0.1, 0.15, 0.2, 0.25, 0.3, 0.35, and 0.4 (cases b1–b8) were considered to

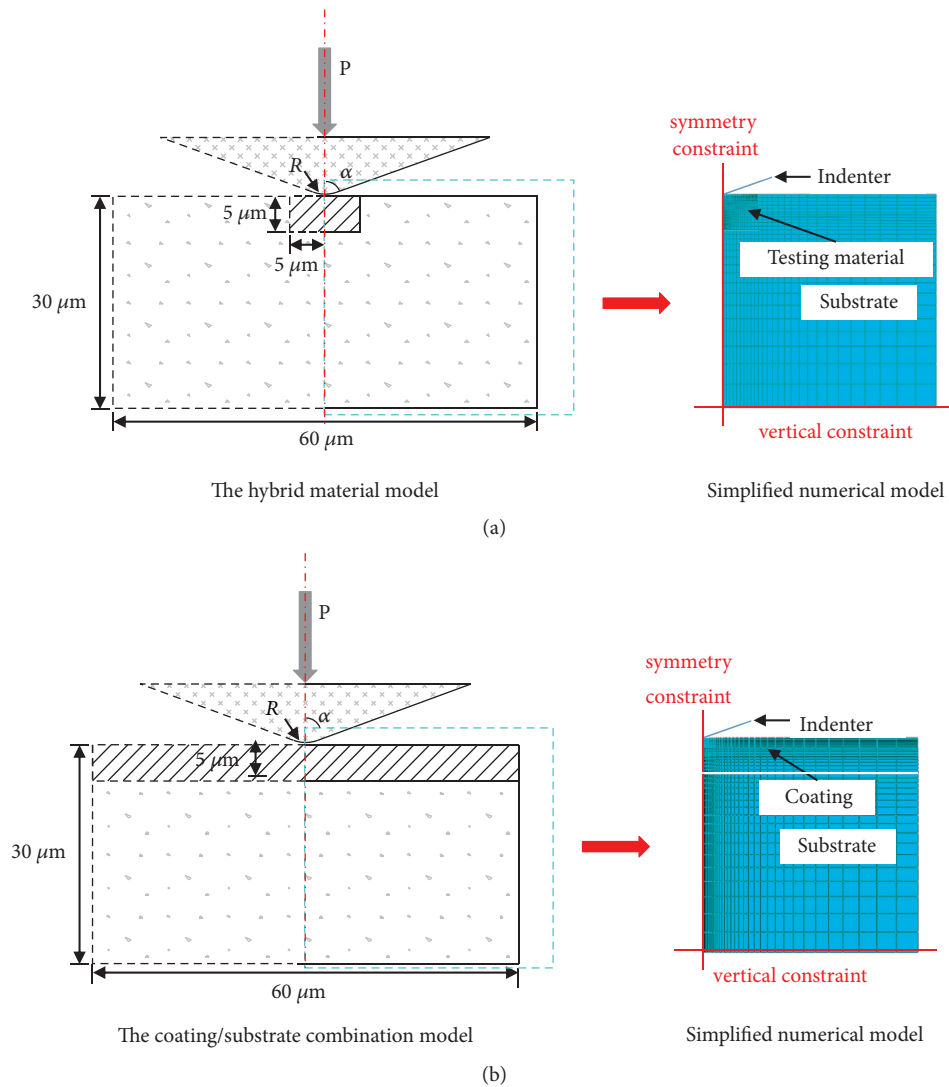


FIGURE 2: Numerical models used in the simulation. $R = 100\ \text{nm}$ and $\alpha = 70.3^\circ$.

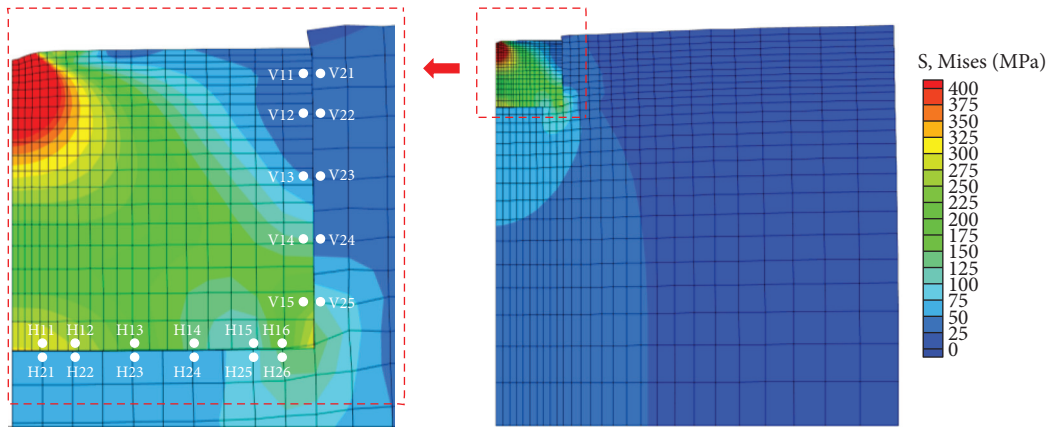
examine the effect of Poisson's ratio of the substrate on the NI experiment. h_{peak} and h_{residual} for eight cases are compared in Table 3, and the calculated curves of the force versus indentation depth are shown in Figure 6. The relationship between the indenter displacement and μ_s are shown in Figure 7.

It is obvious that with the increasing of μ_s , h_{peak} increases correspondingly. h_{peak} has grown from 204.594 nm to 207.138 nm, along with μ_s increasing from 0.05 to 0.4. The increment of 2.544 nm is much less compared with the variation induced by Young's modulus change.

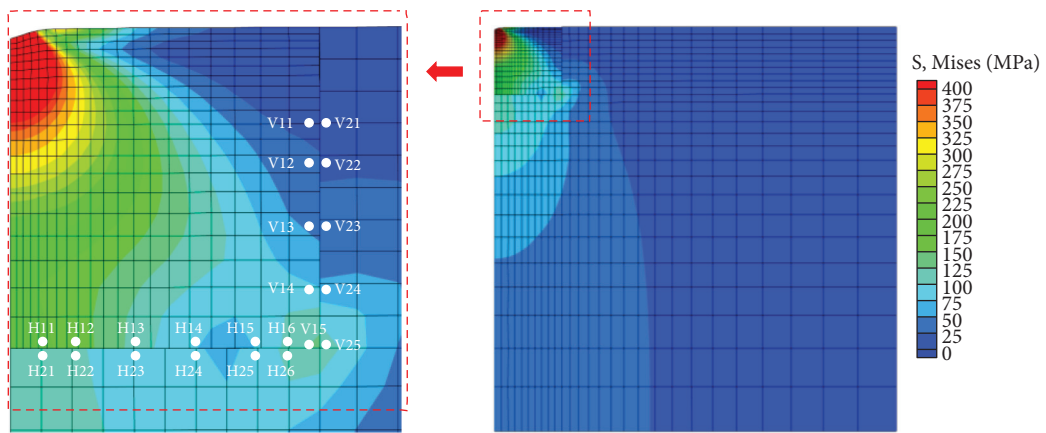
Compared to the positive correlation between μ_s and h_{peak} , the relationship of μ_s and h_{residual} is relatively complex.

When μ_s is less than 0.2, the h_{residual} increases along with μ_s increasing, and the growth rate is rather slow at the initial stage and then grows rapidly but finally slows down, whereas μ_s is bigger than 0.2, along with μ_s increasing; h_{residual} decreases slowly firstly, then the descent speed increases, and finally fluctuating rises. It is interesting that the maximum h_{residual} of eight cases is obtained when the substrate Poisson's ratio μ_s is equal to the testing material, 0.2 in this paper.

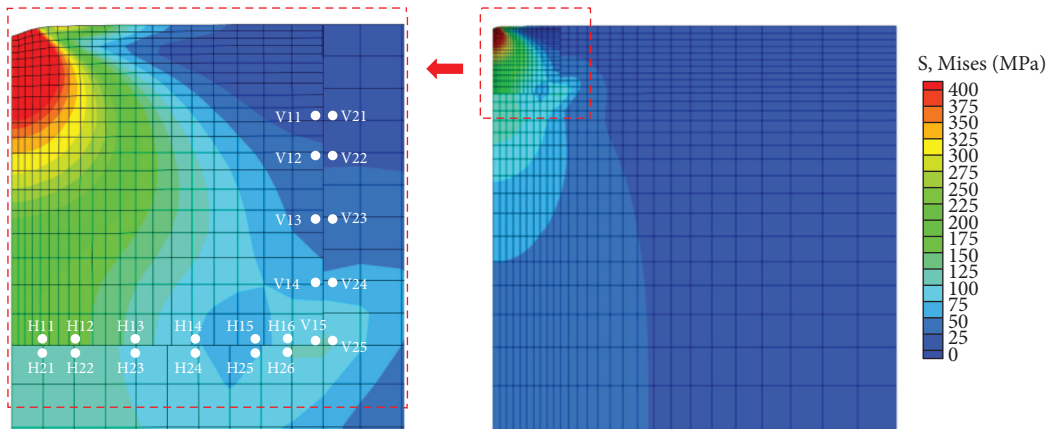
Based on the analysis above, it indicates that the sensitivity of the NI experiment results in the substrate Young's modulus E_s being much stronger than the substrate Poisson's ratio μ_s in the NI experiment. h_{residual} is much more influenced by the substrate Poisson's ratio E_s than h_{peak} .



Case a1: $E_s = 1 \text{ GPa}$, $\mu_s = 0.2$.



Case a14: $E_s = 50 \text{ GPa}$, $\mu_s = 0.2$.



Case a19: $E_s = 100 \text{ GPa}$, $\mu_s = 0.2$.

FIGURE 3: Mises stress distribution and monitor point positions of typical cases.

TABLE 4: Mises stress difference for interface.

| Case | Interface | Point 1 | Mises stress 1 (MPa) | Point 2 | Mises stress 2 (MPa) | Stress difference (MPa) |
|------|-----------------|---------|----------------------|---------|----------------------|-------------------------|
| a1 | Vertical face | V11 | 47.308 | V21 | 35.089 | 12.219 |
| | | V12 | 36.909 | V22 | 32.581 | 4.328↓ |
| | | V13 | 44.173 | V23 | 29.035 | 15.138↑ |
| | | V14 | 107.237 | V24 | 38.401 | 68.836 |
| | | V15 | 194.566 | V25 | 74.681 | 119.885 |
| | Horizontal face | H11 | 269.114 | H21 | 57.006 | 212.109 |
| | | H12 | 203.616 | H22 | 59.392 | 144.224 |
| | | H13 | 139.720 | H23 | 66.652 | 73.068 |
| | | H14 | 111.393 | H24 | 90.475 | 20.918 |
| | | H15 | 188.662 | H25 | 134.802 | 53.860↑ |
| a14 | Vertical face | V11 | 18.991 | V21 | 12.434 | 6.557 |
| | | V12 | 28.005 | V22 | 20.834 | 7.171 |
| | | V13 | 45.095 | V23 | 33.645 | 11.450 |
| | | V14 | 75.659 | V24 | 52.698 | 22.961 |
| | | V15 | 124.927 | V25 | 106.439 | 18.488↓ |
| | Horizontal face | H11 | 163.602 | H21 | 103.427 | 60.175 |
| | | H12 | 117.762 | H22 | 89.125 | 28.637 |
| | | H13 | 78.770 | H23 | 76.849 | 1.921 |
| | | H14 | 79.559 | H24 | 79.814 | -0.255 |
| | | H15 | 106.298 | H25 | 107.846 | -1.548 |
| a19 | Vertical face | V11 | 17.054 | V21 | 10.097 | 6.958 |
| | | V12 | 29.651 | V22 | 21.459 | 8.1924↑ |
| | | V13 | 42.620 | V23 | 36.959 | 5.661↓ |
| | | V14 | 61.786 | V24 | 54.905 | 6.881↑ |
| | | V15 | 97.813 | V25 | 98.184 | -0.371↓ |
| | Horizontal face | H11 | 159.945 | H21 | 113.038 | 46.907 |
| | | H12 | 115.197 | H22 | 94.686 | 20.511 |
| | | H13 | 75.231 | H23 | 76.929 | -1.698 |
| | | H14 | 70.179 | H24 | 75.810 | -5.631 |
| | | H15 | 85.837 | H25 | 100.116 | -14.279 |

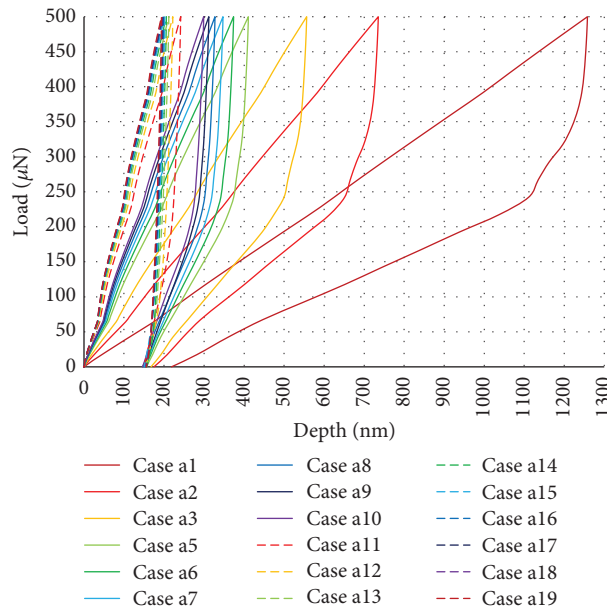


FIGURE 4: The load-depth curves of series 1.

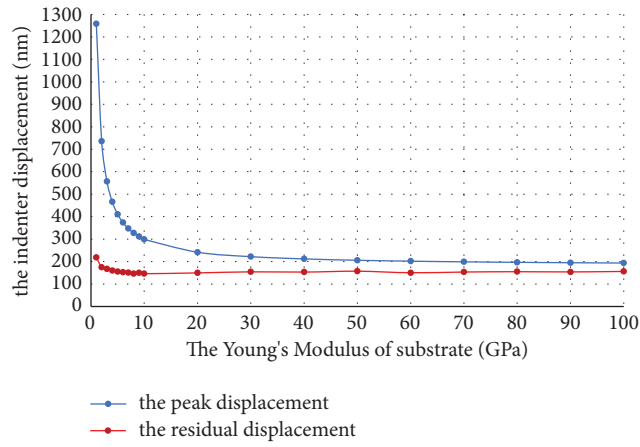


FIGURE 5: The relationship between displacement and E_s .

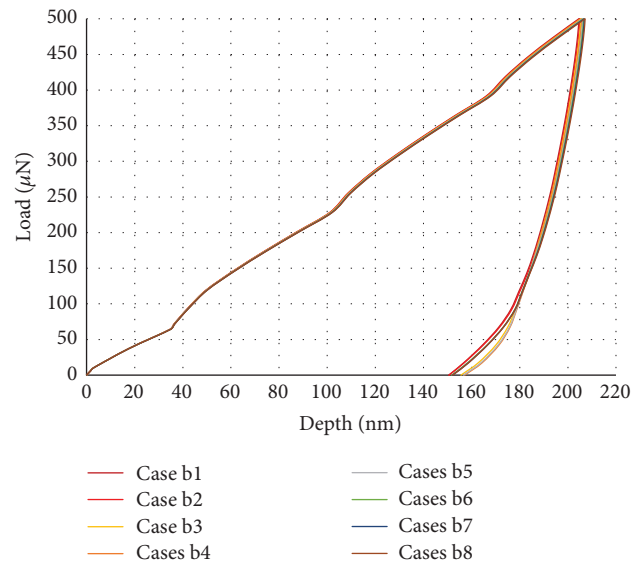


FIGURE 6: The load-depth curves of series 2.

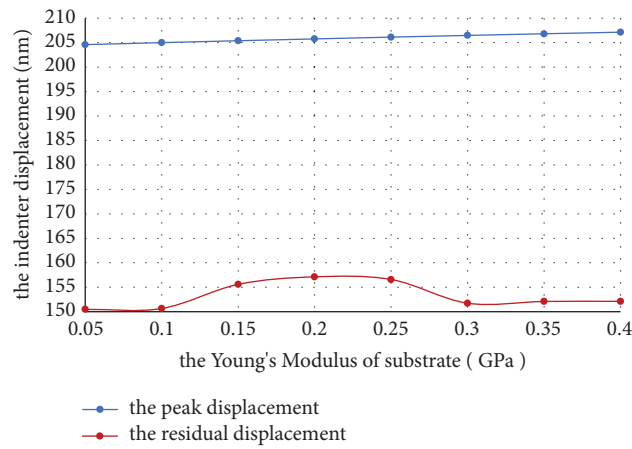


FIGURE 7: The relationship between displacement and μ_s .

5. Conclusion

In this paper, a NI experiment was introduced firstly; this experiment shows the substrate effect in the hybrid material. Then the series of numerical experiments were carried out to explore the substrate effect in the nano-indentation experiment of the hybrid material. The results shows that the numerical experiments present are consistent with experiments. The following are mainly conclusions obtained in this paper.

It was a clear difference of the NI experiment result between the coating/substrate combination and hybrid material under the same experiment condition. The difference is mainly derived from two factors: the lateral stiffness and the discontinuous face. In the coating/substrate model, the lateral stress is actually provided by the coating material in which the mechanical property is identical, whereas the substrate material offers the lateral boundary in the hybrid material model. When Young's modulus of substrate E_s is greater than the testing material, the boundary would be "harder," and the indenter displacement would be smaller correspondingly.

The influence of the discontinuous interface between the testing area and the substrate was also observed through the stress contour. The discontinuous face could distinctly weaken the stress transfer; that is, the Mises stress of the testing material is generally greater than the neighbor point in the substrate. The discontinuous face also causes stress concentration, which always occurs near the bottom corner of the testing material where two interfaces are intersected. Furthermore, the stress difference of the interface generally gradually decreases in the horizontal direction, whereas it fluctuates in the vertical direction, excluding the area of stress concentration.

Detailed parametric studies regarding Young's modulus E_s and Poisson's ratio μ_s of the substrate were conducted. Based on the results, Young's modulus of the substrate E_s has a substantial influence on the NI experiment. In general, the indenter peak displacement h_{peak} decreases with E_s increasing, but the decreasing rate is different. When E_s is small, less than 10 GPa in this paper, h_{peak} descends rapidly. When E_s further increases, h_{peak} curve gradually tends to flat.

As E_s is less than 8 GPa, the residual displacement h_{residual} decreases along with the substrate Young's modulus increasing, similar to h_{peak} , but reduced value is only 72.01 nm, which is far less than the h_{peak} change. As E_s further increased, the curve starts to increase in fluctuation, but the increment is very small.

It could be concluded that the NI experiment result is more sensitive to smaller E_s , including h_{peak} and h_{residual} .

Comparatively, Poisson's ration of substrate μ_s has less impact on the NI experiment. h_{peak} and h_{residual} only vary in 5 nm when μ_s increases from 0.05 to 0.4. By further analysis, h_{peak} is positively associated with μ_s , but there is no obvious correlation between h_{residual} and μ_s . The closer μ_s is to the testing materials, the greater h_{residual} is. When μ_s is equal to the testing materials, h_{residual} reaches its maximum value.

Data Availability

The data used in this study have been already posted in this paper.

Conflicts of Interest

The authors declare that there are no conflicts of interest regarding the publication of this study.

References

- [1] P. Zhan, J. Xu, J. Wang, and C. Jiang, "Multi-scale study on synergistic effect of cement replacement by metakaolin and typical supplementary cementitious materials on properties of ultra-high performance concrete," *Construction and Building Materials*, vol. 307, Article ID 125082, 2021.
- [2] F. M. Borodich, L. M. Keer, and C. S. Korach, "Analytical study of fundamental nanoindentation test relations for indenters of non-ideal shapes," *Nanotechnology*, vol. 14, no. 7, pp. 803–808, 2003.
- [3] J. Chen and S. J. Bull, "On the factors affecting the critical indenter penetration for measurement of coating hardness," *Vacuum*, vol. 83, no. 6, pp. 911–920, 2009.
- [4] Y. H. Lee, J. H. Hahn, S. H. Nahm, J. I. Jang, and D. Kwon, "Investigations on indentation size effects using a pile-up corrected hardness," *Journal of Physics D: Applied Physics*, vol. 41, no. 7, Article ID 074027, 2008.
- [5] M. Zhao, X. Chen, N. Ogasawara et al., "New sharp indentation method of measuring the elastic-plastic properties of compliant and soft materials using the substrate effect," *Journal of Materials Research*, vol. 21, no. 12, pp. 3134–3151, 2006.
- [6] J. Xu, D. J. Corr, and S. P. Shah, "Nanomechanical investigation of the effects of nanoSiO₂ on C-S-H gel/cement grain interfaces," *Cement and Concrete Composites*, vol. 61, pp. 7–17, 2015.
- [7] J. Xu, B. Wang, and J. Zuo, "Modification effects of nanosilica on the interfacial transition zone in concrete: a multiscale approach," *Cement and Concrete Composites*, vol. 81, pp. 1–10, 2017.
- [8] J. Xu, Y. Tang, X. Wang, Z. Wang, and W. Yao, "Application of ureolysis-based microbial CaCO₃ precipitation in self-healing of concrete and inhibition of reinforcement corrosion," *Construction and Building Materials*, vol. 265, Article ID 120364, 2020.
- [9] X. Wu, S. S. Amin, and T. T. Xu, "Substrate effect on the Young's modulus measurement of TiO₂ nanoribbons by nanoindentation," *Journal of Materials Research*, vol. 25, no. 5, pp. 935–942, 2010.
- [10] M. Zhao, X. Chen, Y. Xiang et al., "Measuring elastoplastic properties of thin films on an elastic substrate using sharp indentation," *Acta Materialia*, vol. 55, no. 18, pp. 6260–6274, 2007.
- [11] Y. Liao, Y. Zhou, Y. Huang, and L. Jiang, "Measuring elastic-plastic properties of thin films on elastic-plastic substrates by sharp indentation," *Mechanics of Materials*, vol. 41, no. 3, pp. 308–318, 2009.
- [12] M. N. Zulkifli, A. Jalar, S. Abdullah, I. A. Rahman, and N. K. Othman, "Effect of applied load in the nanoindentation

- of gold ball bonds,” *Journal of Electronic Materials*, vol. 42, no. 6, pp. 1063–1072, 2013.
- [13] T. Csanádi, D. Németh, and F. Lofaj, “Mechanical properties of hard W-C coating on steel substrate deduced from nanoindentation and finite element modeling,” *Experimental Mechanics*, vol. 57, no. 7, pp. 1057–1069, 2017.
- [14] N. Fujisawa, T. F. Zhang, O. L. Li, and K. H. Kim, “Substrate-independent stress-strain behavior of diamond-like carbon thin films by nanoindentation with a spherical tip,” *Journal of Materials Research*, vol. 33, no. 6, pp. 699–708, 2018.
- [15] C. Gamonpilas and E. P. Busso, “On the effect of substrate properties on the indentation behaviour of coated systems,” *Materials Science and Engineering: A*, vol. 380, no. 1-2, pp. 52–61, 2004.
- [16] R. Saha and W. D. Nix, “Effects of the substrate on the determination of thin film mechanical properties by nanoindentation,” *Acta Materialia*, vol. 50, no. 1, pp. 23–38, 2002.
- [17] X. Xing, Y. Wang, G. Xiao, X. Shu, S. Yu, and Y. Wu, “Identifying the elastoplastic properties of ductile film on hard substrate by nanoindentation,” *Vacuum*, vol. 189, Article ID 110252, 2021.
- [18] I. A. Lyashenko and V. L. Popov, “The effect of contact duration and indentation depth on adhesion strength: experiment and numerical simulation,” *Technical Physics*, vol. 65, no. 10, pp. 1695–1707, 2020.
- [19] W.-G. Jiang, J.-J. Su, and X.-Q. Feng, “Effect of surface roughness on nanoindentation test of thin films,” *Engineering Fracture Mechanics*, vol. 75, no. 17, pp. 4965–4972, 2008.
- [20] M. Li, H.-X. Zhang, Z.-L. Zhao, and X.-Q. Feng, “Surface effects on cylindrical indentation of a soft layer on a rigid substrate,” *Acta Mechanica Sinica*, vol. 36, no. 2, pp. 422–429, 2020.
- [21] J. Malzbender, G. de With, and J. den Toonder, “The P-h² relationship in indentation,” *Journal of Materials Research*, vol. 15, no. 5, pp. 1209–1212, 2000.
- [22] J. Malzbender and G. de With, “Indentation load-displacement curve, plastic deformation, and energy,” *Journal of Materials Research*, vol. 17, no. 2, pp. 502–511, 2002.
- [23] L. Min, C. Wei-min, L. Nai-gang, and W. Ling-Dong, “A numerical study of indentation using indenters of different geometry,” *Journal of Materials Research*, vol. 19, no. 1, pp. 73–78, 2004.
- [24] F. Lofaj and D. Németh, “The effects of tip sharpness and coating thickness on nanoindentation measurements in hard coatings on softer substrates by FEM,” *Thin Solid Films*, vol. 644, pp. 173–181, 2017.

Research Article

Surrounding Rock Stability Classification Method of Coal Roadway Based on In Situ Stress

Yongjie Yang , Gang Huang , and Lingren Meng

State Key Laboratory of Mining Disaster Prevention and Control Co-Founded by Shandong Province and the Ministry of Science and Technology, Shandong University of Science and Technology, Qingdao 266590, China

Correspondence should be addressed to Gang Huang; huanggang@sdust.edu.cn

Received 20 October 2021; Accepted 26 November 2021; Published 15 December 2021

Academic Editor: Gaofeng Song

Copyright © 2021 Yongjie Yang et al. This is an open access article distributed under the Creative Commons Attribution License, which permits unrestricted use, distribution, and reproduction in any medium, provided the original work is properly cited.

In situ stress is one of the most important factors affecting surrounding rock stability classification of coal roadway. Most surrounding rock stability classification methods do not fully consider the influence of in situ stress. In this paper, the author applied a fuzzy clustering method to the classification of surrounding rock stability of coal roadway. Taking into account the complexity of the classification of surrounding rock, some factors such as the strength of surrounding rock, in situ stress, the main roof first weighting interval, the size of the chain pillar, and the immediate roof backfilled ratio are selected as the evaluation indexes. The weight coefficients of these evaluation indexes are determined by unary regression and multiple regression methods. Using fuzzy clustering and empirical evaluation method, the classification model of surrounding rock stability of coal roadway is proposed, which is applied to 37 coal roadways of Zibo Mining Group Ltd., China. The result is in good agreement with practical situation of surrounding rock, which proves that the fuzzy clustering method used to classify the surrounding rock in coal roadway is reasonable and effective. The present model has important guiding significance for reasonably determining the stability category of surrounding rock and supporting design of coal roadway.

1. Introduction

Coal mines are dominated by underground mining in China. The total length of new driving roadways in coal mines is up to thousands of kilometres per year in China, of which more than 80% are coal roadways and coal-rock roadways [1]. After excavation, if there is no timely support, surrounding rock of coal roadway is likely to instable failure. Due to the complexity of mining activities, the design of the support for the coal roadway must be based more on the evaluation and classification of the stability of the surrounding rock stability. As a basis for the control of the surrounding rock on the roadway, the stability of the evaluation of the surrounding rock stability has been widely studied by scholars.

It is of great significance to determine a simple and accurate method for classifying surrounding rock; many classification methods for surrounding rock have been proposed, including single factor classification (RQD [2–4])

and multifactor classification (RMR [5, 6], GSI [7], and Q-system [8, 9]). In recent years, the most widely studied classification methods are based on fuzzy mathematics, analytic hierarchy process (AHP), artificial neural networks (ANN), and support vector machines (SVM), etc. Shi et al. [10] adopted comprehensive assigning method to determine the weights of evaluation indexes based on fuzzy analytic hierarchy process (FAHP), and the FAHP model is established for optimized classification of surround rock. Hasegawa et al. [11] used ANN to classify the surrounding rock of mountain tunnels by collecting geophysical datasets at a tunnel face and surrounding rock, but complete surrounding rock data were difficult to obtain. Deng et al. [12] established a BP-ANN classification model for surrounding rock stability of coal roadway in MATLAB environment and applied the model to 13 coal roadway data samples for testing. Li et al. [13] established a highway tunnel classification model based on the SVM theory of particle swarm optimization, and the surrounding rock mass of the tunnel

was divided into five grades. Zheng et al. [14] presented a new reliability rock mass classification method based on a least squares support vector machine (LSSVM) optimized by a bacterial foraging optimization algorithm (BFOA), which can improve the classification accuracy of surrounding rock exhibiting randomness. Furthermore, Wang et al. [15] applied the ideal point method to the classification of surrounding rock stability and considered the influence of groundwater of the tunnel surrounding rock. Wang et al. [16] proposed a novel model to analyse the surrounding rock stability based on set pair analysis (SPA). Based on uncertainty measure theory, He et al. [17] established a stability classification and order-arranging model of surrounding rock. Based on D-S evidence theory and error-eliminating theory, Wu et al. [18] proposed a model for evaluation of underground engineering surrounding rock stability and used four kinds of weighting methods to avoid the difference of single weighting method in calculating index weight.

Although these methods have enabled numerous achievements in the classification of surrounding rock, some shortcomings still exist. In dealing with uncertain problems, the analytic hierarchy process is greatly affected by personal subjective factors, it is difficult to artificial neural networks to find suitable learning algorithms, and support vector machines are inefficient when processing a large number of samples. The stability of the surrounding rock of the roadway is a complex problem that is affected by many factors, and the influence of various factors on the stability of the surrounding rock has a considerable degree of randomness and fuzziness, so the boundary between the stability categories of the surrounding rock is often not clear. Since the classification of the stability on the surrounding rock of the roadway is a fuzzy concept, it is quite effective to choose fuzzy clustering when dealing with the classification of the stability of the surrounding rock on the roadway, which has many influencing factors and strong ambiguity.

In the selection of classification evaluation indexes, most classification methods consider the influence of rock mass structure, the degree of development of joints and cracks, and their properties on the stability of surrounding rock, but it is difficult to determine parameters such as the degree of joints and cracks on-site, and the operability is poor. When considering the influence of in situ stress on the stability classification of surrounding rock, the depth of the roadway is mostly used to represent the influence of in situ stress, or according to the relationship between the weight of the overlying strata and the strength of the rock mass [19, 20], the in situ stress is divided into high stress zone and low stress zone, and then a stress state influence correction factor is considered. Some researchers consider the influence of the initial in situ stress and use a converted in situ stress to represent the initial. The converted stress is only an average of the three principal stresses. The value does not consider the influence of the angle between the horizontal in situ stress and the direction of the roadway on the stability of the surrounding rock. The application of initial in situ stress in the surrounding rock stability classification of roadway is not reasonable and complete; in particular there is no effective method to determine the magnitude and direction of

vertical and maximum (or minimum) horizontal in situ stress near the roadway. In particular, the influence of horizontal in situ stress on the stability of the surrounding rock of the roadway should be studied. When the long axis direction of roadway is parallel to the maximum horizontal in situ stress, the influence is the smallest, which is the most favorable for the stability of roof and floor. When the long axis direction of roadway is perpendicular to the maximum horizontal in situ stress, it is most unfavorable to the stability of roof and floor. In the roadway oblique to the maximum horizontal principal stress at a certain angle, the stress concentration occurs on one rib of the roadway and the stress release occurs on the other rib, so the deformation and failure of the roof (or floor) will be biased towards one rib of the roadway.

It can be seen from the above analysis that the influence of in situ stress on the stability of the surrounding rock of the roadway must be considered, especially the influence of the horizontal in situ stress on the stability of the surrounding rock of the coal roadway. Combined with the fuzzy clustering, the author proposes a SIM-based classification method for surrounding rock stability of coal roadway: SIM, i.e., the strength of surrounding rock, in situ stress, and mining indexes. This method uses site monitoring or laboratory tests to determine the values of evaluation indexes, and the weights of each evaluation index are determined by regression analysis and fitting methods, which are more reliable and accurate. Furthermore, the fuzzy clustering is adopted to classify the coal roadways to determine the surrounding rock grade.

2. Determination of the Evaluation Indexes of the Surrounding Rock Stability in Coal Roadway

The stability of the surrounding rock of a coal roadway depends on the internal stress, the physical and mechanical properties, and the interaction between the two. The internal stress of the surrounding rock depends on the in situ stress, the shape and size of the roadway, the influence of excavation and mining, the support strategy, and others. The physical and mechanical properties of the surrounding rock refer to the strength and physical characteristics of the surrounding rock, including the physical and mechanical parameters of the roof, floor, and rib, and the parameters of the rock blocks, the structure of the rock mass, and the bedding joints and fractures. In addition, the influence of groundwater and time must also be considered. The main factors that affect the stability of the surrounding rock on the coal roadway are shown in Table 1.

The surrounding rock stability classification of coal roadway is supposed to be based on the characteristics of sedimentary rock (and local igneous rock) in coal mine, which requires clear physical meaning of evaluation index, easy access to parameters, simple classification method, and strong practicability. Therefore, the biggest factors affecting the stability of the roadway surrounding rock in Table 1 are screened out, and the factors that have no significant effect

TABLE 1: The factors affecting surrounding rock stability of coal roadway.

| No. | Type | Factor |
|-----|--------------------------------------|---------------------------------------|
| 1 | Strength | Strength of main roof |
| 2 | | Strength of immediate roof |
| 3 | | Strength of coal seam |
| 4 | | Strength of immediate floor |
| 5 | In situ stress | Coal mining method |
| 6 | | Magnitude |
| 7 | Roadway characteristics | Angle |
| 8 | | Width of coal pillar in roadway |
| 9 | Coal seam geological characteristics | Height |
| 10 | | Width |
| 11 | | Buried depth |
| 12 | | Thickness |
| 13 | Thickness of roof and floor | Dip angle |
| 14 | | Buried depth |
| 15 | Abutment pressure characteristics | Main roof |
| 16 | | Immediate roof |
| 17 | | Immediate floor |
| 18 | Groundwater | Immediate roof first caving interval |
| 19 | | Main roof first weighting interval |
| 20 | | Main roof periodic weighting interval |
| 21 | Time | |
| 22 | | |

on the stability are ignored. The initial selected evaluation indexes include the comprehensive strength of surrounding rock, in situ stress, the immediate roof backfilled ratio, the main roof first weighting interval, and the chain pillar size of coal roadway. Among them, the comprehensive strength of surrounding rock is divided into the strength of roof, floor, and rib. In situ stress is divided into vertical and horizontal in situ stress. The immediate roof backfilled ratio, the main roof first weighting interval, and the chain pillar size of coal roadway are called mining index.

2.1. Comprehensive Strength of Surrounding Rock. The surrounding rock of the roadway includes the roof, floor, and rib, and the roof includes the immediate roof and the main roof, and under some conditions there is a false roof, and the floor includes the immediate floor and the main floor. For the coal roadway, the ribs are coal seam, but when the coal seam is thin, the ribs also cover part of the rock strata. To reasonably characterize the strength of surrounding rock, the concept of comprehensive strength of surrounding rock is proposed, which covers the comprehensive strength of the roof, floor, and rib. The thickness of each rock stratum, the thickness of the coal seam, and the strength of the coal and rock in each stratum are comprehensively considered. When calculating the comprehensive strength of surrounding rock, the strength of rock block is determined first, then the strength of rock mass is calculated, and finally the comprehensive strength is calculated. Since the strength of the rock block can usually be obtained directly through the laboratory test, the calculation of the rock mass strength and the comprehensive strength is introduced only introduced in the following.

The strength and the structural parameters of the rock mass (i.e., layered thickness, joint fracture spacing, etc.) are considered when calculating the rock mass strength. The

rock mass strength is obtained from laboratory experiments, while the structural parameters of the rock mass can be expressed by the rock mass strength coefficient K_{rm} (equation (1)) [21].

$$K_{rm} = \frac{R_{rm}}{R_{rb}}, \quad (1)$$

where R_{rm} represents the uniaxial compressive strength of the rock mass, MPa. R_{rb} represents the uniaxial compressive strength of rock block, MPa.

Therefore, it is easy to obtain the rock mass strength when the rock block strength and the rock mass strength coefficient are known. Owing to the influence of the thickness, structure, bedding, joint, and fracture spacing of the rock mass, the parameters of the rock mass strength index are difficult to obtain, so it is difficult to apply on site. He et al. [22–24] proposed an improved discontinuous deformation analysis (DDARF) method to achieve the simulation of the joint distribution by performing a numerical simulation of the deformation and fracture processes of the surrounding rock. However, this method requires special petrographic measurement techniques and image processing methods. Therefore, a method to estimate the rock mass strength index based on the stratigraphy column is proposed, which is corrected by numerical simulation and on-site testing, so that the rock mass strength index is more accurate and convenient to use. According to the characteristics of the description of the rock mass structure characteristics in the stratigraphy column, the weight of each factor (degree of joint fracture, bedding, filling, and cementation) is determined using the analytic hierarchy process (equation (2)), so the rock mass strength index can be obtained.

$$K_{rm} = \alpha J_n + \beta B_n + \gamma J_f, \quad (2)$$

where K_{rm} is the rock mass strength coefficient. J_n is the development degree of joints. B_n is the development degree of beddings. J_f is the development degree of cemented filling. α is the weight of joints. β is the weight of beddings. γ is the weight of cemented filling.

After determining the rock strength of each rock strata, the comprehensive strength of surrounding rock of roadway can be calculated by weighted average (equation (3)) according to rock thickness. The comprehensive strength of the roof is weighted average according to the strength of each rock strata in the range of two times the height of the roadway, the floor is weighted average in the range of one time the height of the roadway, and the comprehensive strength of the rib is weighted average according to the strength of each coal and rock strata in the height of the roadway.

$$R = \frac{\sum_{i=1}^n M_i \cdot r_i}{\sum_{i=1}^n M_i}, \quad (3)$$

where R represents the comprehensive strength of the surrounding rock. M_i represents the thickness of the i -th layer of surrounding rock. r_i represents the rock strength of the i -th layer of surrounding rock.

2.2. In Situ Stress Index. The initial in situ stress is the main factor to be considered in the classification of the stability of the surrounding rock of the roadway. However, due to the large workload of in situ stress measurement, high technical requirements, and high testing costs, only a limited number of representative locations can be selected for testing according to the geological structure characteristics of the mine area, and it is difficult to infer the magnitude and direction of the in situ stress near each roadway from the data of a limited number of in situ stress measurement points in the mine area.

Therefore, based on the results of many initial in situ stress measurements, the relationship between the buried depth of the measuring point and the vertical in situ stress and the maximum (minimum) horizontal in situ stress is established (Figure 1), so that the magnitude of the three initial in situ stresses can be preliminarily determined from the buried depth. Then according to the measured in situ stress, combined with the geological structure and movement law of the mine, determine the horizontal in situ stress direction, and then consider the angle between the horizontal in situ stress and the long axis direction and the buried depth of the roadway to determine the vertical and horizontal in situ stress. The classification results of surrounding rock stability are more scientific and reliable by considering vertical stress and horizontal stress of rib in roadway classification.

According to the relevant knowledge of geology, the direction of horizontal in situ stress is relatively stable in a large tectonic area. Therefore, the maximum and minimum horizontal in situ stress directions at various stress measurement points can be used to indicate the direction of the maximum and minimum horizontal in situ stresses of the nearby roadway. Then, according to the direction of

the angle between the roadway heading direction and the horizontal stress direction, the horizontal stress of the rib of roadway can be calculated.

2.3. Mining Index. For the roadway, it will inevitably be affected by the abutment pressure produced by the mining of the coal face, and in some cases, mining activity is the main factor that affects the stability of the surrounding rock of the roadway. The width of the coal pillar of the roadway, the main roof first weighting interval, and immediate roof backfilled ratio are selected as the main factors affecting the mining and at the same time as the evaluation indexes of the stability of the surrounding rock of the roadway.

2.3.1. The Chain Pillar of the Roadway. Depending on the width of the chain pillar and the layout of the roadway, the chain pillar can be divided into four categories: the gob-side entry retained coal pillar, the gob-side entry coal pillar, the wide coal pillar, and the strip coal pillar [25, 26]. Because the working face of 37 sample entries is mostly coal mining under buildings, strip-mining stopping is used. The chain pillars are mostly strip coal pillars, so gob-side retained entry (and gob-side entry) is rarely used, and statistical laws cannot be formed. Therefore, in the working face of gob-side retained entry (and gob-side entry), the surrounding rock category is degraded by 1-2 categories.

2.3.2. The Immediate Roof Backfilled Ratio N . The immediate roof backfilled ratio N reflects the filling degree of gob after immediate roof breaking. The larger the immediate roof backfilled ratio is, the smaller the subsidence of the main roof is, and the slower the stope abutment pressure appears, and on the contrary, the stronger the stope abutment pressure appears. Therefore, it is selected as one of the classification indexes of roadway surrounding rock stability.

2.3.3. The Main Roof First Weighting Interval C_0 . The main roof first weighting interval C_0 reflects the intensity of the abutment pressure behaviour of the stope. The larger the main roof first weighting interval is, the stronger the abutment pressure behaviour of the stope is, and the greater the impact on the stability of the surrounding rock of the roadway is. In contrast, the smaller the main roof first weighting interval is, the weaker the abutment pressure behaviour of the stope is, and the less obvious the impact on the stability of the surrounding rock of the roadway is.

3. Determination of the Weight of the Classification Index

The surface displacement of surrounding rock is one of the important factors to reflect the stability, which includes roof-to-floor displacement and rib-to-rib displacement. In order to eliminate the influence of roadway size, the author uses the displacement convergence to reflect the surrounding rock stability, which also includes the roof-to-floor and rib-to-rib displacement convergence. The eight surrounding

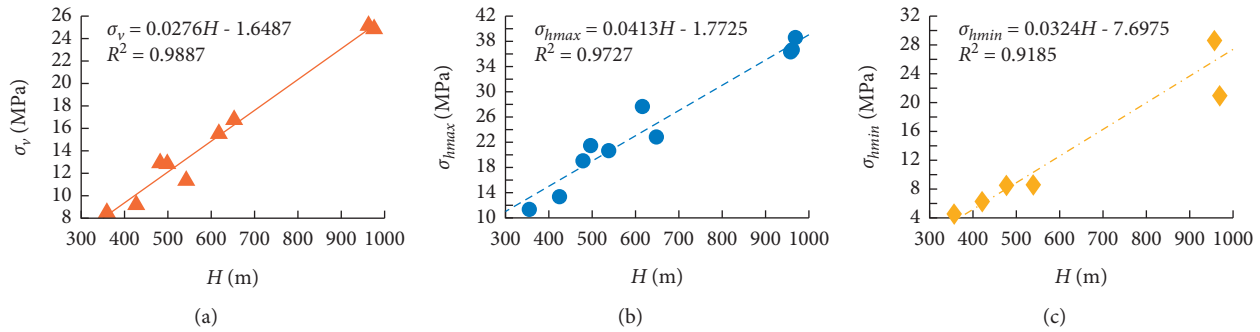


FIGURE 1: Statistical relationship between in situ stress and buried depth.

rock stability evaluation indexes have different degrees of influence on the overall stability. There are primary and secondary distinctions. Because the evaluation index of chain pillar type cannot be characterized by numerical value, when determining the influence of this index on the surrounding rock stability, the strength of surrounding rock should be degraded (or not degraded) according to the chain pillar type and then classified according to the strength of surrounding rock after change. Therefore, only the weights of the remaining seven indicators need to be determined. According to the statistical data of on-site ground pressure of roadway, the regression analysis of each classification index is carried out by using the unary nonlinear regression method, and the relationship curve between each evaluation index and the roof-to-floor (rib-to-rib) displacement convergence is obtained, so as to determine the quantitative relationship between each evaluation index and the surrounding rock stability.

3.1. Unary Regression. The deformation of the roadway during the roadway excavation is affected by the physical and mechanical properties of the surrounding rock, the magnitude of the in situ stress, the shape and size of the roadway section, the excavation technology, and support scheme, but it is not affected by mining. Firstly, the functional relationship between the displacement convergence in surrounding rock of roadway and each index during excavating is established, and then the relationship between the displacement convergence in surrounding rock of roadway and each index during the mining is established.

3.1.1. The Functional Relationship between the Displacement Convergence in Surrounding Rock of Roadway and Each Index during Excavating

- (1) The functional relationship between the displacement convergence in surrounding rock of roadway and the comprehensive strength of surrounding rock during excavating:

According to field measured data and nonlinear regression, the relationship between the roof-to-floor

convergence (rib-to-rib convergence) of roadway and the comprehensive strength of surrounding rock is established, as shown in Figure 2.

ε_v represents the roof-to-floor displacement convergence of the roadway. ε_h represents the rib-to-rib displacement convergence of the roadway. R_{rz} represents the comprehensive strength of the roof, MPa. b_{rz} represents the comprehensive strength of rib, MPa. R_{rz} represents the comprehensive strength of the floor, MPa. σ_v represents the vertical in situ stress, MPa. σ_h represents the horizontal in situ stress, MPa.

- (2) The functional relationship between the displacement convergence in surrounding rock of roadway and the in situ stress during excavating

Based on field measurement, the relationship between the displacement convergence in surrounding rock of roadway and the in situ stress is established, as shown in Figures 3 and 4.

3.1.2. The Functional Relationship between the Convergence in Surrounding Rock of Roadway and Each Index during Mining

The surrounding rock of the roadway is affected by the front abutment pressure caused by mining. The confining pressure of roadway increases which exceeds the deformation of the roadway during excavating. Similarly, based on field measurement, unary regression is used to establish the relationship between the displacement convergence in surrounding rock of the roadway and each index; the result is shown in Table 2.

3.2. Multiple Regression. The deformation of the roadway is composed of the deformation during excavation and during mining, so the total deformation of the roadway is the sum of these two deformations, and the total displacement convergence in surrounding of roadway is also the sum of these two displacement convergences.

Therefore, the fitting equation for the roof-to-floor displacement convergence of the roadway is obtained as follows:

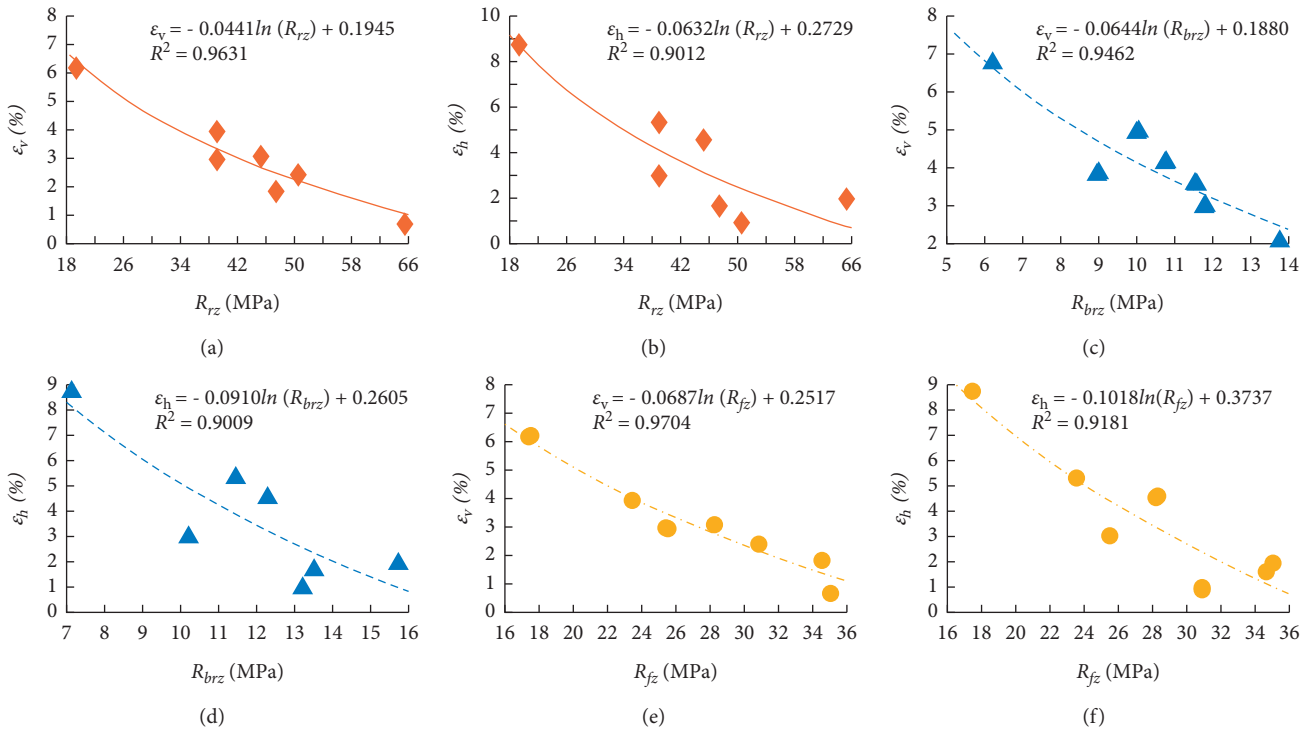


FIGURE 2: Statistical relationship between comprehensive strength and displacement convergence of coal roadway.

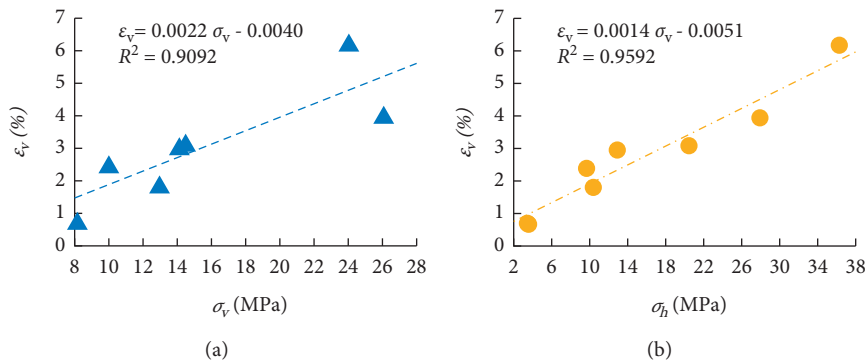


FIGURE 3: Statistical relationship between in situ stress and roof-to-floor displacement convergence of roadway.

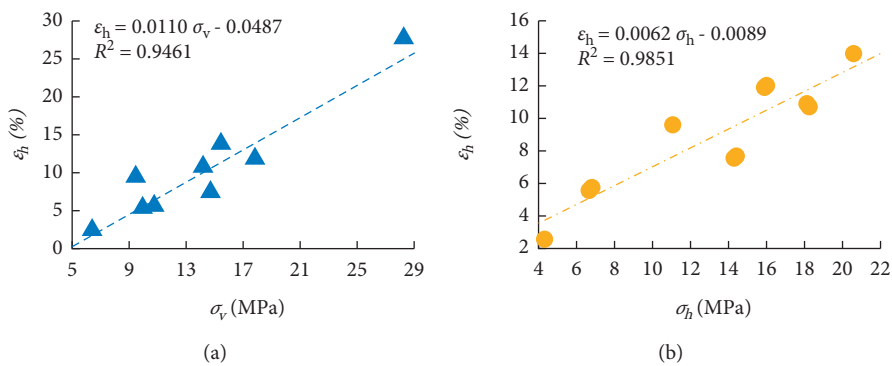


FIGURE 4: Statistical relationship between in situ stress and rib-to-rib displacement convergence of roadway.

TABLE 2: Fitting equations between each index and displacement convergence of the coal roadway.

| Displacement convergence | Classification index | Fitting relation | Correlation coefficient |
|--------------------------|----------------------|---|-------------------------|
| ε_v | R_{rz} | $\varepsilon_v = -0.12 \ln(R_{rz}) + 0.49$ | $R^2 = 0.93$ |
| | R_{brz} | $\varepsilon_v = -0.13 \ln(R_{brz}) + 0.40$ | $R^2 = 0.95$ |
| | R_{fz} | $\varepsilon_v = -0.09 \ln(R_{fz}) + 0.39$ | $R^2 = 0.91$ |
| | σ_v | $\varepsilon_v = 0.01\sigma_v - 0.01$ | $R^2 = 0.95$ |
| | σ_h | $\varepsilon_v = 0.01\sigma_h + 0.02$ | $R^2 = 0.91$ |
| | N | $\varepsilon_v = 0.05N + 0.04$ | $R^2 = 0.90$ |
| | C_0 | $\varepsilon_v = -0.19 \ln(C_0) + 0.04$ | $R^2 = 0.92$ |
| ε_h | R_{rz} | $\varepsilon_h = -0.15 \ln(R_{rz}) + 0.60$ | $R^2 = 0.90$ |
| | R_{brz} | $\varepsilon_h = -0.17 \ln(R_{brz}) + 0.51$ | $R^2 = 0.94$ |
| | R_{fz} | $\varepsilon_h = -0.13 \ln(R_{fz}) + 0.51$ | $R^2 = 0.91$ |
| | σ_v | $\varepsilon_h = 0.01\sigma_v - 0.05$ | $R^2 = 0.92$ |
| | σ_h | $\varepsilon_h = 0.01\sigma_h + 0.01$ | $R^2 = 0.93$ |
| | N | $\varepsilon_v = 0.06N + 0.04$ | $R^2 = 0.90$ |
| | C_0 | $\varepsilon_v = -0.20 \ln(C_0) + 0.76$ | $R^2 = 0.93$ |

N represents the immediate roof backfilled ratio. C_0 represents the main roof first weighting interval.

$$\begin{aligned} \varepsilon_v = & -0.12 \ln(R_{rz}) + 0.02 \ln(R_{brz}) - 0.09 \ln(R_{fz}) \\ & + 0.01\sigma_h - 0.01\sigma_v - 0.14 \ln(C_0) - 0.03N + 1.28. \end{aligned} \quad (4)$$

Similarly, the fitting formula of rib-to-rib displacement convergence of roadway is obtained as follows:

$$\begin{aligned} \varepsilon_h = & -0.02 \ln(R_{rz}) + 0.10 \ln(R_{brz}) - 0.08 \ln(R_{fz}) \\ & + 0.02\sigma_h - 0.01\sigma_v - 0.06 \ln(C_0) - 0.02N + 0.30. \end{aligned} \quad (5)$$

With the fitting equation of displacement convergence in surrounding rock of roadway, it is possible to predict the deformation of the surrounding rock of roadway based on the comprehensive strength of surrounding rock, in situ stress, the immediate roof backfilled ratio, and the main roof first weighting interval, combined with the size of roadway.

4. Surrounding Rock Stability Classification of Coal Roadway Based on Fuzzy Clustering

4.1. Determination of the Optimal Classification Number. The fuzzy clustering process of surrounding rock stability classification is shown in Figure 5. After fuzzy clustering, it is necessary to determine the optimal number of coal roadway classification.

Transforming each classification index into a comprehensive index according to the weight is expressed by the displacement convergence of surrounding rock. According to the basic principle of fuzzy clustering [26], with the different values of λ , the classification results are also different; the optimal classification results can be selected according to F -statistics. The calculation formula of F -statistics is

$$F = \frac{\sum_{i=1}^r (\bar{y}_{i0} - \bar{y}_{00})^2 / (r-1)}{\sum_{i=1}^r \sum_{j=1}^n (y_{ij} - \bar{y}_{i0})^2 / (n-r)}. \quad (6)$$

For the fuzzy clustering process, when the classification result changes from 2 to 12, each F value and its $F_{0.05}$ value (under 0.05 confidence) level are shown in Tables 3 and 4. According to mathematical statistics analysis, if $F > F_{0.05}$, the difference between classes is significant; that is, the classification result is reasonable.

It can be seen in Tables 3 and 4 that when $\lambda = 0.75$, $F - F_{0.05}$ is the maximum of all classifications, so the fuzzy clustering result of $\lambda = 0.75$ is the best; that is, the coal seam roadway samples are clustered into four categories.

4.2. Surrounding Rock Stability Classification Results of Coal Roadway. Based on the results of fuzzy cluster analysis and empirical evaluation, the surrounding rock of 37 coal roadways is divided into four categories, which are very stable (I), relatively stable (II), medium stable (III), and unstable (IV). The displacement convergence in surrounding rock of each type of roadway is predicted, and the final classification results of surrounding rock stability are shown in Table 5.

4.3. Field Application: Taking Class IV Surrounding Rock for Example. According to the SIM surrounding rock stability classification results of the above 37-roadway sample data, the No.3302 roadway with typical geological and mining conditions was selected for the industrial test in the class IV unstable surrounding rock, and the support effect of the No.2306 roadway under similar geological conditions was compared to verify the rationality of the SIM surrounding rock stability classification results based on the in situ stress.

According to the geological conditions of the roadway No.3302, through laboratory test and field test, the results of each evaluation index determination are shown in Table 6.

According to the results of the SIM surrounding rock stability classification (Table 5), the surrounding rock of the No.3302 roadway belongs to the class IV unstable surrounding rock.

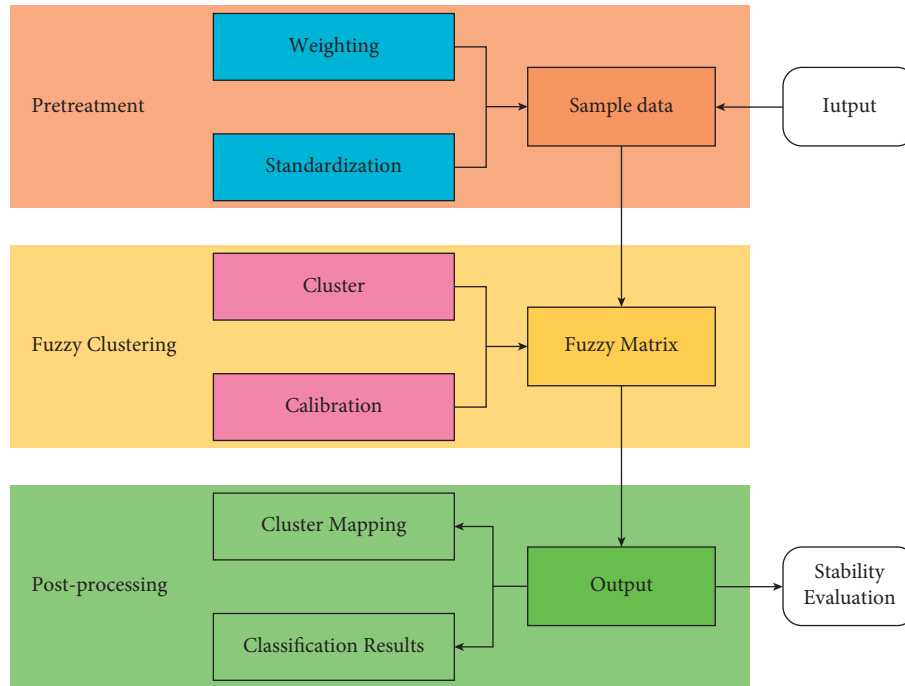


FIGURE 5: Fuzzy clustering process of surrounding rock stability classification.

TABLE 3: Selection comparison table of λ (according to roof-to-floor convergence).

| Items | 2 | 3 | 4 | 5 | 6 | 7 | 12 |
|--------------|-------|-------|------|------|------|------|------|
| λ | 0.65 | 0.70 | 0.75 | 0.77 | 0.80 | 0.85 | 0.89 |
| F | 3.89 | 2.99 | 3.79 | 2.87 | 3.18 | 2.86 | 2.70 |
| $F_{0.05}$ | 4.14 | 3.25 | 2.86 | 2.67 | 2.50 | 2.39 | 2.25 |
| $F-F_{0.05}$ | -0.26 | -0.25 | 0.93 | 0.20 | 0.68 | 0.47 | 0.45 |

TABLE 4: Selection comparison table of λ (according to rib-to-rib displacement convergence).

| Items | 2 | 3 | 4 | 6 | 7 | 10 |
|--------------|-------|------|-------|------|------|-------|
| λ | 0.70 | 0.74 | 0.75 | 0.80 | 0.85 | 0.87 |
| F | 2.27 | 3.43 | 13.72 | 3.01 | 2.87 | 2.11 |
| $F_{0.05}$ | 4.14 | 3.25 | 2.86 | 2.50 | 2.39 | 2.28 |
| $F-F_{0.05}$ | -1.87 | 0.18 | 10.86 | 0.51 | 0.48 | -0.17 |

TABLE 5: Classification results of surrounding rock stability of coal roadway.

| Grade | Strength of surrounding rock | | | In situ stress | | N (M) | C_0 (%) | Displacement convergence prediction | |
|-----------------------|------------------------------|--------------|----------------|---------------------|---------------------|------------|--------------|-------------------------------------|-------------------|
| | Roof (MPa) | Rib (MPa) | Floor (MPa) | σ_v (MPa) | σ_h (MPa) | | | Roof-to-floor (%) | Rib-to-rib (%) |
| I, very stable | >50.5 | >15.3 | >38.5 | <8.9 | <9.6 | <0.6 | >34 | <6.0 | <5.6 |
| II, relatively stable | 31.8~50.5 | 10.4~15.3 | 25.4~38.5 | 8.9~15.6 | 9.6~20.0 | 0.6~1.4 | 27.2~34.0 | 6.0~13.5 | 5.6~15.4 |
| III, medium stable | 18.3~31.8 | 6.8~10.4 | 14.6~25.4 | 15.6~27.8 | 20.0~32.4 | 1.4~2.4 | 21.0~27.2 | 13.5~19.5 | 15.4~25 |
| IV, unstable | <18.3 | <6.8 | <14.6 | >27.8 | >32.4 | >2.4 | <21.0 | >19.5 | >25.0 |

TABLE 6: Determination results of surrounding rock stability evaluation index of No.3302 roadway.

| Evaluation index | R_{rz} (MPa) | R_{brz} (MPa) | R_{fz} (MPa) | σ_v (MPa) | σ_h (MPa) | N | C_0 (m) |
|------------------|-------------------|--------------------|-------------------|---------------------|---------------------|-----|--------------|
| Value | 18.9 | 7.2 | 12.3 | 26.3 | 29.1 | 2.7 | 16.3 |

TABLE 7: Support scheme before and after optimization of No.3302 roadway.

| Type of surrounding rock | Support way | Support parameters | |
|--------------------------|--------------|--------------------|--------------------|
| | | Primary support | Reinforced support |
| Roof | Anchor bolt | Diameter/mm | 20 |
| | | Length/mm | 2400 |
| | | Spacing/mm | 800 × 1000 |
| Rib | Anchor bolt | Diameter/mm | 20 |
| | | Length/mm | 2200 |
| | | Spacing/mm | 800 × 1000 |
| | Anchor cable | Diameter/mm | 17.8 |
| | | Length/mm | 7000 |
| | | Spacing/mm | 1000 |

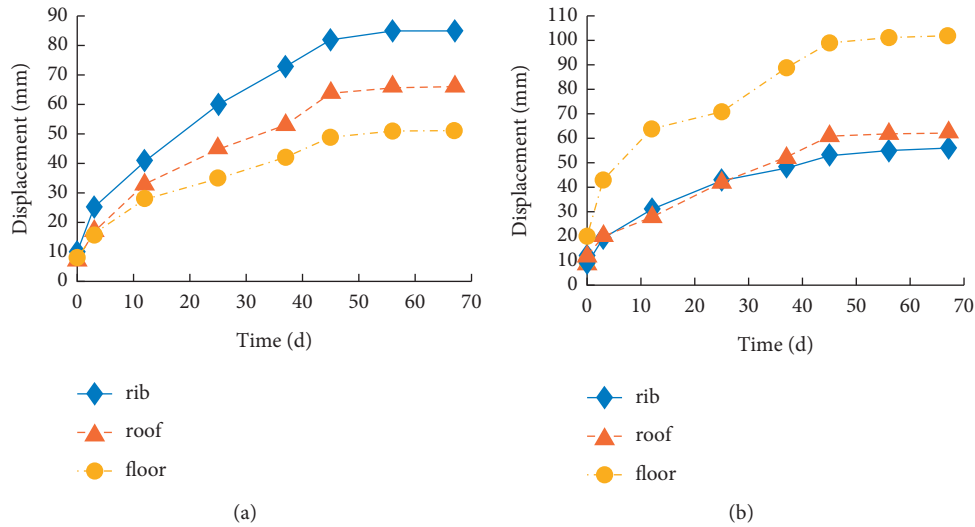


FIGURE 6: Surrounding rock deformation of No.3302 coal roadway. (a) 1# measuring point. (b) 3# measuring point.

4.3.1. *Optimization of the Support Scheme.* The original support parameters of No.3302 roadway were determined by engineering analogy method, namely, the support parameters of No.2306 roadway under similar geological conditions. However, the test results show that the in situ stress of the two roadways is quite different. At this time, the roadway support scheme No.3302 using the engineering analogy method is unreasonable and unscientific. Therefore, according to the classification results of surrounding rock stability of SIM based on in situ stress, the support scheme of the No.3302 roadway was optimized, and the support scheme of No.3302 roadway before and after optimization is shown in Table 7.

4.3.2. *On-Site Monitoring.* To verify the SIM reasonableness of the classification results of the SIM surrounding rock stability and the effectiveness of the optimized support

scheme, we conducted on-site monitoring of the No.3302 roadway surrounding rock deformation with 10 measurement points, among which the monitoring results of 1# measuring point and 3# measuring point are shown in Figure 6.

From Figure 6, the deformation of the surrounding rocks in No.3302 roadway gradually increases, and displacement convergence gradually decreases, with the maximum convergence of 85 mm for the rib-to-rib and 165 mm for the roof-to-floor, which is smaller than the maximum convergence of the surrounding rocks in No.2306 roadway (236 mm for the rib-to-rib and 452 mm for the roof-to-floor). The above monitoring results show that the optimized roadway support scheme effectively controls the surrounding rock deformation and proves the reasonableness of the SIM surrounding rock stability classification method based on the in situ stress.

5. Conclusion

- (1) Among the many factors that affect the stability of the surrounding rock, the evaluation indexes of coal roadway are determined, including comprehensive strength of surrounding rock (roof, rib, floor), in situ stress (σ_v, σ_h), and mining index (the immediate roof backfilled ratio N , the main roof first weighting interval C_0 , and the type of chain pillar).
- (2) A method for calculating the strength of surrounding rock is proposed, which combines the strength of the rock block, the rock mass strength coefficient, the thickness of roof coal seam, and floor. The strength of roof (and rib and floor) of coal roadway is determined by thickness weighted average method, which solves the problem of selection of strength index in surrounding rock classification of roadway.
- (3) The fitting equation between each evaluation index and the displacement convergence in surrounding rock of coal roadway was determined by unary regression and multiple regression, and the weight of each classification index was determined. On the basis of this fitting equations, the deformation of the surrounding rock of coal roadway can be predicted.
- (4) Based on the principle of fuzzy clustering, the fuzzy clustering model of surrounding rock stability classification of coal roadway is established. 37 typical coal roadways to be classified are reasonably divided into four categories: very stable, relatively stable, medium stable, and unstable.

Data Availability

The data used to support the findings of this study are available from the corresponding author upon request.

Conflicts of Interest

The authors declare that they have no conflicts of interest.

Acknowledgments

This research was funded by the National Natural Science Foundation of China (Grant nos. 51574156 and 52074166).

References

- [1] H. P. Kang and J. H. Wang, *Rock Bolting Theory and Complete Technology for Coal Roadways*, China Coal Industry Publishing House, Beijing, China, 2018.
- [2] D. U. Deere, "Technical description of rock cores for engineering purpose," *Rock Mechanics and Engineering Geology*, vol. 1, no. 1, pp. 17–22, 1964.
- [3] D. U. Deere, A. J. Hendron, F. D. Patton, and E. J. Cording, "Design of surface and near-surface construction in rock," in *Proceedings of the 8th US symposium on rock mechanics (USRMS)*, Minneapolis, MN, USA, September 1966.
- [4] D. U. Deere, "Rock quality designation (RQD) after twenty years," Contract Report GL-89-1, Deere Consultant, Gainesville, FL, USA, 1989.
- [5] Z. T. Bieniawski, "Engineering classification of jointed rock masses," *Civil Engineering Siviele Ingenieurswese*, vol. 15, no. 12, pp. 335–343, 1973.
- [6] Z. T. Bieniawski, "Determining rock mass deformability: experience from case histories," *International Journal of Rock Mechanics and Mining Science & Geomechanics Abstracts*, vol. 15, no. 5, pp. 237–247, 1978.
- [7] E. Hoek and E. T. Brown, "Practical estimates of rock mass strength," *International Journal of Rock Mechanics and Mining Sciences*, vol. 34, no. 8, pp. 1165–1186, 1997.
- [8] N. Barton, F. Løset, R. Lien, and J. Lunde, "Application of Q-system in design decisions concerning dimensions and appropriate support for underground installations," *Subsurface Space*, vol. 2, pp. 553–561, 1981.
- [9] N. Barton, "Some new Q-value correlations to assist in site characterisation and tunnel design," *International Journal of Rock Mechanics and Mining Sciences*, vol. 39, no. 2, pp. 185–216, 2002.
- [10] S.-S. Shi, S.-C. Li, L.-P. Li, Z.-Q. Zhou, and J. Wang, "Advance optimized classification and application of surrounding rock based on fuzzy analytic hierarchy process and Tunnel Seismic Prediction," *Automation in Construction*, vol. 37, pp. 217–222, 2014.
- [11] N. Hasegawa, S. Hasegawa, T. Kitaoka, and H. Ohtsu, "Applicability of neural network in rock classification of mountain tunnel," *Materials Transactions*, vol. 60, no. 5, pp. 758–764, 2019.
- [12] G. Deng and Y. Fu, "Fuzzy rule based classification method of surrounding rock stability of coal roadway using artificial intelligence algorithm," *Journal of Intelligent and Fuzzy Systems*, vol. 40, no. 4, pp. 8163–8171, 2021.
- [13] X. H. Li and Q. Wang, "Prediction of surrounding rock classification of highway tunnel based on PSO-SVM," in *Proceedings of the International Conference on Robots and Intelligent System (ICRIS)*, pp. 443–446, Peoples R China, Haikou, China, June 2019.
- [14] S. Zheng, A. N. Jiang, X. R. Yang, and G. C. Luo, "A new reliability rock mass classification method based on least squares support vector machine optimized by bacterial foraging optimization algorithm," *Advances in Civil Engineering*, vol. 2020, Article ID 3897215, 13 pages, 2020.
- [15] Y. Wang, N. Zhao, H. Jing, B. Meng, and X. Yin, "A novel model of the ideal point method coupled with objective and subjective weighting method for evaluation of surrounding rock stability," *Mathematical Problems in Engineering*, vol. 2016, Article ID 8935156, 9 pages, 2016.
- [16] M. Wang, X. Xu, J. Li, J. Jin, and F. Shen, "A novel model of set pair analysis coupled with extenics for evaluation of surrounding rock stability," *Mathematical Problems in Engineering*, vol. 2015, Article ID 892549, 9 pages, 2015.
- [17] H. He, Y. Yan, C. Qu, and Y. Fan, "Study and application on stability classification of tunnel surrounding rock based on uncertainty measure theory," *Mathematical Problems in Engineering*, vol. 2014, Article ID 626527, 5 pages, 2014.
- [18] S. Wu, S. Yang, and X. Du, "A model for evaluation of surrounding rock stability based on D-S evidence theory and error-eliminating theory," *Bulletin of Engineering Geology and the Environment*, vol. 80, no. 3, pp. 2237–2248, 2021, (in English).
- [19] X. Liu, D. Fan, Y. Tan et al., "New detecting method on the connecting fractured zone above the coal face and a case study," *Rock Mechanics and Rock Engineering*, vol. 54, no. 8, pp. 4379–4391, 2021.
- [20] X. Liu, S. Song, Y. Tan et al., "Similar simulation study on the deformation and failure of surrounding rock of a large section

- chamber group under dynamic loading,” *International Journal of Mining Science and Technology*, vol. 31, no. 3, pp. 495–505, 2021.
- [21] Y. Xue, Z. Li, D. Qiu et al., “Classification model for surrounding rock based on the PCA-ideal point method: an engineering application,” *Bulletin of Engineering Geology and the Environment*, vol. 78, no. 5, pp. 3627–3635, 2019.
- [22] P. He, L. P. Li, Q. Q. Zhang, F. Xu, J. Hu, and J. Zhang, “Gaussian process model of an advanced surrounding rock classification based on tunnel seismic predictions,” in *Proceedings of the Fourth Geo-China International Conference on Sustainable Civil Infrastructures - Innovative Technologies for Severe Weathers and Climate Changes*, pp. 210–217, Shanghai, China, July 2016.
- [23] P. He, S.-C. Li, L.-P. Li, Q.-Q. Zhang, F. Xu, and Y.-J. Chen, “Discontinuous deformation analysis of super section tunnel surrounding rock stability based on joint distribution simulation,” *Computers and Geotechnics*, vol. 91, pp. 218–229, 2017.
- [24] P. He, S. Q. Sun, G. Wang, and W.-T. Li, “Gaussian process model of surrounding rock classification based on digital characterization of rock mass structure and its application,” *Mathematical Problems in Engineering*, vol. 2020, Article ID 5264072, 15 pages, 2020.
- [25] G. C. Zhang, Z. J. Wen, S. J. Liang et al., “Ground response of a gob-side entry in a longwall panel extracting 17 m-thick coal seam: a case study,” *Rock Mechanics and Rock Engineering*, vol. 53, pp. 497–516, 2020.
- [26] G. C. Zhang, C. W. Zang, M. Chen et al., “Ground response of entries driven adjacent to a retreating longwall panel,” *International Journal of Rock Mechanics and Mining Sciences*, vol. 138, p. 104630, 2021.
- [27] Y. Liu, C. Hou, J. Yao et al., “Classification scheme of surrounding rock stability of mining roadway in slowly inclined and inclined coal seams in China,” *Coal Science and Technology*, vol. 6, pp. 2–6, 1988.

Research Article

Temperature Control Technology for Construction of Jinsha River Bridge

Hui-Wu Jin ¹, Guo-An Wang,¹ and Zhan-Ming Chen²

¹School of Transportation Engineering, Jiangsu Vocational Institute of Architectural Technology, Xuzhou, Jiangsu 221116, China

²Jiangyin Construction Engineering Group Co., Ltd., Jiangyin, Jiangsu 214400, China

Correspondence should be addressed to Hui-Wu Jin; 821748687@qq.com

Received 20 September 2021; Accepted 22 October 2021; Published 3 November 2021

Academic Editor: Gaofeng Song

Copyright © 2021 Hui-Wu Jin et al. This is an open access article distributed under the Creative Commons Attribution License, which permits unrestricted use, distribution, and reproduction in any medium, provided the original work is properly cited.

The key problem of mass concrete temperature control is to effectively control the maximum temperature inside concrete, the temperature difference between inside and outside concrete, and the temperature difference between surface and environment. The size of the main tower cap of No. 3 Jinsha River Bridge is 37 m × 23.5 m × 5.5 m, and the cubic volume of concrete reaches 4782.3 m³, which is poured in two times. In order to ensure construction quality of mass concrete structure, prevent the large mass concrete temperature stress, through the numerical simulation of the temperature control and optimization scheme, by optimizing the mixture ratio design, reducing the temperature of concrete pouring into the mold, cooling water cycling, insulation keeping in good health and a series of measures to effectively achieve the control goal, and eliminating the temperature cracks. The measured data show that the maximum temperature inside concrete, the temperature difference between inside and outside, and the temperature difference between surface and environment are qualified, but the temperature difference control of cooling water inlet and outlet has hysteresis effect, and the temperature difference between inlet and outlet will be greater than 10°C, which should be noticed.

1. Introduction

Concrete has been widely used in all kinds of buildings, such as bridges, dams, and other structures. In the construction of large bridges, especially bridges across rivers, seas, and valleys, the size records of concrete structures have been constantly refreshed. However, due to the poor thermal conductivity of concrete, a lot of heat that the cement hydration reaction produced is not easy to dissipate. The heat accumulation within structure causes the internal structure of concrete rapid heating up, the uneven temperature field both inside and outside the structure, and the temperature stress in the structure. Excessive temperature stress easily causes structural cracks affecting the structure durability. Structural cracks caused by temperature stress will have serious consequences on structural damage especially for mass concrete. According to the Construction Code for Mass Concrete (GB 50496-2018) [1,2], mass concrete with the minimum size of concrete structure entity not less than 1 m, or concrete that is expected to cause harmful cracks due

to temperature change and shrinkage caused by hydration of cementing materials in concrete, is regarded as mass concrete. Therefore, temperature control is an urgent problem to be solved in mass concrete construction, and reasonable and effective technical measures must be taken to deal with it properly. Domestic and foreign scholars and engineers have carried out a lot of research work on temperature control during the construction of mass concrete and obtained a lot of research results.

Wan et al. [3] studied the crack prevention construction technology of mass concrete for the main bridge cap of South Dongting Bridge and pointed out many technical measures: the optimized design of concrete cofferdam reduces the total quantity of heat of hydration, thinning layered casting thickness increases concrete cooling capacity, improving the heat dissipation efficiency of the internal and external heat, reducing temperature rise of concrete, controlling the temperature of concrete casting into the mold, lowering temperature peak of caps concrete, adopting the water storage curing meet the requirements of large volume

concrete heat preservation and heat insulation method, and so on. Yuan et al. [4] used the measured temperature field of hydration heat in No. 0 block of a continuous box girder and established a cooling pipe water circulation model by using finite element analysis method under the condition that the noncooling pipe water circulation model was consistent with the measured temperature field and analyzed the cooling effect and crack control effect of the cooling pipe water circulation model. He et al. [5] analyzed the casting thickness effect on the internal temperature and stress of mass concrete and cooling water and selected the suitable casting and temperature control scheme for Rongjiang Bridge project. Jin et al. [6,7] studied the concrete temperature field and stress field of concrete by simulating the concrete pouring process of the cap in a low-temperature environment, proposed the temperature control standard and measures, and verified the numerical analysis conclusion of the study based on the monitoring results of the temperature field. Qiao [8] put forward the measures when adding fly ash into the concrete and taking measures to reduce the temperature of concrete entering the mold and monitored the temperature of a large bridge cap in the construction. Yang et al. [9,10] took targeted temperature control measures for the temperature control of the cap based on the field measured data and finite element calculation model, analyzed the concrete temperature of the cap, the steel stress, and the water temperature of the inlet and outlet of the cooling pipe, drew a conclusion that the temperature control measures for mass concrete are necessary and effective. Wang et al. [11] analyzed the actual anticracking effect of the temperature control different construction schemes and temperature control measures, such as the whole gating, layer pouring, cooling water pipe, and so on. Zhang et al. [12] obtained the specific cooling effect of spatial three-dimensional cooling net on the basis of the gravity anchorage of a suspension bridge as the research object, the MIDAS/civil finite element software simulation of mass concrete construction is a three-dimensional network and only layout cooling pipe cooling, one-time casting thickness of single-layer thickness and double-layer thickness of layered casting process, and comparative analysis of these four conditions of temperature field and temperature stress field. Li et al. [13] put forward the "curing" dynamic design method, with the mass concrete temperature control scheme design for main pier pile caps of a Yangtze River Bridge, calculation of big-volume concrete internal temperature field and stress field simulation, and developed the temperature control standard of harmful temperature crack and the corresponding temperature control measures according to the calculated results.

According to the theoretical calculation, the maximum internal temperature of concrete and the allowable stress corresponding to each age of concrete can be obtained, but the occurrence time of the maximum temperature and the change curve of temperature with time cannot be determined. The numerical simulation method can overcome the deficiency of theoretical calculation effectively, get the time-history curve of concrete temperature and stress, and intuitively display the temperature field and stress field inside concrete at each time point. Midas software is well used to calculation of the temperature field. Boundary conditions and

construction process simulation are the key problems, which are directly related to the accuracy of calculation results.

In this paper, the No. 3 main tower cap of Jinsha River Bridge is taken as the research object, and a series of temperature control measures, such as optimizing the mix ratio design, reducing the temperature of concrete pouring into the mold, cooling water circulation, heat preservation, and health preservation, are studied to explore the effective means to achieve the temperature control target effectively and eliminate temperature cracks; at the same time, the measured data and simulation data are compared and analyzed to provide reference for temperature control of mass concrete construction.

2. Project Overview

Jinsha River Bridge with the main bridge 340 m + 72 m + 48 m + 32 m single-tower cable-stayed bridge, the starting pile number is K96 + 279, and the ending pile number is K96 + 844. The side spans of the superstructure are prestressed concrete box beams, and the middle spans are P-K steel box beams. The approach bridge adopts 2 × 35 m composite beams. The substructure adopts box pier, door frame pier, column pier, column abutment, and the foundation is bored pile foundation. The concrete grade is C40, in which the cap size of No. 3 main tower is 37 m × 23.5 m × 5.5 m, and the concrete square volume reaches 4782.3 m³, which is poured twice. The bridge layout is shown in Figure 1.

3. Design of Temperature Control Scheme for Mass Concrete Cap

3.1. Technical Route of Temperature Control Scheme. In order to ensure the construction quality of mass concrete structure and avoid the harmful temperature crack of mass concrete, it is necessary to accurately predict and analyze the temperature field and temperature stress of mass concrete. How to design a reasonable temperature control scheme and ensure that the change of temperature field inside concrete is in a safe and controllable range are considered; the general idea is as follows:

- (1) The adiabatic temperature rise and peak temperature of concrete can be reduced through raw material selection and mix ratio test
- (2) According to the theoretical calculation of temperature control and construction environmental conditions, choose the surface insulation measures suitable for the construction season, reduce the temperature difference between inside and outside of concrete, make the distribution of temperature field in concrete as uniform as possible, and reduce the temperature gradient
- (3) Through the internal cooling water circulation system, reduce the internal temperature peak of concrete, control the internal cooling rate, real-time monitoring of temperature, and intelligent control according to the monitoring data

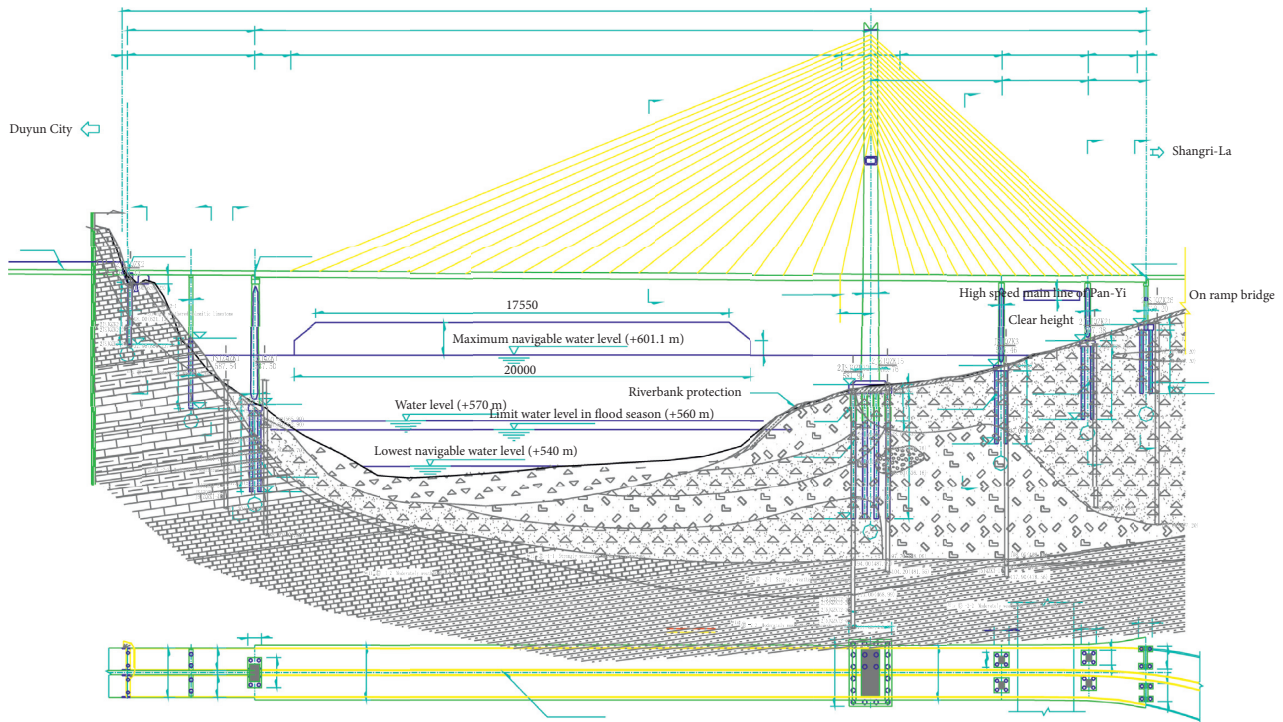


FIGURE 1: The layout of Jinsha River Bridge.

- (4) Control the temperature difference between upper and lower layers, shorten the interlayer age difference as far as possible, and prevent the possible interlayer cracks

The specific process is shown in Figure 2.

3.2. Selection of Concrete Raw Materials and Mixing Ratio

3.2.1. Selection Raw Materials of Concrete

Cement: for cap C40 and tower base C50 concrete, in order to slow down the hydration reaction speed of cement and the growth rate of early strength of concrete, reduce the temperature appreciation of concrete; 42.5 ordinary Portland cement from Shuicheng Conch Panjiang Cement Company is selected.

Admixture: polycarboxylic acid high-efficiency water reducing agent with stable performance and high water reducing rate is preferred, which can effectively reduce the amount of cement per square meter of concrete, thus reducing the temperature rise of hydration heat of concrete. Through the adaptability test of water reducing agent and cement, the composition of water reducing agent is adjusted to ensure the effective initial setting time of concrete and meet the construction time of concrete pouring on-site.

Fly ash: in order to reduce the water consumption per unit of concrete, reduce the cement hydration heat of concrete and ensure the working performance of concrete; grade 1 fly ash is used.

Fine aggregate and coarse aggregate: the mud content of fine aggregate should be less than or equal to 3.0%, fineness modulus ≥ 2.5 . Coarse aggregate is 5~25 mm continuous graded gravel with mud content $\leq 1.0\%$ and should be washed in advance. The concrete is tested on-site and deducted from the total water consumption according to the measured water ratio of coarse aggregate and fine aggregate to ensure the accuracy of the actual water-cement ratio.

3.2.2. Concrete Mix Design. The raw materials and mixing ratio of C40 concrete for the main pier cap of Jinsha River Bridge are shown in Table 1.

3.3. Layout of Cooling Water Pipes. Cooling water pipe layout of cap and tower is shown in Figure 3. Cooling water pipes are all 40 mm in diameter with the horizontal spacing 1.0 m. The thickness of the first cap is 3.0 m and the second one 2.5 m, while the thickness of the tower is 2.0 m. The height spacing between the cooling water pipe and the top surface is 0.5 m + 2 × 1.0 m + 0.5 m, 0.75 m + 1.0 m + 0.75 m, and 0.5 m + 1.0 m + 0.5 m.

4. Numerical Simulation of Temperature Control

4.1. Calculation Parameters and Calculation Model

4.1.1. Thermal Parameters and Mechanical Parameters. The values of thermal and mechanical parameters of concrete for cap C40 and tower C50 are shown in Table 2. The

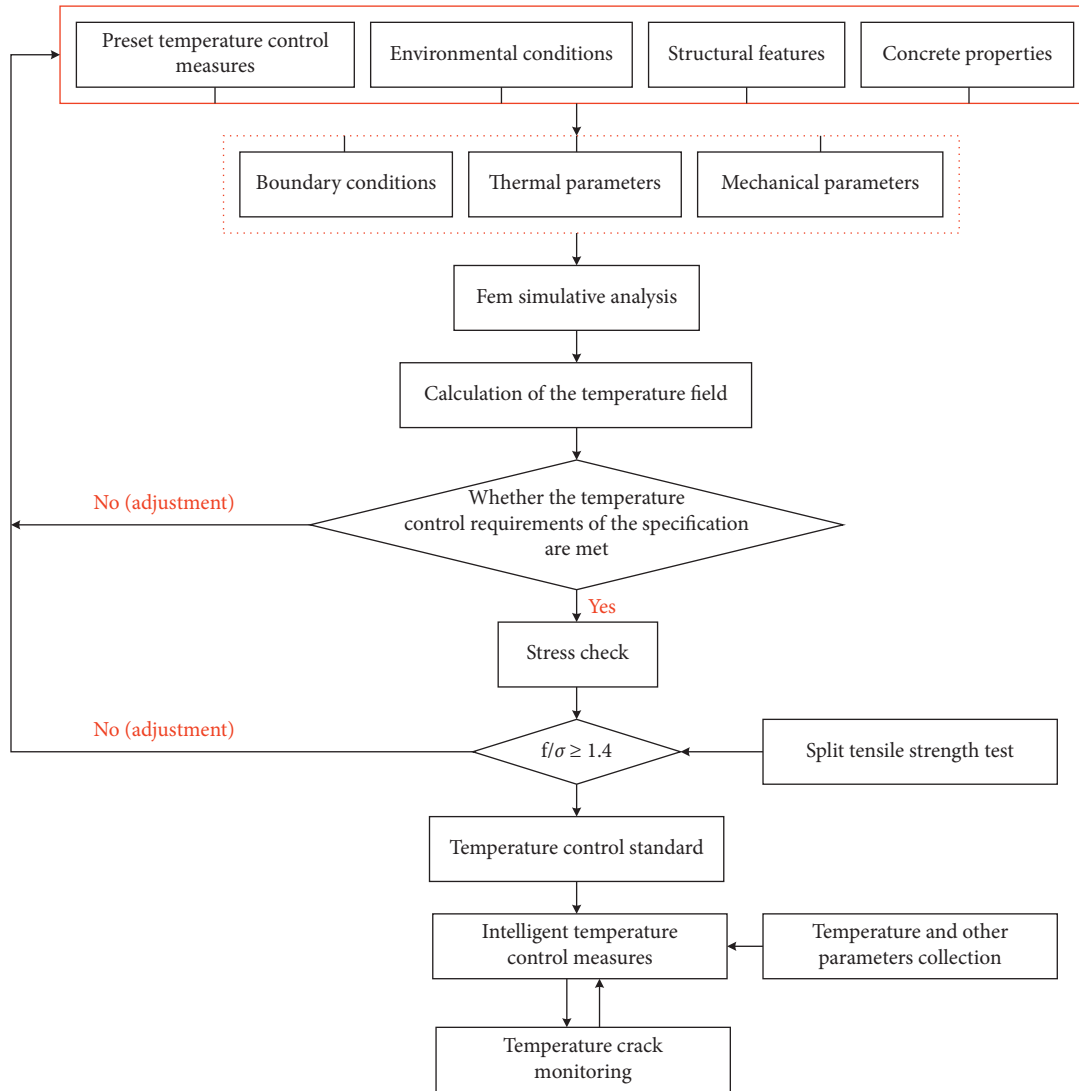


FIGURE 2: Temperature control flowchart.

TABLE 1: The lithology parameters of the 3D model.

| | | | | | | | | |
|---------------------------------|---|-------------------------------|--------|------|--------|----------------------------|-----------|--------------------|
| Project name | Main pier cap of Jinsha River Bridge | | | | | | | |
| Project | C40 concrete mix design | | | | | | | |
| | Material name | Material specification | | | | Manufacture factory | | |
| Raw materials | Cement | 42.5 ordinary Portland cement | | | | Water city conch pan river | | |
| | Flyash | — | | | | — | | |
| | Sand | — | | | | Mingsheng of Jinyang | | |
| | Gravel | — | | | | Mingsheng of Jinyang | | |
| | Admixture | — | | | | Changan of Shijiazhuang | | |
| | Mixing water | Tap water | | | | — | | |
| Proportions of C40 concrete mix | Materials | Cement | Flyash | Sand | Gravel | Water | Admixture | Water-binder ratio |
| | Consumption for concrete (m ³ /kg) | 285 | 154 | 761 | 1129 | 158 | 4.39 | 0.36 |

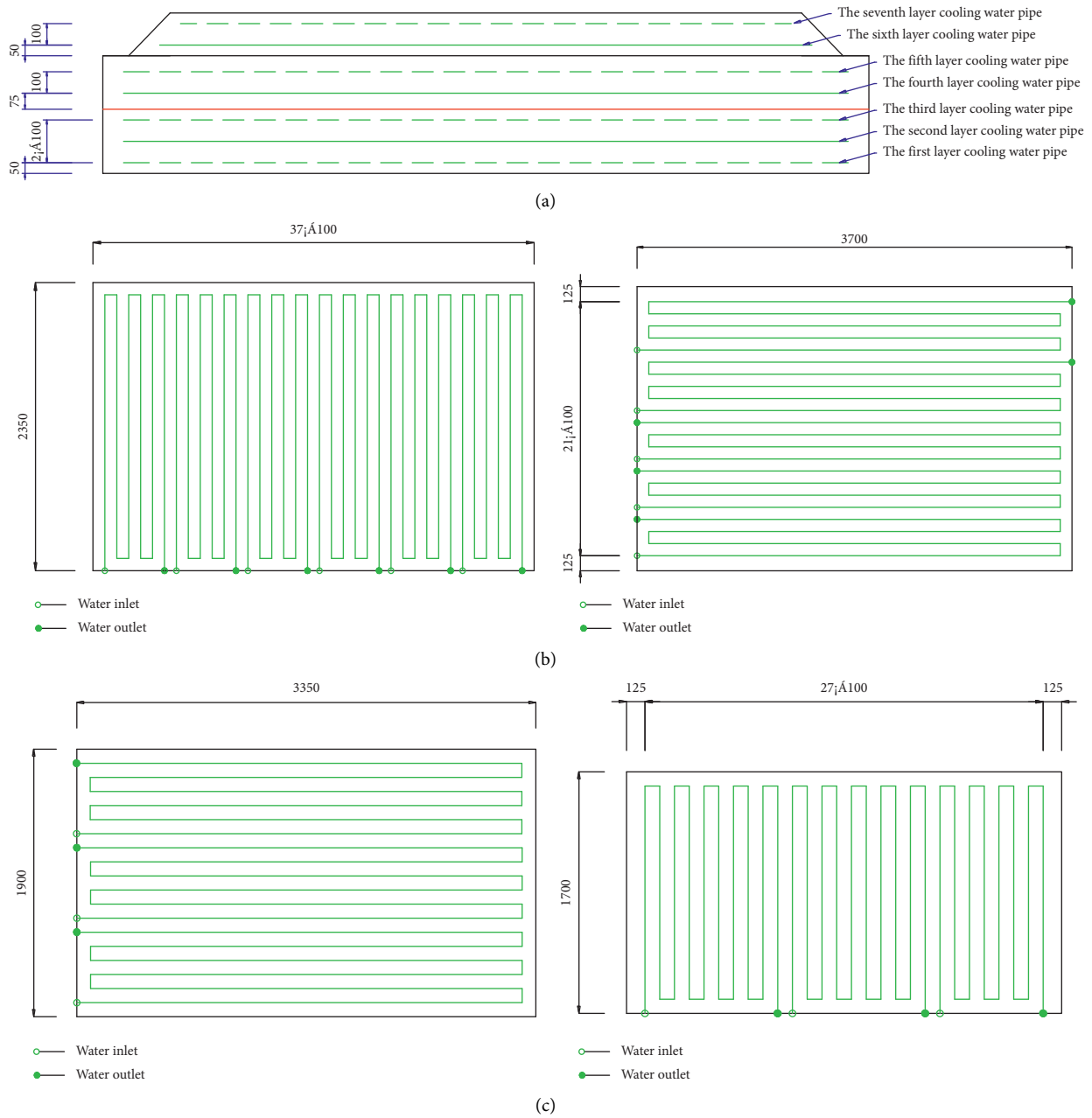


FIGURE 3: Cooling water pipe layout of cap and tower. (a) Elevation layout of cooling water pipes for cap and tower. (b) Cooling water pipe layout of cap. (c) Tower cooling water pipe layout.

TABLE 2: Summary of calculation parameters of cap concrete.

| Physical properties | Silicate concrete |
|--|--------------------|
| Density (kg/m^3) | 2491 |
| Coefficient of linear expansion ($1/T$) | 1×10^{-5} |
| Poisson's ratio | 0.2 |
| Specific heat capacity ($\text{kJ}/(\text{kg}\cdot^\circ\text{C})$) | 0.96 |
| Pyroconductivity ($\text{kJ}/(\text{m}\cdot\text{hr}\cdot\text{T})$) | 10.6 |
| Construction season | 3~5 months |
| Average temperature during construction ($^\circ\text{C}$) | 22~28 |
| Temperature of concrete entering mold ($^\circ\text{C}$) | 24~26 |
| Adiabatic temperature rise ($^\circ\text{C}$) | 40/46 |

adiabatic temperature of ordinary Portland cement is the actual value (modified according to the temperature peak measured by No. 8 cap).

The mechanical parameters of concrete, for Portland cement concrete mix ratio, used the standard value. Concrete shrinkage and creep is calculated according to "Code for Design of Highway Reinforced Concrete and Prestressed Concrete Bridges" JTG D62-2015 in Midas/Civil. Ambient temperature is selected according to the temperature and casting temperature of concrete, and the preliminary selected ambient temperature is calculated to be 24°C . In this calculation, the temperature of concrete entering mold is

temporarily set at $24^{\circ}\text{C}\sim 26^{\circ}\text{C}$. In the construction process of cap and tower, the temperature control is calculated according to the actual casting temperature of concrete. The water temperature of the cooling pipe shall be considered as the river water, the river water temperature shall be 24°C , and the flow shall be $3\text{ m}^3/\text{h}$ in the heating stage and $1.0\text{ m}^3/\text{h}$ in the cooling stage. In the process of temperature control, the inlet flow rate or inlet temperature should be adjusted according to the inlet temperature of cooling water and the monitoring of the internal temperature field of the cap tower.

4.1.2. Boundary Conditions. The 3D models in Figures 4 and 5 are established by MIDAS/civil finite element software.

(1) *Convective Boundary.* The insulation measures proposed for the top surface of the cap and tower are as follows: the first layer of plastic film + the second layer of geotextile + the third layer of rain cloth, and its equivalent heat transfer coefficient is $20\text{ kJ}/(\text{h}\cdot^{\circ}\text{C})$; the side of the cap is as follows: the first layer of geotextile + the second layer of rain cloth, and its equivalent heat transfer coefficient is $15\text{ kJ}/(\text{h}\cdot^{\circ}\text{C})$. In the actual construction, the insulation measures can be adjusted according to the actual environmental conditions and the measured temperature field.

(2) *Constraint Boundary.* Consolidation is adopted at the bottom of cushion of cap and tower. In accordance with the sequence of pouring and construction, the 1~2 layers of the cap are activated successively, and the actual age difference is considered for simulation calculation [14~16].

(3) *Pouring Interval.* The pouring interval is 10 days. It should be shortened as far as possible in the actual construction [17,18].

4.2. Calculation Results of Temperature Control

4.2.1. Temperature Simulation Results. According to the relevant parameters of Portland cement concrete mix ratio, the overall calculation results of cap and tower temperature are shown in Table 3.

According to the results of temperature calculation, the peak temperature of the first layer-concrete of the cap is 54.1°C under the condition of 24°C of the temperature of concrete entering mold, and the temperature difference of the inner surface is less than 20°C . Figure 6 shows the calculation results of maximum temperature field, and Figure 7 shows the temperature time-history curve.

The peak temperature of the second-layer concrete of the cap is 55.4°C under the condition of 24°C the temperature of concrete entering mold, and the temperature difference between inside and outside surface is less than 20°C . Figure 8 shows the calculation results of the maximum temperature field, and Figure 9 shows the temperature time-history curve.

The peak temperature of the tower base concrete is 61.8°C under the condition of 26°C of the concrete entering

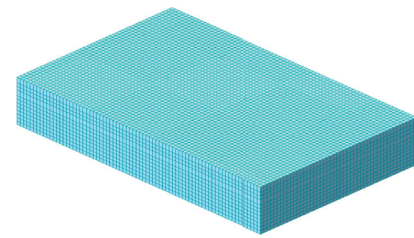


FIGURE 4: Cap model drawing.

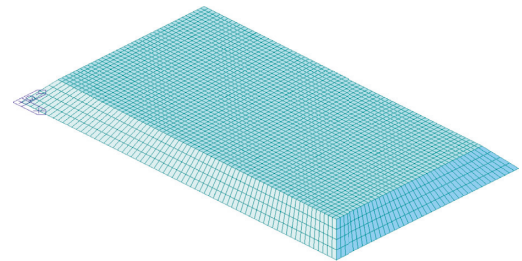


FIGURE 5: Tower base model diagram.

mold, and the temperature difference between inside and outside surface is less than 20°C . Figure 10 shows the calculation results of the maximum temperature field, and Figure 11 shows the temperature time-history curve.

4.2.2. Stress Simulation Results. The overall stress calculation results of cap and tower base are shown in Table 4.

In the process of temperature change of concrete, the general change law of stress is as follows: in the stage of temperature rise, the surface tensile stress is the largest around the temperature peak time inside concrete; in the cooling stage, the internal stress gradually changes from compressive stress to tensile stress.

According to the stress calculation results, the maximum principal tensile stress of the first layer concrete of cap is between 1.33 MPa and 2.02 MPa . The calculation results of the maximum principal tensile stress distribution are shown in Figure 12, and the stress time-history curve is shown in Figure 13.

The maximum principal tensile stress of the second layer concrete of cap is between 1.86 MPa and 2.01 MPa . The calculation results of the maximum principal tensile stress distribution are shown in Figure 14, and the stress time-history curve is shown in Figure 15.

The maximum principal tensile stress of tower concrete is between 1.77 MPa and 2.29 MPa . The calculation results of the maximum principal tensile stress distribution are shown in Figure 16, and the stress time-history curve is shown in Figure 17 (SIG-maximum principal tensile stress).

4.2.3. Numerical Simulation Conclusion

- (i) When the temperature of concrete entering mold is $24^{\circ}\text{C}\sim 26^{\circ}\text{C}$, the theoretical peak temperature of the concrete in each layer of cap and tower is $54.1^{\circ}\text{C}\sim 61.8^{\circ}\text{C}$.

TABLE 3: Temperature calculation results.

| Position | Layer | Temperature of casting concrete (°C) | Peak temperature (°C) | Time of peak temperature (h) | Temperature rise value (°C) | Temperature difference between inside and outside (°C) |
|------------|-----------------------|--------------------------------------|-----------------------|------------------------------|-----------------------------|--|
| Cap | First-layer concrete | 24 | 54.1 | 48 | 30.1 | 16.1 |
| | Second-layer concrete | 24 | 55.4 | 48 | 31.4 | 17.4 |
| Tower base | First-layer concrete | 26 | 61.8 | 48 | 35.8 | 18.5 |

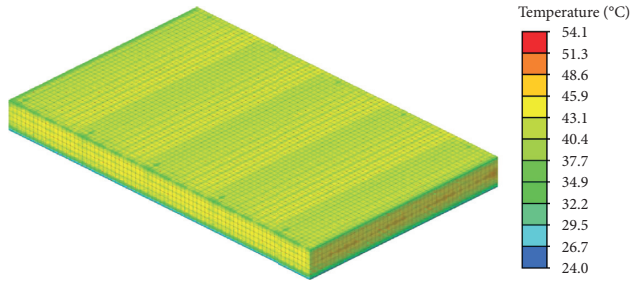


FIGURE 6: Distribution of the maximum temperature field on the first floor of cap (unit: °C).

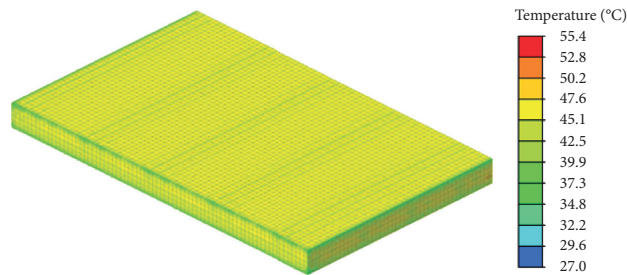


FIGURE 7: Time-history curve of concrete temperature in the first layer of cap.

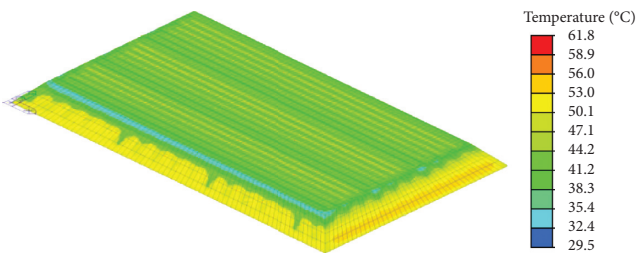


FIGURE 8: Distribution of maximum temperature field on the second floor of cap (unit: °C).

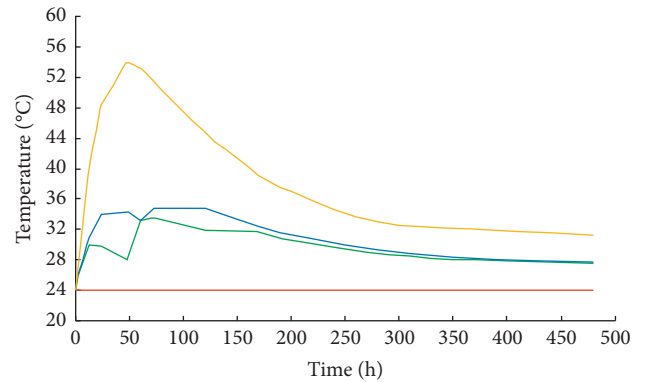


FIGURE 9: Time-history curve of concrete temperature of the second layer of cap.

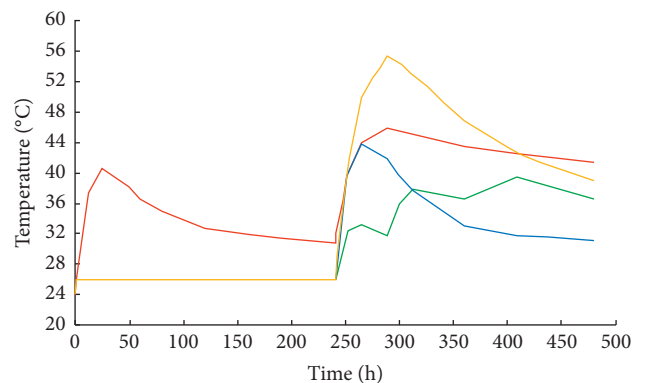


FIGURE 10: Distribution of the maximum temperature field of the tower (unit: °C).

(ii) According to the stress calculation results, the theoretical principal tensile stress of each layer of concrete is 1.86 MPa~2.29 MPa during the heating period, and 1.33 MPa~2.01 MPa after the cooling stage at the temperature of 24°C~26°C. The maximum principal tensile stress of each layer of concrete is less than the allowable stress in the heating and cooling stages, which meets the relevant requirements.

(iii) In the construction process, the temperature of concrete entering mold should be reduced as far as possible to reduce the temperature peak, to reduce the total temperature contraction deformation in the cooling stage. At the same time, pay attention to heat preservation in the maintenance process of the cap, reduce the temperature difference between inside and outside.

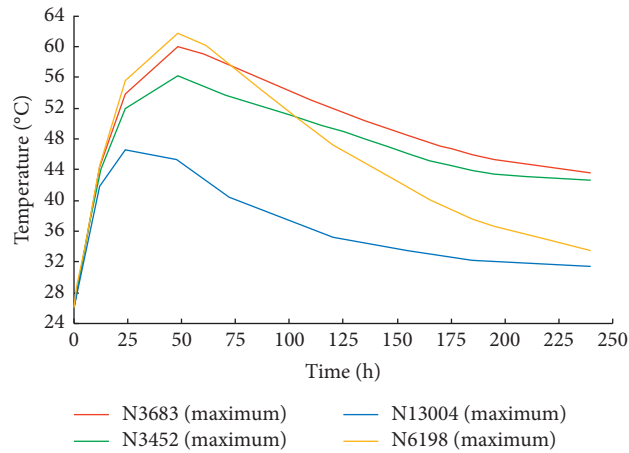


FIGURE 11: Concrete temperature time-history curve of tower.

TABLE 4: Stress calculation results.

| Position | Layer | Maximum principal tensile stress at heating stage | | | | Maximum principal tensile stress at cooling stage | | | |
|------------|-----------------------|---|------------------|------------------------|---------------|---|------------------|------------------------|---------------|
| | | Stress value (MPa) | Concrete age (d) | Allowable stress (MPa) | Safety factor | Stress value (MPa) | Concrete age (d) | Allowable stress (MPa) | Safety factor |
| Cap | First-layer concrete | 2.02 | 2.5 | 2.44 | 1.21 | 1.33 | 10 | 3.16 | 2.38 |
| | Second-layer concrete | 1.86 | 2.5 | 2.44 | 1.31 | 2.01 | 10 | 3.16 | 1.57 |
| Tower base | First-layer concrete | 2.29 | 2.5 | 2.71 | 1.18 | 1.77 | 10 | 3.45 | 1.95 |

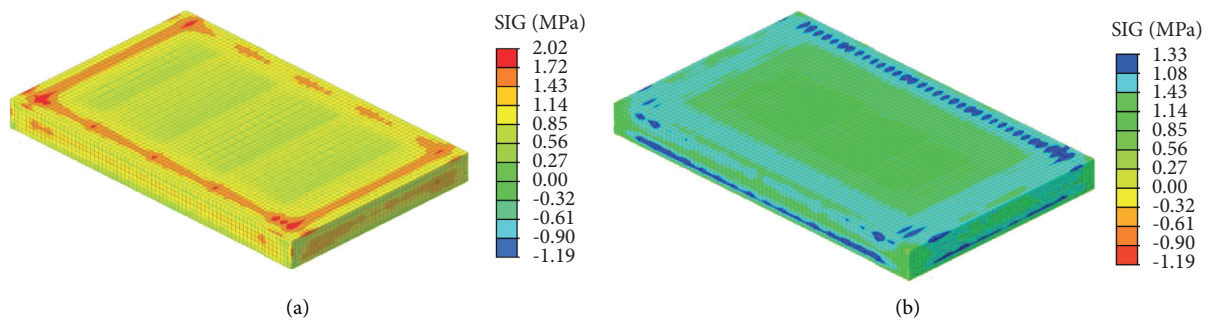


FIGURE 12: Cloud diagram of main tensile stress in the first layer of cap (unit: MPa). (a) Heating stage. (b) Cooling stage.

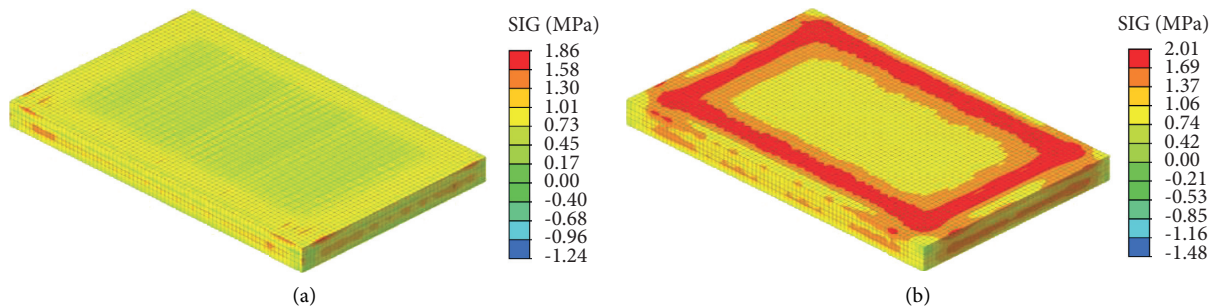


FIGURE 13: Time-history curve of main tensile stress in the first layer of cap.

(iv) Try to reduce the construction interval between each layer of cap and tower base, so as to reduce the constraint between each layer of concrete. In order to avoid interlayer cracks caused by excessive

binding force of the first layer concrete on the second layer, the temperature difference between the two layers of the cap must be controlled, so the interlayer age difference should be reduced as far as

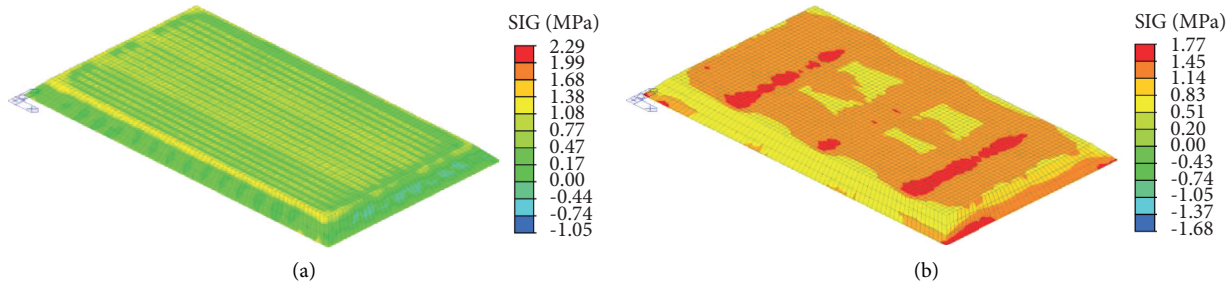


FIGURE 14: Cloud diagram of main tensile stress in the second layer of cap (unit: MPa). (a) Heating stage. (b) Cooling stage.

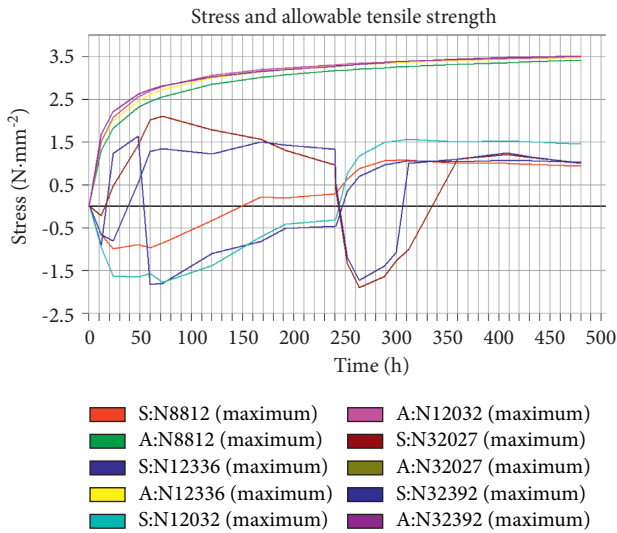


FIGURE 15: Time-history curve of main tensile stress at the second layer of cap.

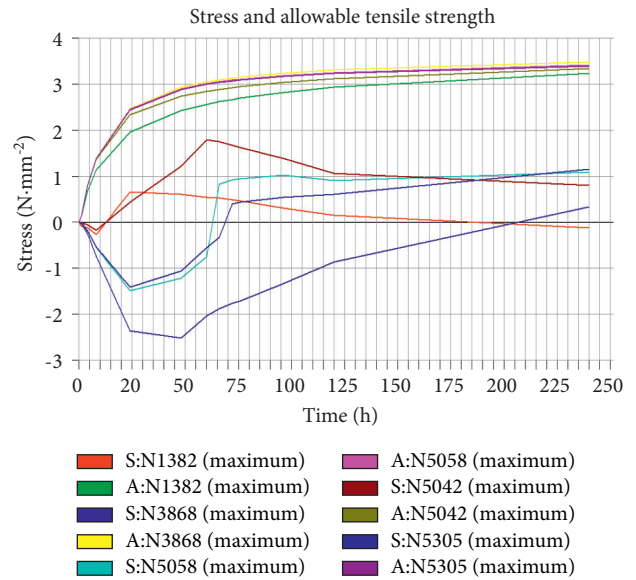


FIGURE 17: Time-history curve of tower principal tensile stress.

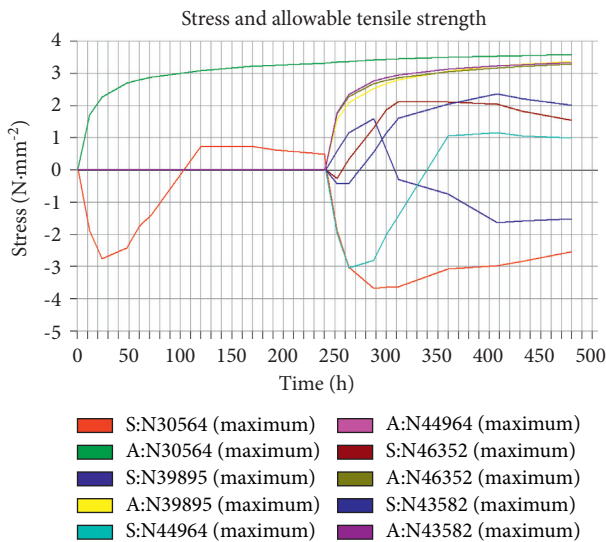


FIGURE 16: Cloud diagram of main tensile stress of tower (unit: MPa). (a) Heating stage. (b) Cooling stage.

possible. The concrete pouring interval of the main tower cap is controlled at about 7 days, generally not more than 10 days. The actual pouring finish time of the first layer of the cap construction is at

20:00 on May 29, 2020. The second pouring time is at 10:00 on June 10, 2020, and the interval is within 10 days.

5. Temperature Control Standard

According to the relevant requirements of the current codes and regulations, and in combination with the actual situation of the construction of the tower base of Jinsha River Bridge, the main temperature control standards are drawn up in Table 5.

It is an important measure for temperature control of mass concrete to reduce the temperature of concrete entering mold as much as possible. Under the condition of concrete fit ratio and heat transfer boundary condition, the higher the temperature of concrete entering mold is, the higher the temperature peak value is, and the greater the temperature difference between inside and outside concrete, temperature deformation, and temperature stress are. In addition, the higher the injection temperature, the faster the hydration reaction rate of concrete, most of the hydration heat will be released in the initial stage of concrete pouring, strength and elastic modulus will also increase, adverse to temperature control.

TABLE 5: Temperature control standard of cap.

| Serial number | Temperature control item | Control standard | Basis |
|---------------|--|-------------------------------------|---|
| 1 | Pouring temperature of concrete | $\leq 26^{\circ}\text{C}$ | Construction conditions and calculation results of temperature control |
| 2 | Maximum internal temperature of concrete | $\leq 65^{\circ}\text{C}$ | |
| 3 | Temperature difference between inside and outside of concrete (including equivalent temperature of concrete shrinkage) | $\leq 20^{\circ}\text{C}$ | 《Code for construction of mass concrete》(GB 50496-2018); 《code for construction of concrete structures》(GB50666-2011); calculation results of temperature control |
| 4 | Cooling rate inside casting concrete | $\leq 2.0^{\circ}\text{C}/\text{d}$ | |
| 5 | Temperature difference between surface and atmosphere of pouring concrete | $\leq 20^{\circ}\text{C}$ | 《Technical code for construction of highway bridges and culverts》(JTG/TF50-2011) |
| 6 | Temperature difference between inlet and outlet of cooling water | $\leq 10^{\circ}\text{C}$ | |
| 7 | The temperature difference between the cooling water and the inside concrete when the water is first supplied or resupplied after interruption | $\leq 25^{\circ}\text{C}$ | 《Technical specification for temperature crack control of mass concrete in water transport engineering》(JTS 202-1-2010) |
| 8 | Temperature difference between curing water and concrete surface | $\leq 15^{\circ}\text{C}$ | |

According to the calculation results, the order of the influence of various raw materials on the temperature of concrete is coarse aggregate > fine aggregate and water > cement and fly ash. Therefore, reducing the temperature of coarse aggregate and mixing water is the most effective way to reduce the concrete temperature of out-of-machine. The concrete temperature can be reduced by 0.40°C and 0.24°C for each decrease of coarse aggregate and mixing water by 1°C .

It is necessary to measure the temperature of water, cement, aggregate, and admixture before concrete mixing and estimate the temperature of concrete after mixing according to the empirical formula. If it cannot meet the requirements of the temperature of concrete entering mold, some measures should be taken such as adding ice and precooling of aggregate for trial mixing until the requirements are met.

6. Temperature Control Effect

6.1. Temperature Monitoring Scheme

6.1.1. Temperature Monitoring Content. Temperature monitoring mainly includes temperature measurement of environmental system and temperature field measurement of concrete. Temperature measurement of environmental system includes atmospheric temperature and inlet and outlet temperature of cooling water. Atmospheric temperature measurement includes the analysis of seasonal temperature difference, daily temperature, and cold wave. Select representative cooling water pipes and install temperature sensors in the inlet and outlet of water pipes and the middle of straight line section to measure the temperature of cooling water.

6.1.2. Layout of Concrete Temperature Measuring Points. The pipes of cooling water are made of Q235B with diameter of 32 mm and wall thickness of 2.5 mm. The bending part of

the pipe is pretreated with cold bending. The pipe is closely connected with silk buckle and raw tape.

The layout principle of temperature monitoring point of cap: the actual distribution and temperature field characteristics of cooling water pipe in concrete should be fully considered, and the corresponding specification requirements should be met:

- (i) According to the characteristics of structural symmetry, half of the structure is selected as the main test area, and the other half of the key measurement points are arranged
- (ii) Two temperature measuring elements are buried at important measuring points to prevent damage and ensure data integrity
- (iii) Fully consider the distribution law of temperature field, as well as the position of cooling water pipe, water inlet and outlet
- (iv) Fully reflect the evaluation of temperature control indicators

The specific arrangement of measuring points on the cap is shown in Figure 18. The final arrangement of measuring points may need to be adjusted appropriately according to the construction scheme and calculation results. Numbering rules of temperature measuring points: measuring points along the bridge are $X_n - (1 \sim N)$, such as $X_2 - (1 \sim N)$ in the second layer. Cross bridge direction measurement point is $Y_n - (1 \sim N)$ such that the second layer is $Y_2 - (1 \sim N)$. The central measurement point is $Z_n - 0$.

6.2. Temperature Monitoring Results. Before the concrete is put into the mold, check whether the instrument is damaged after being buried and observe the temperature in the concrete. Automatic temperature acquisition instrument is adopted to collect temperature data once per hour. According to the predicted calculation results of temperature field and stress field, combined with the comparative analysis of

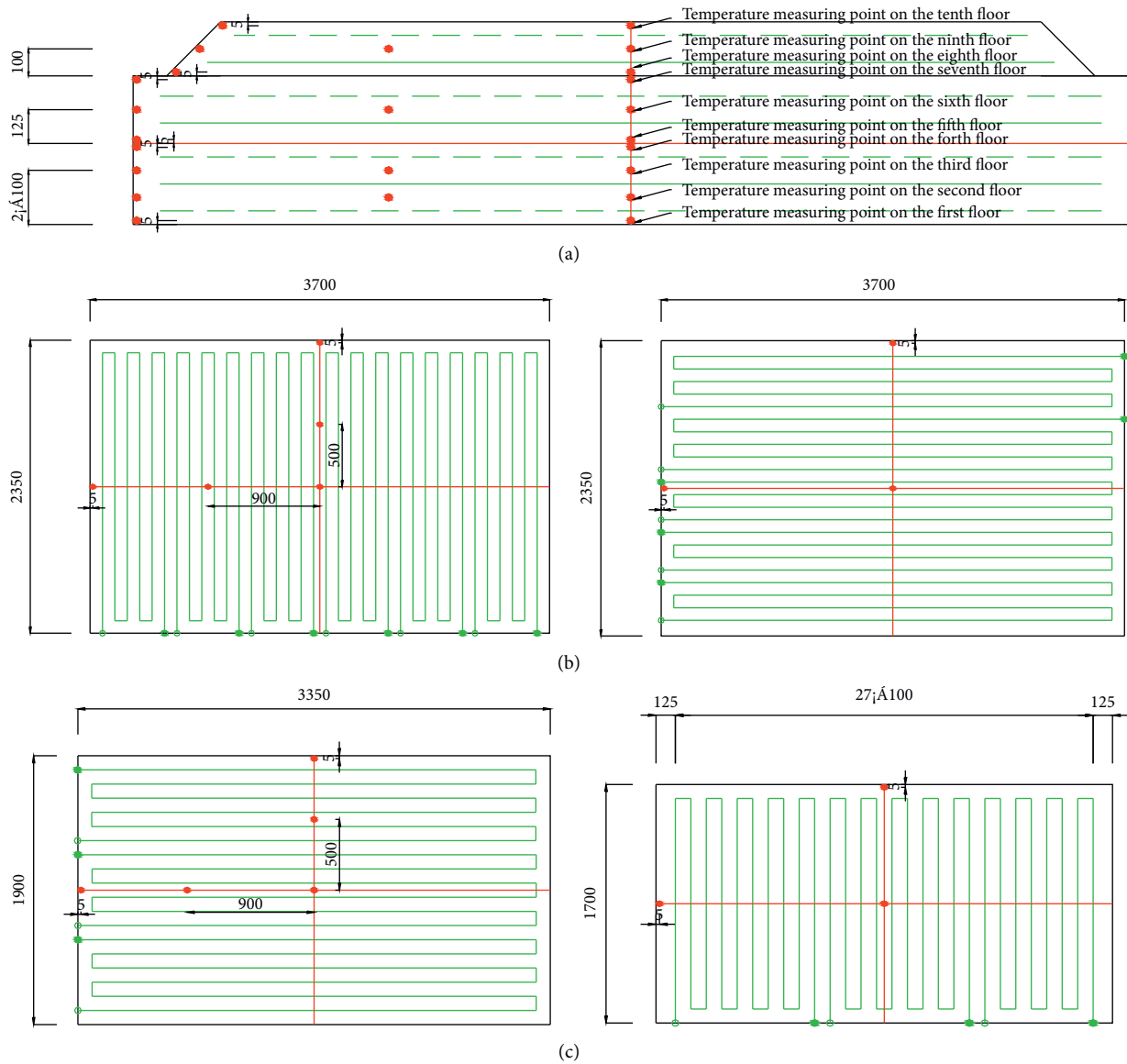


FIGURE 18: Layout of temperature measuring points. (a) Elevation layout of temperature measuring point of cap. (b) Floor plan of temperature measuring point of cap. (c) Layout of temperature measuring point of tower.

monitoring results, the termination time of measurement is determined. Ambient air temperature and inlet and outlet temperature of cooling water are monitored synchronously with the temperature of concrete, as shown in Figures 19 and 20. The corresponding data are shown in Table 6. The insulation measures proposed in the numerical simulation of temperature control are the same as those in the construction.

The monitoring data of the first pouring concrete of the cap was collected from May 29, 2020, to June 16, 2020 (there

was a lack of measurement data four times due to power outages in the middle), and the monitoring data of the second pouring of the cap was collected from June 10, 2020, to June 17, 2020.

The measured results show that the measured values of the first and second pouring of the temperature control project meet the requirements of the specification. The data show that the measures of this project can achieve good temperature control effect.

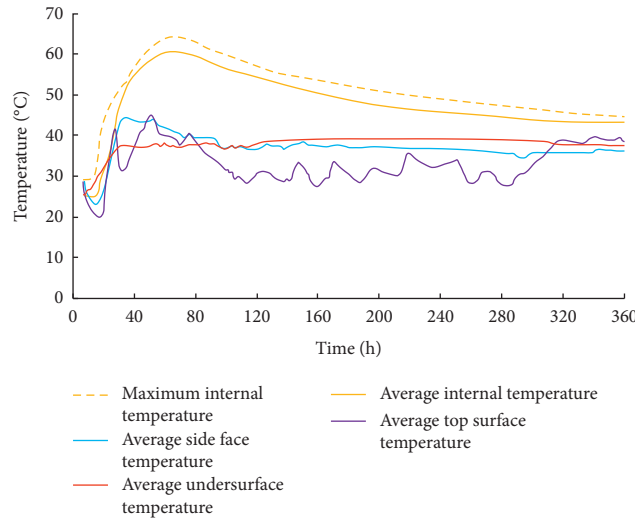


FIGURE 19: Monitoring results of the first pouring temperature of cap.

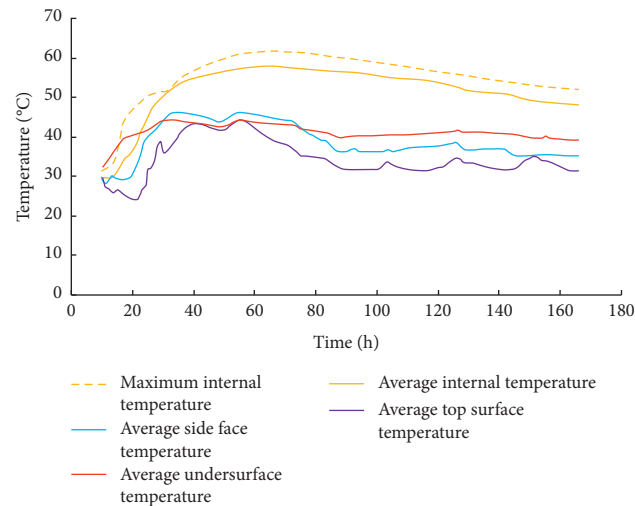


FIGURE 20: Monitoring results of second pouring temperature of cap.

TABLE 6: Analysis of measured results of cap temperature.

| Serial number | Temperature control item | Control standard | Measured value of first pouring (°C) | Measured value of second pouring (°C) |
|---------------|--|------------------------------|--------------------------------------|---------------------------------------|
| 1 | Temperature of pouring concrete | $\leq 26^{\circ}\text{C}$ | 25~30 | 24~28.5 |
| 2 | Maximum temperature of internal concrete | $\leq 65^{\circ}\text{C}$ | 64.5 | 61.6 |
| 3 | Temperature difference between the inner surface of concrete pouring body (including equivalent temperature of concrete shrinkage) | $\leq 28^{\circ}\text{C}$ | 26.6 | 24.6 |
| 4 | The rate of cooling of inside concrete | $\leq 2.0^{\circ}\text{C/d}$ | 2.1 | 1.98 |
| 5 | Temperature difference between surface of concrete and atmosphere | $\leq 20^{\circ}\text{C}$ | 16.1 | 17.1 |
| 6 | Temperature difference between inlet and outlet of cooling water | $\leq 10^{\circ}\text{C}$ | — | 9.8 |
| 7 | The temperature difference between the cooling water and the inside concrete when the water is first supplied or resupplied after interruption | $\leq 25^{\circ}\text{C}$ | 24.8 | — |
| 8 | Temperature difference between curing water and concrete surface | $\leq 15^{\circ}\text{C}$ | True | True |

7. Conclusions

- (1) The internal temperature of concrete reached the peak value 33 hours later after the first pouring while reached the peak value 41 hours later after the second pouring. The peak value time appeared earlier than the simulated peak time, indicating that temperature monitoring and temperature control measures are very necessary.
- (2) The 3D models in Figures 4 and 5 are established by MIDAS/civil finite element software. The simulated temperature peak value of the first pouring is 10.1°C lower than the measured value, and the simulated temperature peak value of the second pouring is 6.2°C lower than the measured value, which is mainly caused by the high temperature of pouring concrete.
- (3) In the whole casting process, the temperature difference between inlet and outlet of cooling water is small can meet the requirements of 10°C. But around the time when the internal temperature reaches the peak, the inlet and outlet temperature difference is large; the measured values are up to 25.1°C. It is recommended to adopt full water storage heat preservation and maintenance system, strengthen the regulation of reservoir water temperature, according to the change of temperature day and night. The temperature difference between water storage and concrete surface is controlled at about 10°C.
- (4) There is time lag effect in controlling the cooling rate of concrete pouring body by adjusting the temperature or flow of cooling water. Comparatively speaking, it is easy to control the temperature of concrete entering mold. The measured results show that the measured values of the first and second pouring of the temperature control project meet the requirements of the specification. The data show that the measures of this project can achieve good temperature control effect.

Data Availability

All data used to support the findings of this study are included within the article, and there are not any restrictions on data access.

Conflicts of Interest

The authors declare that they have no conflicts of interest.

Acknowledgments

This work was supported by the excellent teaching team of “Qinglan Project” in Jiangsu Universities, “Innovative Teaching Team of Road and Bridge Engineering Technology Specialty” (Teacher Letter Su (2021) no. 11) project.

References

- [1] J. H. Gao and S. L. Liu, “Analysis of thermal theory calculation and temperature control measures for mass concrete construction,” *Construction Machinery*, no. 2, pp. 52–58, 2019.
- [2] Z. Zhang, J. Bai, Y. Chen, and S. Yan, “An innovative approach for gob-side entry retaining in highly gassy fully-mechanized longwall top-coal caving,” *International Journal of Rock Mechanics and Mining Sciences*, vol. 80, pp. 1–11, 2015.
- [3] H. Wan and Z. H. Tan, “Anti-crack construction technology of mass concrete for main bridge cap of south dongting super large bridge,” *Journal of China & Foreign Highway*, vol. 37, no. 3, pp. 141–144, 2017.
- [4] J. F. Yuan, J. D. Zhang, and D. Liu, “Analysis on hydration heat and temperature control measures of high strength concrete block 0# of long-span continuous box girder bridge,” *Journal of China & Foreign Highway*, vol. 39, no. 5, pp. 97–101, 2019.
- [5] Y. He, J. L. He, P. Yu, B. Zhang, and X. Fu, “Study on temperature control of mass concrete for tower pile cap,” *Journal of Railway Science and Engineering*, vol. 17, no. 2, pp. 372–378, 2020.
- [6] S. C. Jin, W. Y. Xu, and Y. Y. Huang, “Study on the temperature control measures for pile cap mass concrete constructed layer by layer in winter,” *Railway Engineering*, vol. 59, no. 11, pp. 55–58, 2019.
- [7] G. A. Zhu, L. M. Dou, Z. L. Li, W. Cai, K. Yong, and J. Li, “Mining-induced stress changes and rock burst control in a variable-thickness coal seam,” *Arabian Journal of Geosciences*, vol. 5, no. 9, pp. 365–376, 2016.
- [8] M. Qiao, “Research and application of key technologies of temperature control in mass concrete construction of pile cap of a super-large bridge,” *Highway Engineer*, vol. 44, no. 5, pp. 135–141, 2019.
- [9] Y. X. Yang, H. X. Zhou, J. L. Ma et al., “Study on temperature control and distribution of mass concrete cap,” *Bulletin of the Chinese Ceramic Society*, vol. 38, no. 5, pp. 1497–1509, 2019.
- [10] Z. Yang, C. Liu, S. Tang, L. Dou, and J. Cao, “Rock burst mechanism analysis in an advanced segment of gob-side entry under different dip angles of the seam and prevention technology,” *International Journal of Mining Science and Technology*, vol. 28, no. 6, pp. 891–899, 2018.
- [11] Y. C. Wang, Y. Hua, and C. Zhang, “Influence of different temperature control measures on crack resistance of large-size concrete structure,” *Journal of Highway and Transportation Research and Development*, vol. 36, no. 3, pp. 109–116, 2019.
- [12] D. D. Zhang and Z. H. Yang, “Research on temperature control of large volume concrete construction by using space cooling net,” *Highway Engineer*, vol. 42, no. 3, pp. 282–285, 2017.
- [13] J. Z. Li and Y. L. Wang, “Study on dynamic curing design of pile cap massive concrete of Shanghai-Nantong Yangtze river bridge,” *Railway Standard Design*, vol. 60, no. 2, pp. 93–99, 2016.
- [14] Z. Q. Yang, C. Liu, F. S. Li, L.-m. Dou, G.-w. Li, and D.-w. Wang, “The mechanism and application of high-pressure water jet technology to prevent compound dynamic disaster,” *Arabian Journal of Geosciences*, vol. 14, no. 13, pp. 1–20, 2021.
- [15] Z.-Q. Yang, C. Liu, G.-A. Wang, G.-W. Li, and F.-S. Li, “Structural characteristics analysis of overlying rocks and prevention measures with a long-wall face passing across abandoned roadways: a case study,” *Shock and Vibration*, vol. 2021, Article ID 6665341, 15 pages, 2021.

- [16] J. He, *Research of Mining Dynamic Loading Effect and its Induced Rock Burst in Coal Mine*, China University of Mining and Technology, Xuzhou, China, 2013.
- [17] G. C. Zhang, L. J. Chen, Z. J. Wen et al., "Squeezing failure behavior of roof-coal masses in a gob-side entry driven under unstable overlying strata," *Energy Science & Engineering*, vol. 8, pp. 1–14, 2020.
- [18] M. Hu, W. Zhao, Z. Lu, J. Ren, and Y. Miao, "Research on the reasonable width of the waterproof coal pillar during the mining of a shallow coal seam located close to a reservoir," *Advances in Civil Engineering*, vol. 2019, Article ID 3532784, 14 pages, 2019.

Research Article

Analysis of the Influence of Upper Protective Layer Mining on the Effect of Pressure Relief and Protection of Coal and Rock Masses between the Lower Overburden Layers

Jiixin Dang ^{1,2}, Min Tu ^{1,2}, Xiangyang Zhang ^{1,2} and Qingwei Bu ^{1,3}

¹Key Laboratory of Coal Mine Safety and Efficiently Caving of Ministry of Education, Anhui University of Science and Technology, Huainan 232001, China

²School of Mining Engineering, Anhui University of Science and Technology, Huainan 232001, China

³School of Mining and Coal, Inner Mongolia University of Science and Technology, Baotou 014010, China

Correspondence should be addressed to Min Tu; mtu@aust.edu.cn

Received 26 September 2021; Accepted 12 October 2021; Published 31 October 2021

Academic Editor: Ruimin Feng

Copyright © 2021 Jiixin Dang et al. This is an open access article distributed under the Creative Commons Attribution License, which permits unrestricted use, distribution, and reproduction in any medium, provided the original work is properly cited.

Protective seam mining is an effective gas pressure relief method in deep mining. Effective theoretical calculation methods in the current studies on the prediction of pressure relief protection effect of interbed coal and rock masses and their distribution laws are lacking. Thus, the evaluation and research with respect to pressure relief effect in protective seam mining relatively lag behind. This situation restricts the engineering feasibility evaluation and decision making in the protective seam mining. Therefore, the influence of upper protective seam mining on the pressure relief protection effect of coal and rock mass between underlying beds was investigated in this study. On the basis of an analysis of concrete engineering projects, a mechanical model was constructed for the pressure relief protection effect of upper protective seam mining on the coal and rock mass between underlying beds. The distribution equation of pressure relief expansion ratio in the underlying protected seam was also derived. The influence laws of main influencing factors on the pressure relief protection effect of the protected seam were revealed as well. In the end, the pressure relief effect was analyzed and verified for the protected seam before and after mining through numerical simulation and similarity simulation test. The pressure relief effect of upper protective seam mining on the coal and rock mass between underlying beds and the distribution characteristics were deeply explored in this study, which could provide a theoretical reference for the decision making in the gas extraction engineering design and pre-evaluation of extraction effect. Results show that the effective pressure relief zone (expansion rate > 0.3%) of the protected seam beneath the goaf is located within the range of approximately 40 m from the coal wall to the rear part. It also presents an approximate “Λ-shaped distribution characteristic,” that is, it experiences migration and evolution with the advancement in the working face. Moreover, the peak pressure relief lags behind the coal wall on the working face by nearly 10–20 m. In the numerical simulation, the expansion ratio in the goaf also presents an approximate “Λ-shaped distribution.” Its effective pressure relief zone is the 50 m range from the coal wall to the rear part of the goaf, and the peak value lags behind the coal wall by around 15 m. The theoretical results and numerical simulation results are basically consistent with the physical experiment results. The expansion rates are 1.25%, 1.268%, and 1.32%, respectively. The elastic modulus E of coal seam and interbed spacing H are the main influencing factors of the swelling deformation and are negatively correlated with the expansion ratio. In the actual mining process, E and H of the protected layer can be measured to infer the expansion deformation of the protected layer.

1. Introduction

The deep high ground stress and coal and gas outburst disaster become increasingly severe as the coal resource development and utilization extend to deep parts. During

the deep mining process, the mining disturbance behaviors have a great bearing on the changes in the mechanical state of deep coal body and seepage field. Protective seam mining is an effective regional gas pressure relief method, and a large quantity of pressure relief gas at the protected seam is

emitted into the working face and goaf via the floor cracks in the mining process; thus, extracting the pressure relief gas in the protected seam is necessary [1–5].

Domestic (Chinese) and foreign scholars have always been dedicated to the studies on protective seam pressure relief mining and coal and gas disaster. Wang et al. [6] studied the evolution laws of floor cracks in the short-distance protective seam mining. They demonstrated that the coal mass in the pressure relief and permeability improving zone had large swelling deformation and high permeability, and this zone was also an efficient pressure relief gas intercept and extraction zone. Ren et al. [7] acquired the load-carrying condition of the protected seam through the similar material simulation test and determined the stress state after the coal seam deformation through the force analysis of the protected coal seam. They concluded that greater mining disturbance borne by the protected seam meant greater peak breaking stress of the coal mass and higher volumetric strain during the upper protective seam mining process under the same test conditions. Xue et al. [8] obtained the expression of internal displacement of the rock mass using a semi-infinite body model. They also constructed a “two-zone” crack distribution model and its simplified mechanical model to probe the pressure relief mechanism of protected seam. On the basis of a study of gas emission laws on the short-distance protective seam mining face, Wang et al. [9] optimized the pressure relief gas extraction parameters of protective seam. They obtained that the gas emissions on the protective seam mining face mostly came from the pressure relief gases at the protected seam. Zhang et al. [10] discussed the local stress concentration and rock breaking behavioral mechanisms in rock intercalation after the protective seam mining from longitudinal and transverse perspectives via numerical simulation and mechanical analysis. Under the engineering background of 10# mine in Pingdingshan, Zhang et al. [11] studied the crack evolution laws and distribution characteristics in the coal and rock mass between two coal seams. They found that the cracks were expanded with the increase in intensity of mining activity, and most cracks developed at low angle or became parallel to the stratum. Through physical model and numerical simulation, Wang et al. [12] investigated the stress distribution and crack evolution laws in surrounding rocks during the protective seam mining process under certain mining conditions. They stated that the displacement of surrounding rock and the evolution of cracks were affected by the support pattern.

At present, extensive research has been conducted at home and abroad on the development of overburden fissure zones and gas pressure relief caused by traditional protective coal seam mining, and important research results have been obtained [13–15]. Good research progress has also been made in the expansion trend area below the mined-out area. However, with the continuous advancement of the protective layer working face, there is currently no fixed theoretical formula for the expansion rate and expansion range of coal and rock masses with different buried depths under the goaf. It is impossible to grasp the expansion and deformation at different positions of the coal and rock mass underneath the goaf during the advancement of the working

face, nor can it accurately grasp the swelling area of the coal and rock mass underneath. The previous engineering experience or similar working face treatment methods are often used to determine the expansion changes of the underlying coal body, often with large deviations. Although there are related mechanical models to analyze the interaction between the protective layer and the protected layer, it still fails to reveal the specific factors that affect the expansion and deformation of the protected layer. Therefore, it is difficult to understand the real-time change law of the expanded range of the mined-out area. This paper takes the 11129 working face of Zhangji Coal Mine of Huainan Mining Group as the engineering background and explores the changing law and range of the expansion ratio of the protective layer under the goaf. The stress evolution process and the effective expansion zone change of the protected coal seam are theoretically deduced. The analytical solution of the expansion rate of the protected layer and its effective pressure relief range in the mining mode of the protective layer is given. It is verified by a combination of numerical simulation and similar simulation experiment. The research is expected to guide the engineering design and pre-evaluation decision making of protective layer mining and gas drainage pressure relief effects.

2. Analysis of Project Profile

The 8# coal in east (1) mining area of Zhangji Coal Mine has complicated geological conditions and high risk of coal and gas outburst. Thus, it does not meet the direct mining conditions. Upper protective seam mining is adopted to realize pressure relief and gas extraction of 8# coal. Meanwhile, 9# coal is mined at protective seam, where the average thickness of 9-1# coal is 1.9 m and that of 9-2# coal is 0.9 m. The average thickness of dirt band is 1.4 m, and the upper roof consists of siltstone with an average thickness of 8.0 m. The immediate roof is composed of quartz sandstone with an average thickness of 7.6 m. The lithology of immediate floor is mudstone with an average thickness of 2.5 m. The lithology of lower floor is siltstone with an average thickness of 5.2 m. The average thickness of 8# coal at the underlying protected seam is 4 m, and it is 9 m away from 9# coal. The recoverable strike and inclined lengths of 11129 working face, which is the first mining face of 9# coal, are 1,200 and 240 m, respectively. Its burial depth from the ground is 710 m. The general occurrence state of coal seam is a monoclinical structure, which is locally developed with secondary folds. The coal seam is generally high in the west and low in the east, and the dip angle ranges from 2° to 6°. The comprehensive histogram of the working face is shown in Figure 1.

8# coal at the protected seam is of low permeability, low gas drainage rate, and complicated geological conditions. Thus, the upper protective seam mining should be conducted for 8# coal to realize gas extraction and pressure relief. (1) The coal pillars reserved in the 9# coal goaf form displacement and stress fields in the mining process of 8# coal, which brings difficulty for the supporting and roadway layout of 8# coal working face and impedes the safety mining

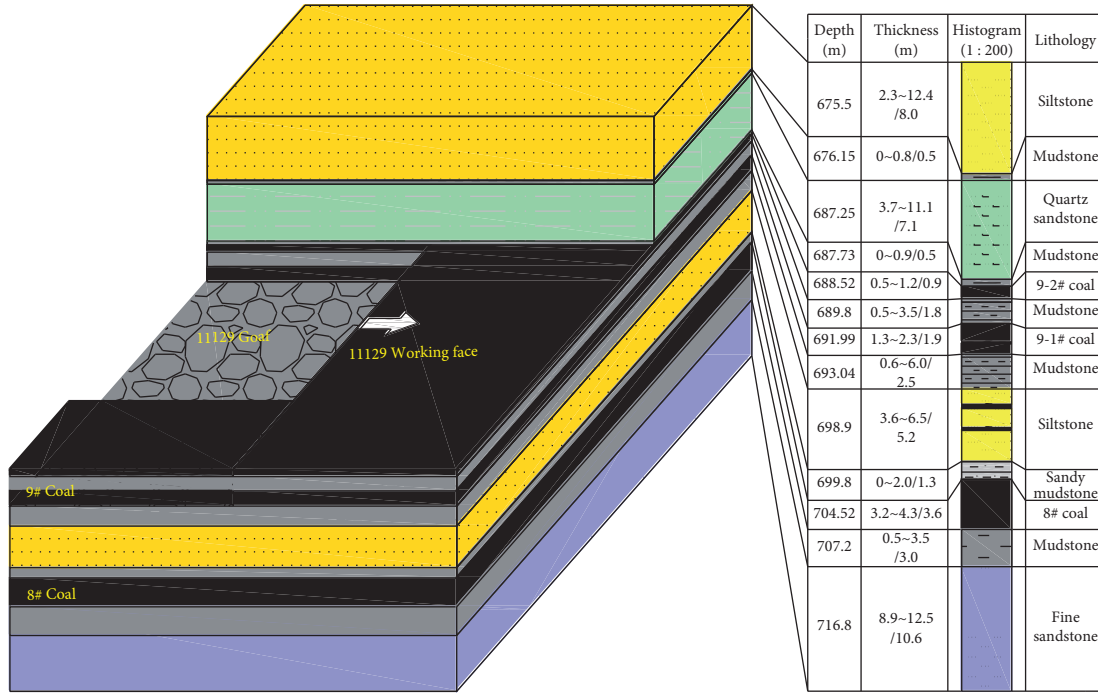


FIGURE 1: Comprehensive histogram of mining face in Zhangji Coal Mine.

and gas extraction of 8# coal. (2) During the 8# coal mining process at protected seam, the existence of 9# coal goaf will accelerate the fracture of bearing bed. As a result, the 9# coal goaf runs through 8# coal working face. Consequently, gas, water, and gangues in the goaf at upper coal seam are poured into 8# coal working face, and this condition harms the safety production of this coal mine [16]. (3) The pressure relief of 8# coal is good for gas extraction. Thus, the pressure relief zone and gas extraction engineering are closely combined to realize safe and efficient mining of 8# coal and maximize the economic benefit.

3. Mechanical Model Analysis of Pressure Relief Protection Effect of Upper Protective Seam Mining on Coal and Rock Masses between Underlying Beds

3.1. Mechanical Model of Mining-Induced Stress Distribution on the Floor of Working Face. Coal seam is usually under elastic deformation state before mining; in the mining process, the initial stress field of rock on the floor is affected by the mining, the floor in front of the working face is under the action of concentrated stress, the floor stress field is changed and redistributed, and the floor stress distribution depends on the transfer of concentrated stress in front of the working face to the lower rock mass of the coal seam floor [17, 18]. The following assumptions are considered: the coal and rock mass under the initial stress state of rock do not influence the stress redistribution of underlying coal and rock mass, the abutment pressure in front of the working face can be regarded as the triangular banding load from the coal wall to stress peak point and the trapezoid banding load

in front of the stress peak point, the floor is regarded as a uniform elastomer, and the problem is solved by a plain strain problem. The underlying rock and coal stress is then theoretically calculated [18].

To facilitate the computational analysis, the stress change in the coal mass and goaf is expressed in the form of increment:

$$\Delta\sigma_x = \sigma_x - \sigma_0. \quad (1)$$

The initial stress of rock is deducted from formula (1), and the distribution law of the stress increment at the coal side can be obtained. The maximum value of its stress increment is $(k-1)P$, while that in the goaf is $-P$. Thus, the distribution law of abutment pressure increment in coal body on the working face and the goaf can be acquired [19], as shown in Figures 2 and 3.

The expression of vertical stress is [19]

$$P(\xi) = m\xi + n. \quad (2)$$

According to the equilibrium of elastic mechanics, the equilibrium can be reached only when the following condition is satisfied:

$$(d_1 + d_2) \frac{k-1}{2} P = d_3 P + \frac{d_4}{2} P. \quad (3)$$

The following condition is then solved:

$$d_1 + d_2 = \frac{2d_3 + d_4}{k-1}. \quad (4)$$

To solve the stress at one point M within the half planar body, the coordinate axes are taken as shown in Figure 3, and the coordinates of point M are (x, y) . A minimum

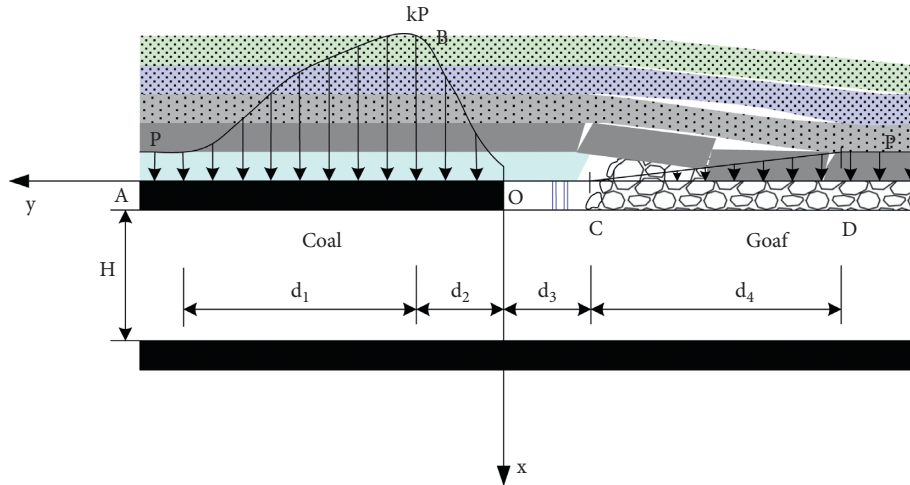


FIGURE 2: Abutment pressure distribution graph before and behind the working face.

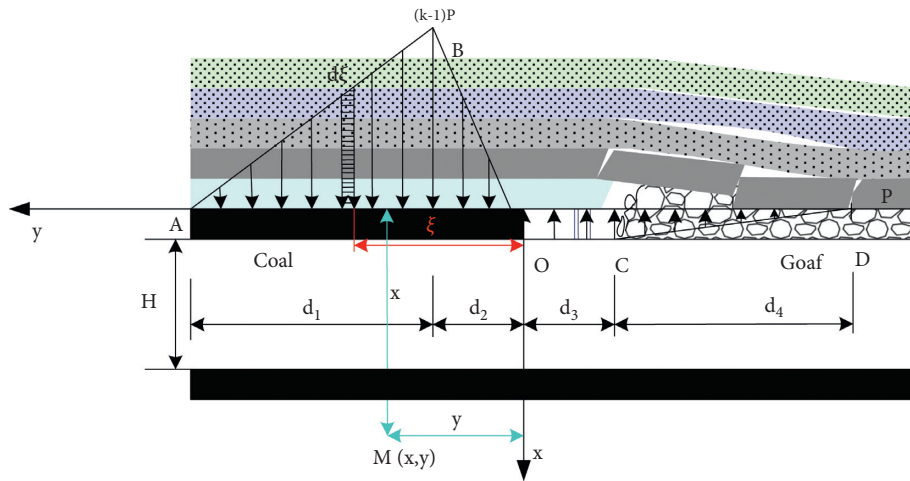


FIGURE 3: Simplified additional stress distribution graph before and behind the working face. P —vertical initial stress of rock, γH ; d_1 —length from peak advanced abutment pressure to the abutment pressure falling within the initial stress zone of rock; d_2 —length from coal wall of the working face to the peak abutment pressure; d_3 —length of goaf with zero initial stress of rock; d_4 —length from residual abutment pressure in the goaf until the initial stress of rock is recovered; and H —interbed spacing.

length $d\xi$ is taken at the place with a distance of ξ from the origin of coordinates O on the straight line Oy . The force $dP=qd\xi$ it bears is regarded as a minimal concentrated force, and the vertical and horizontal distances from point M to this minimal concentrated force dP are x and $y-\xi$, respectively. Thus, the stress caused by the minimal concentrated force $dF=qd\xi$ at point M is as observed in the following formula:

$$\left. \begin{aligned} d\sigma_x &= \frac{2qd\xi}{\pi} \frac{x^3}{[x^2 + (y - \xi)^2]^2} \\ d\sigma_y &= \frac{2qd\xi}{\pi} \frac{x(y - \xi)^2}{[x^2 + (y - \xi)^2]^2} \end{aligned} \right\} \quad (5)$$

The stresses caused by all minimal concentrated forces are superposed to solve the vertical and horizontal stress

distributions in front of the working face. Therefore, the integral equation of formula (5) is obtained as follows:

$$\left. \begin{aligned} \sigma_x &= -\frac{2}{\pi} \int \frac{p(\xi)x^3 d\xi}{[x^2 + (y - \xi)^2]^2} \\ \sigma_y &= -\frac{2}{\pi} \int \frac{p(\xi)x(y - \xi)^2 d\xi}{[x^2 + (y - \xi)^2]^2} \end{aligned} \right\} \quad (6)$$

The vertical and horizontal stresses are solved using formula (6).

The equation for the mining-induced stress distribution in the surrounding rocks on the floor perpendicular to the working face is

$$\sigma_x = -\frac{2}{\pi} \int \frac{(m\xi + n)x^3 d\xi}{[x^2 + (y - \xi)^2]^2} \quad (7)$$

The following condition is then solved:

$$\sigma_x = \left\{ \frac{mx^3 + (y - \xi)(my + n)x}{\pi[x^2 + (y - \xi)^2]^2} - \frac{(my + n)}{\pi} \arctan\left(\frac{y - \xi}{x}\right) \right\} \left| \begin{array}{c} d_1, \\ d_2, \\ d_3, \\ d_4 \end{array} \right. \quad (8)$$

The equation for the mining-induced stress distribution in the surrounding rocks on the floor in the advancement direction of the working face is

$$\sigma_y = -\frac{2}{\pi} \int \frac{(m\xi + n)x(y - \xi)^2 d\xi}{[x^2 + (y - \xi)^2]^2} \quad (9)$$

The following condition can be solved:

$$\sigma_y = -\frac{x}{\pi} \left\{ \frac{m[x^2 + y(y - \xi)] + n(y - \xi)}{x^2 + (y - \xi)^2} + \frac{n + my}{x} \arctan\left(\frac{y - \xi}{x}\right) - m \log[x^2 + (y - \xi)^2] \right\} \left| d_1, d_2, d_3, d_4 \right. \quad (10)$$

3.2. Mechanical Relation of Upper Protective Seam Mining with the Pressure Relief Protection Effect of Coal and Rock Masses between Underlying Beds. According to the physical

and geometric equations in the plane strain problem of the elastic mechanics, the vertical displacement can be solved as follows:

$$\begin{aligned} u_x &= \int \varepsilon_x dx = \int \frac{1 - \mu^2}{E} \left(\sigma_x - \frac{\mu}{1 - \mu} \sigma_y \right) dx \\ &= \frac{1}{2\pi E} \left\{ 2x(my + n)(2\mu^2 + \mu - 1) \arctan\left(\frac{y - \xi}{x}\right) \right. \\ &\quad \left. + (1 + \mu) \left[mx^2(3\mu - 1) + (-\mu mx^2 + (y - \xi)(my(\mu - 1) + n(4\mu - 2) + m\xi(3\mu - 1)) \log[x^2 + (y - \xi)^2] \right] \right\} \left| \begin{array}{c} d_1, \\ d_2, \\ d_3, \\ d_4 \end{array} \right. + K, \end{aligned} \quad (11)$$

where m and n are stress coefficients of $P(\xi)$ corresponding to d_1 , d_2 , d_3 , and d_4 ; E is the elastic modulus; μ is Poisson's ratio; and K is a constant.

The floor stress distribution in the advancement direction of the working face is divided into four stress zones: AB, BO, OC, and CD. The integrals of the abovementioned formulas are

solved. Then, complete stress distribution, strain, and displacement equations in vertical direction of the floor can be obtained.

In the protective seam mining process, the displacements of 8# coal roof and floor are calculated using the aforementioned formula, and the expansion ratio Q is further calculated as

$$\begin{aligned}
Q &= \frac{\Delta u}{h} \times 100\% \\
&= \frac{100\%}{2\pi h E} \left\{ \left[2x(m y + n)(2\mu^2 + \mu - 1) \arctan\left(\frac{y - \xi}{x}\right) \right. \right. \\
&\quad \left. \left. + (1 + \mu) \left[m x^2 (3\mu - 1) + (-\mu m x^2 + (y - \xi)(m y (\mu - 1) + n(4\mu - 2) + m \xi (3\mu - 1)) \log[x^2 + (y - \xi)^2] \right] \right] \right\} \\
&\quad \cdot (d_1, d_2, d_3, d_4) \left. \right\} (x_{=a} - x_{=a+h}),
\end{aligned} \tag{12}$$

where Δu is the displacement difference between roof and floor of the protected seam, m ; h is the average thickness of protected seam, m ; and a is the distance from protective seam to the roof of protected seam, m .

The fluctuation of expansion ratio Q can reflect the evolution law of pressure relief at the protected seam, and $Q > 0.3\%$ is taken as an effective pressure relief zone.

4. Influence Factor Analysis of Upper Protective Seam Mining on Pressure Relief Protection Effect of Protected Seam

The pressure relief effect of the protected seam is mainly related to stress concentration coefficient k , elastic modulus E of coal seam, coal seam thickness h , and interbed spacing H . According to the mine ground pressure laws and geological structural conditions, the engineering parameter k is taken as 2.5, μ value is 0.3, $E = 1$ GPa, $h = 4$ m, $H = 9$ m, $d_1 = 30$ m, $d_2 = 10$ m, $d_3 = 10$ m, and $d_4 = 40$ m. After external and human factors are excluded, different parameters are taken to comparatively analyze the changes in the roof stress and expansion ratio of 8# coal, as shown in Table 1 and Figures 4–11.

As shown above, the concentrated stress coefficient k mainly influences the abutment pressure in front of the coal wall, and it is in direct proportion to the abutment pressure. With the continuous increase in the coefficient k , 8# coal beneath the abutment pressure goes through swelling deformation, which has a very minor influence on the stress and swelling deformation in the rear goaf. Under $k = 2.5$, the maximum increment of abutment pressure in front of the coal wall is 18.5 MPa. As the elastic modulus is continuously increased, no influence is generated on the stress change of the protected seam, and the expansion ratio is gradually reduced. Moreover, the elastic modulus becomes inversely proportional to expansion ratio, and it is the result of joint action of coal seam properties and surrounding environment. Before the protective seam mining, the elastic modulus of the protected seam should be measured in advance to estimate the overall swelling deformation of the protected seam during the protective seam mining process. During the upper protective seam mining process, the change in the thickness of overlying coal seam has no obvious influence on the overall stress change or swelling deformation. As a result,

the thickness of coal seam is not the primary influencing factor of the swelling deformation. With the increase in the burial depth of the protected seam, the downward stress propagation is continuously reduced with the increase in interbed spacing, the swelling deformation is gradually mitigated, and the peak swelling deformation is gradually distant from the coal wall. The scopes of influence at two sides are also slightly enlarged, and both approach 0 in the end.

In summary, the main influencing factors of the swelling deformation of the protected seam are elastic modulus E of the coal seam and interbed spacing H . Other factors exert minor influences. In the actual mining process, the layer spacing H can be estimated, and the underlying coal rock mass is sampled by drilling holes into the protected layer. The mechanical properties of the rock samples were tested using the MTS rock mechanical performance testing machine, and the stress-strain curves of the rock samples were obtained, and then the elastic modulus E of the underlying coal rock mass was obtained.

5. Instance Analysis of Upper Protective Seam Mining Project in Zhangji Coal Mine

5.1. Example Calculation of Protective Seam Mining on 11129 Working Face of Zhangji Coal Mine. According to the geological conditions of 11129 working face and mine ground pressure law, the distance from the coal wall of the working face to the peak stress concentration is $d_2 = 10$ m, the distance from the peak stress concentration to the initial stress zone of rock in deep coal and rock mass in the front is $d_1 = 30$ m, the spatial width of the working face is $d_3 = 10$ m, the distance from the goaf to the initial stress zone of rock in the rear deep compacted goaf is solved as $d_4 = 40$ m, the stress concentration coefficient k is taken as 2.5, the initial stress of rock is 19 MPa, and the distance from the working face to the origin is 40 m. The aforementioned formula was used to calculate the displacement change of the roof and floor of the protected seam beneath the floor in the advancement direction of the working face. Mathematical software Wolfram Mathematica was used to solve the OA, AB, BC, and CD segments. The total vertical stress was obtained through the superposition, and the integral was taken to solve the vertical displacement.

TABLE 1: Values of different influencing factors.

| Stress concentration coefficient, k | Elastic modulus, E (GPa) | Coal thickness, h (m) | Interbed spacing, H (m) |
|---------------------------------------|----------------------------|-------------------------|---------------------------|
| 1.5 | 0.5 | 2 | 5 |
| 2 | 1 | 3 | 13 |
| 2.5 | 1.5 | 4 | 21 |
| 3 | 2 | 5 | 25 |

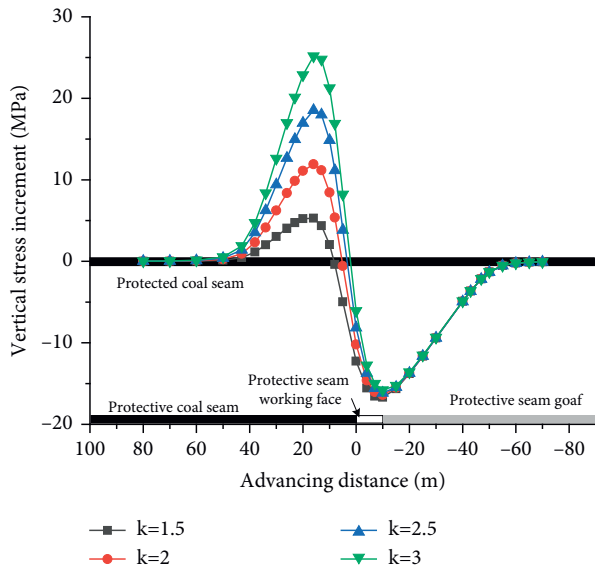


FIGURE 4: Different stress concentration coefficient stress variation curves.

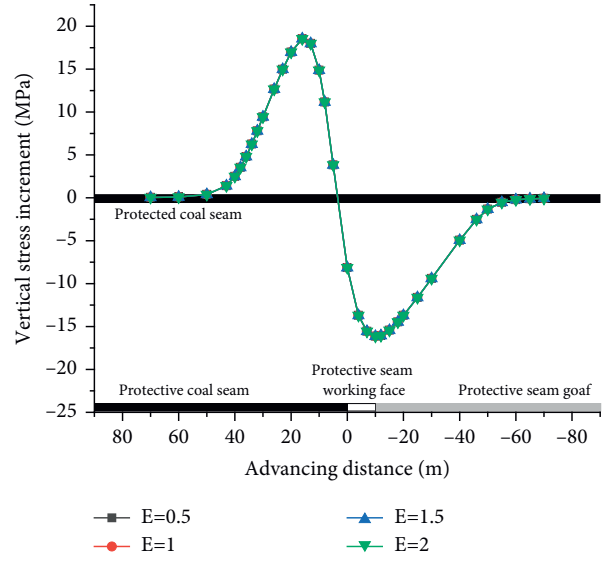


FIGURE 6: Different elastic modulus stress change curves.

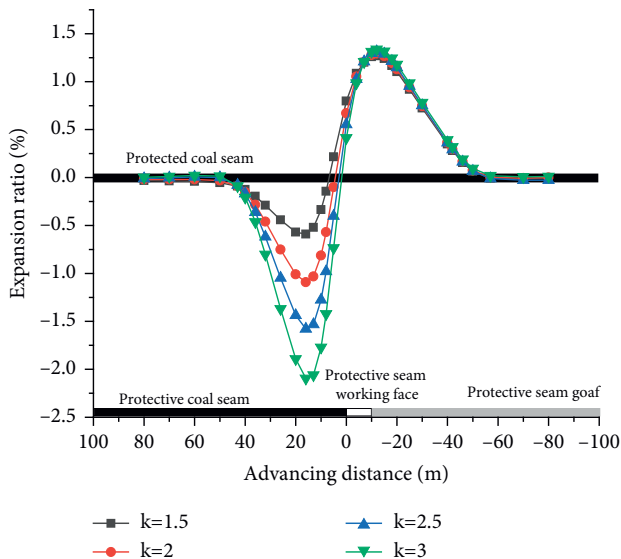


FIGURE 5: Variation curve of expansion rate with different stress concentration coefficients.

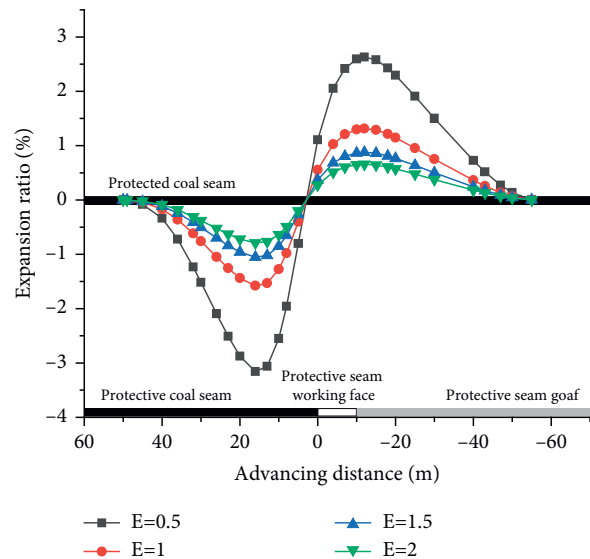


FIGURE 7: Variation curve of expansion rate with different elastic moduli.

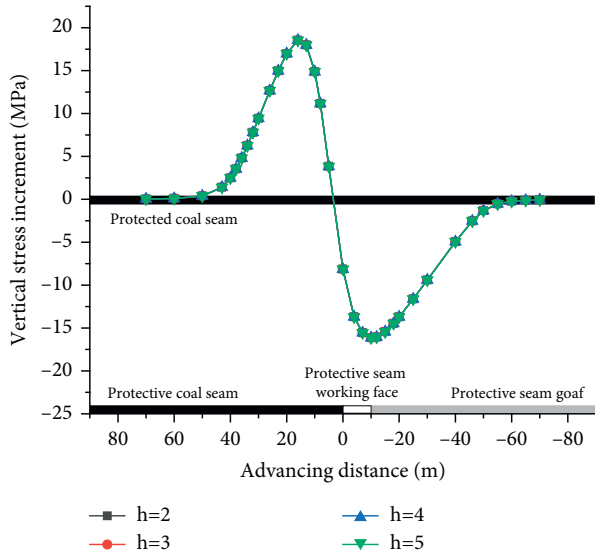


FIGURE 8: Stress variation curves of different coal thicknesses in the protected layer.

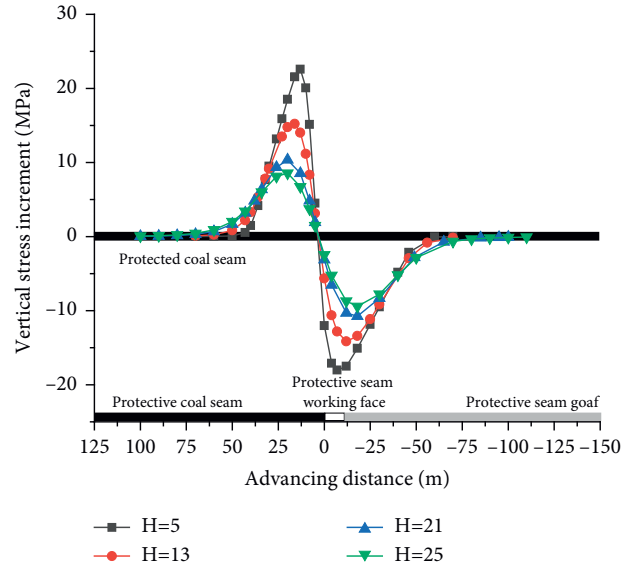


FIGURE 10: Stress variation curve diagram of different buried depths.

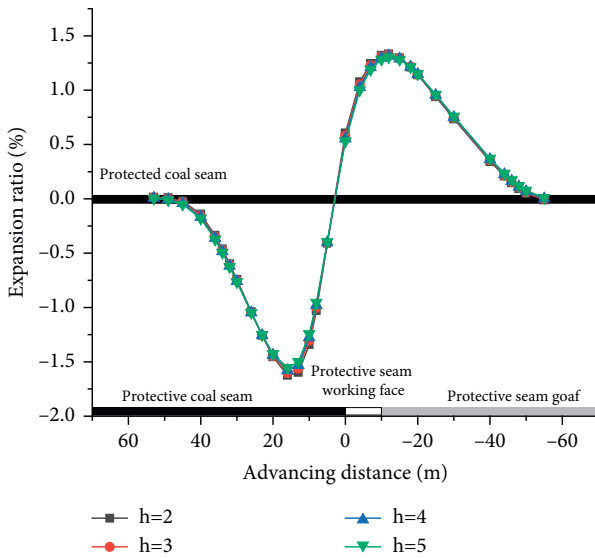


FIGURE 9: Variation curve of expansion rate of different coal thicknesses in the protected layer.

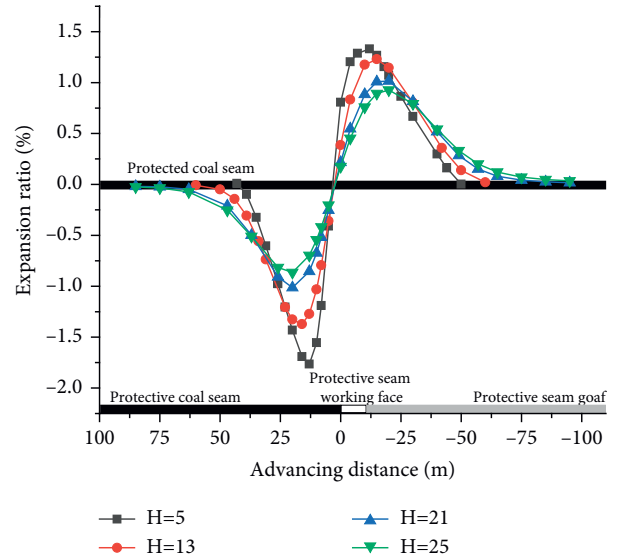


FIGURE 11: Variation curve of expansion rate at different buried depths.

The expression of vertical displacement in different phases is

$$\begin{cases} OA: p(\xi) = -0.95\xi, \\ AB: p(\xi) = -4.75\xi + 171, \\ BC: p(\xi) = -19, \\ CD: p(\xi) = -0.475\xi - 42.75. \end{cases} \quad (13)$$

The vertical stress $\Delta\sigma_x$ of the protected seam is

$$\begin{aligned} \Delta\sigma_x = \sigma_{x1} + \sigma_{x2} + \sigma_{x3} + \sigma_{x4} = & \frac{19(C - D)}{\pi} + 0.1512x \\ & + B(-54.431 - 1.512y) \\ & + F(-13.608 - 0.151y) + D(13.608 + 0.151y) \\ & + 0.302y(A - B) + C(54.431 + 1.512y) \end{aligned}$$

$$\begin{aligned}
& + \frac{x[-1632.93 - 1.814x^2 + y(-108.862 - 1.814y)]}{x^2 + (30 + y)^2} \\
& + \frac{19x}{\pi} \left[\frac{40 + y}{x^2 + (40 + y)^2} - \frac{50 + y}{x^2 + (50 + y)^2} \right] \\
& + \frac{x[608.387 + 0.151x^2 + y(21.168 + 0.151y)]}{x^2 + (50 + y)^2} \\
& + \frac{x[2177.24 + 1.512x^2 + y(114.91 + 1.512y)]}{x^2 + (40 + y)^2},
\end{aligned} \tag{14}$$

where

$$\begin{aligned}
A &= \arctan \frac{y}{x}, B = \arctan \frac{30 + y}{x}, C = \arctan \frac{40 + y}{x}, \\
D &= \arctan \frac{50 + y}{x}, F = \arctan \frac{90 + y}{x}.
\end{aligned} \tag{15}$$

The roof and floor displacement u_x of the protected seam is

$$\begin{aligned}
u_x &= \int \varepsilon_x dx \\
&= -0.74298B + 1.10072C + 0.221126D - 0.557237H \\
&+ B[-0.000354x^2 + y(-0.049532 - 0.000826y)] + H[-29 \times 10^{-6}x^2 + y(-0.01238 - 0.0000688y)] \\
&+ D[-29 \times 10^{-6}x^2 + y(0.007826 + 0.0000688y)] \\
&+ C[0.0002948x^2 + y(0.055036 + 0.000688y)] \\
&+ A(0.000059x^2 + 0.0001376y^2) \\
&+ x \left[0.000157y \arctan \frac{y}{x} + (-0.0283 - 0.00094y) \arctan \frac{30 + y}{x} \right. \\
&\left. + (0.031449 + 0.000786y) \arctan \frac{40 + y}{x} + (0.003931 + 0.000079y) \arctan \frac{50 + y}{x} + (-0.007076 - 0.000079y) \arctan \frac{90 + y}{x} \right] + K,
\end{aligned} \tag{16}$$

where

$$\begin{aligned}
A &= \log[x^2 + y^2], B = \log[x^2 + (30 + y)^2], \\
C &= \log[x^2 + (40 + y)^2], \\
D &= \log[x^2 + (50 + y)^2], H = \log[x^2 + (90 + y)^2].
\end{aligned} \tag{17}$$

The change in the roof and floor displacement is calculated. Then, the formula of expansion ratio Q at the protected seam is further solved as

$$Q = \frac{\Delta u}{h} \times 100\% = \frac{u_{x=9} - u_{x=13}}{h} \times 100\%. \tag{18}$$

According to the aforementioned calculation results, the change charts of the roof and floor displacement of the protected seam and the expansion ratio are drawn as shown in Figures 12 and 13.

The distribution environment of roof and floor displacement changes in 8# coal was analyzed, as shown in Figure 12. As the upper protective seam mining was influenced by the abutment pressure concentration on the front coal seal, 8# coal undertook increasing vertical pressure. Its roof and floor displacements reached the maximum

values of 0.32 and 0.26 m, respectively. With the stress relief of surrounding rocks in the goaf behind the coal wall, underlying 8# coal experienced upward swelling deformation. The maximum deformation of the top plate is 0.34 m at 15 m behind the coal wall, and the maximum deformation of the bottom plate is 0.289 m at 18 m behind the coal wall. The expansion deformation value of the top and bottom plates of the protected layer gradually attenuates as it approaches and moves away from the coal wall and eventually approaches zero.

On the basis of Figure 13, the change curve chart of expansion ratio at the protective seam beneath the floor of the working face was analyzed. The protective seam mining facilitated the stress relief of surrounding rocks on the floor behind the coal wall and was influenced by the downward transfer of abutment pressure on the front coal wall. The coal and rock mass on the working face and that beneath the goaf went through swelling deformation, and the expansion ratio of underlying coal and rock mass reached the maximum value of 1.25% at the place 12 m behind the coal wall. With the advancement in the working face, the expansion ratio of overlying coal and rock mass was gradually reduced and approached 0. The effective scope of expansion (expansion

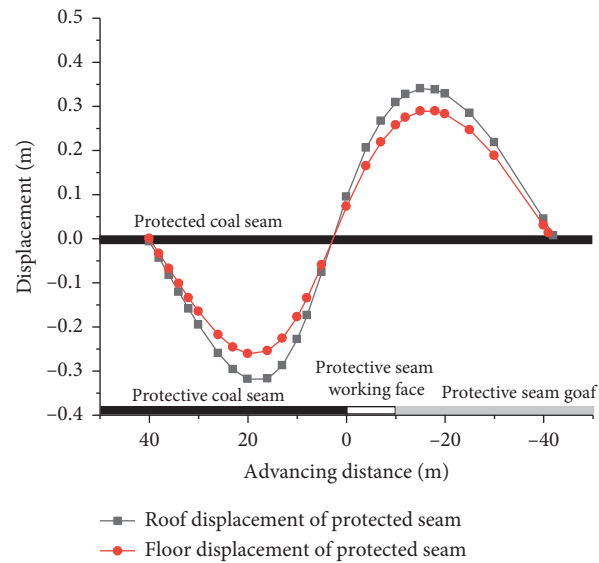


FIGURE 12: Curve of displacement change of the top and bottom plates of the protected layer.

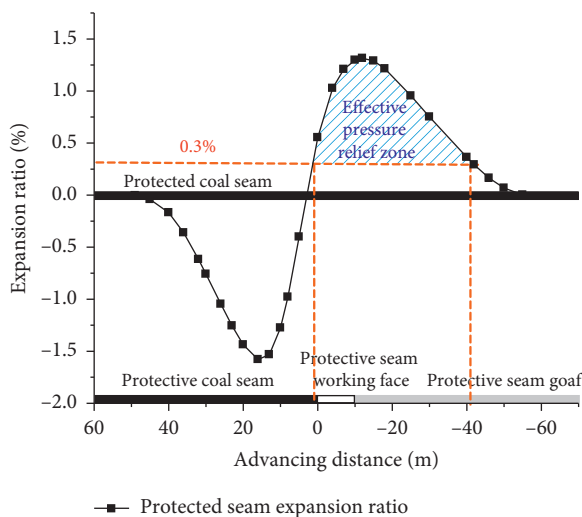


FIGURE 13: Change curve of expansion rate of protected layer.

ratio > 0.3%) was from the coal wall to the place 40 m behind the coal wall, and the floor heaving was the most obvious in this scope. Meanwhile, the pressure relief effect of the protected seam was the best.

5.2. Simulation Analysis of Protective Seam Mining Effect on 11129 Working Face in Zhangji Coal Mine. A numerical model was established via FLAC3D numerical simulation software, with dimensions of 540 m × 1000 m × 169 m (Figure 14). The mechanical properties of rock samples were tested by MTS rock mechanical property testing machine, and the stress-strain curve of rock samples was obtained. The elastic modulus can be solved by slope. In order to ensure the reliability of data, the average value of

three lithologic experiments in each group is taken. The mechanical parameters of the roof and floor are shown in Table 2. Fixed horizontal displacement constraints were set at the bottom edge, front, back, left, and right boundaries of the model. The Mohr–Coulomb failure criterion was also adopted to analyze the mechanical characteristics of coal and rock mass in this model. Domestic and foreign scholars have conducted several experiments and studies on the abutment effect of equivalent filled rock mass in goafs [20–24]. In the present study, the goaf was simulated with double-yield model. The stress-strain relation of the rock mass in the goaf is presented in Table 3, and the mechanical parameters of the rock mass in the double-yield goaf are presented in Table 4.

The advancement in 11129 working face from the open-off cut along the strike (positive direction of axis y) was simulated, the open-off cut was nearly 200 m from the boundary, and the influence of boundary effect was eliminated. The excavation step size was 25 m, the goaf was filled, balanced, and advanced by 600 m along the strike, and the mining was stopped at $y = 800$ m. The displacement changes of 8# coal roof and floor at 9 m beneath it during the mining process are shown in Figures 15–19.

Figures 15–17 shows that with the advancement in the working face, a goaf was formed, the stress was redistributed, and an abutment pressure zone higher than the initial stress of rock was formed in the coal and rock mass around the goaf. The surrounding coal and rock masses subsided, and the overlying coal and rock mass in the goaf experienced upward swelling deformation. The overall displacement was large at two sides and small in the middle, and that in the middle presented a waved change. The maximum floor heaving amounts of underlying 8# coal roof and floor in the goaf were 0.268 and 0.215 m, respectively. The maximum

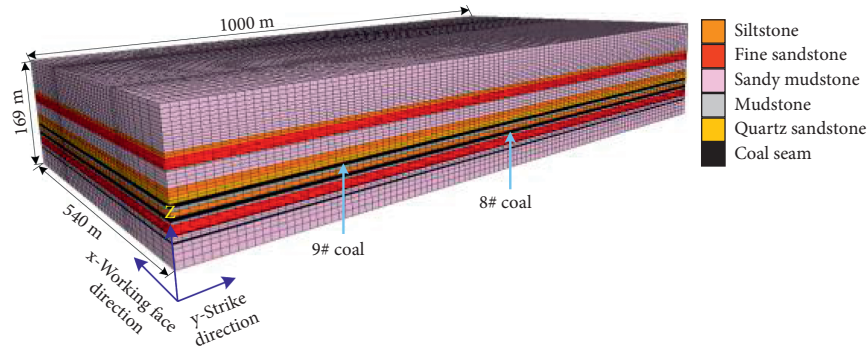


FIGURE 14: 3D numerical simulation model.

TABLE 2: Mechanical parameters of roof and floor rock strata at the coal seam.

| Lithology | Density (kg/m ³) | Bulk modulus (GPa) | Shear modulus (GPa) | Tensile strength (MPa) | Cohesion (MPa) | Internal friction angle (°) |
|------------------|------------------------------|--------------------|---------------------|------------------------|----------------|-----------------------------|
| Sandy mudstone | 2605 | 2.16 | 1.69 | 0.38 | 2.6 | 27 |
| Siltstone | 3211 | 10.48 | 8.19 | 0.44 | 2.85 | 28 |
| Quartz sandstone | 2600 | 21.03 | 13.53 | 0.47 | 2.8 | 30 |
| 9-2# coal | 1300 | 0.83 | 0.38 | 0.29 | 1.8 | 24 |
| Mudstone | 2554 | 3.23 | 1.85 | 0.32 | 2.2 | 28 |
| 9-1# coal | 1300 | 0.83 | 0.38 | 0.29 | 1.8 | 24 |
| Mudstone | 2554 | 3.23 | 1.85 | 0.32 | 2.2 | 28 |
| Siltstone | 3211 | 10.48 | 8.19 | 0.44 | 2.85 | 28 |
| Sandy mudstone | 2605 | 2.16 | 1.69 | 0.38 | 2.6 | 27 |
| 8# coal | 1300 | 0.83 | 0.38 | 0.29 | 1.8 | 24 |
| Mudstone | 2554 | 3.23 | 1.85 | 0.32 | 2.2 | 28 |

TABLE 3: Stress-strain relation of rock mass in the double-yield model goaf.

| Strain | Stress (MPa) | Strain | Stress (MPa) | Strain | Stress (MPa) |
|--------|--------------|--------|--------------|--------|--------------|
| 0.01 | 0.37 | 0.07 | 4.00 | 0.13 | 15.9 |
| 0.02 | 0.79 | 0.08 | 5.01 | 0.14 | 21.2 |
| 0.03 | 1.26 | 0.09 | 6.25 | 0.15 | 29.7 |
| 0.04 | 1.80 | 0.10 | 7.79 | 0.16 | 45.7 |
| 0.05 | 2.42 | 0.11 | 9.75 | 0.17 | 87.5 |
| 0.06 | 3.15 | 0.12 | 12.3 | | |

TABLE 4: Mechanical parameters of main rock materials in the goaf.

| Category | Density (kg/m ³) | Bulk modulus (GPa) | Shear modulus (GPa) | Internal friction angle (°) | Dilatancy angle (°) |
|----------|------------------------------|--------------------|---------------------|-----------------------------|---------------------|
| Value | 2000 | 11.1 | 8.3 | 13 | 7 |

abutment pressure borne by the coal wall around 8# coal beneath the goaf was 37.4 MPa, which was higher than the initial stress (18.4 MPa) of rock. The marginal position of the goaf carried the minimum stress, and the stress in the middle of the goaf was gradually increased [25–27].

As shown in Figures 18 and 19, the overall central displacements of the roof and floor fluctuated within 0.1–0.2 m and 0.07–0.15 m, the overall average expansion ratio was 1.286% when the mining face was advanced by 600 m, and the scope of influence of average expansion was

from the coal wall to 50 m behind the coal wall. The peak pressure relief lagged behind the coal wall by nearly 20 m, and it presented an “Λ-shaped distribution” on the whole. With the advancement in the working face, the goaf was gradually compacted, and local rebounding and recompaction process existed within a small scope.

5.3. Similarity Simulation Test Analysis of Protective Seam Mining Effect of 11129 Working Face in Zhangji Coal Mine.

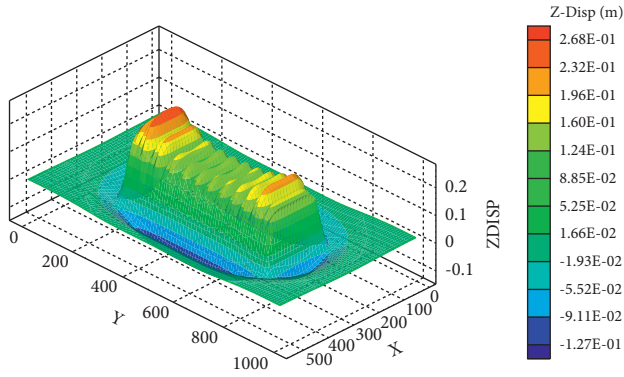


FIGURE 15: Simulation diagram of the displacement of the protected roof.

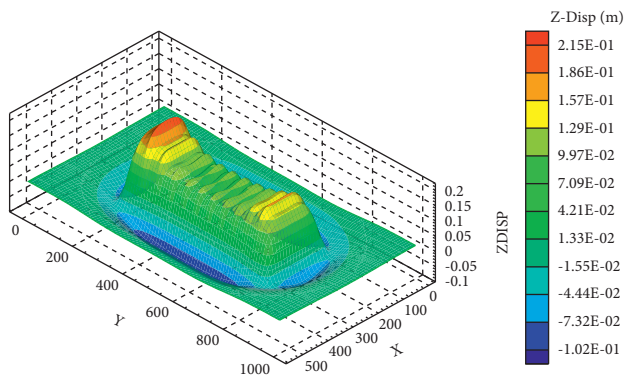


FIGURE 16: The simulation diagram of the displacement change of the protected bottom plate.

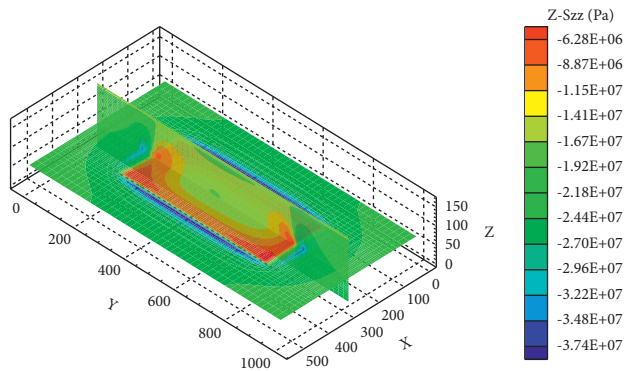


FIGURE 17: The stress change simulation diagram of the protected roof.

The similarity simulation test was conducted under the engineering background of 9# coal at the upper protective seam and 8# coal at the protected seam in Zhangji Coal Mine. The model testbed was made of steel frame with dimensions of 3.0 m (length) × 1.2 m (height) × 0.3 m (width). The model test should satisfy the following conditions: geometric similarity, kinematic similarity, dynamic

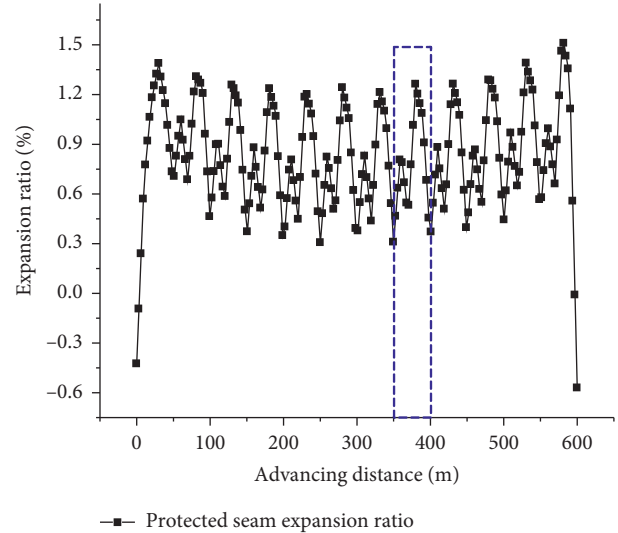


FIGURE 18: Change curve of protected expansion rate.

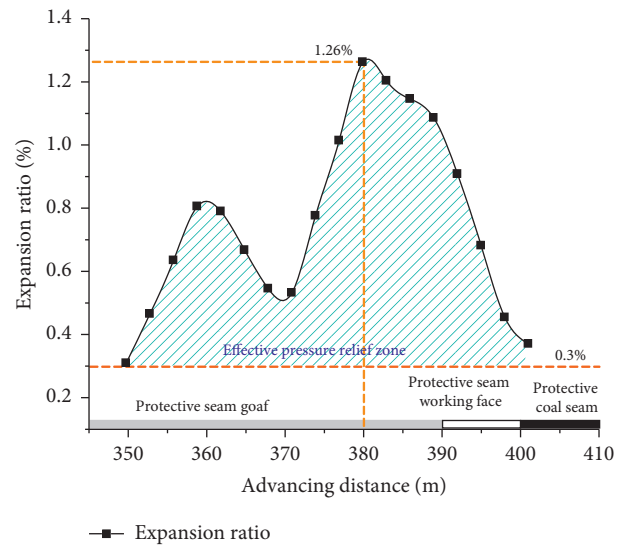


FIGURE 19: The curve of the average expansion range of 350m~400 m intercepted by the protected layer.

similarity, similarity of boundary conditions, and proportionating physical quantities. Therefore, the linear ratio was taken as 1 : 100, volume weight ratio was 3 : 5, and time ratio was 1 : 12. The ratio table of the main layers of the experimental model is shown in Table 5. The model and the distribution of measuring points are shown in Figures 20 and 21.

Strain gauges were laid on the protected seam and deformation monitoring points were arranged to perform real-time monitoring of 8# coal pressure and deformation of coal and rock mass. A total of 8 strain gauges are arranged in the horizontal direction, the middle 2#-7# strain gauges are spaced 30 cm apart, and the two ends of the strain gauges 1# and 8# are spaced 30 cm apart from the end of the steel

TABLE 5: Experimental model ratio.

| Lithology | Thickness (cm) | Matching number (sand : lime : plaster) | Sand (kg) | Lime (kg) | Plaster (kg) | Water (kg) |
|------------------|----------------|---|-----------|-----------|--------------|------------|
| Sandy mudstone | 16.5 | 9 : 0.5 : 0.5 | 200.48 | 11.14 | 11.14 | 22.75 |
| Siltstone | 8.0 | 8 : 0.6 : 0.4 | 96.0 | 7.2 | 4.8 | 10.8 |
| Mudstone | 0.5 | 8 : 0.6 : 0.4 | 6.0 | 0.45 | 0.3 | 0.7 |
| Quartz sandstone | 7.6 | 7 : 0.5 : 0.5 | 89.8 | 6.4 | 6.4 | 10.3 |
| 9-2# coal | 0.9 | 8 : 0.7 : 0.3 | 10.8 | 0.95 | 0.41 | 1.2 |
| Mudstone | 1.8 | 8 : 0.6 : 0.4 | 21.6 | 1.62 | 1.08 | 2.4 |
| 9-1# coal | 1.9 | 8 : 0.7 : 0.3 | 22.8 | 2.0 | 0.86 | 2.6 |
| Mudstone | 2.5 | 8 : 0.6 : 0.4 | 30.0 | 2.25 | 1.5 | 3.4 |
| Siltstone | 5.2 | 8 : 0.6 : 0.4 | 62.4 | 4.68 | 3.12 | 7.0 |
| Sandy mudstone | 1.3 | 9 : 0.5 : 0.5 | 15.8 | 0.88 | 0.88 | 1.8 |
| 8# coal | 3.6 | 8 : 0.7 : 0.3 | 43.2 | 3.78 | 1.62 | 4.9 |

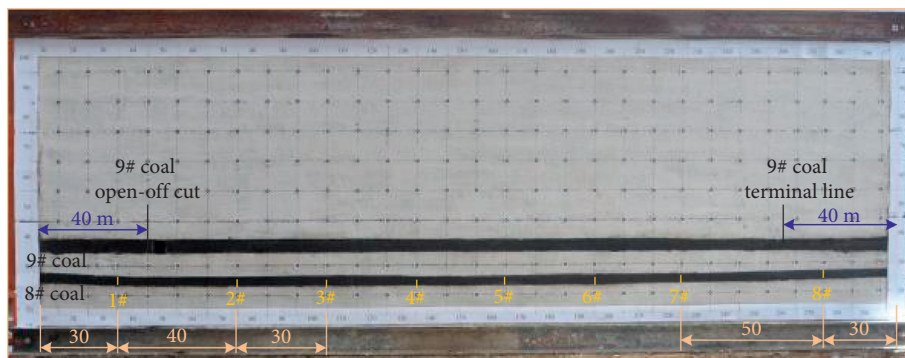


FIGURE 20: Unexcavated model diagram of similar simulation test.

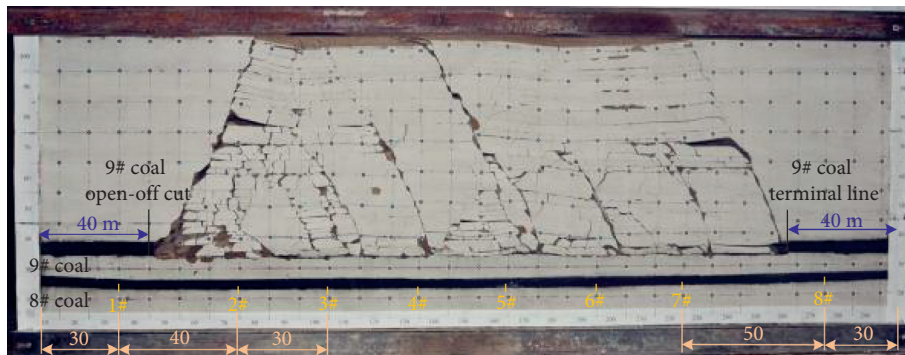


FIGURE 21: Model diagram after excavation of similar simulation test.

frame. The strain change curves at measuring points 1#–8# are shown in Figures 22 and 23.

As shown in Figures 22 and 23, the protective seam mining resulted in the stress relief of the underlying protected seam, and the roof and floor of the protected seam experienced upward swelling deformation. As the working face was advanced from the open-off cut to 40 m before the mining stopping line, the maximum roof and floor displacements were 0.267 and 0.216 m, respectively. The maximum expansion ratio (1.32%) was reached at 14.5 m behind the coal wall. The effective pressure relief zone was from the coal wall to 47 m behind the coal wall, which was approximate to the theoretical analysis and numerical simulation results.

5.4. Guidance and Suggestions for the Gas Extraction Design Scheme of Underlying Protected Seam. The 9# coal was close to the underlying 8# coal seam, and pressure relief gas of 8# coal (8# coal gas pressure was 1.52 MPa, and gas content was 5.5 m³/t) would surge into the goaf of 9# coal working face during the mining period of 9# coal working face. The extraction and drainage were simultaneously implemented in the upper protective seam mining, drilling was done toward upper strata in the floor roadway in the form of meshes, and the gas drainage of 8# coal seam was conducted within the effective pressure relief zone. Thus, the gas in the pressure relief zone was effectively prevented from permeating into the upper goaf, and the safe and efficient mining of the working face could be guaranteed.

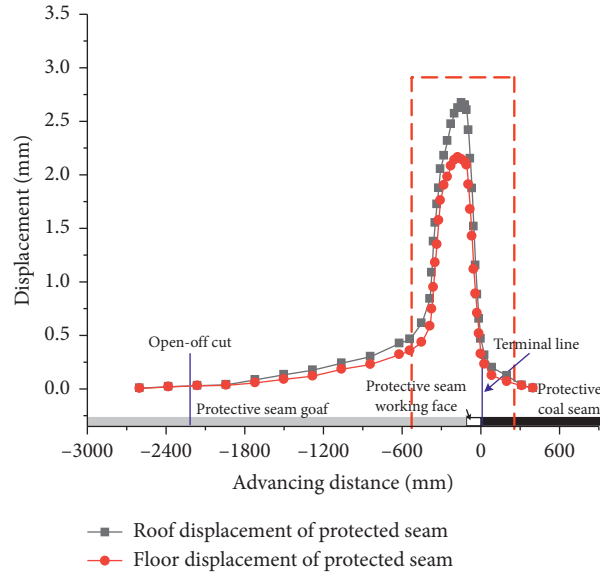


FIGURE 22: Displacement curve of the top and bottom plates of the protected layer.

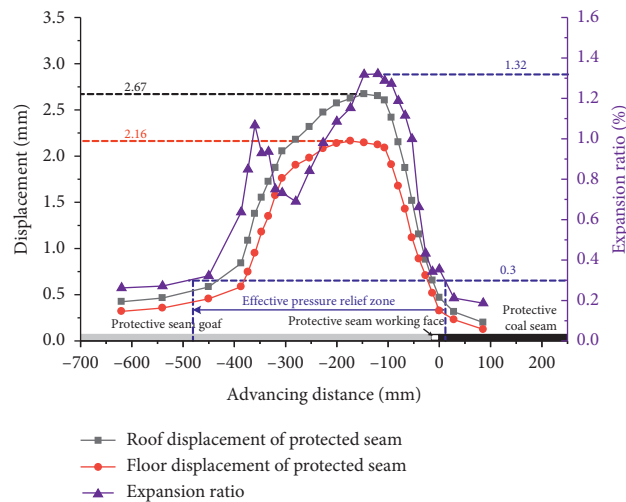


FIGURE 23: Change curve of protective layer expansion rate.

6. Conclusions

- (1) A mechanical model was constructed for the pressure relief protection effect of upper protective seam mining on the coal and rock mass between underlying beds. The equation for the expansion ratio distribution of underlying protected seam was also acquired. The pressure relief evolution laws of the protected seam before and after mining were further analyzed and verified through numerical simulation and similarity simulation test. The theoretical results are basically consistent with the numerical simulation results. The expansion rates are 1.25% and 1.268%, respectively, and the physical experimental results are 1.32%. The major reason for the results may be man-made reasons in the process of model making and mining.
- (2) The effective pressure relief zone of the protected seam was located within the range from the coal wall to nearly 40 m behind it, and it presented an approximate “ Λ -shaped distribution.” With the advancement, migration, and evolution of the working face, the peak pressure relief lagged behind the coal wall by around 10–20 m. The numerically simulated expansion ratio in the goaf also presented an approximate “ Λ -shaped distribution.” The effective pressure relief zone was from the coal wall to approximately 50 m behind the goaf, and the peak value lagged behind the coal wall of the working face by around 15 m.
- (3) The elastic modulus E of coal seam and interbed spacing H were the main influencing factors of the swelling deformation, and they were negatively

correlated with the expansion ratio. Meanwhile, the influence of coal seam thickness on the overall selling deformation could be neglected. The interbed spacing was one of the primary influencing factors of the stress change of the protected seam. The change in the stress concentration coefficient k had an obvious effect on bearing the pressure of the coal and rock mass in front of the coal wall. However, it had no obvious pressure relief effect on the underlying protected seam in the rear goaf.

- (4) The expansion ratio and expansion zone of the protected seam were mastered in a real-time way, and the pressure relief degree and its scope of influence were reflected. With the advancement in the working face of protective layer, the peak expansion ratio in the goaf was also followed up timely. A good pressure relief zone was also provided for the gas extraction from the highly gassy coal seam. This study provides a theoretical reference for the decision making in the gas extraction engineering design and pre-evaluation of extraction effect.

Data Availability

The data generated or analyzed during this study are included within this article.

Conflicts of Interest

The authors declare that they have no conflicts of interest.

Authors' Contributions

Jiaxin Dang and Qingwei Bu conducted theoretical calculation and analysis; Jiaxin Dang, Min Tu and Xiangyang Zhang conducted field data collection; Jiaxin Dang and Qingwei Bu conducted numerical simulation analysis; Jiaxin Dang wrote the manuscript.

Acknowledgments

This study was supported by the NSFC Project (52074008), Anhui Collaborative University Innovation Project (GXXT-2020-056), Inner Mongolia Natural Science Foundation Project (2019MS05055), and Open Research Fund Project of Key Laboratory of Safety and High-Efficiency Coal Mining of Ministry of Education (JYBSYS2019208).

References

- [1] M. B. Díaz Aguado and C. González Nicieza, "Control and prevention of gas outbursts in coal mines, Riosa-Olloniego coalfield, Spain," *International Journal of Coal Geology*, vol. 69, no. 4, pp. 253–266, 2007.
- [2] K. Noack, "Control of gas emissions in underground coal mines," *International Journal of Coal Geology*, vol. 35, no. 1–4, pp. 57–82, 1998.
- [3] S. Zhenqi, L. Yixue, and C. Mengbo, "Discussion on the manifestation of abutment pressure before and after rock beam fracture and its application," *Shandong Mining Institute Journal*, vol. 1, no. 1, pp. 27–39, 1984.
- [4] R. M. Flores, "Coalbed methane: from hazard to resource," *International Journal of Coal Geology*, vol. 35, no. 1, pp. 3–26, 1998.
- [5] Z. Cao, X. He, E. Wang, and B. Kong, "Protection scope and gas extraction of the low-protective layer in a thin coal seam: lessons from the DaHe coalfield, China," *Geosciences Journal*, vol. 22, no. 3, pp. 487–499, 2018, https://www.infona.pl/resource/bwmeta1.element.springer-000000012303/tab/jContent/facet?field=%5ejournalYear%5ejournalVolume&value=%5e_02018%5e_00022.
- [6] W. Wang, Y. P. Cheng, and L. Yuan, "Floor fracture evolution and relief gas drainage timeliness in deeper underground short-distance upper protective coal seam extraction," *Journal of China Coal Society*, vol. 41, no. 3, 2016.
- [7] W. Ren, H. Zhou, D. Xue, and L. Wang, "Mechanical behavior and permeability of coal and rock under strong mining disturbance in protected coal seam mining," *Meitan Xuebao/Journal of the China Coal Society*, vol. 44, no. 5, pp. 1473–1481, 2019.
- [8] D. J. Xue, H. W. Zhou, L. Kong, T. Zhao, H. Yi, and X. L. Tang, "Mechanism of unloading-induced permeability increment of protected coal seam under mining," *Yantu Gongcheng Xuebao/Chinese Journal of Geotechnical Engineering*, vol. 34, no. 10, pp. 1910–1916, 2012.
- [9] H. F. Wang, Y. P. Cheng, D. M. Wu, and H. Y. Liu, "Gas emission and parameter optimization of gas extraction in mining face of short distance protective seam," *Journal of China Coal Society*, vol. 35, no. 4, pp. 590–594, 2010.
- [10] M. Zhang, H. Shimada, T. Sasaoka, K. Matsui, and L. Dou, "Evolution and effect of the stress concentration and rock failure in the deep multi-seam coal mining," *Environmental Earth Sciences*, vol. 72, no. 3, pp. 629–643, 2014.
- [11] D. Zhang, X. Qi, G. Yin, and B. Zheng, "Coal and rock fissure evolution and distribution characteristics of multi-seam mining," *International Journal of Mining Science and Technology*, vol. 23, no. 6, pp. 835–840, 2013.
- [12] W. Cheng, Z. Nong, L. Guichen, and Z. Nianchao, "Destressed mining of multi-seams: surrounding rock control during the mining of a roadway in the overlying protected seam," *Mining Science and Technology*, vol. 21, no. 2, pp. 159–164, 2011.
- [13] H. P. Xie, H. W. Zhou, D. J. Xue, and P. Peak, "Theory, technology and engineering of simultaneous exploitation of coal and gas in China," *Journal of China Coal Society*, vol. 39, no. 8, pp. 1391–1397, 2014.
- [14] Y. Liu, F. Zhou, J. Wang, and J. Liu, "Approach to increasing the quality of pressure-relieved gas drained from protected coal seam using surface borehole and its industrial application," *International Journal of Coal Science & Technology*, vol. 2, no. 1, pp. 46–51, 2015.
- [15] P. Lu, P. Li, J. Chen, C. Zhang, J. Xue, and T. Yu, "Gas drainage from different mine areas: optimal placement of drainage systems for deep coal seams with high gas emissions," *International Journal of Coal Science & Technology*, vol. 2, no. 1, pp. 84–90, 2015.
- [16] H. Wang, *Study on the Strata Behavior Characteristics of Fully Mechanized Caving under the Goaf of Continuous Seam Group*, p. 14, Liaoning Technical University, Fuxin, China, 2016.
- [17] F. K. Xiao, L. Q. Duan, and Z. H. Ge, "Laws of floor breaking in coal mining face and gas extraction application," *Journal of China Coal Society*, vol. 35, no. 3, pp. 417–419, 2010.
- [18] M. Xiangrui, X. Chenghui, G. Zhaoning, G. Zhaoning, and W. Xiangqian, "Stress distribution and damage mechanism of

- mining floor,” *Journal of China Coal Society*, vol. 35, no. 11, pp. 1832–1836, 2010.
- [19] H. Zhang, *Study on Stress Transmission Laws of Mining Floor and its Influence on Stability of Floor Roadway*, pp. 11–14, China University of Mining and Technology, Xuzhou, China, 2011.
- [20] F. Qi, *Study on the Deformation Mechanism and Control of Surrounding Rock with Roof Cutting and Pressure Re-leasing in High Stress Roadway Driving along Next Goaf*, China University of Mining and Technology, Xuzhou, China, pp. 73–74, 2020.
- [21] M. Shabanimashcool and C. C. Li, “Numerical modelling of longwall mining and stability analysis of the gates in a coal mine,” *International Journal of Rock Mechanics and Mining Sciences*, vol. 51, pp. 24–34, 2012.
- [22] D. N. Whittles, I. S. Lowndes, S. W. Kingman, C. Yates, and S. Jobling, “Influence of geotechnical factors on gas flow experienced in a UK longwall coal mine panel,” *International Journal of Rock Mechanics and Mining Sciences*, vol. 43, no. 3, pp. 369–387, 2006.
- [23] Z. Zhang, J. Bai, Y. Chen, and S. Yan, “An innovative approach for gob-side entry retaining in highly gassy fully-mechanized longwall top-coal caving,” *International Journal of Rock Mechanics and Mining Sciences*, vol. 80, pp. 1–11, 2015.
- [24] H. Yavuz, “An estimation method for cover pressure re-establishment distance and pressure distribution in the goaf of longwall coal mines,” *International Journal of Rock Mechanics and Mining Sciences*, vol. 41, no. 2, pp. 193–205, 2004.
- [25] L. R. Alejano and E. Alonso, “Considerations of the dilatancy angle in rocks and rock masses,” *International Journal of Rock Mechanics and Mining Sciences*, vol. 42, no. 4, pp. 481–507, 2005.
- [26] W. Li, J. Bai, S. Peng, X. Wang, and Y. Xu, “Numerical modeling for yield pillar design: a case study,” *Rock Mechanics and Rock Engineering*, vol. 48, no. 1, pp. 305–318, 2015.
- [27] B. G. D. Smart and S. M. Haley, “Further development of the roof strata tilt concept for pack design and the estimation of stress development in a caved waste,” *Mining Science and Technology*, vol. 5, no. 2, pp. 121–130, 1987.

Research Article

A Novel Evaluation Method of Hydrogen Production from Coal Based on AHP and GRA-TOPSIS

Shuheng Zhong,¹ Kangdi Yang ,¹ and Yongji Wang^{1,2}

¹School of Energy and Mining Engineering, China University of Mining and Technology, Beijing, 10083, China

²China Association for Science and Technology Enterprise Innovation Service Center, Beijing, 100026, China

Correspondence should be addressed to Kangdi Yang; 23220106@qq.com

Received 22 August 2021; Accepted 23 September 2021; Published 4 October 2021

Academic Editor: Gaofeng Song

Copyright © 2021 Shuheng Zhong et al. This is an open access article distributed under the Creative Commons Attribution License, which permits unrestricted use, distribution, and reproduction in any medium, provided the original work is properly cited.

Coal is the cornerstone of China's energy. However, with the proposed goal of carbon peak and carbon-neutral in China, coal enterprises are in urgent need of exploring the path of transformation. Coal to hydrogen is an important way to achieve sustainable development of the coal industry. In this paper, four hydrogen production technologies, including coal gasification, coke oven gas, electrolytic water, and solar energy, are studied. A comprehensive evaluation model based on GRA-TOPSIS was constructed. The research shows that the coke oven gas is the most suitable hydrogen production technology for the transformation and development of coal enterprises. The evaluation model of hydrogen production technology in the transformation and development of coal enterprises constructed in this paper has a certain guiding effect on the technology selection of coal enterprises in the development of the hydrogen industry.

1. Introduction

On March 5, 2021, the government work report stated that this year China will make solid efforts to achieve a carbon peak and carbon neutrality and formulate an action plan to achieve a carbon peak by 2030. Optimizing industrial structure and energy structure is the main means to promote carbon peak and carbon-neutral in the overall realization of the carbon-neutral goal. In the past decade and for a period of time in the future, China's energy structure is still dominated by coal [1]. Under the background of China's "carbon peak by 2030" and "carbon-neutral by 2060" goals, large state-owned enterprises, especially energy enterprises, are facing the urgent need of low-carbon transformation, and hydrogen energy is one of the important directions of their transformation [2,3]. It is of great significance to realize the efficient and clean utilization of coal resources, not only for the transformation and development of enterprises but also for the acceleration of national carbon peak and carbon-neutral work.

According to the 14th five-year plan, hydrogen energy has been included in the strategic development position as an important industry in the future [4]. China's hydrogen mainly comes from natural gas or coal to produce hydrogen, coke oven gas, and so on. The vast majority are blue hydrogen and gray hydrogen. The green hydrogen project is currently in the demonstration stage. With the guidance of China's policies and the implementation of a large number of hydrogen energy projects, the hydrogen energy technology continues to break through, the industrial system is gradually improved, and the development of the hydrogen energy field in China has accelerated into the industrialization stage.

Hydrogen energy can be produced from various resources, using different raw materials, methods, and technologies, including fossil fuels and renewable resources [5–7]. Meanwhile, China is rich in coal resources, and hydrogen production from coal is the main form of hydrogen production in China [8], which can significantly increase the added value of coal products [9–12].

However, hydrogen production technology is complex, and the transformation and development of energy enterprises often require comprehensive consideration from multiple aspects. Therefore, a comprehensive evaluation system model based on energy, economy, environment, technology, and society has been established based on the comprehensive study of hydrogen technology selection of various hydrogen production technologies. In view of the mainstream mature hydrogen production technology and the consideration of renewable energy utilization, four hydrogen production technologies including coal gasification hydrogen production, coke oven gas hydrogen production, water electrolysis hydrogen production, and solar energy hydrogen production were selected for a comprehensive evaluation, to obtain the optimal hydrogen production technology through hydrogen energy transformation and upgrading of energy enterprises. It is of great significance to the transformation and upgrading of the coal industry and coal chemical industry which take hydrogen as the breakthrough point.

2. Literature Review

The technical economy is the internal driving force in the development of coal industry transformation; there are many influential factors in the technology economy; the need for multiple factors and changes impacts the economy analysis [13]. Building the corresponding technical and economic evaluation model, for many factors, at the same time tries to realize the evaluation process of standardization and automation in order to facilitate the comparative analysis between evaluation results and between evaluation results and samples [14].

Deciding how to assess hydrogen production technology scientifically is a problem that needs to be handled. In general, there are two types of methods to solve this problem: (1) synthetical assessment approaches, e.g., weighted sum, analytical hierarchy process (AHP) [15], and the technique for order performance by similarity to ideal solution (TOPSIS) [16]. AHP and evidential reasoning, AHP and TOPSIS, and fuzzy synthetic evaluation are (2) the approaches based on theory of life cycle assessment [17, 18].

Li Yiyang established a model applicable to the evaluation system of hydrogen production technology by using the life cycle evaluation theory, which included the evaluation of material consumption, energy consumption, environment, and economy [19]. The research results showed that the comprehensive benefit of hydrogen production from biomass supercritical water gasification was the highest. Luo Bing introduced the two main methods of hydrogen production from biomass, namely, thermalization method and microbial conversion method, from the aspects of hydrogen production mechanism, technological process, existing problems, and development prospects. After comparing and understanding several hydrogen production methods, it is found that the hydrogen production technology from biomass is the most efficient and environmental protection technology, which can not only optimize the fuel structure and improve the air pollution status in China but

also reduce the secondary pollution caused by the unreasonable utilization mode at present [20]. Xie Xinshuo used traditional hydrogen production technologies (gasification hydrogen production, natural gas hydrogen production, and so on) and new hydrogen production technologies (thermochemical hydrogen production, renewable energy power generation hydrogen production, biomass gasification hydrogen production, and so on) as the object; the research on its life cycle assessment shows that wind power hydrogen production technology has the best environmental protection, and nuclear thermochemical hydrogen production has the potential for large-scale application in the future [21]. Niu Jiao established an evaluation model based on an improved fuzzy evaluation method. The hydrogen production technology with the highest comprehensive benefit is natural gas steam reforming hydrogen production technology, and the hydrogen production technology with the lowest comprehensive benefit is hydrogen production by electrolysis of water [22].

The above research results are a single or multidimensional systematic evaluation of various hydrogen-making technologies by experts and scholars, but the actual application of hydrogen-making technology in a certain field has not been fully considered. Under the current background of “carbon peak and carbon neutrality” and restricted by foreign technology, the traditional 3E evaluation model cannot better reflect the influence of technical factors and social factors [23]. The olefin industry is evaluated based on the 3E model, but it does not reflect the impact of its social and technological factors [24]. Hence, coal enterprises urgently need a set of scientific, comprehensive, and targeted evaluation indicators and evaluation methods. Therefore, this article adds two dimensions of technology and society to the analysis of the 3E model, that is, comprehensive analysis of each hydrogen production technology from the five dimensions of energy, economy, environment, technology, and society and combines with a specific mining group for practical applications.

3. Impact Analysis and Model Construction

3.1. Impact Analysis. Considering the complexity of hydrogen production technology, in this section, we provide theoretical support for the model establishment in Section 3.2 by analyzing the influencing factors at five different levels of hydrogen production technology.

The influence of hydrogen technology in the energy dimension is mainly reflected in the influence of resource suitability, hydrogen efficiency, and the proportion of end-energy consumption change and the proportion of clean energy consumption increase. Therefore, the applicability of resources, hydrogen efficiency, and the proportion of changes in end-use energy consumption are introduced as indicators in energy.

Compared with other energy sources, the cost gap between various types of hydrogen technology is large. At the same time, in order to simplify the calculation, the investment cost of hydrogen plant construction is used as a

separate index. Therefore, the following economic influencing factors were used to establish the indicator: (1) the cost per unit of hydrogen production; (2) investment costs; (3) gross enterprise product.

In the environmental impact of the main performance in the “three wastes,” that is, “emissions, waste residue, waste water,” the most significant environmental impact is the emission of exhaust gases; therefore, in the environmental impact factor subsystem, CO₂ and NOX emissions (kg) are used to better reflect the environmental impact factor.

The main connotation of hydrogen production technology is the advanced degree of technology, the hydrogen purity index reflects the advanced degree of technology, and the proportion of scientific researchers indirectly reflects the development level of high and new technology. Secondly, external dependence and technology maturity of technology are the important basis for the long-term development of China’s coal enterprises [25, 26].

3.2. Model Construction. As a new energy source, hydrogen production technology has abundant sources of raw materials and complex hydrogen production processes. There are relatively few research studies on the development of hydrogen energy technology by coal companies. It is reasonable to plan and deploy various technologies in different periods and regions. For issues such as the order of development of hydrogen production, it is necessary to conduct an objective and scientific evaluation of various hydrogen production technologies. Therefore, the premise of the evaluation is to establish a scientific and reasonable evaluation index system. Based on the analysis of influencing factors in Section 3.1, the following comprehensive evaluation index system is established, as shown in Table 1.

3.2.1. Standardized Processing of Indicators

- (1) *Standardized Treatment of Indicators.* In the comprehensive evaluation, due to the existence of different types of qualitative and quantitative indicators, or the value gap between the indicators, the original indicators affect the accuracy of the evaluation in the calculation and analysis. The presence of indicators with high numerical values has a greater impact on the whole, and the role of indicators with lower numerical levels is relatively weakened. Therefore, we need to standardize all indicators to improve the accuracy of the results. In this paper, the indicator is standardized by the extreme difference method.
- (2) *Consistent Processing of Indicator Types.* In the comprehensive evaluation of multiple indicators, some are indicators with higher indicator values, called positive indicators, and some are indicators with smaller indicator values that evaluate the better, called reverse indicators. First of all, the indicator must be trended, generally the reverse indicator into

a positive indicator, which is the consistent processing of the indicator type.

3.2.2. Comparison Based on AHP and GRA-TOPSIS. The article chooses the analytic hierarchy process to determine the weights. There are two advantages to determine the weights through the analytic hierarchy process. First, the data requirements for determining the weights through the analytic hierarchy process are relatively small, and it is relatively simple in actual operation. The indicators are analyzed systematically to improve accuracy.

In order to overcome the shortcomings of gray correlation and Technique for Order Preference by Similarity to an Ideal Solution (TOPSIS) method, this paper combines the characteristics of the two methods and integrates the two methods organically. Considering that the traditional TOPSIS method evaluates the schemes according to the Euclidean distance, sometimes it cannot fully reflect the pros and cons of the schemes, and it cannot reflect the difference between the changing trends of various factors within the sample and the ideal sample. Therefore, this paper constructs the gray correlation and TOPSIS (GRA-TOPSIS), makes full use of the characteristics of the gray correlation degree to reflect the situation change between the plan data curves and the similarity of the curve geometry, combines the Euclidean distance and the gray correlation degree, and constructs one from the two aspects of position and shape. This new relative closeness makes up for the shortcomings of the TOPSIS method. This method has clear thought, simple calculation, and strong practicability which we call it AHP and GRA-TOPSIS. The key calculation steps are as follows:

- (1) Dimensionless procession of indicators: the data outline of each indicator is not consistent in order to eliminate the impact of the data outline and the convenience of research to standardize the data, in which the positive indicator refers to the evaluation results that play a positive role in promoting the indicators, and such indicators belong to the larger the better indicators. Conversely, negative indicators refer to indicators that play a negative role in promoting evaluation results and are among the smaller and better indicators.

Positive indicator is as follows:

$$x'_{ij} = \frac{x_{ij} - x_{\min}}{x_{\max} - x_{\min}}. \quad (1)$$

Negative indicator is as follows:

$$x'_{ij} = \frac{x_{\max} - x_{ij}}{x_{\max} - x_{\min}}. \quad (2)$$

- (2) Build a decision matrix: M evaluation objects and N evaluation indexes are set, and the original decision matrix is $X = (x_{ij})_{m \times n}$.
- (3) Weighted normalized matrix of evaluation indicators is as follows:

TABLE 1: Comprehensive evaluation index system of hydrogen production technology.

| Goal level (G) | Criterion level (A) | Factor level (B) |
|---|--|--|
| Comprehensive evaluation index system of hydrogen production technology (I) | Energy (A ₁) | Resource suitability (b ₁₁) |
| | | Hydrogen production efficiency (b ₁₂) |
| | | The proportion of end-user energy consumption changes (b ₁₃) |
| | | Increased share of clean energy consumption (b ₁₄) |
| | Economic (A ₂) | The cost per unit of hydrogen production (b ₂₁) |
| | | Investment costs (b ₂₂) |
| | Environment (A ₃) | Gross domestic product (b ₂₃) |
| | | Wastewater emissions (b ₃₁) |
| | | Slag emissions (b ₃₂) |
| | | CO ₂ emissions (b ₃₃) |
| NO _x emissions (b ₃₄) | | |
| Technology (A ₄) | Technical reliability (b ₄₁) | |
| | Hydrogen purity (b ₄₂) | |
| Social (A ₅) | The proportion of researchers (b ₄₃) | |
| | External dependence of technology (b ₄₄) | |
| | Technical maturity (b ₄₅) | |
| | | Policy applicability (b ₅₁) |
| | | Social recognition (b ₅₂) |

$$Z = (\omega_j y_{ij})_{m \times n}$$

$$= \begin{bmatrix} \omega_1 y_{11} & \omega_2 y_{12} & \cdots & \omega_n y_{1n} \\ \omega_1 y_{21} & \omega_2 y_{22} & \cdots & \omega_n y_{2n} \\ \vdots & \vdots & \ddots & \vdots \\ \omega_1 y_{m1} & \omega_2 y_{m2} & \cdots & \omega_n y_{mn} \end{bmatrix}. \quad (3)$$

- (4) Determine the positive ideal solution and negative ideal solutions of the weighted normalization matrix:

$$\begin{aligned} Z^+ &= (Z_1^+, Z_2^+, \dots, Z_n^+) \\ &= \omega, \\ Z^- &= (Z_1^-, Z_2^-, \dots, Z_n^-) \\ &= 0. \end{aligned} \quad (4)$$

In this formula,

$$\begin{aligned} Z_j^+ &= \max Z_{ij} = \omega_j, \\ Z_j^- &= \min Z_{ij} = 0, \quad j \in N. \end{aligned} \quad (5)$$

- (5) Calculate the Euclid distance between the schemes and the positive ideal solution and negative ideal solutions as follows:

$$\begin{aligned} d_i^+ &= \sqrt{\sum_{j=1}^n (Z_{ij} - Z_j^+)^2} \\ d_i^- &= \sqrt{\sum_{j=1}^n (Z_{ij} - Z_j^-)^2}. \end{aligned} \quad (6)$$

- (6) Calculate the gray correlation coefficient matrix between each scheme and the positive ideal solution and the negative ideal solution R^+ and R^- as follows:

$$R^+ = (r_{ij}^+)_{m \times n}, R^- = (r_{ij}^-)_{m \times n},$$

$$r_{ij}^+ = \frac{\min_i \min_j |z_j^+ - z_{ij}^+| + \varepsilon \max_i \max_j |z_j^+ - z_{ij}^+|}{|z_j^+ - z_{ij}^+| + \varepsilon \max_i \max_j |z_j^+ - z_{ij}^+|}, \quad (7)$$

$$r_{ij}^- = \frac{\min_i \min_j |z_j^- - z_{ij}^-| + \varepsilon \max_i \max_j |z_j^- - z_{ij}^-|}{|z_j^- - z_{ij}^-| + \varepsilon \max_i \max_j |z_j^- - z_{ij}^-|}.$$

In this formula, $\varepsilon \in (0, 1)$ is the resolution factor, and experience is valued at 0.5.

- (7) Calculate the gray correlation between each scheme and the positive and negative ideal solutions as follows:

$$\begin{aligned} r^+ &= \frac{1}{n} \sum_{j=1}^n r_{ij}^+, \\ r^- &= \frac{1}{n} \sum_{j=1}^n r_{ij}^-. \end{aligned} \quad (8)$$

- (8) Euclid distance and correlation degree are dimensionless as follows:

$$\begin{aligned} D_i^+ &= \frac{d_i^+}{\max d_i^+}, \\ D_i^- &= \frac{d_i^-}{\max d_i^-}, \\ R_i^+ &= \frac{r_i^+}{\max r_i^+}, \\ R_i^- &= \frac{r_i^-}{\max r_i^-}. \end{aligned} \quad (9)$$

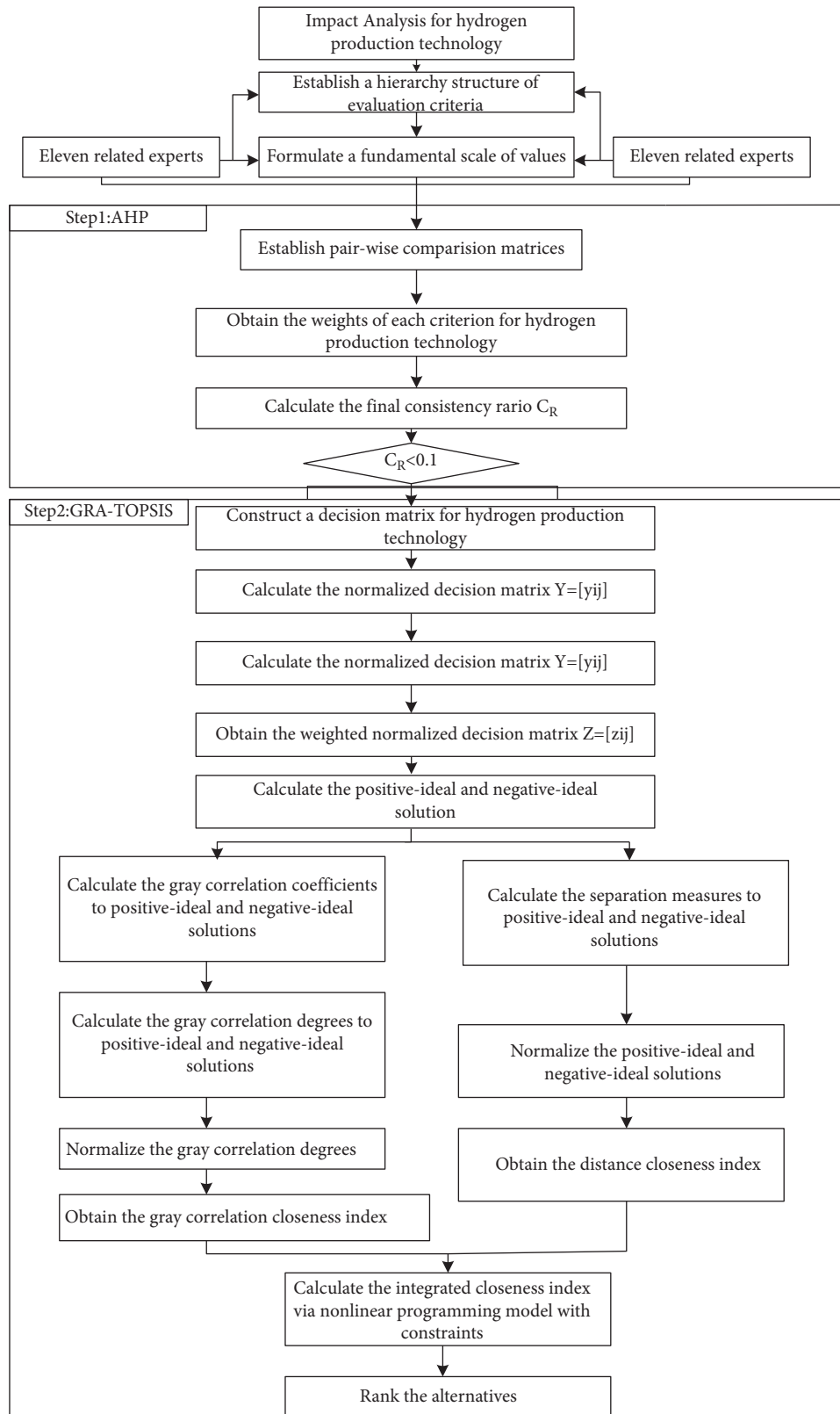


FIGURE 1: Model frame diagram.

TABLE 2: Weight value of the comprehensive evaluation index of hydrogen production technology.

| Goal level | Criterion level (A) | Weight (W_i) | Factor level (B) | Weight (W_{ii}) | Comprehensive weights |
|--------------------------|---------------------|------------------|------------------|---------------------|-----------------------|
| Comprehensive evaluation | A ₁ | 0.3719 | b_{11} | 0.4420 | 0.1644 |
| | | | b_{12} | 0.3436 | 0.1278 |
| | | | b_{13} | 0.0994 | 0.0370 |
| | A ₂ | 0.1651 | b_{14} | 0.1150 | 0.0428 |
| | | | b_{21} | 0.7003 | 0.1156 |
| | | | b_{22} | 0.2230 | 0.0368 |
| | | | b_{23} | 0.0767 | 0.0127 |
| | A ₃ | 0.2854 | b_{31} | 0.2014 | 0.0575 |
| | | | b_{32} | 0.1559 | 0.0445 |
| | | | b_{33} | 0.3535 | 0.1009 |
| | | | b_{34} | 0.2892 | 0.0825 |
| | A ₄ | 0.1074 | b_{41} | 0.2810 | 0.0302 |
| | | | b_{42} | 0.2828 | 0.0304 |
| | | | b_{43} | 0.0693 | 0.0074 |
| | | | b_{44} | 0.0903 | 0.0097 |
| b_{45} | | | 0.2766 | 0.0297 | |
| A ₅ | 0.0703 | b_{51} | 0.6562 | 0.0461 | |
| | | b_{52} | 0.3438 | 0.0242 | |

TABLE 3: Dimensionless processing results.

| Scheme | D_i^+ | D_i^- | R_i^+ | R_i^- |
|--------------------|---------|---------|---------|---------|
| Coal gasification | 0.9241 | 0.8306 | 0.9975 | 0.8807 |
| Coke oven gas | 0.5057 | 1.0000 | 1.0000 | 0.8696 |
| Electrolytic water | 1.0000 | 0.9589 | 0.9255 | 1.0000 |
| Solar | 0.8778 | 0.8331 | 0.9615 | 0.9229 |

TABLE 4: Comparison with AHP-TOPSIS and AHP-GC.

| Scheme | AHP-TOPSIS | AHP-GC | AHP-GC&TOPSIS |
|--------------------|-------------|------------|---------------|
| Coal gasification | 0.473357269 | 0.4689064 | 0.5032 |
| Coke oven gas | 0.664142924 | 0.46512623 | 0.5925 |
| Electrolytic water | 0.489509419 | 0.51934562 | 0.4851 |
| Solar | 0.4869367 | 0.48975801 | 0.4992 |

TABLE 5: Comprehensive evaluation and ranking table of hydrogen production technical scheme.

| Scheme | P_i^+ | P_i^- | Relative closeness | Rank |
|--------------------|---------|---------|--------------------|------|
| Coal gasification | 0.9140 | 0.9024 | 0.5032 | 2 |
| Coke oven gas | 1.0000 | 0.6877 | 0.5925 | 1 |
| Electrolytic water | 0.9422 | 1.0000 | 0.4851 | 4 |
| Solar | 0.8973 | 0.9004 | 0.4992 | 3 |

(9) Combine dimensionless distance and correlation degree. The greater the D_i^- and R_i^+ is, the closer the scheme is to the positive ideal solution. The larger the D_i^+ and R_i^- is, the farther away the scheme is from the positive ideal solution. Therefore, the combination formula can be determined as follows:

$$P_i^+ = \alpha D_i^- + \beta R_i^+, P_i^- = \alpha D_i^+ + \beta R_i^- \quad (10)$$

In this formula, $\alpha = \beta = 1/2$.

(10) Relative closeness of the construction scheme is as follows:

$$Q_i^+ = \frac{P_i^+}{P_i^+ + P_i^-} \quad (11)$$

(11) The relative closeness degree Q_i^+ of each scheme was calculated and ranked. The greater the relative closeness degree was, the closer it was to 1, indicating the higher the evaluation of the scheme was. On the contrary, the lower the relative closeness, the worse the scheme.

In order to explain the model more intuitively, the model frame diagram is shown as follows (see Figure 1).

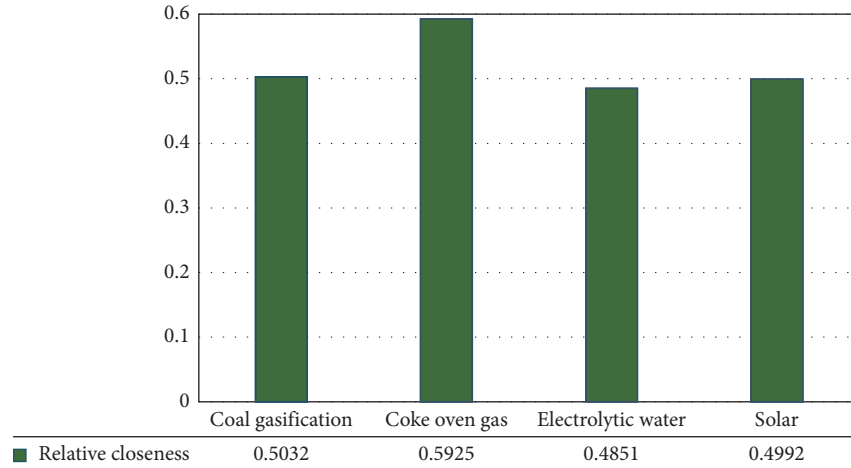


FIGURE 2: Relative closeness of comprehensive evaluation of hydrogen production technology.

4. Application

In this section, the use of AHP and Gray Correlation Ideal Solution is illustrated by evaluating the hydrogen production technologies in a certain mining group. The mining group is a modern enterprise group that spans regions and industries. It is actively exploring the application of hydrogen purification and storage technology and the industrial production of hydrogen fuel cells.

4.1. Data Collection. The data and related information come from enterprises such as experts, scholars, and university experts with professional knowledge and management experience. Through the questionnaires collected in this study, 11 experts were consulted, and the comparison matrix for each standard was matched and used to evaluate the decision matrix hydrogen production technology. The four alternatives can make the evaluation results more in line with the development of the mining group.

4.2. Hierarchical Structure of Hydrogen Production Technologies Evaluation. Based on the related literature and expert interview, five kinds of dimensions and their parameters have been given. We establish a hierarchical structure for their comprehensive evaluation, which is shown in Table 2.

4.3. Comprehensive Evaluation Based on Gray Correlation-TOPSIS Method. According to the formula, the gray association between each scheme and the positive and negative ideal solution is calculated as follows:

$$\begin{aligned} r^+ &= [0.8436 \ 0.8458 \ 0.7828 \ 0.8132], \\ r^- &= [0.7555 \ 0.7459 \ 0.8578 \ 0.7917]. \end{aligned} \quad (12)$$

Euclid distance and gray relational degree were dimensionless and were obtained D_i^+ , D_i^- and R_i^+ , R_i^- . The results are shown in Table 3.

According to formula (10), scale distance and correlation degree will not be combined. Finally, according to formula (11), the relative proximity of the hydrogen scheme samples is constructed, and according to the size of the relative schedule, the samples are sorted; the closer the proximity 1, the better the scheme.

4.4. Results and Analysis. In this paper, the AHP-TOPSIS method and AHP-GC method are used to compare the results of the proposed methods. The weight of each influencing factor adopted by the three methods is the same. The closeness index results of the three methods are shown in Table 4.

It can be seen from Table 4 that the results of the three methods are basically consistent and close, which shows that the proposed AGT is reasonable and feasible to evaluate the performance of the design scheme. Because the gray closeness index of Option 1 and Option 2 is similar, AHP-GC cannot determine the best solution between Option 1 and Option 3, and AGT can do this. In other words, the result of AGT is a comprehensive evaluation value of AHP-TOPSIS and AHP-GC. When evaluating the performance of the design plan, a mixed feature involving positional relationship and situation changes between data sequences is used. Therefore, the AGT method overcomes the one-sidedness of the AHP-TOPSIS and AHP-GC methods and makes the evaluation results more objective and true.

Through the previous evaluation and research on various hydrogen production technologies, the ranking of the comprehensive evaluation of various hydrogen production technologies has been obtained. Now, the research results are further analyzed, and the ranking is as shown in Table 5.

It can be seen from Figure 2 that coke oven gas hydrogen production is the most closely related hydrogen production technology, with a closeness of 0.5925, indicating that coke oven gas hydrogen production is the preferred hydrogen production technology for a mining group's transformation and development of hydrogen energy. On the one hand, because coke oven gas is compared with the traditional hydrogen production method,

hydrogen extraction is not only a more environmentally friendly comprehensive utilization of resources but also has very considerable economic benefits; on the other hand, in the example, coal enterprises are the mainstay, and the output of coke oven gas is abundant. Through reasonable purification technology, hydrogen energy can be produced on a large scale, compared with electrolysis of water to produce hydrogen, and the cost is low. The second in the ranking of relative closeness is the traditional coal gasification hydrogen production, which has already been produced on a large scale in China, with relatively mature technology and low cost, but there are also problems such as high carbon emissions and many gas impurities. The hydrogen production technology ranked last is hydrogen production by electrolysis of water, with a relative closeness of 0.4851.

5. Conclusions

This paper takes coal gasification hydrogen production, coke oven gas hydrogen production, electrolysis water hydrogen production, and solar hydrogen production as the research objects and conducts a multidimensional comprehensive evaluation by constructing a multilevel comprehensive evaluation index system. At the same time, the model was verified based on the actual situation of a certain mining group, and the following conclusions were drawn.

The GRA-TOPSIS method is used to construct a comprehensive evaluation model of hydrogen production technology. By combining Euclidean distance and gray correlation, a new relative closeness is constructed from two aspects of position and shape, which can make up for the respective defects of GRA and TOPSIS; through calculations according to the comprehensive closeness of various hydrogen production technologies, the comprehensive closeness of coke oven gas hydrogen production technology is the highest, which is the most suitable hydrogen production technology choice for a certain mining group's hydrogen energy development, followed by coal gasification hydrogen production technology; this model can provide a certain theoretical basis for coal enterprises to select hydrogen production technology as a breakthrough point for transformation.

There are still some shortcomings in the research of this paper, and future research can be further deepened and broadened. In this research, the qualitative indicators are quantified by the expert scoring method and the range method. However, with the improvement of national policies and the development of hydrogen production technology, related cognition and data will also change. A more scientific and comprehensive evaluation model is still needed to adapt to future development; as currently emerging hydrogen production technologies such as biomass hydrogen production have certain difficulties in data collection, with the deepening of relevant research, a more comprehensive approach can be considered. Other emerging hydrogen production technologies could be included in the research object.

Data Availability

The data that support the findings of this study are available from the corresponding author, Kangdi Yang, upon reasonable request.

Disclosure

To make the research open and transparent, a preprinted version of this manuscript was placed in Research Square [27]. The authors have cited this version in the last and hope to update its link.

Conflicts of Interest

The authors declare that there are no conflicts of interest.

Acknowledgments

The authors wish to acknowledge financial support from the National Key Research and Development Plan (Grant no. 2017YFC1503103).

References

- [1] R. Ding, X. Zhou, R. Zhang, and W. Lu, "Research on the measurement and countermeasure of coal overcapacity in China: based on panel data of 25 provinces in China," *Energy Engineering*, vol. 117, no. 1, pp. 27–39, 2020.
- [2] C. Dga, A. Fb, B. Ds, C. Mdb, A. Nw, and A. &Rg, "The role of renewable energy in the global energy transformation-science direct," *Energy Strategy Reviews*, vol. 24, pp. 38–50, 2019.
- [3] D. Parra and L. Valverde, F. J. Prino and K Martin, "A review on the role, cost and value of hydrogen energy systems for deep decarbonisation," *Renewable & Sustainable Energy Reviews*, vol. 101, pp. 279–294, 2019.
- [4] The Central People's Government of the People's Republic of China, "The Fourteenth Five-Year Plan for the National Economic and Social Development of the People's Republic of China and the Outline of the Long-Term Goals for 2035," 2021, http://www.gov.cn/xinwen/2021-03/13/content_5592681.htm.
- [5] J. L. Silveira, *Sustainable Hydrogen Production Processes*, Springer, Berlin, Germany, 2017.
- [6] M. El-Shafie, S. Kambara, and Y. Hayakawa, "Hydrogen production technologies overview," *Journal of Power and Energy Engineering*, vol. 7, no. 1, pp. 107–154, 2019.
- [7] N. Saithong, S. Authayanun, Y. Patcharavorachot, and A. Arpornwichanop, "Thermodynamic analysis of the novel chemical looping process for two-grade hydrogen production with CO₂ capture," *Energy Conversion and Management*, vol. 180, pp. 325–337, 2019.
- [8] S. Chai, G. Zhang, G. Li, and Y. Zhang, "Industrial hydrogen production technology and development status in China: a review," *Clean Technologies and Environmental Policy*, vol. 23, no. 7, pp. 1931–1946, 2021.
- [9] A. X. Y. Mah, W. S. Ho, C. P. C. Bong et al., "Review of hydrogen economy in Malaysia and its way forward," *International Journal of Hydrogen Energy*, vol. 44, no. 12, pp. 5661–5675, 2019.
- [10] J. Wang, W. Wei, and J. Zhang, "Theoretical description of drawing body shape in an inclined seam with longwall top

- coal caving mining,” *International Journal of Coal Science & Technology*, vol. 7, no. 1, pp. 182–195, 2020.
- [11] J. Wang, S. Yang, W. Wei, J. Zhang, and Z. Song, “Drawing mechanisms for top coal in longwall top coal caving (LTCC): a review of two decades of literature,” *International Journal of Coal Science & Technology*, 2021.
- [12] H. Wu, D. Ma, A. J. S. Spearing, and GuoyanZhao, “Fracture phenomena and mechanisms of brittle rock with different numbers of openings under uniaxial loading,” *Geomechanics and Engineering*, vol. 25, no. 6, pp. 481–493, 2021.
- [13] Y. Y. Zhang, *Research on the Carbon Emissions of Modern Coal Chemical Industry and its Economic Impact (PhD Dissertation)*, China University of Mining and Technology, Xuzhou, Beijing, China, 2017, <https://kns.cnki.net/KCMS/detail/detail.aspx?dbname=CDFDLAST2018&filename=1017237807>.
- [14] B. Hu and Y. J. Han, “Modeling of technical and economic evaluation of coal upstream industrial chain projects,” *Coal Economic Research*, vol. 36, no. 5, pp. 49–54, 2016.
- [15] T. L. Saaty, “How to make a decision: the analytic hierarchy process,” *European Journal of Operational Research*, vol. 48, no. 1, pp. 9–26, 1994.
- [16] C.-T. Chen, “Extensions of the topsis for group decision-making under fuzzy environment,” *Fuzzy Sets and Systems*, vol. 114, no. 1, pp. 1–9, 2000.
- [17] S. Prince-Richard, M. Whale, and N. Djilali, “A techno-economic analysis of decentralized electrolytic hydrogen production for fuel cell vehicles,” *International Journal of Hydrogen Energy*, vol. 30, no. 11, pp. 1159–1179, 2005.
- [18] P. Konstantopoulou, D. Giannopoulos, and M. &Founti, “Multicriteria analysis of hydrogen production technologies,” in *Proceedings of the International Hydrogen Energy congress and Exhibition IHEC*, Ankara, Turkey, July 2005.
- [19] Y. Li, “Several Hydrogen Production Methods of Life Cycle Assessment Studies,” Master’s Degree Thesis, xian building university of science and technology, Hefei, China, 2010.
- [20] B. Luo, Y. Zhou, B. Yu, R. Xiao, and C. Yang, “Comparison of chemical and biological hydrogen production processes,” *Ceramic*, vol. 12, no. 1, pp. 23–28, 2019, <https://www.energy.gov/eere/fuelcells/hydrogen-production-processes>.
- [21] XieXinshuo, W. Yang, W. Shi, S. Zhang, Z.& Wang, and J. Zhou, “Progress in life cycle assessment of hydrogen production technology,” *Chemical Industry Progress*, vol. 37, no. 6, pp. 2147–2158, 2018.
- [22] J. Niu, “Study on System Evaluation System of Hydrogen Production Technology,” Master Thesis, Beijing University of Chemical Technology, Beijing, China, 2007.
- [23] Y.-J. Xing, T.-L. Chen, M.-Y. Gao, S.-L. Pei, W.-B. Pan, and P.-C. Chiang, “Comprehensive performance evaluation of green infrastructure practices for urban watersheds using an engineering-environmental-economic (3E) model,” *Sustainability*, vol. 13, no. 9, p. 4678, 2021.
- [24] M. Dai, F. Yang, Z. Zhang, G. Liu, and X. Feng, “Energetic, economic and environmental (3E) multi-objective optimization of the back-end separation of ethylene plant based on adaptive surrogate model,” *Journal of Cleaner Production*, vol. 310, Article ID 127426, 2021.
- [25] D. Z. Kong, S. J. Pu, Z. H. Cheng, G. Y. Wu, and Y. Liu, “Coordinated deformation mechanism of the top coal and filling body of gob-side entry retaining in a fully mechanized caving face,” *International Journal of Geomechanics*, vol. 21, no. 4, 2021.
- [26] F. Wen, “The Fuel Cell Car Hydrogen System Evaluation and Case Study of Beijing,” A Master’s Degree Thesis, tsinghua university, Beijing, China, 2003.
- [27] S. Zhong and K. Yang, “Comprehensive Evaluation of Hydrogen Production from Coal Base on AHP& GRA-TOPSIS,” 06 May 2021, https://assets.researchsquare.com/files/rs-480265/v1_covered.pdf?c=1631865863.